UNIVERSITY OF CAMBRIDGE

Department of Materials Science and Metallurgy

Lithium-based inorganic-organic framework materials

Hamish Hei-Man Yeung

Saint Catharine's College

A dissertation submitted for the degree of Doctor of Philosophy

Preface

This dissertation is submitted for the degree of Doctor of Philosophy at the University of Cambridge, UK. The research described herein was carried out by myself in the period October 2008 to July 2012, under the supervision of Prof. Anthony K. Cheetham, Goldsmith's Professor of Materials Science, Department of Materials Science and Metallurgy, University of Cambridge.

To the best of my knowledge, the work described in this dissertation is original, except where due reference has been made to the work of others. This dissertation is my own work and contains nothing which is the outcome of work done in collaboration with others, except as specified in the text.

No part of this dissertation, or any similar to it, has been, or is currently being submitted for any degree at this, or any other university.

This dissertation is less than 60,000 words in length.

I have also i) resided in Cambridge for at least three terms, ii) undertaken the minimum requirements of research terms, iii) submitted this thesis by my submission date, and iv) formally applied for examiners to be appointed.

Hamish Hei-Man Yeung

Cambridge

September 2012

Final version with minor corrections November 2012

Abstract

This dissertation describes research into lithium-based inorganic-organic frameworks, which has led to an increased understanding of the structural diversity and properties of these materials. The crystal structures of 11 new forms of lithium tartrate, based on chiral, racemic and *meso* forms of the ligand, have been discovered, including eight anhydrous isomers of dilithium tartrate, $Li_2(C_4H_4O_6)$. An experimental and computational study of their formation behaviour and energetics has shown that both kinetic and thermodynamic conditions can be used to control their phase behaviour, and the main structural factors affecting their relative energies were found to be density and hydrogen bonding.

Three crystal structures topologically identical to lithium succinate, $Li_2(C_4H_4O_4)$, have been discovered using substituted forms of the ligand: lithium L-malate, $Li_2(C_4H_4O_5)$, lithium methylsuccinate, $Li_2(C_5H_6O_4)$, and lithium tetrafluorosuccinate, $Li_2(C_4F_4O_4)$. The cell parameters and mechanical properties of these non-porous frameworks were found to depend on inter-ligand interactions and metal-ligand bond strength. The effects of different ligand substituents on the atomic structure of the binary mixed-ligand solid solution, $Li_2(\text{succinate})_{1-x}(\text{tetrafluorosuccinate})_x$, and the ternary system, $Li_2(\text{succinate})_x(\text{L-malate})_y(\text{methylsuccinate})_z$ [where $(x + y + z) = 1$], have also been investigated. Topotactic dehydration of the ligand in lithium L-malate results in the formation of $Li_2(\text{L-malate})_{1-x}(\text{fumarate})_x$, suggesting a new route to mixed-ligand inorganic-organic frameworks.

Investigation into frameworks based on other dicarboxylate ligands produced four structurally diverse lithium-based inorganic-organic frameworks: 2-D frameworks lithium 2,2-dimethylsuccinate, $Li_2(C_6H_8O_4)$, and lithium hydrogen D,L-malate, $LiH(C_4H_4O_5)$, and 3-D frameworks lithium fumarate, $Li_2(C_4H_2O_4)$, and its singly protonated analogue, lithium hydrogen fumarate, $LiH(C_4H_2O_4)$. A survey of all known lithium dicarboxylates revealed that their structural trends are a function of the ligand geometry, metal:ligand ratio and degree of solvation. The electrochemical properties of nine lithium-based inorganic-organic frameworks were investigated by impedance spectroscopy and electrochemical cycling, revealing many areas to be improved in order for them to become viable materials for battery applications, such as ligand conjugation length, particle size and lithium mobility.

Overall, this work has achieved a greater understanding of lithium-based inorganic-organic frameworks, revealing insight into polymorphism, phase behaviour, energetics, topological similarity, mechanical properties, ligand solid solutions, topotactic reaction, structure control and lithium battery properties. In total, 18 new crystal structures and three mixed-ligand solid solution systems are reported. The work provides a solid platform upon which new lithium-containing inorganic-organic materials may be designed and studied.

Acknowledgements

First and foremost my thanks go to Tony Cheetham, my supervisor, mentor and source of inspiration for this work. Under his guidance I have learnt to work independently, have courage in my convictions, think creatively, display enthusiasm for my work and be excited by the infinite possibilities of scientific research.

I would also like to thank all the people who have contributed to this scientific journey from the very beginning. At Bedford Modern School I was lucky enough to have teachers that showed me that science could be clear, fun, interesting, exciting and cool; particular credit must go to Mr Else, Mr Temple and Dr Wilkes. Under the guidance of Peter Wothers at St Catharine's College (keeping it in the BMS family!), I had several undergraduate supervisors who really pushed me and helped to focus my abilities.

My heartfelt thanks go to the people who have made my working environment so enjoyable and fruitful: my friends and co-workers in the Functional Inorganic and Hybrid Materials group. Many of these people contributed in important ways to this research, and I am extremely grateful to them for that. The experience, generosity and encouragement of post-docs and visiting researchers have been invaluable: Thiru Alagarsamy, Paul Saines, Jin-Chong Tan, Wei Li, Erica Bithell, Barbara Reisner, Satoshi Tominaka, Sebastian Henke and Naoyuki Komuro. My PhD fellow students have helped me, both in science and in staying sane throughout my PhD: Ryan Burwood, Tom Bennett, Ali Kalaji, Isabelle Etchart, Prashant Jain, Crystal Merrill, Josh Furman, Patrick Beldon, Shuai Cao, Shakiba Kaveh and Anna Smith. It's also been a genuine pleasure to work with and alongside visiting students Mark, Dhivya, Reka, Note, Be and Keng.

Without collaborators this PhD could not have happened, therefore I am grateful to the following people for their work - Monica Kosa and Michele Parrinelo for computational work on the lithium tartrates, Thomas Koester, Fiona Strobridge and Clare Grey for solid state NMR studies, Thomas Pilz and Martin Janssen for impedance spectroscopy, Tomislav Friscic for helping me get started on mechanosynthesis, Brent Melot for electrochemical measurements, Chiu Tang, Steve Thompson and Alistair Lennie for PXRD at Diamond Beamline I11, Paul Forster and Josh Furman for synchrotron X-ray structure determinations of lithium tartrates, Wei Li and Jin-Chong Tan for mechanical properties measurements and Simon Humphrey for supervision during my first year's work on organophosphine-based frameworks.

My funding has come from the EPRSC and the ERC. Thank you, taxpayers!

I have been lucky enough to be in a department with top rate facilities, and I would like to thank all the people responsible for its maintenance and the training and advice I have received, particularly Mary Vickers and Andrew Moss in the X-ray laboratory, Robert Cornell in the polymer lab, Ken Thorn and his team in the workshop, Simon Griggs in the SEM room, Dave Duke, Nathan Cliff and Les Allen in maintenance, James Goodchild and Lori Richardson in purchasing and stores, and all the people that ever said "Good morning" or "Hi" with a smile in the corridors. They make such a difference! I'd like to acknowledge the people in charge of facilities at Chemistry, which have been essential to my work: Alan and Patricia in microanalysis and Peter Grice, Duncan Howe and Andrew Mason in NMR.

I have found from experience that teaching is not an easy job, but during my PhD several people have made the experience of learning new methods, theory and techniques not only useful but enjoyable too. Thank you Hans-Beat Buergi, Tony Linden, Lukas Palatinus and all the tutors at the Zurich School of Crystallography 2009, John Evans and the tutors at the Durham Powder Diffraction & Rietveld Refinement School 2010, and all the lecturers of the Cambridge Materials Department 1st year PhD courses I attended.

Outside of my PhD, I am grateful to all the people who have enriched my life in other activities. I am sure that the influence of such a diverse circle of friends cannot but have helped my research indirectly, but more importantly they have been an outlet for frustrations, a voice of encouragement and the source of innumerable good times in Cambridge and further afield. Special thanks go to my old friends And, Linds, Andrew and the Catz Chemists, Charlotte, Harry, Saquib, Sophie, Olivia, Alex, Fiona, Rachelle and other Catz MCR members, particularly the Committee 2009-10, Shaun Hall, Raphael Assier, Ben Roberts and my ping-pong buddies, and my classmates at Chinese lessons.

My family has been a reassuring presence throughout the last few years, and despite for the most part being in a different place to them, I feel I am continually growing closer to my sisters, my Mum and my Dad. It's also been great to share with them - my research, many tasty meals, celebrations, concerts, holidays, thoughts, postcards and so much more that words cannot express. Finally, to Katie: My love, my sweetheart, the source of sanity in the CD rack. You have kept me going through all weathers and through you I am finding out who I really am. Thank you, this is for you.

Table of contents

List of figures

Chapter 1. Introduction

Chapter 2. Experimental methods

Chapter 3. Structural diversity, energy trends and phase behaviour of lithium tartrate frameworks

Chapter 4. Isostructural compounds and multi-component ligand solid solutions in the lithium succinate family

Chapter 5. Structure control, electrochemical behaviour and ionic transport in lithium-based frameworks

Chapter 6. Appendix

List of tables

Chapter 1. Introduction

Chapter 3. Structural diversity, energy trends and phase behaviour of lithium tartrate frameworks

Chapter 4. Isostructural compounds and multi-component ligand solid solutions in the lithium succinate family

Chapter 5. Structure control, electrochemical behaviour and ionic transport in lithium-based frameworks

Chapter 1. Introduction

1.1. Organisation of this research and thesis

This research has been carried out primarily in the research group and laboratory of Anthony Cheetham in the Department of Materials Science and Metallurgy (MSM), Cambridge University, UK, under his supervision. Time was divided approximately evenly between the synthesis of materials and their characterisation, the latter of which was carried out in part at Beamline I11 of the Diamond Light Source synchrotron radiation facility, UK. Additional analysis was performed by collaborators in the author's research group and other locations, and certain routine analyses were carried out by services at the Department of Chemistry, Cambridge University, UK, as detailed in the next section.

This thesis comprises five chapters. This chapter provides an introduction to the research, followed by Chapter 2, which is devoted to the experimental methods used. Three results chapters make up the bulk of the thesis, and may be summarised as follows: Chapter 3 describes the exploration of structural diversity in lithium tartrate frameworks, which was the initial focus of this research. Chapter 4 describes the investigation of materials with structures similar to lithium succinate, both in pure form and as solid solutions. Finally, reflecting the practical aims of this research, Chapter 5 contains analysis of structure diversity, lithium mobility and electrochemical behaviour in a number of new and existing lithium-based frameworks. The main conclusions and outlook of this work as a whole are found at the end of this chapter. Supplementary information is contained as an appendix in CD format and in Chapter 6.

1.2. Contributors

All the work detailed in this thesis was performed independently by the author, except where noted in the text. In particular, the following people gave important research contributions:

Paul Forster (University of Nevada, Las Vegas) - data collection at the Advanced Light Source and structure solution of dilithium D,L-tartrate **4**.

Tomislav Friscic (Department of Chemistry) - initial assistance with mechanochemical synthesis.

Joshua Furman (the author's research group) - initial data collection for dilithium *meso*-tartrate **6** at the Advanced Light Source.

Monica Kosa (ETH Zurich and Bar Ilan University) - energy and mechanical property calculations and molecular dynamics simulations of lithium tartrates.

Thomas Koester (Department of Chemistry) - solid state NMR measurements on lithium succinate and isostructural compounds.

Wei Li (the author's research group) - nanoindentation on lithium succinate and isostructural compounds.

Brent Melot (University of Southern California) - electrochemical cycling measurements.

Thomas Pilz (MPI Stuttgart) - impedance spectroscopy.

Paul Saines (the author's research group) - assistance with collection and analysis of high-resolution synchrotron powder X-ray diffraction data.

Dhivya Sashidhar (the author's research group) - initial investigations into lithium chlorosuccinate.

Jin-Chong Tan (the author's research group) - mechanical property measurements on dilithium tartates and exfoliation studies of dilithium 2,2-dimethylsuccinate.

1.3. Objectives of this research

The main aim of this research was to further understanding of inorganic-organic frameworks, with a view to their use in energy applications, such as lithium batteries and gas storage. Particular focus was devoted to the synthesis and structure determination of new non-porous, lithium-based inorganic-organic frameworks, in order to investigate their diversity and potential as functional materials.

Diversity of alkaline earth-based frameworks involving the chiral, racemic and *meso* isomers of tartaric acid, $C_4H_6O_6$, has been studied previously in the author's research group.[1] A similar investigation using lithium as the metal node was expected to yield an interesting range of materials, which would enable the study of different structures, phase behaviour and energetics (Chapter 3). In addition, framework isomerism in the lithium tartrates enabled different computational methods to be compared, which could help to determine the level of theory needed to simulate the structures of inorganic-organic frameworks accurately.

Investigation of lithium-based frameworks involving ligands other than tartaric acid was also expected to result in the discovery of new compounds, whose structures and properties could be investigated. It was found that certain ligands based on substituted succinic acid - L-malic acid, tetrafluorosuccinic acid and methylsuccinic acid - formed topologies identical to that of lithium succinate (Chapter 4). Experiments were then focused on the analysis of differences in fine structure caused by different ligand substituents, the possibility of combining different ligands in solid solutions, and the effect this would have on the framework structure.

Four other new lithium-based frameworks - lithium 2,2-dimethylsuccinate, lithium fumarate, lithium hydrogen fumarate and lithium hydrogen D,L-malate - were found to exhibit a range of structures, and this gave an opportunity to survey a number of frameworks, in order to investigate the factors affecting their architectures (Chapter 5). Due to the flexibility of the lithium coordination sphere, it is important to understand how factors such as ligand geometry, degree of hydration and metal:ligand ratio influence the connectivity, dimensionality and topology of frameworks.

With a view towards relevant applications, the last aim of this research was to investigate the properties of lithium-based frameworks. Ionic conductivity and lithium insertion were measured in a number of new materials in order to give insight into the structural features that might be beneficial or detrimental to new lithium battery materials.

1.4. Background to the research

1.4.1. *Definitions and classification of inorganic-organic frameworks*

The definition of an inorganic-organic framework has recently been subject of much debate, and the different names they have been called are almost as numerous as the new structures discovered, therefore clarification of a few definitions used in this thesis is necessary.

An inorganic-organic framework is defined here as a chemical compound composed of inorganic and organic components connected to form a single phase solid material that has repeating infinite connectivity. Organic components are generally small organic molecules, which have the capability to bind to metal ions *via* functional groups, and when they do so are known as ligands. Inorganic components may be single metal atoms coordinated by ligand atoms, metal-ligand clusters containing more than one metal atom, or extended arrays of metal atoms linked by single ligand atoms.

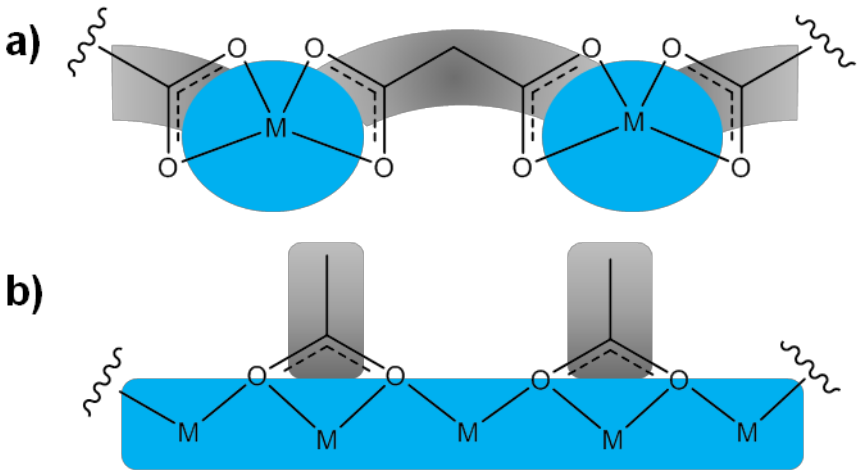

Figure 1. Different classes of connectivity in inorganic-organic frameworks: a) "organic", consisting of isolated metal (M, blue) nodes connected through multiple ligand atoms (grey), and b)"inorganic", consisting of metal atoms connected by single ligand atoms.

The overall dimensionality of an inorganic-organic structure may be O-D (molecular units), 1-D (chains, ribbons, ladders etc.), 2-D (layers or sheets) or 3-D (frameworks), and in each direction the connectivity may be of two types. "Inorganic" connectivity consists of M-X-M repeat units, where M and X denote a metal and a non-metal atom, such as O, S, F etc., respectively, and "organic" connectivity consists of M-L-M units, where L denotes a pathway through multiple ligand atoms (Figure 1). This can give rise to a number of different combinations of connectivities, as introduced by Cheetham *et al*. in a comprehensive review.[2]

Any given inorganic-organic framework may thereby be denoted I^mO^n, where *m* is the dimensionality of *I*norganic connectivity and *n* is that of *O*rganic connectivity between metal centres (Table 1). The overall dimensionality is the sum (*m*+ *n*), whose maximum is three; organic connectivity is not counted in any direction also containing inorganic connectivity. Structures with (*m*+ *n*) = 3 may be thought of as frameworks, (*m*+ *n*) = 2 as sheets, (*m*+ *n*) = 1 as chains and (*m*+ *n*) = 0 as isolated molecules or clusters.

Metal-organic-metal connectivity, O^n (n = 0-3)	Dimensionality of inorganic connectivity, I^m (m = 0-3)			
	0	**1**	**2**	**3**
0	Molecular complexes I^0O^0	Hybrid inorganic chains I^1O^0	Hybrid inorganic layers I^2O^0	3-D Inorganic hybrids I^3O^0
1	Chain coordination polymers I^0O^1	Mixed inorganic-organic layers I^1O^1	Mixed inorganic-organic 3-D framework I^2O^1	----
2	Layered coordination polymers I^0O^2	Mixed inorganic-organic 3-D framework I^1O^2	----	----
3	3-D Coordination polymers I^0O^3	----	----	----

Table 1. Classification of inorganic-organic materials reproduced from Cheetham et al., showing the dimensionality of different structures with respect to both extended inorganic connectivity (I^m) and organic connectivity between metal centres (O^n).[2]

One major divide within the field of inorganic-organic frameworks is that between porous systems and non-porous ones, largely due to the difference in their physical properties. Porous inorganic-organic frameworks, which contain voids with diameters above 0.2 nm,[3] exist at the boundary between conventional porous inorganic materials, such as zeolites, and porous carbonaceous materials, such as activated carbons and polymers, and they have properties that mirror both. For example, they combine extremely high porosity and high internal surface areas commonly found in zeolites with low density and mechanical flexibility of organic linkers and coordination bonds. This is achieved by substitution of heavier inorganic building units (e.g. based on Si-O-Si linkages in zeolites) by lighter organic ligands coordinated to metal centres (e.g. resulting in Zn-Im-Zn linkages, where Im = imidazole, in zeolitic imidazole frameworks).[4]

The high surface areas of porous inorganic-organic frameworks have been the main reason for investigation of their potential applications in gas storage, separation, sensing and catalysis.[5] In addition, the ability to tune the pore chemistry by functionalising the ligands is a unique advantage over conventional materials. Pores can be made with varying diameter,[6] chirality,[7] exposed binding sites,[8] fluorinated surfaces,[9] large flexibility[10] and responsiveness towards external and internal stimuli.[5, 11]

The other attribute of inorganic-organic frameworks that attracts great interest is their huge diversity of topologies and possible components. The periodic table contains many metallic elements that form inorganic structures, whilst organic chemistry has the power to make thousands of ligands that may be combined with those inorganic building blocks to give extended connectivity in the form of an inorganic-organic framework. Non-porous inorganic-organic frameworks, which generally contain no voids with accessible volume, have so far been less studied than porous ones. However, they have the potential to combine functional properties of both inorganic and organic materials, with the added value of tunability *via* the ligands and stability compared to classical organic materials.[2] This gives rise to a diverse range of properties, including chirality, non-linear optics, magnetism, conductivity, luminescence and multiferroicity.[12] They can also yield hitherto unknown or unexpected properties *via* their hybrid nature, an exciting prospect for exploration of new materials.[13]

1.4.2. *History of inorganic-organic frameworks*

In 1990, Hoskins and Robson were the first to demonstrate the construction of infinite structures comprising of metal "nodes" connected by organic "linkers".[14] This began a gradual increase in interest in the area of coordination polymers, with several groups subsequently reporting new structures, particularly of porous materials.[15] The early 2000's saw an increase in the number of publications on coordination polymers that is still rising, reaching over 1200 in 2011 (Figure 2). A major development occurred in 2003 with the discovery by O'Keeffe, Yaghi and co-workers that pore sizes in relatively robust inorganic-organic frameworks could be systematically changed in isoreticular frameworks by variation in the ligand.[6] These porous structures, often referred to as metal-organic frameworks, MOFs, all contained the same octahedral Zn-O-C clusters, which functioned as secondary building units, linked by linear dicarboxylate linkers of different lengths, containing various functional groups. The resulting materials had pore sizes from 3.8 Å to 28.8 Å and densities down to 0.21 g cm^{-3}, which gave rise to room temperature hydrogen storage capacities up to 2 wt. %.[16]

These reports prompted a newly increased research effort into MOFs, which is now at a similar level to coordination polymers (Figure 2).

In their landmark 2004 review of porous coordination polymers, PCPs, Kitagawa *et al*. described three generations of porous compounds.[5] The 1st generation of PCPs have pores sustained only with guest molecules and collapse irreversibly upon their removal. The 2nd generation are more robust: their pores are stable upon removal of guest molecules. The 3rd generation are robust enough to withstand guest removal, but also have flexible frameworks that respond reversibly to external stimuli, such as light, electric field and other guest molecules. At this time, new materials were being produced less by serendipity and more by design, as understanding of the construction of frameworks grew with collective experience.[17] Not only porous materials were being studied; the properties and potential applications of inorganic-organic frameworks in general were also being realised and related to their structures.[2, 12]

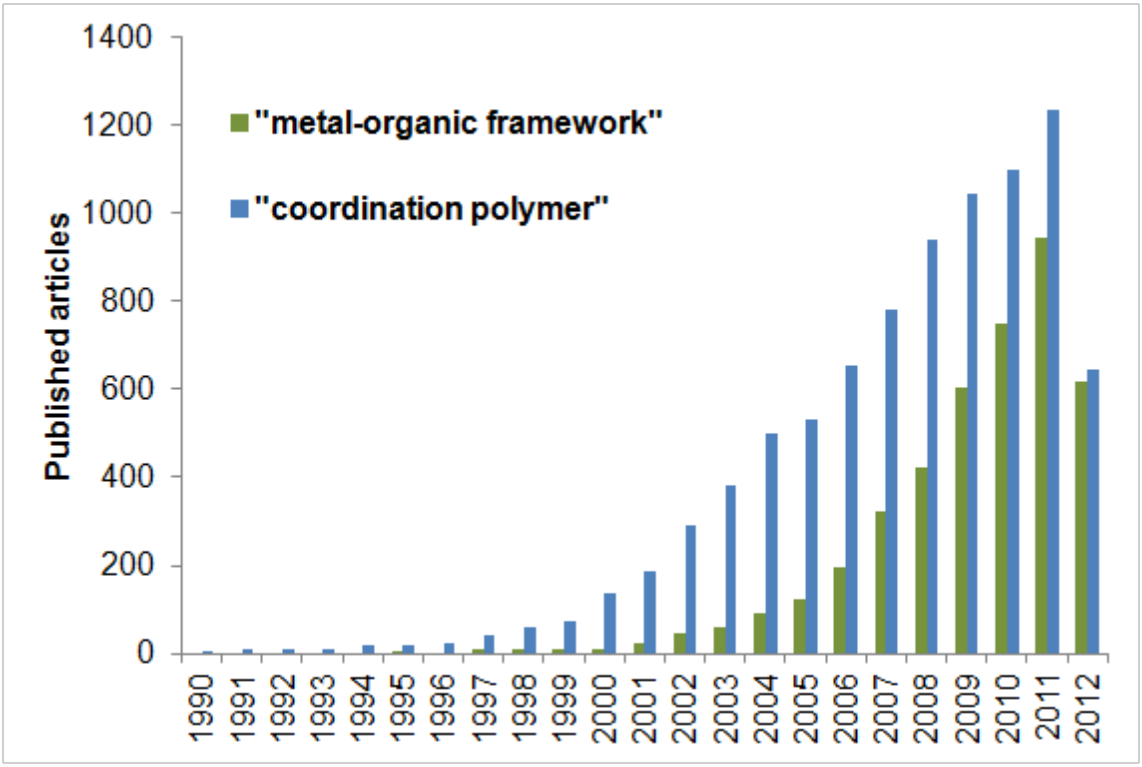

Figure 2. Increase in published articles featuring the keywords "metal-organic framework" (green) and "coordination polymer" (blue) since 1990. Values from Web of Knowledge, correct as of 9 August 2012.

1.4.3. *Current trends in inorganic-organic frameworks*

With the experience of two decades of intense research into discovery of new inorganic-organic frameworks and their properties, increased emphasis is now being placed on real-life applications. The often highly specific interactions with diverse guest species have made responsive porous frameworks subject to investigation as sensors,[18] with luminescent frameworks acting simultaneously as both receptor and transducer.[19] Fabrication of thin films has allowed transduction by other means, such as optical interferometry, mechanical displacement and gravimetric changes.[20] In addition, engineering of surfaces and interfaces, composites, nanoparticles and core/shell structures has developed inorganic-organic frameworks from bulk materials to more application-specific configurations.[21] Magnetic, optical and electronic properties, often traditionally associated with condensed matter physics, are also being investigated in many inorganic-organic frameworks, which offer great scope for structure and property variation along with reasonable stability required for applications.[13]

Research into catalysis by porous inorganic-organic frameworks is involved in exploitation of features not often found together in other porous materials, such as the wide range of possible active site architectures, flexibility and chirality.[22] Post-synthetic modification, PSM, has been used to introduce additional functionality in porous inorganic-organic frameworks that may not be possible *via* direct synthesis of pre-functionalised reactants.[23] Various chemical reactions have been reported on both the organic ligands and the metal nodes, which can be used to tailor pore chemistry whilst maintaining framework integrity. One important possibility arising from PSM is the controlled delivery of bioactive species, such as NO, H_2S and drug molecules.[24] Hydrogen storage in porous frameworks is still intensively researched, but absorption of other volatile species has also been productive.[25] Due to the urgent need for carbon sequestration technology, the most prominent of these has been carbon dioxide, whose interaction with framework pores is generally much stronger than that of hydrogen.[26] Iodine, a radioactive product of nuclear fission, has been successfully absorbed by zeolitic imidazolate frameworks, ZIFs (Figure 3).[27]

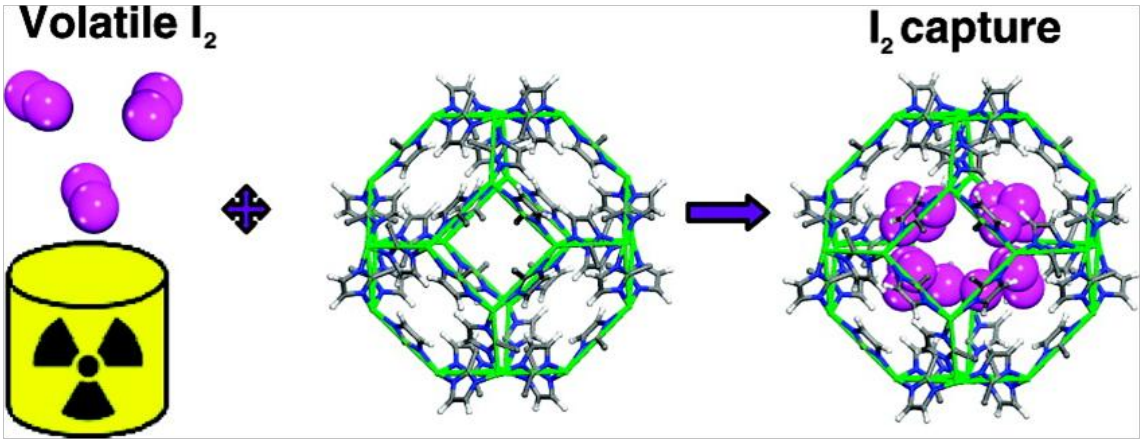

Figure 3. Iodine capture in ZIF-8, Zn(2-methylimidazolate)$_2$, which is secure until framework decomposition at ~575 K. Reproduced with permission,[27] copyright 2011 ACS.

Computational study of inorganic-organic frameworks is still in its early stages, drawing on experience with organic and inorganic materials in areas such as structure prediction and property simulation.[28] However, many challenges remain to be addressed, including development of accurate interatomic potentials, modelling of vibrational modes and accounting for framework flexibility. Mechanical property measurements are also currently under-developed, but can shed light on the durability of inorganic-organic frameworks and their behaviour under various conditions.[29] This work is important for industrial application of the materials, where they must withstand large cyclic changes in temperature and pressure. For example, framework amorphization has been found to occur *via* high pressure, high temperature and mechanical stress in ZIFs, leading to changes in gas uptake properties that can be irreversible.[30] However, this flexibility has been put to good use in responsive, dynamic, "soft crystals", in which adsorbed molecules and external stimuli can modulate the framework metrics or interaction with other guests.[11]

1.4.4. *Lithium in inorganic-organic frameworks*

Lithium has been largely unexplored as a metal node for inorganic-organic frameworks, and despite potential gravimetric advantages over other metals and interest in lithium-containing systems for battery applications, very few new lithium-based frameworks have been reported. Furthermore, insertion of lithium ions into porous frameworks has been shown both experimentally and computationally as a way to enhance gas uptake and selectivity (Figure 4).[8c, 31]

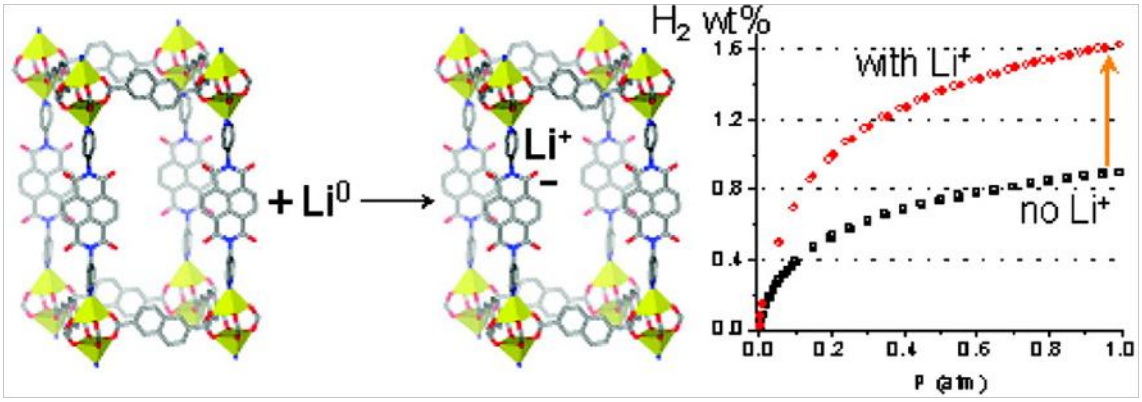

Figure 4. Chemical reduction of the I^0O^3 framework $Zn_2(NDC)_2(diPyNI)$ (NDC = 2,6-dicarboxylate, diPyNI = N,N'-di-(4-pyridyl)-1,4,5,8-naphthalenetetracarboxydiimide), resulting in enhanced hydrogen storage capacity. Reproduced with permission,[31] copyright 2007 ACS.

Most porous inorganic-organic frameworks contain divalent or trivalent metals, which are linked by polyanionic ligands to form a three dimensional net. Combination of monovalent metals with the single anionic ligand required for charge balance limits the number of possible connectivities, particularly for higher dimensionalities. Strategies to synthesize extended lithium-based frameworks have therefore tended to involve a combination of neutral and anionic binding functionalities either on the same ligand[32] or on different moieties,[33] which allows for the monovalent nature of lithium and enables connectivity in three dimensions. Where reported, these frameworks have shown limited gas sorption capability, mainly due to small pore sizes.

Dicarboxylate ligands have also been used in the synthesis of lithium-based frameworks with porous properties. The lithium-rich bismuth pyridinedicarboxylate, $Li_5Bi(2,6\text{-pdc})_4(H_2O)_2$, was shown to have negligible solvent-accessible volume, but absorbed CO_2 due to the formation of open Li sites upon water loss.[34] Another pyridinedicarboxylate, $Li_2(2,5\text{-pdc})(dmf)$, where dmf = dimethylformamide, showed dynamic structural change upon removal of coordinated DMF.[35] In this case, loss of porosity is due to the framework rearranging reversibly to fill the Li coordination spheres. Finally, measurement by quartz crystal microbalance of water and methanol uptake was enabled by the hydrophilic structure of a lithium 1,3-benzenedicarboxylate, $Li_2(1,3\text{-bdc})(dmf)_{0.5}\cdot H_2O$.[36] Mention should also be given to a recently reported lithium azobenzenetetracarboxylate, Li2(3,3',5,5'-abtc)(dmf), which retains crystallinity and remains porous after removal of coordinated DMF. The resulting 3-coordinate Li sites give rise to CO_2 sorption properties.[37]

The crystal structures of many other lithium dicarboxylates have been determined (see Chapter 5), but no systematic study of them has been undertaken to date. Clearly, research into the properties of lithium-based inorganic-organic framework is less advanced than that of other metals, largely due to the flexibility of its coordination sphere, which precludes formation of well-determined metal-based building blocks for framework synthesis. However, the work described in this thesis has uncovered hitherto unknown diversity in lithium-based framework materials and points towards several ways of exploiting chemical concepts in their design and synthesis. These include polymorphism, ligand isomerism and dehydration (Chapter 3), topological similarity, ligand substitution, solid solutions and topochemical reaction (Chapter 4), and ligand geometry- and compositional control of structure and properties (Chapter 5). This work will provide a solid platform upon which new lithium-containing inorganic-organic materials may be designed and studied.

1.5. References

(1) (a) Kam, K. C.; Young, K. L. M.; Cheetham, A. K. *Cryst. Growth Des.* **2007**, *7*, (8), 1522-1532. (b) Appelhans, L. N.; Kosa, M.; Radha, A. V.; Simoncic, P.; Navrotsky, A.; Parrinello, M.; Cheetham, A. K. *J. Am. Chem. Soc.* **2009**, *131*, (42), 15375-15386.

(2) Cheetham, A. K.; Rao, C. N. R.; Feller, R. K. *Chem. Commun.* **2006**, (46), 4780-4795.

(3) *IUPAC. Compendium of Chemical Terminology*. McNaught, A. D.; Wilkinson, A., Ed.; 2nd ed.; Blackwell Scientific Publications: Oxford, **1997**.

(4) Hayashi, H.; Cote, A. P.; Furukawa, H.; O'Keeffe, M.; Yaghi, O. M. *Nat. Mater.* **2007**, *6*, (7), 501-506.

(5) Kitagawa, S.; Kitaura, R.; Noro, S. *Angew. Chem., Int. Ed.* **2004**, *43*, (18), 2334-2375.

(6) Eddaoudi, M.; Kim, J.; Rosi, N.; Vodak, D.; Wachter, J.; O'Keeffe, M.; Yaghi, O. M. *Science* **2002**, *295*, (5554), 469-472.

(7) (a) Kepert, C. J.; Prior, T. J.; Rosseinsky, M. J. *J. Am. Chem. Soc.* **2000**, *122*, (21), 5158-5168. (b) Seo, J. S.; Whang, D.; Lee, H.; Jun, S. I.; Oh, J.; Jeon, Y. J.; Kim, K. *Nature* **2000**, *404*, (6781), 982-986. (c) Thushari, S.; Cha, J. A. K.; Sung, H. H. Y.; Chui, S. S. Y.; Leung, A. L. F.; Yen, Y. F.; Williams, I. D. *Chem. Commun.* **2005**, (44), 5515-5517. (d) Wu, C. D.; Hu, A.; Zhang, L.; Lin, W. B. *J. Am. Chem. Soc.* **2005**, *127*, (25), 8940-8941. (e) Vaidhyanathan, R.; Bradshaw, D.; Rebilly, J. N.; Barrio, J. P.; Gould, J. A.; Berry, N. G.; Rosseinsky, M. J. *Angew. Chem., Int. Ed.* **2006**, *45*, (39), 6495-6499. (f) Tan, Y.-X.; He, Y.-P.; Zhang, J. *Inorg. Chem.* **2011**, *50*, (22), 11527-11531.

(8) (a) Forster, P. M.; Eckert, J.; Chang, J. S.; Park, S. E.; Férey, G.; Cheetham, A. K. *J. Am. Chem. Soc.* **2003**, *125*, (5), 1309-1312. (b) Forster, P. M.; Eckert, J.; Heiken, B. D.; Parise, J. B.; Yoon, J. W.; Jhung, S. H.; Chang, J. S.; Cheetham, A. K. *J. Am. Chem. Soc.* **2006**, *128*, (51), 16846-16850. (c) Mulfort, K. L.; Farha, O. K.; Stern, C. L.; Sarjeant, A. A.; Hupp, J. T. *J. Am. Chem. Soc.* **2009**, *131*, (11), 3866. (d) Wiers, B. M.; Foo, M. L.; Balsara, N. P.; Long, J. R. *J. Am. Chem. Soc.* **2011**, *133*, (37), 14522-14525. (e) Jeong, N. C.; Samanta, B.; Lee, C. Y.; Farha, O. K.; Hupp, J. T. *J. Am. Chem. Soc.* **2012**, *134*, (1), 51-4.

(9) (a) Yang, C.; Wang, X. P.; Omary, M. A. *Angew. Chem.-Int. Edit.* **2009**, *48*, (14), 2500-2505. (b) Hulvey, Z.; Falcao, E. H. L.; Eckert, J.; Cheetham, A. K. *J. Mater. Chem.* **2009**, *19*, (25), 4307-4309. (c) Hulvey, Z.; Sava, D. A.; Eckert, J.; Cheetham, A. K. *Inorg. Chem.* **2011**, *50*, (2), 403-405.

(10) Uemura, K.; Matsuda, R.; Kitagawa, S. *J. Solid State Chem.* **2005**, *178*, (8), 2420-2429.

(11) Horike, S.; Shimomura, S.; Kitagawa, S. *Nat. Chem.* **2009**, *1*, (9), 695-704.

(12) Janiak, C. *Dalton Trans.* **2003**, (14), 2781-2804.

(13) Rao, C. N. R.; Cheetham, A. K.; Thirumurugan, A. *J. Phys.-Condes. Matter* **2008**, *20*, (8).

(14) Hoskins, B. F.; Robson, R. *J. Am. Chem. Soc.* **1990**, *112*, (4), 1546-1554.

(15) (a) Abrahams, B. F.; Hoskins, B. F.; Robson, R. *J. Am. Chem. Soc.* **1991**, *113*, (9), 3606-3607. (b) Subramanian, S.; Zaworotko, M. J. *Angew. Chem.-Int. Edit.* **1995**, *34*, (19), 2127-2129. (c) Yaghi, O. M.; Li, G. M.; Li, H. L. *Nature* **1995**, *378*, (6558), 703-706. (d) Venkataraman, D.; Gardner, G. B.; Lee, S.; Moore, J. S. *J. Am. Chem. Soc.* **1995**, *117*, (46), 11600-11601. (e) Lu, J.; Paliwala, T.; Lim, S. C.; Yu, C.; Niu, T. Y.; Jacobson, A. J. *Inorg. Chem.* **1997**, *36*, (5), 923-929. (f) Vaid, T. P.; Lobkovsky, E. B.; Wolczanski, P. T. *J. Am. Chem. Soc.* **1997**, *119*, (37), 8742-8743. (g) Ayyappan, S.; Cheetham, A. K.; Natarajan, S.; Rao, C. N. R. *Chem. Mater.* **1998**, *10*, (11), 3746-3755.

(16) Rosi, N. L.; Eckert, J.; Eddaoudi, M.; Vodak, D. T.; Kim, J.; O'Keeffe, M.; Yaghi, O. M. *Science* **2003**, *300*, (5622), 1127-1129.
(17) (a) Forster, P. M.; Burbank, A. R.; Livage, C.; Férey, G.; Cheetham, A. K. *Chem. Commun.* **2004**, (4), 368-369. (b) Forster, P. M.; Stock, N.; Cheetham, A. K. *Angew. Chem., Int. Ed.* **2005**, *44*, (46), 7608-7611.
(18) Chen, B. L.; Xiang, S. C.; Qian, G. D. *Acc. Chem. Res.* **2010**, *43*, (8), 1115-1124.
(19) Kreno, L. E.; Leong, K.; Farha, O. K.; Allendorf, M.; Van Duyne, R. P.; Hupp, J. T. *Chem. Rev.* **2012**, *112*, (2), 1105-1125.
(20) Shekhah, O.; Liu, J.; Fischer, R. A.; Woll, C. *Chem. Soc. Rev.* **2011**, *40*, (2), 1081-1106.
(21) Bradshaw, D.; Garai, A.; Huo, J. *Chem. Soc. Rev.* **2012**, *41*, (6), 2344-2381.
(22) (a) Ma, L. Q.; Abney, C.; Lin, W. B. *Chem. Soc. Rev.* **2009**, *38*, (5), 1248-1256. (b) Lee, J.; Farha, O. K.; Roberts, J.; Scheidt, K. A.; Nguyen, S. T.; Hupp, J. T. *Chem. Soc. Rev.* **2009**, *38*, (5), 1450-1459.
(23) (a) Wang, Z. Q.; Cohen, S. M. *Chem. Soc. Rev.* **2009**, *38*, (5), 1315-1329. (b) Cohen, S. M. *Chem. Rev.* **2012**, *112*, (2), 970-1000.
(24) Horcajada, P.; Gref, R.; Baati, T.; Allan, P. K.; Maurin, G.; Couvreur, P.; Férey, G.; Morris, R. E.; Serre, C. *Chem. Rev.* **2012**, *112*, (2), 1232-1268.
(25) Ma, S. Q.; Zhou, H. C. *Chem. Commun.* **2010**, *46*, (1), 44-53.
(26) (a) Phan, A.; Doonan, C. J.; Uribe-Romo, F. J.; Knobler, C. B.; O'Keeffe, M.; Yaghi, O. M. *Acc. Chem. Res.* **2010**, *43*, (1), 58-67. (b) D'Alessandro, D. M.; Smit, B.; Long, J. R. *Angew. Chem.-Int. Edit.* **2010**, *49*, (35), 6058-6082.
(27) Sava, D. F.; Rodriguez, M. A.; Chapman, K. W.; Chupas, P. J.; Greathouse, J. A.; Crozier, P. S.; Nenoff, T. M. *J. Am. Chem. Soc.* **2011**, *133*, (32), 12398-12401.
(28) (a) Mellot-Draznieks, C. *J. Mater. Chem.* **2007**, *17*, (41), 4348-4358. (b) Keskin, S.; Liu, J.; Rankin, R. B.; Johnson, J. K.; Sholl, D. S. *Ind. Eng. Chem. Res.* **2009**, *48*, (5), 2355-2371.
(29) Tan, J.-C.; Cheetham, A. K. *Chem. Soc. Rev.* **2011**, *40*, (2), 1059-1080.
(30) (a) Bennett, T. D.; Goodwin, A. L.; Dove, M. T.; Keen, D. A.; Tucker, M. G.; Barney, E. R.; Soper, A. K.; Bithell, E. G.; Tan, J.-C.; Cheetham, A. K. *Phys. Rev. Lett.* **2010**, *104*, (11). (b) Bennett, T. D.; Cao, S.; Tan, J.-C.; Keen, D. A.; Bithell, E. G.; Beldon, P. J.; Friscic, T.; Cheetham, A. K. *J. Am. Chem. Soc.* **2011**, *133*, (37), 14546-14549.
(31) Mulfort, K. L.; Hupp, J. T. *J. Am. Chem. Soc.* **2007**, *129*, (31), 9604.
(32) (a) Abrahams, B. F.; Grannas, M. J.; Hudson, T. A.; Robson, R. *Angew. Chem., Int. Ed.* **2010**, *49*, (6), 1087-1089. (b) Zhao, X.; Wu, T.; Zheng, S. T.; Wang, L.; Bu, X. H.; Feng, P. Y. *Chem. Commun.* **2011**, *47*, (19), 5536-5538.
(33) (a) MacDougall, D. J.; Morris, J. J.; Noll, B. C.; Henderson, K. W. *Chem. Commun.* **2005**, (4), 456-458. (b) Zheng, S. T.; Li, Y. F.; Wu, T.; Nieto, R. A.; Feng, P. Y.; Bu, X. H. *Chem.-Eur. J.* **2010**, *16*, (44), 13035-13040. (c) Zhao, X.; Wu, T.; Bu, X. H.; Feng, P. Y. *Dalton Trans.* **2011**, *40*, (32), 8072-8074.
(34) Thirumurugan, A.; Li, W.; Cheetham, A. K. *Dalton Trans.* **2012**, *41*, (14), 4126-4134.
(35) Banerjee, D.; Kim, S. J.; Li, W.; Wu, H. H.; Li, J.; Borkowski, L. A.; Philips, B. L.; Parise, J. B. *Cryst. Growth Des.* **2010**, *10*, (6), 2801-2805.
(36) Liu, Y. Y.; Zhang, J.; Xu, F.; Sun, L. X.; Zhang, T.; You, W. S.; Zhao, Y.; Zeng, J. L.; Cao, Z.; Yang, D. W. *Cryst. Growth Des.* **2008**, *8*, (9), 3127-3129.
(37) El Osta, R.; Frigoli, M.; Marrot, J.; Guillou, N.; Chevreau, H.; Walton, R. I.; Millange, F. *Chem. Commun.* **2012**, *48*, (86), 10639-10641.

Chapter 2. Experimental methods.

2.1. Introduction

The experimental methods used in this research can be broadly categorised into four groups: synthesis of materials, structure characterisation, property characterisation and computational methods. Synthesis of materials involved using conventional crystallization techniques, solvothermal methods and mechanochemistry in order to obtain new and existing phases for further study. Various characterisation techniques were used to confirm the structure and purity of the as-synthesised material. In cases where the crystal structure was unknown and single crystals could be obtained, single crystal X-ray diffraction was used to determine the unit cell, space group and precise atomic positions, making it perhaps the most useful tool available. For known materials, confirmation of bulk structure and phase purity involved powder X-ray diffraction, Fourier transform infrared spectroscopy, thermogravimetric analysis, elemental analysis, optical microscopy, scanning electron microscopy and solid-state- and solution nuclear magnetic resonance spectroscopy. Following structural characterisation, other techniques- nanoindentation, impedance spectroscopy and electrochemical cycling -were used to investigate the physical properties of selected compounds. Finally, in order to gain further insight into the phase behaviour of some materials, computational calculations using density functional theory were performed to determine their formation energies.

Within this thesis, specific details of the experimental methods used are given in each results chapter, according to the results presented. This chapter provides a brief overview of all the methods, and lists a number of useful references, to which the reader is directed for more information.

2.2. Synthesis

2.2.1. *Crystallization*

Within the scope of this thesis, the principle aim of crystallization reactions was to produce crystals of a suitable size and quality for structure determination by single crystal X-ray diffraction (Section 2.3.1). Many methods exist by which to prepare single crystals,[1] of varying complexity and applicability to inorganic-organic framework materials. In general, the methods used herein can be classed as "reactant diffusion" crystallizations, in which precursor reagents, usually in the form of solutions, are combined and left to stand at room temperature (Figure 1a), or placed at elevated temperature in an oven (Figure 1b). Conditions were chosen to permit slow neutralisation of the acidic ligand precursors by basic metal precursors, followed by coordination bonding to form an inorganic-organic framework.

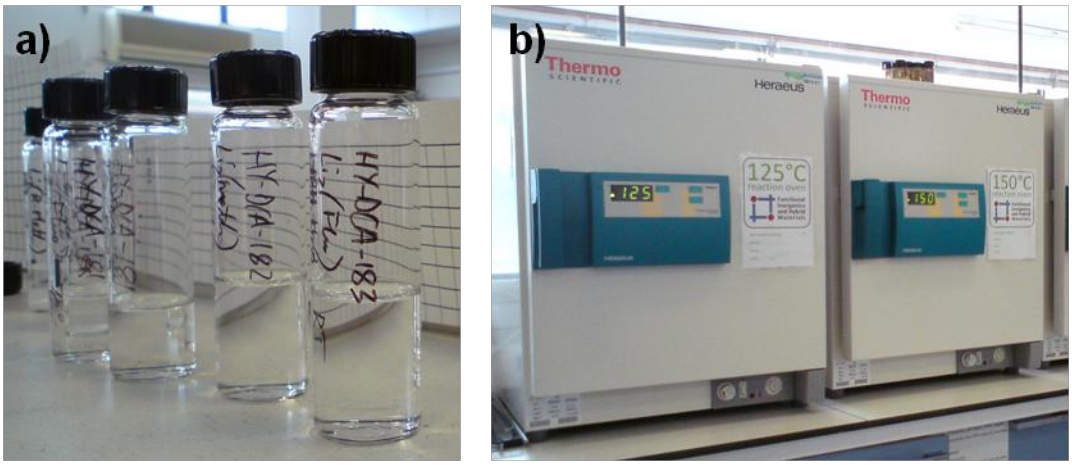

Figure 1. Crystallization: a) reactant diffusion reactions in PTFE-capped borosilicate glass vials, and b) temperature-controlled ovens used for reactions at elevated temperatures.

2.2.2. *Solvothermal synthesis*

Solvothermal synthesis is a variation of conventional crystallization, in which the reactant mixture is heated above the boiling point of the solvent in an autoclave (Figure 2).[2] These conditions allow higher temperatures to be reached than are possible under ambient pressure, when the solvent would otherwise evaporate. The closed environment of an autoclave results in solvent retention under autogeneous pressure and at higher temperatures the solubility of reactants increases and the free energy of the reaction has an increasing entropic contribution. This can give rise to reaction products that are not obtainable using conventional methods, as well as enabling studies of phase behaviour across a wide temperature range.

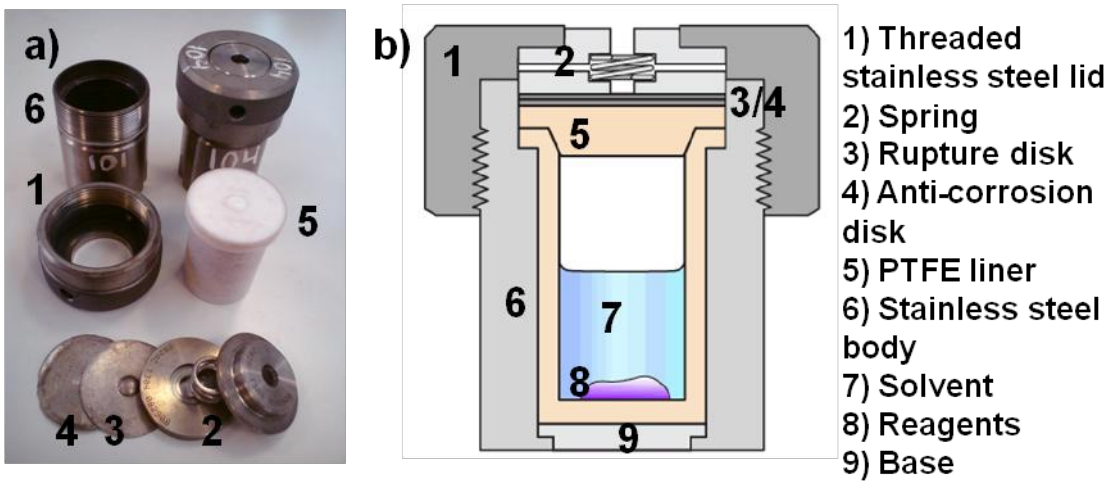

Figure 2. PTFE-lined stainless steel autoclave: a) individual parts, and b) schematic courtesy of Jin-Chong Tan.

2.2.3. *Mechanochemical synthesis*

Mechanochemical synthesis involves combining solid reagents in a mill, where the energy required to overcome the activation energy for the reaction is provided by mechanical force between particles and added ball bearings, rather than temperature-induced kinetic energy (Figure 3).[3] These conditions result in the formation of sub-micron sized powder products, whose structures must be confirmed by powder X-ray diffraction (Section 2.3.2). Indeed, similar procedures are commonly used to reduce particle size in various materials, such as ceramics, biomaterials and drugs. Small amounts of liquid (commonly 50 µl - 100 µl) may be added to aid kinetics or to template the formation of certain crystal structures, in which case the procedure may be called "liquid-assisted grinding", LAG.[4]

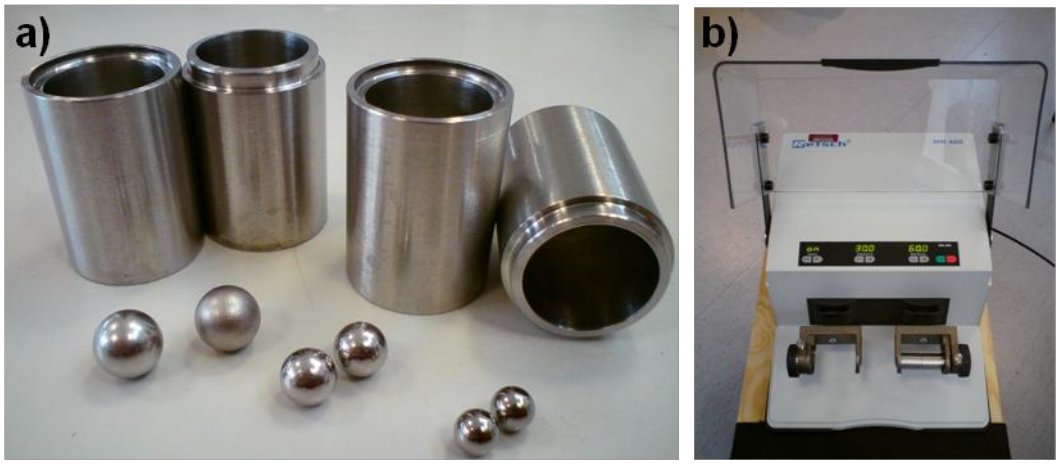

Figure 3. Mechanochemistry: a) stainless steel grinding jars and balls, and b) mixer mill.

2.3. Characterisation

2.3.1. *Single crystal X-ray diffraction*

Single crystal X-ray diffraction is used to determine the crystal structure of materials, including the cell parameters, space group and precise atomic positions.[5] The interaction between electrons in a molecule and X-rays, which have wavelengths of the same order of magnitude as interatomic distances, results in scattering of the light. The result is a superposition of X-rays, F, with contributions of amplitude f_i from each atom i, according to the equation:

$$F\left[\frac{\mathbf{s}-\mathbf{s_0}}{\lambda}\right] = \sum_{i=1}^{q} f_i[\frac{\mathbf{s}-\mathbf{s_0}}{\lambda}]\exp\,[2\pi i(\mathbf{s}-\mathbf{s_0})\cdot\frac{\mathbf{r}_i}{\lambda}]$$

where $\mathbf{s}$ and $\mathbf{s_0}$ are the X-ray source and detector positions, respectively, λ is the X-ray wavelength, q is the number of atoms in the molecule, and $\mathbf{r}_i$ is the position of atom i. Scattered light from all molecules within a crystal is superimposed, and the consequent diffraction pattern, G, consists of spots, whose positions and intensities are a direct function of the crystal symmetry and atomic positions, according to the equation:

$$G(\mathbf{r}^*) = \left[\frac{\sin\pi M\mathbf{a}\cdot\mathbf{r}^*}{\sin\pi\mathbf{a}\cdot\mathbf{r}^*}\frac{\sin\pi N\mathbf{b}\cdot\mathbf{r}^*}{\sin\pi\mathbf{b}\cdot\mathbf{r}^*}\frac{\sin\pi P\mathbf{c}\cdot\mathbf{r}^*}{\sin\pi\mathbf{c}\cdot\mathbf{r}^*}\right]\sum_{i=1}^{q} f_i[\frac{\mathbf{s}-\mathbf{s_0}}{\lambda}]\exp\,[2\pi i(hx_i+ky_i+lz_i)]$$

where $\mathbf{r}^*$ is the reciprocal position vector; M, N and P are the number of unit cell repeats of the unit cell vectors $\mathbf{a}$, $\mathbf{b}$ and $\mathbf{c}$; h, k and l are Miller indices and x, y and z are fractional atomic coordinates. The simple result of the square brackets is that G is only non-zero at integer h, k, and l, therefore determination of atomic positions only has to deal with those values in the summation, which is also known as the structure factor, $F(hkl)$.

A diffractometer has three main components: an X-ray source, a goniometer and a detector, which together enable the collection of diffraction data for many orientations of the crystal (Figure 4). The data is processed using a computer and the crystal structure is solved and refined by least squares minimisation,[6] and the whole experiment may take a matter of hours in the simplest of cases.

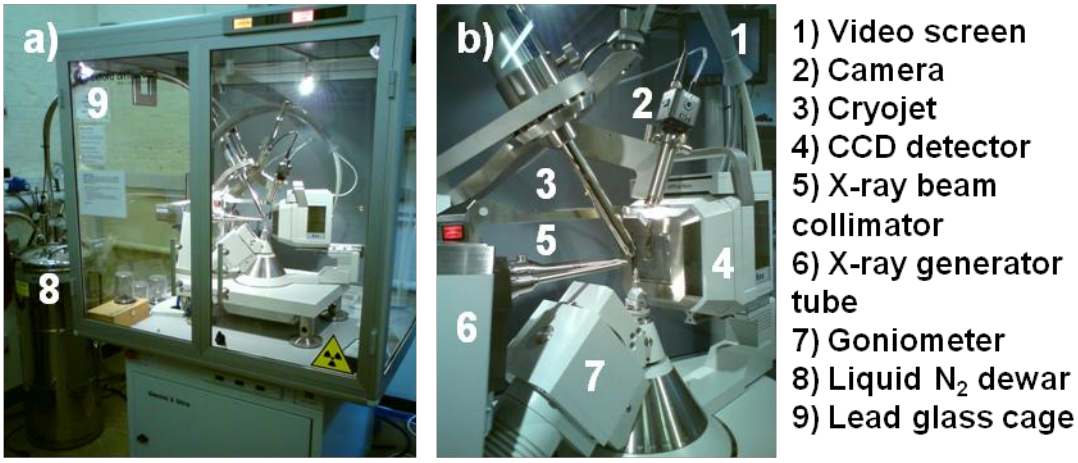

Figure 4. Single crystal diffractometer: a) the entire apparatus apart from connected PC, and b) a close-up of the arrangement around a diffracting crystal.

Laboratory crystal structure determination by X-ray diffraction was performed on a Oxford Diffraction Gemini E Ultra diffractometer equipped with dual source Cu radiation (λ = 1.54184 Å, operating at 40 kV and 40 mA with confocal mirrors to increase flux) and Mo radiation (λ = 0.7107 Å, operating at 50 kV and 40 mA). Data were collected at 120 K using ω scans and the mean detector area resolution was 10.4 pixels mm^{-1}. Data collection, cell determination and refinement, intensity integration and face indexation were performed using CrysAlisPro software.[7] Structures were solved by direct methods and full matrix least-squares refinements against $|F^2|$ were carried out using the SHELXTL-PLUS package of programs[8] within the WinGX interface.[9] All non-hydrogen atoms were refined anisotropically; hydrogen atoms were then inserted using a riding model and refined with isotropic displacement parameters constrained to 1.2 and 1.5 times those of their adjacent carbon (non-methyl) and oxygen and methyl carbon atoms, respectively. Visualization of structures was carried out using Diamond[10] and Mercury[11] programs.

2.3.2. *Powder X-ray diffraction*

Powder X-ray diffraction is commonly used to confirm the bulk structure of a material, by refinement of a model usually derived from the crystal structure determined by single crystal X-ray diffraction.[12] In certain cases, it may be used to solve the structure of an unknown material, given prerequisite knowledge of the constituent molecules. The experimental setup is similar to single crystal X-ray diffraction, although the sample is in powder form, held in a capillary or a flat plate (Figure 5). This means that, in theory, crystallites are present in random orientations such that the diffraction pattern consists of rings rather than discrete

spots, and reflections from distinct crystal planes that have similar *d*-spacings may occur at the same angle, according to Bragg's law:

$$n\lambda = 2d_{hkl}sin\theta$$

where $n = 1, 2, 3\ldots$, λ = X-ray wavelength, d_{hkl} = spacing between crystal planes of Miller indices (hkl) and θ = diffraction angle. Data may be analysed by visual inspection and comparison with simulated patterns for phase identification, or by more computationally involved methods for structure refinement. Le Bail refinement involves least squares optimisation of profile parameters and unit cell parameters, and needs no prior knowledge of atomic positions.[13] Rietveld refinement involves the additional refinement of atomic positions, which relate to the intensities of diffraction peaks.[14] Both methods have been used in this research.

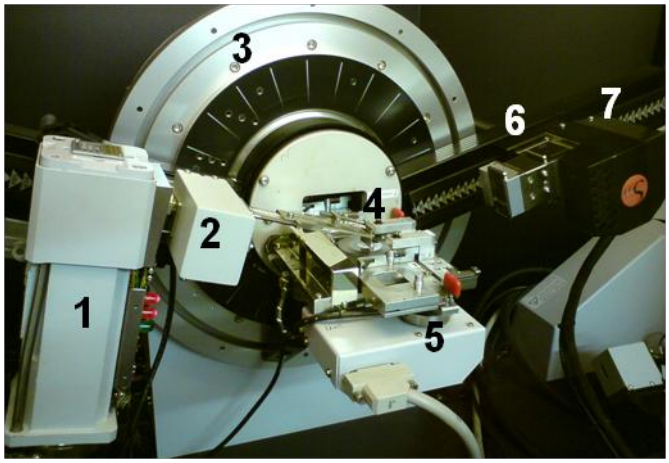

Figure 5. Powder X-ray diffractometer setup for flat plates in Bragg-Brentano operation.

Laboratory data were collected on a Bruker D8 theta/theta (fixed sample) diffractometer with LynxEye position sensitive detector, in Bragg Brentano parafocusing geometry, reflection mode using Cu Kα radiation (λ = 1.5418 Å). Scans were taken over an angular range of 5° - 60° (2θ) with step size 0.01°. Rietveld analysis of the data was carried out using the X'Pert HighScore Plus program.[15]

2.3.3. *Synchrotron powder X-ray diffraction*

Synchrotrons are a source of very bright, intense X-ray light, which is a result of the acceleration of electrons around a ring. The X-rays produced are usually of shorter wavelengths than those of laboratory diffractometers, and so are able to probe atomic

structure to much higher resolution. In addition, much faster measurements are possible due to the high flux of X-rays and the custom built detectors available. The synchrotron facility used in this research was the powder X-ray diffraction beamline I11 at Diamond Light Source (Figure 6).[16]

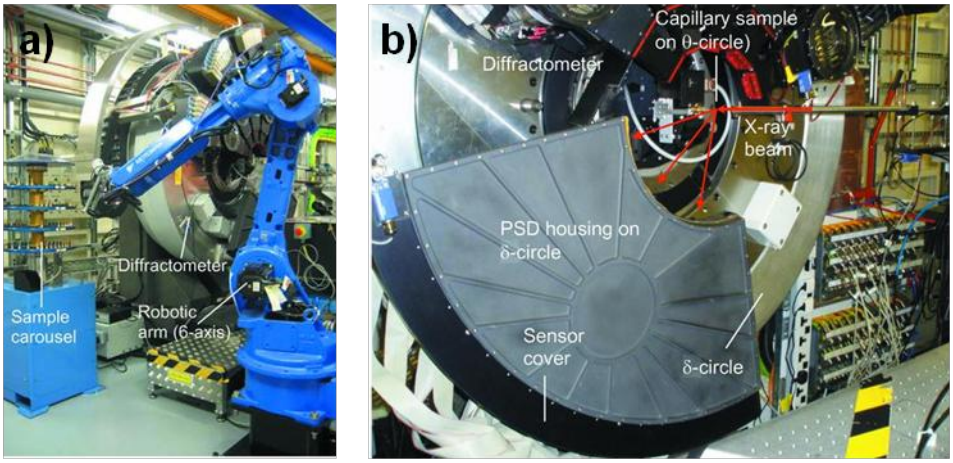

Figure 6. Synchrotron powder X-ray diffraction at I11, Diamond: a) robotic sample changer and carousel, and b) Mythen (PSD) detector setup. Figures from a) Parker et al.[17] and b) Thompson et al.[16]

High resolution synchrotron X-ray powder diffraction patterns were obtained using beamline I11 at the Diamond Light Source.[16] The position sensitive detector Mythen strip was used with mean wavelengths of 0.826124 Å and 0.827153 Å, calibrated using a NIST Si 640c standard. Samples were held in 0.7 mm and 0.8 mm glass capillaries, which were rotated continuously during the measurement to reduce the effects of preferred orientation. Data were collected at room temperature over the range 3° - 93° 2θ. For analysis, data binnings of 0.004° were used, and refinements were only performed over the range for which peaks were observed, using GSAS[18] *via* the EXPGUI[19] interface.

2.3.4. *Fourier transform infrared spectroscopy*

Fourier transform infrared spectroscopy is used to determine the types of chemical bonding within a material, due to the interaction between infrared light and molecular vibrations.[20] The vibrational frequency of a chemical bond depends on the elements involved and the strength of bonding, and the intensity of the corresponding spectral peak relates to the dipole moment of the bond. This gives different functional groups characteristic spectra, which act as a fingerprinting tool for confirmation of chemical composition. In addition, small

perturbations in the position of a peak corresponding to a functional group may give information about changes in the bonding caused by local structure variation. The infrared spectroscopy technique used in this research was attenuated total reflectance, using a diamond crystal (Figure 7). The sample is pressed onto the diamond crystal, through which the infrared beam is passed by total internal reflection. The spectrometer measures the absorption of infrared light due to the interaction between the sample and the evanescent wave, which extends into the sample by a few microns.

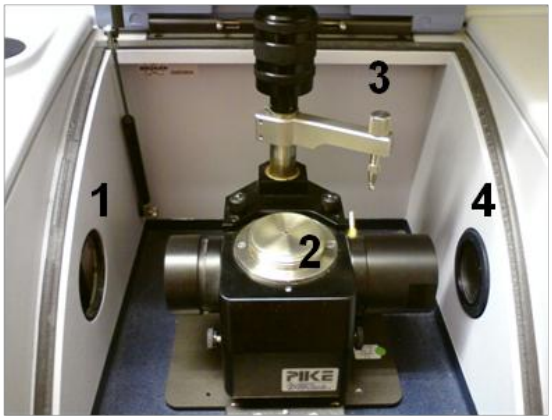

1) Incident beam
2) Diamond ATR crystal
3) Sample clamp
(moved out of position)
4) Detected beam

Figure 7. Fourier transform infrared spectroscopy using a diamond attenuated total reflectance setup.

Fourier-transform infrared spectroscopy was carried out using a Bruker Tensor 27 Infrared Spectrometer with a diamond attenuated total reflectance (ATR) attachment in absorbance mode. Multiple spectra were recorded in the range 4000-500 cm^{-1} and subsequently averaged.

2.3.5. *Thermogravimetric analysis*

Thermogravimetric analysis is used to observe changes in the mass of a sample upon heating (Figure 8).[21] In general, inorganic-organic frameworks undergo stepwise mass loss, with evaporation of solvent molecules occurring at lower temperatures than decomposition of the organic ligands and collapse of the framework. The final product is often an inorganic compound of the framework's metallic elements; its identity can depend on the gas used in the analysis, as can the precise temperatures of each mass loss step. Simultaneous differential scanning calorimetry and thermogravimetric analysis allows the heat flow profile of the heating process to be measured. This gives information about any phase transitions and can identify whether a mass loss step is exothermic or endothermic. The conditions used in this

research were compressed air, which results in oxidation of the ligand molecules, and a maximum temperature of 700 °C, chosen in order to avoid evaporation of volatile lithium.

Thermogravimetric analysis was performed using a TA Instruments Q500 TGA instrument with an air flow of 60 ml min^{-1} at a heating rate of 10 °C min^{-1}, from room temperature to 700 °C using 9 - 13 mg samples.

1) Control screen
2) Thermocouple
3) Sample pan (moved out of position)
4) Furnace
5) Gas inlet

Figure 8. Thermogravimetric analysis.

2.3.6. *Elemental analysis*

Elemental analysis was performed by the Microanalysis service at the University of Cambridge Chemical Laboratory, using an Exeter Analytical CE 440 elemental analyser. Carbon, hydrogen and nitrogen were measured as a fraction of the total sample mass by flash combustion, followed by separation and detection of the resulting gases, N_2, CO_2 and H_2O, by column chromatography.

2.3.7. *Optical microscopy*

Aside from simple visual inspection, optical microscopy is the first analytical tool for examining a reaction product (Figure 9). Information such as the colour, morphology and purity may be obtained, and rotation of crossed polarisers can indicate the crystallinity of a sample. In this case, the image of a single crystal will darken every 90° rotation, and imperfections such as cracks, inclusions and agglomeration may be uncovered. The images, of micron-scale resolution, may be recorded by a digital camera on top of the optics column.

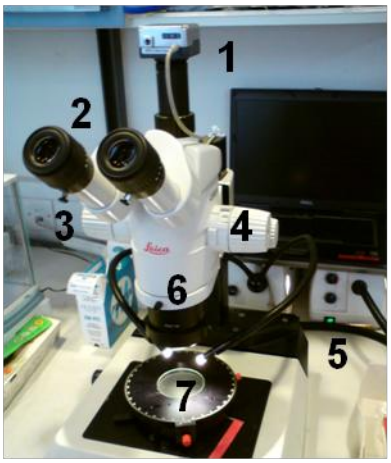

1) Digital camera and linked computer
2) Eyepieces
3) Focussing knob
4) Magnification knob
5) Light sources
6) Polariser
7) Rotating stage + polariser

Figure 9. Optical microscopy.

2.3.8. *Scanning electron microscopy*

Scanning electron microscopy uses a focussed beam of electrons to image a sample, obtaining resolution down to the nanometre scale.[22] The interaction of the electron beam with the sample knocks valence electrons out of their shells, generating secondary electrons, which are accelerated by a voltage bias towards a photomultiplier detector. The image is a result of the contrast differences in secondary electrons as the beam is scanned across the sample surface. Scanning electron microscopy can also be used to measure elemental composition by energy dispersive spectroscopy, and to image samples using backscattered electrons.

2.3.9. *Nuclear magnetic resonance spectroscopy*

Nuclear magnetic resonance, NMR, spectroscopy uses the interaction between radio waves and nuclear spins to identify the nuclear environments in a compound.[23] Elements such as ^{1}H and ^{13}C have nuclear spin $I = 1/2$ and so split into two levels in the presence of a magnetic field. Radio waves of different frequencies are absorbed depending on the energy difference between the levels. The particular elements examined and the electronic fields around the nuclei, which are a result of their chemical environments, give rise to absorption at different frequencies. In addition, peaks may be split by coupling with other nearby nuclei. Thus, an NMR spectrum gives information about the functional groups present and the proximity of nuclei to others.

Two main NMR methods were used in this research. Sample preparation for solution NMR, most commonly used in organic chemistry, involves dissolving the compound in question in an aprotic solvent to minimise the number of peaks in the spectra and placing the solution in

a precision-ground tube. Solid-state NMR uses the material as-synthesized, pressed into a small rotor that is spun at the "magic angle", 54.74°, at which interaction anisotropy averages to zero.[24] In a solid-state ^{13}C-^{1}H cross polarisation experiment, magnetization is initially formed in the ^{1}H spin system and then transferred to the ^{13}C spins by applying radio frequency fields simultaneously on both resonance frequencies. The efficiency of this polarization transfer depends strongly on the magnetic dipolar couplings between the ^{1}H and ^{13}C spins. If the coupling is strong (i.e. the ^{1}H-^{13}C distance is short), short contact times are sufficient to achieve a strong polarization transfer. If the couplings are small (i.e. the ^{1}H-^{13}C distance is large), longer contact times are required to transfer magnetization from ^{1}H to ^{13}C. If cross polarisation experiments are repeated with different contact times and the ^{13}C signal intensities are plotted as a function of contact time, typical build-up curves can be drawn whose shapes depend on the magnitudes of ^{1}H-^{13}C coupling and competing relaxation processes. The curves may thus be understood as a fingerprint of different carbon environments.

2.3.10. *Nanoindentation*

Nanoindentation probes the mechanical properties of a material by measuring the relationship between the displacement of an indenter tip into the material's surface and the applied force.[25] Due to limitations in tip geometry, resolution in the plane of the surface is typically at the micron scale, whilst depth resolution is closer to the nanometer scale. Single crystals must be prepared so that the facet to be examined is flat and, for anisotropic property measurements, the orientation of the crystal must also be known. This information is typically obtained by face indexation using a single crystal X-ray diffractometer.

2.3.11. *Impedance spectroscopy*

Impedance spectroscopy measures the response of a material to an alternating potential difference as a function of frequency.[26] Different dielectric processes, such as electronic polarization, dipole relaxation and ionic conductivity, are active at different frequencies and show different impedance responses. Ionic conductivity predominates at low frequencies, and gives rise to a semi-circle in the "Nyquist plot" of the real part of the complex impedance vs. the imaginary part. From this plot the resistance and capacitance of different contributions to ionic conductivity, such as the bulk material and the grain boundaries, can be obtained.

2.3.12. *Electrochemical cycling*

Electrochemical cycling is used to analyse the charge-discharge behaviour of a material in the configuration of a working cell. The potential difference across a cell consisting of lithium metal and the material in question, separated by a liquid electrolyte, is varied such that the current remains constant. Thus, the current relates directly to the number of lithium ions reacted, and the voltage profile yields information about the processes occurring, such as lithium insertion and solid electrolyte interphase formation.[27]

2.3.13. *Computational calculations*

Density functional theory investigates the electronic structure of many-bodied systems, such as molecules and crystal structures.[28] It uses functionals, functions of the electron density, to determine properties of materials, such as the lattice parameters, ground state electronic energy, band gap and vibrational spectrum. Different functionals, which approximate the structure in different ways, offer a variety of levels of refinement and agreement with experimental data.[29]

2.4. References

(1) Jones, P. G. *Chem. Br.* **1981**, *17*, (5).
(2) Walton, R. I. *Chem. Soc. Rev.* **2002**, *31*, (4), 230-238.
(3) Braga, D.; Grepioni, F. *Angew. Chem.-Int. Edit.* **2004**, *43*, (31), 4002-4011.
(4) Friscic, T.; Jones, W. *Cryst. Growth Des.* **2009**, *9*, (3), 1621-1637.
(5) *International Tables for Crystallography, Vol C: Mathematical, physical and chemical tables*. Prince, E., Ed.; 2nd ed.; IUCr: **2006**.
(6) Muller, P.; Herbst-Irmer, R.; Spek, A. L.; Schneider, T. R.; Sawaya, M. R., *Crystal Structure Refinement: A Crystallographer's Guide to SHELXL*. Muller, P., Ed.; Oxford University Press: **2006**.
(7) *CrysAlis CCD, CrysAlis RED and associated programs*, Oxford Diffraction Ltd., Abingdon, U.K., **2006**.
(8) Sheldrick, G. M. *Acta Crystallogr., Sect. A: Found. Crystallogr.* **2008**, *64*, 112-122.
(9) Farrugia, L. J. *J. Appl. Crystallogr.* **1999**, *32*, 837-838.
(10) Brandenburg, K.; Putz, H. *Diamond*, 3.2; CRYSTAL IMPACT GbR, Bonn, Germany, **2009**.
(11) Macrae, C. F.; Edgington, P. R.; McCabe, P.; Pidcock, E.; Shields, G. P.; Taylor, R.; Towler, M.; van de Streek, J. *J. Appl. Crystallogr.* **2006**, *39*, 453-457.
(12) McCusker, L. B.; Von Dreele, R. B.; Cox, D. E.; Louer, D.; Scardi, P. *J. Appl. Crystallogr.* **1999**, *32*, 36-50.
(13) Lebail, A.; Duroy, H.; Fourquet, J. L. *Mater. Res. Bull.* **1988**, *23*, (3), 447-452.
(14) Rietveld, H. M. *J. Appl. Crystallogr.* **1969**, *2*, 65-&.
(15) *X'Pert HighScore Plus*, 2.0; PANalytical B.V., **2004**.
(16) Thompson, S. P.; Parker, J. E.; Marchal, J.; Potter, J.; Birt, A.; Yuan, F.; Fearn, R. D.; Lennie, A. R.; Street, S. R.; Tang, C. C. *J. Synchrotron Radiat.* **2011**, *18*, (4), 637-648.
(17) Parker, J. E.; Thompson, S. P.; Cobb, T. M.; Yuan, F. J.; Potter, J.; Lennie, A. R.; Alexander, S.; Tighe, C. J.; Darr, J. A.; Cockcroft, J. C.; Tang, C. C. *J. Appl. Crystallogr.* **2011**, *44*, 102-110.
(18) Larson, A. C.; Von Dreele, R. B. *General Structure Analysis System (GSAS)*; 1994.
(19) Toby, B. H. *J. Appl. Crystallogr.* **2001**, *34*, 210-213.
(20) Williams, D. H.; Fleming, I., In *Spectroscopic Methods in Organic Chemistry*, 5th ed.; McGraw-Hill: **1995**; pp 28-62.
(21) Heal, G. R.; Laye, P. G.; Price, D. M.; Warrington, S. B.; Wilson, R. J., *Principles of thermal analysis and calorimetry*. Haines, P. J., Ed.; Royal Society of Chemistry: Cambridge, **2002**.
(22) Reimer, L., *Scanning electron microscopy: physics of image formation and microanalysis*. Springer: Berlin, **1998**.
(23) Williams, D. H.; Fleming, I., In *Spectroscopic Methods in Organic Chemistry*, 5th ed.; McGraw-Hill: **1995**; pp 63-169.
(24) Duer, M. J., *Introduction to solid-state NMR spectroscopy*. Blackwell: Oxford, **2004**.
(25) Oliver, W. C.; Pharr, G. M. *J. Mater. Res.* **2004**, *19*, (1), 3-20.
(26) *Impedance spectroscopy: theory, experiment, and applications*. Barsoukov, E.; Macdonald, J. R., Ed.; 2nd ed.; Wiley-Interscience: Hoboken, N.J., **2005**.
(27) Weppner, W., In *Solid State Electrochemistry*, Bruce, P. G., Ed. Cambridge University Press: Cambridge, **1995**; pp 199-228.
(28) Argaman, N.; Makov, G. *Am. J. Phys.* **2000**, *68*, (1), 69-79.
(29) (a) Krack, M.; Parrinello, M. *Forschungszentrum Julich, NIC Series* **2004**, *25,* 29. (b) VandeVondele, J.; Krack, M.; Mohamed, F.; Parrinello, M.; Chassaing, T.; Hutter, J. *Comput. Phys. Commun.* **2005**, *167*, (2), 103-128.

Chapter 3. Structural diversity, energy trends and phase behaviour of lithium tartrate frameworks.

3.1. Introduction

3.1.1. *Polymorphism in inorganic-organic frameworks*

Polymorphism is widely known in the field of organic molecules and pharmaceutical cocrystals,[1] but is relatively unexplored in the field of inorganic-organic frameworks. Makal *et al*. recently proposed a scheme of classification for "framework isomers", accounting for various differences in guest inclusion, ligand conformation and isomer for frameworks of the same elemental composition.[2] They define "ligand-originated isomers" as frameworks of the same elemental composition having different ligand isomers; the majority of the new lithium tartrate frameworks discussed in this chapter are of this type. Three other framework types are defined: frameworks with identical topologies but different levels of interpenetration are classed as "interpenetration isomers", "conformational isomers" contain the same molecular units but with different twists or bends (the lithium tartrate isomers in this chapter that contain the same ligand isomer are of this type), and "orientation isomers" contain molecular units that are identical when considered as independent moieties, but which are connected in different orientations within the crystal structure. However, this classification scheme is clearly designed with porous frameworks in mind, and is of limited use when referring to non-porous inorganic-organic frameworks, which contain no accessible pore space or guest species and in which interpenetration does not occur. Furthermore in such systems, use of the term "polymorph" to describe different structures with identical molecular composition makes the definition of "conformational isomers" redundant. The isomeric lithium tartrate structures described in this chapter can be classified by two of the above terms, "ligand originated isomers" and "polymorphs" (Figure 1).

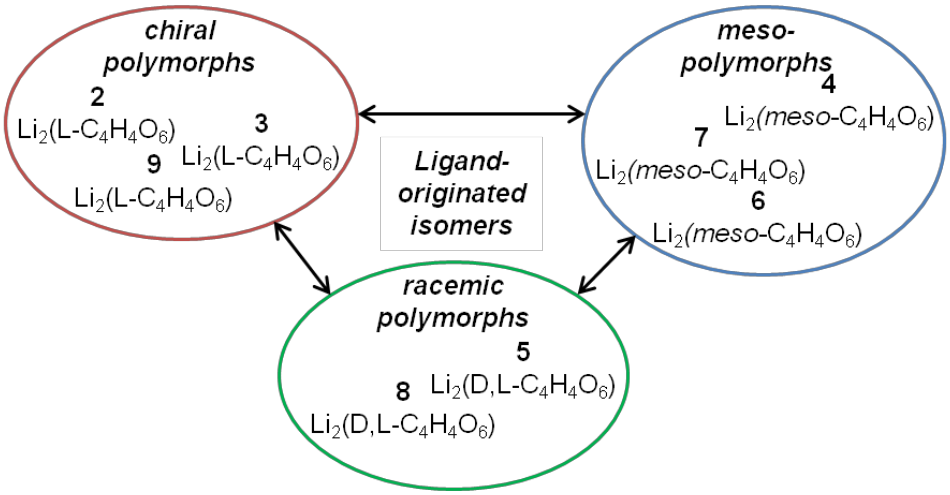

Figure 1. Classes of isomeric frameworks in the dilithium tartrates described in this chapter.

The non-porous systems previously studied have generally consisted of just two polymorphs[3] and only a handful of attempts have been made to rationalise the phase behaviour of non-porous inorganic-organic frameworks by calculation of the structures' energies.[4] In those cases, the level of theory used to calculate framework energies is often inadequate and is rarely accurate enough to distinguish between polymorphs whose energy difference is on the same scale as intermolecular interactions such as hydrogen bonds. Bailey *et al*. have rationalised the difference in energy of layered racemic and chiral zinc cyclohexane *trans*-1,2-dicarboxylate analogues, $Zn(C_8H_{10}O_4)$, very simply in terms of internal intra-layer and non-bonded inter-layer energies.[5] Finer structural elements, such as ligand conformation,[6] are more difficult to describe due to their complex interplay with the inorganic structural elements and electrostatic interactions in the structural models. Therefore one aim of this research is to understand what level of theory is necessary to account for phase behaviour in inorganic-organic frameworks and what the important structural factors to consider in doing so are. In particular, contributions from zero-point vibrational energy and thermal vibrational modes, which were not previously assessed, may prove important.

3.1.2. *Tartrate-based inorganic-organic framework materials*

Tartaric acid, $C_4H_6O_6$, contains two chiral centres and can exist in one of three isomeric molecular forms, L-, D- and *meso*-tartaric acid (Figure 2). The L- and D- conformers are enantiomeric and the *meso*- form is achiral, forming three distinct crystal structures. The racemate of the chiral L- and D- enantiomers crystallizes as a fourth polymorph, D,L-tartaric acid.

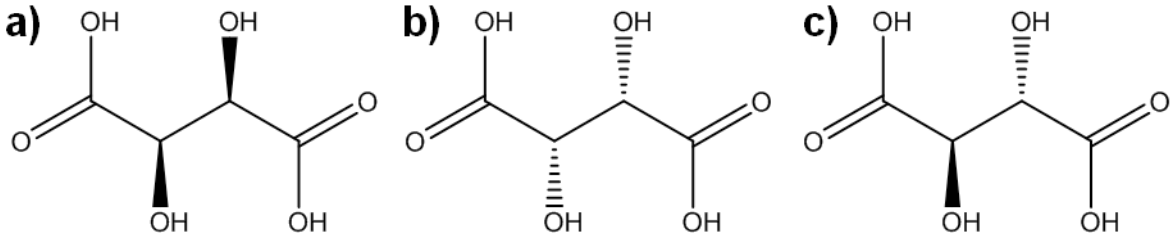

Figure 2. Configurations of a) L-tartaric acid, b) D-tartaric acid and c) meso-tartaric acid.

Tartaric acid has been used as a ligand in inorganic-organic frameworks in combination with many metal ions. The crystal structure of one of the most well-known tartrates, potassium sodium tartrate tetrahydrate, $KNa(C_4H_4O_6)\cdot 4H_2O$, otherwise known as Rochelle Salt, was first determined in 1940.[7] It has long been known as a ferroelectric[8] in which hydrogen bonding between the chiral tartrate ligand and framework water molecules enables switching of the materials' spontaneous dipole moment. Similar dielectric properties have since been found in many other L- and D-tartrates due to the chiral properties of the ligand giving rise to inherently non-centrosymmetric structures.[9] Other chiral, non-porous, inorganic-organic frameworks, such as the transition metal L-tartrates $M(C_4H_4O_6)$ (where M = Mn^{II}, Fe^{II}, Co^{II}, Ni^{II}), are also being investigated for magnetic properties.[10] Those chiral properties are also of interest for porous inorganic-organic frameworks, which could be useful for enantiomorphic separation and catalysis applications.[11]

Previous research in the author's research group has uncovered a large diversity in the structures of alkaline earth tartrates, $M(C_4H_4O_6)\cdot xH_2O$ (where M = Mg^{2+}, Ca^{2+}, Sr^{2+} and Ba^{2+}).[12] Kam *et al*. discovered nine crystalline modifications of magnesium tartrate using hydrothermal synthesis.[12a] Variations in ligand isomer resulted in the formation of chiral D-tartrate, achiral D,L-tartrate and *meso*-tartrate isomers, in which the level of hydration decreased and the overall dimensionality increased upon raising the synthesis temperature (Figure 3). Appelhans *et al*. found that, in addition, variation in cation size altered the metal coordination geometry and thus changed the resulting structures in calcium, barium and strontium tartrates.[12b] The phase selection and energetics of these materials were investigated by computational and calorimetric methods. This prior work suggests that the alkali metal tartrates, $M_2(C_4H_4O_6)\cdot xH_2O$ (where M = Li^+, Na^+, K^+, Rb^+), which so far have not been systematically studied, may also yield diverse structures.

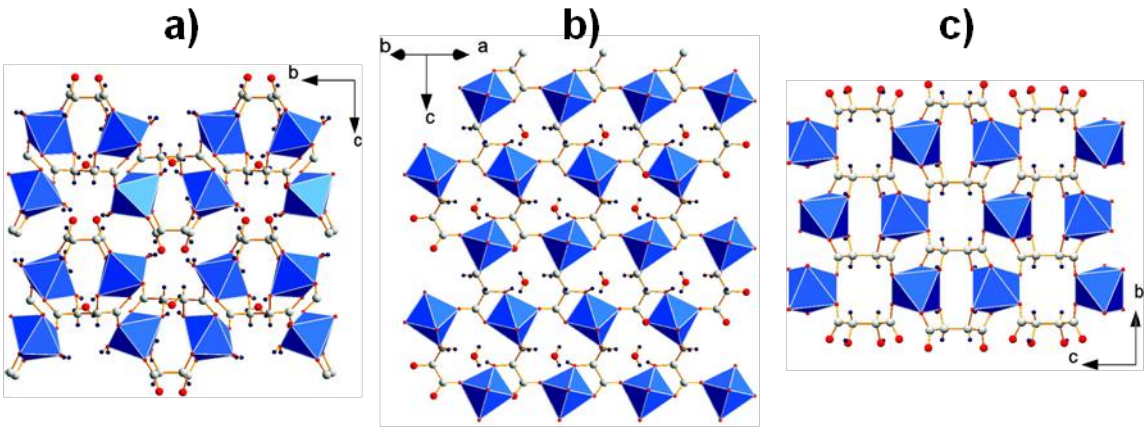

Figure 3. Structures of chiral magnesium tartrates: a) hydrated 2-D framework [Mg(D-$C_4H_4O_6$)(H_2O)]·1.5H_2O, b) hydrated 3-D framework [Mg(D-$C_4H_4O_6$)]·H_2O, and c) anhydrous 3-D framework Mg(D-$C_4H_4O_6$). C, H and O atoms and MgO_6 polyhedra are coloured grey, blue, red and blue, respectively. Reproduced with permission,[12a] copyright 2007 ACS.

3.1.3. *Lithium tartrates, $Li_{2-x}H_x(C_4H_4O_6)\cdot nH_2O$*

Inspection of the Cambridge Structural Database[13] shows the existence of just three lithium tartrates, all of which are hydrated. The structure of lithium hydrogen *meso*-tartrate monohydrate was reported by Stouten *et al.* in 1988, and consists of chains of edge-sharing LiO_5 polyhedra, leading to the notation by Cheetham *et al.* of I^1O^0.[14] The chains are connected by extensive inter-ligand and water hydrogen bonding (Figure 4a).[15] Bott *et al.* reported the structure of lithium hydrogen L-tartrate monohydrate in 1994,[16] which was improved by Gelbrich *et al.* in 2004 (Figure 4b).[17] It contains Li_2O_8 dimers, connected by the ligand to form I^0O^1 chains, which exhibit many hydrogen bonds. Gelbrich *et al.* then reported the structure of dilithium D,L-tartrate trihydrate in 2006 (Figure 4c).[18] It also contains dimeric Li-based polyhedra, which are connected by the ligands to form heavily hydrogen bonded I^0O^2 sheets.

It is interesting to note that Gelbrich and co-workers were "unable to obtain any other dilithium tartrates",[18] and that no anhydrous phases were formed. The crystallization methods used tended to be slow evaporation of aqueous solutions at ambient temperature, and no mention is made of other attempted techniques.

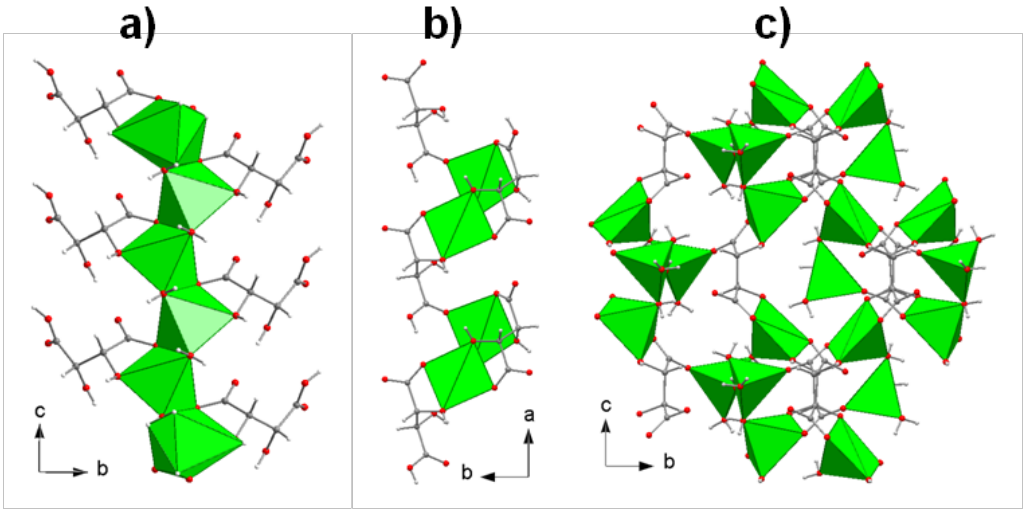

Figure 4. Structures of known hydrated lithium tartrates: a) lithium hydrogen meso-tartrate monohydrate, b) lithium hydrogen L-tartrate monohydrate, and c) dilithium D,L-tartrate trihydrate. C, H and O atoms and LiO_4 tetrahedra are coloured grey, white, red and green, respectively.

3.1.4. *Strategies to synthesize and investigate anhydrous lithium tartrates*

Phase behaviour of inorganic-organic frameworks, particularly with respect to degree of hydration, has been found to be dependent on temperature, pH, concentration and reaction time.[19] Lithium-containing systems are generally highly water-soluble due to the large energy gain upon solvation of lithium cations. Therefore it is unsurprising that previously reported lithium tartrates crystallized upon evaporation of water, rather than directly from solution with substantial mother liquor remaining (as is more commonly the case with other inorganic-organic frameworks). Synthesis from water also led to the incorporation of water as a framework component, which must be avoided for potential applications in lithium batteries or dielectrics due to its detrimental effect on thermal and electrochemical stability (see Chapter 5).

Given the above, a possible approach towards synthesis of crystalline anhydrous lithium tartrates would be to find a solvent system that enables dissolution of molecular precursors and precipitation of lithium-based frameworks. For this reason, non-aqueous solvents were chosen for exploratory synthesis of new phases, along with raised temperatures up to 200 °C to drive off residual water. Once the diverse nature of the phase space of anhydrous lithium tartrates became apparent, mixed solvent systems with a controlled water fraction were used, to increase the likelihood of reaching a thermodynamic product.

This approach resulted in the discovery of eleven new crystalline lithium tartrate frameworks, eight of which are isomeric and have the same elemental composition, $Li_2(C_4H_4O_6)$. This chapter describes the atomic structure of each material in detail, and investigates variations in structural features in order to explain the differences in their energies as well as their phase behaviour, which was investigated as a function of ligand isomer, solvent and temperature.

3.2. Experimental

3.2.1. *Synthesis*

All reagents, lithium acetate dihydrate (98 %, Fisher Scientific UK), lithium nitrate (98 %, Sigma), D,L-tartaric acid (99.5 %, Fisher Scientific UK), L-tartaric acid (>99 %, Fisher Scientific UK) and *meso*-tartaric acid monohydrate (≥97 %, Sigma-Aldrich), and solvents, ethanol and tetrahydrofuran (THF) (both reagent grade, Fisher Scientific UK), in-house deionised water and N,N-dimethylformamide (DMF, reagent grade, Acros Organics) were used as received under aerobic conditions. Reactions were carried out in 4 and 12 mL borosilicate glass vials with PTFE-lined caps (Fisher Scientific UK) and 23 mL PTFE-lined stainless steel autoclaves obtained from Parr Instrument Company.[20]

3.2.1.1. Synthesis of lithium hydrogen L-tartrate in $P2_1$, LiH(L-$C_4H_4O_6$), **1**

A mixture of lithium acetate dihydrate (2.0 mmol), L-tartaric acid (1.0 mmol), THF (7.5 mL) and ethanol (7.5 mL) was placed inside a 23 mL PTFE-lined stainless steel autoclave and stirred for 10 minutes. The autoclave was then sealed and heated at 100 °C for two days then cooled over two hours to room temperature. The resulting solid, consisting of colourless plates and white powder, was washed with ethanol and dried in air at 60 °C for one day. The plates were used for structure determination by single crystal X-ray diffraction. However, the powder X-ray diffraction pattern of the product did not match the simulated pattern for **1**; rather it appeared to contain multiple unknown phases. Thermo-gravimetric analysis indicates the presence of a solvated impurity and an unknown anhydrous phase, although it is unclear whether they are lithium hydrogen tartrates, dilithium tartrates or other compositions (see Appendix). A phase-pure sample of **1** could not be obtained for further analyses.

3.2.1.2. Synthesis of dilithium L-tartrate in $P2_12_12_1$, Li_2(L-$C_4H_4O_6$), **2**

A mixture of lithium acetate dihydrate (2.0 mmol), L-tartaric acid (1.0 mmol) and ethanol (9.25 mL) was placed inside a 23 mL PTFE-lined stainless steel autoclave and stirred for 10 minutes. The autoclave was sealed and heated at 150 °C for three days, then cooled over two hours to room temperature. The final product, consisting of colourless flat rods (123 mg, 79 %), was washed with ethanol and dried in air at 60 °C for one day. A suitable rod was selected for structure determination by single crystal X-ray diffraction, but the product contained approximately 14 % **3**. A phase-pure sample was prepared in the following way: a

solution of L-tartaric acid (1.0 mmol) in ethanol (5 mL) was added dropwise to a solution of lithium acetate dihydrate (2.0 mmol) in ethanol (5 mL) inside a 23 mL PTFE-lined stainless steel autoclave and the resulting mixture was stirred for 10 minutes. The autoclave was sealed and heated at 150 °C for six days, then cooled over two hours to room temperature. The final product, consisting of white powder and colourless flat rods (156 mg, 96 %), was washed with ethanol and dried in air at 60 °C for one day. Elemental analysis: C 29.63 %, H 2.45 % (Calculated for $C_4H_4Li_2O_6$: C 29.67 %, H 2.49 %).

3.2.1.3. Synthesis of dilithium L-tartrate in *C*222$_1$, Li_2(L-$C_4H_4O_6$), **3**

A mixture of lithium acetate dihydrate (2.0 mmol) in ethanol (5 ml) and L-tartaric acid (1.0 mmol) in ethanol (5 mL) was placed inside a 23 mL PTFE-lined stainless steel autoclave and stirred for 10 minutes. The autoclave was sealed and heated at 150 °C for 3 days and then cooled over three days to room temperature. The final product, consisting of colourless flat rods and hexagonal platelets (148 mg, 91 %), was washed with ethanol and dried in air at 60 °C for one day. The platelets were used for structure determination by single crystal X-ray diffraction, but the product contained approximately 23 % **2**. A phase-pure sample was prepared in the following way: A solution of L-tartaric acid (1.0 mmol) in ethanol (5 mL) was combined with a solution of lithium acetate dihydrate (2.0 mmol) in ethanol (5 mL) inside a 23 mL PTFE-lined stainless steel autoclave and the resulting mixture was stirred for 10 minutes. The autoclave was sealed and heated at 150 °C for one day, followed by 125 °C for three days, then cooled naturally to room temperature. The final product, consisting of colourless microcrystalline powder (66 mg, 41 %), was washed with ethanol and dried in air at 60 °C for one day. Elemental analysis: C 29.60 %, H 2.42 % (Calculated for $C_4H_4Li_2O_6$: C 29.67 %, H 2.49 %).

3.2.1.4. Synthesis of dilithium *meso*-tartrate in *C*2/*c*, Li_2(*meso*-$C_4H_4O_6$), **4**

A mixture of lithium acetate dihydrate (2.0 mmol), *meso*-tartaric acid monohydrate (1.0 mmol) and DMF (5 mL) was placed inside a 23 mL PTFE-lined stainless steel autoclave and stirred for 10 minutes. The autoclave was then sealed and heated at 180 °C for three days, then cooled over two hours to room temperature. The resulting solid, consisting of colourless flat rods and white powder, was washed with isopropanol and dried in air at 60 °C for one day. The rods were used for structure determination by single crystal X-ray diffraction. However, the powder X-ray diffraction pattern of the product did not match the simulated pattern for **4**; rather it appeared to contain two or more phases. Thermo-gravimetric analysis

indicates the presence of two anhydrous impurities, one of which is **6**. The other phase is as-yet unknown. A phase pure sample of **4** could not be obtained for other analyses.

3.2.1.5. Synthesis of dilithium D,L-tartrate in *C*2/*c*, $Li_2(D,L\text{-}C_4H_4O_6)$, **5**

A mixture of $LiNO_3$ (2.0 mmol), D,L-tartaric acid (1.0 mmol) and isopropanol (10 mL) was placed inside a 23 mL PTFE-lined stainless steel autoclave and stirred for 10 minutes. The autoclave was sealed and heated at 180 °C for five days then cooled over two hours to room temperature. The final product, consisting of colourless needles (105 mg, 68 %), was washed with ethanol and dried in air at 60 °C for one day. A suitable needle of **5** was selected for structure determination by single crystal X-ray diffraction, but the product contained approximately 30 % **2**. A phase-pure sample was prepared in the following way: A solution of D,L-tartaric acid (1.0 mmol) in ethanol (5 mL) was added dropwise to a solution of lithium acetate dihydrate (2.0 mmol) in ethanol (5 mL) inside a 23 mL PTFE-lined stainless steel autoclave and the resulting mixture was stirred for 10 minutes. The autoclave was sealed and heated at 150 °C for three days, then cooled naturally to room temperature. The final product, consisting of white powder (134 mg, 83 %), was washed with ethanol and dried in air at 60 °C for one day. Elemental analysis: C 29.93 %, H 2.58 % (Calculated for $C_4H_4Li_2O_6$: C 29.67 %, H 2.49 %).

3.2.1.6. Synthesis of dilithium *meso*-tartrate in $P2_1/c$, $Li_2(meso\text{-}C_4H_4O_6)$, **6**

A solution of lithium acetate dihydrate (2 mmol) in water:ethanol (1:2, 5 ml) was layered under a solution of *meso*-tartaric acid monohydrate (1 mmol) in water:ethanol (1:2, 5 ml) in a 23 mL PTFE-lined stainless steel autoclave, which was heated at 125 °C. After three days the autoclave was cooled to 25 °C and the product, colourless crystals of **6** (124 mg, 76 %), was filtered, washed (water:ethanol 1:2) and dried in air. Another bulk sample used for further analysis was synthesized at 100 °C. Elemental analysis found C 29.65 %, H 2.47 %, (calculated C 29.67 %, H 2.49 %).

3.2.1.7. Synthesis of dilithium *meso*-tartrate in *Cc*, $Li_2(meso\text{-}C_4H_4O_6)$, **7**

A solution of lithium acetate dihydrate (2 mmol) in water:ethanol (1:2, 5 ml) was layered under a solution of *meso*-tartaric acid monohydrate (1 mmol) in water:ethanol (1:2, 5 ml) in a 12 ml borosilicate vial, which was heated to 60 °C. After three days it was cooled to 25 °C and the contents, colourless crystals of **8** (96 mg, 59 %) were filtered, washed (water:ethanol 1:2) and dried in air. Another bulk sample used for further analysis was synthesized at room

temperature using a water:ethanol ratio for the acid solution of 1:4, and drying in air at 60 °C. Elemental analysis found C 29.43 %, H 2.51 %, (calculated C 29.67 %, H 2.49 %).

3.2.1.8. Synthesis of dilithium D,L-tartrate in $P2_1/c$, $Li_2(D,L\text{-}C_4H_4O_6)$, **8**

A solution of lithium acetate dihydrate (2 mmol) in water:ethanol (1:4, 5 ml) was layered under a solution of D,L-tartaric acid (1 mmol) in water:ethanol (1:9, 5 ml) in a 12 ml borosilicate vial, which was left to stand at 25 °C. After six days the vial contained colourless plates suitable for single crystal X-ray diffraction studies. A bulk sample used for further analysis was synthesized as follows: a solution of lithium acetate dihydrate (2 mmol) in water:ethanol (1:2, 5 ml) was layered under a solution of D,L-tartaric acid (1 mmol) in water:ethanol (1:4, 5 ml) in a 23 mL PTFE-lined stainless steel autoclave, which was heated at 100 °C. After three days the autoclave was cooled to 25 °C and the product, colourless crystals of **8** (30 mg, 18 %) was filtered, washed (water:ethanol 1:4) and dried in air. Elemental analysis found C 29.45 %, H 2.39 % (calculated C 29.67 %, H 2.49 %).

3.2.1.9. Synthesis of dilithium L-tartrate in $C2$, $Li_2(L\text{-}C_4H_4O_6)$, **9**

A solution of lithium acetate dihydrate (2 mmol) in water:ethanol (1:2, 5 ml) was layered under a solution of L-tartaric acid (1 mmol) in water:ethanol (1:4, 5 ml) a 23 mL PTFE-lined stainless steel autoclave, which was heated at 125 °C. After three days the autoclave was cooled to 25 °C and colourless crystals were hand-picked from the reaction product for single crystal X-ray diffraction studies. A purer sample of **9** (containing ~20 % **2**) for further analyses was obtained as follows: lithium acetate dihydrate (2 mmol), L-tartaric acid (1 mmol), water (3 ml) and ethanol (7 ml) were placed in a 23 mL PTFE-lined stainless steel autoclave, which was heated at 150 °C. After 7 days the autoclave was cooled to 25 °C and the product, colourless rods (93 mg, 57 %), was filtered, washed in solvent and dried at 60 °C overnight.

3.2.1.10. Synthesis of dilithium D,L-tartrate dihydrate in $P1$, $Li_2(D,L\text{-}C_4H_4O_6)(H_2O)_2$, **10**

A solution of lithium acetate dihydrate (2 mmol) in water:ethanol (1:2, 5 ml) was layered under a solution of D,L-tartaric acid (1 mmol) in water:ethanol (1:4, 5 ml) in a 4 ml borosilicate vial, which was left to stand at 20 °C. After 6 days the precipitate, a mixture of colourless triangular prisms and needles, was separated from the mother liquor. A suitable triangular prism was selected for structure determination of $Li_2(D,L\text{-}C_4H_4O_6)(H_2O)_2$, **10**.

Powder X-ray diffraction analysis showed a mixture of **4**, **8** and **10**, but a phase-pure sample could not be obtained.

3.2.1.11. Synthesis of dilithium *meso*-tartrate hemihydrate in *C*222$_1$, Li_2(*meso*-$C_4H_4O_6$)(H_2O)$_{0.5}$, **11**

A solution of lithium acetate dihydrate (2 mmol) in water:ethanol (1:2, 5 ml) was layered under a solution of *meso*-tartaric acid (1 mmol) in water:ethanol (1:4, 5 ml) in a 4 ml borosilicate vial, which was left to stand at 20 °C. After 6 days the precipitate, consisting of colourless square plates surrounded by polycrystalline material, was separated from the mother liquor and a suitable square plate was selected for structure determination of Li_2(*meso*-$C_4H_4O_6$)(H_2O)$_{0.5}$, **11**. The remaining precipitate was dried in air over two months to yield a white powder, which was used for further analysis; PXRD found it to consist of pure Li_2(*meso*-tart), **7**. Elemental analysis found C 29.43 %, H 2.51 % (calculated C 29.67 %, H 2.49 %).

3.2.1.12. Phase behaviour of lithium L-tartrates from ethanolic solution

Lithium acetate dihydrate (2 mmol), D,L-tartaric acid (1 mmol) and ethanol (10 ml) were placed in a 12 ml borosilicate vial, which was left to stand at 25 °C. Similar mixtures were prepared and placed in ovens at various temperatures up to 200 °C, using autoclaves as reaction vessels above 60 °C. After three days the vessels at elevated temperatures were cooled to 25 °C and the contents were filtered, washed (ethanol) and dried in air. Products were colourless or white solids (see Table 14 for phases and morphologies); yields ranged from 133 mg to 153 mg (82 % - 94 % for $Li_2C_4H_4O_6$).

3.2.1.13. Phase behaviour of lithium L-tartrates from mixed water:ethanol solution

A solution of lithium acetate dihydrate (2 mmol) in water:ethanol (1:2, 5 ml) was layered under a solution of L-tartaric acid (1 mmol) in water:ethanol (1:4, 5 ml) in a 12 ml borosilicate vial, which was left to stand at 25 °C. Similar mixtures were prepared and placed in ovens at various temperatures up to 200 °C, using autoclaves as reaction vessels above 60 °C. After four days the vessels at elevated temperatures were cooled to 25 °C and the contents were filtered, washed (water:ethanol 1:4) and dried in air. The vial at 25 °C had very little precipitate at this time, so was left a further seven days before filtering. Products were colourless or white solids (see Table 14 for phases and morphologies); yields ranged from 84 mg to 98 mg (52 % - 60 % for $Li_2C_4H_4O_6$).

3.2.1.14. Phase behaviour of lithium *meso*-tartrates from ethanolic solution

Lithium acetate dihydrate (2 mmol), *meso*-tartaric acid (1 mmol) and ethanol (10 ml) were placed in a 12 ml borosilicate vial, which was left to stand at 25 °C. Similar mixtures were prepared and placed in ovens at various temperatures up to 200 °C, using autoclaves as reaction vessels above 60 °C. After three days the vessels at elevated temperatures were cooled to 25 °C and the contents were filtered, washed (ethanol) and dried in air. Products were white solids (see Table 14 for phases and morphologies); yields ranged from 88 mg to 157 mg (54 % - 97 % for $Li_2C_4H_4O_6$).

3.2.1.15. Phase behaviour of lithium *meso*-tartrates from mixed water:ethanol solution

A solution of lithium acetate dihydrate (2 mmol) in water:ethanol (1:2, 5 ml) was layered under a solution of *meso*-tartaric acid (1 mmol) in water:ethanol (1:2, 5 ml) in a 12 ml borosilicate vial, which was left to stand at 25 °C. Similar mixtures were prepared and placed in ovens at various temperatures up to 200 °C, using autoclaves as reaction vessels above 60 °C. After three days the vessels at elevated temperatures were cooled to 25 °C and the contents were filtered, washed (water:ethanol 1:2) and dried in air. The vial at 25 °C had very little precipitate at this time, so was left a further four days before filtering. Products were colourless or white solids (see Table 14 for phases and morphologies); yields ranged from 91 mg to 125 mg (56 % - 77 % for $Li_2C_4H_4O_6$).

3.2.1.16. Phase behaviour of lithium D,L-tartrates from ethanolic solution

Lithium acetate dihydrate (2 mmol), D,L-tartaric acid (1 mmol) and ethanol (10 ml) were placed in a 12 ml borosilicate vial, which was left to stand at 25 °C. Similar mixtures were prepared and placed in ovens at various temperatures up to 200 °C, using autoclaves as reaction vessels above 60 °C. After three days the vessels at elevated temperatures were cooled to 25 °C and the contents were filtered, washed (ethanol) and dried in air. Products were colourless or white solids (see Table 14 for phases and morphologies); yields ranged from 133 mg to 153 mg (84 % - 94 % for $Li_2C_4H_4O_6$).

3.2.1.17. Phase behaviour of lithium D,L-tartrates from mixed water:ethanol solution

A solution of lithium acetate dihydrate (2 mmol) in water:ethanol (1:2, 5 ml) was layered under a solution of D,L-tartaric acid (1 mmol) in water:ethanol (1:4, 5 ml) in a 12 ml borosilicate vial, which was left to stand at 25 °C. Similar mixtures were prepared and placed

in ovens at various temperatures up to 200 °C, using autoclaves as reaction vessels above 60 °C. After three days the vessels at high temperatures were cooled to 25 °C and the contents were filtered, washed (water:ethanol 1:4) and dried in air. The vials at 25 °C and 60 °C had very little precipitate at this time, so were left a further three days before filtering. Products were colourless or white solids (see Table 14 for phases and morphologies); yields ranged from 27 mg to 51 mg (17 % - 31 % for $Li_2C_4H_4O_6$).

3.2.2. *Single crystal X-ray diffraction*

Crystal structure determinations by X-ray diffraction of **1, 3** and **4** were performed by the National Crystallography Service, Southampton, on a Bruker-Nonius APEX II CCD camera on κ-goniostat diffractometer equipped with 10 cm confocal mirrors, Bruker-Nonius FR591 rotating anode radiation source (Mo Kα radiation, $\lambda = 0.71073$ Å) operating at 50 kV and 85 mA. Data were collected at 120(2) K using φ and ω scans. The mean detector area resolution was 4096 x 4096 pixels / 62 x 62 mm. Data collection, cell determination and refinement, and data reduction were performed using the COLLECT,[21] DirAx,[22] DENZO,[23] and Scalepack[23] programs. An empirical correction based on symmetry equivalent reflections was applied using the SADABS 2007/2 program.[24] Structure solution and refinement were performed as described in Chapter 2.

Crystal structure determinations by X-ray diffraction of **2** and **6 - 11** were performed using a laboratory diffractometer as described in Chapter 2.

The structure of **5** was determined by Dr. Paul Forster, using microcrystal diffraction at the Advanced Light Source on the 11.3.1 beamline using 0.7790 Å radiation. Data were collected at 100 K using the APEXII software package.[25] The structure was solved with direct methods and refined using the SHELXTL software suite.[26] Towards the end of the refinement, Fourier peaks were observed corresponding to a second orientation of the tartrate ligand and refined using a partial occupancy model. Hydrogen atoms were added geometrically and refined using the riding model. Visualisation of structures was carried out using Diamond[27] and Mercury[28] programs.

3.2.3. *Computational energy calculations*

Calculations were performed by Dr. Monica Kosa, taking the initial xyz coordinates of phases **1 - 9** from the experimental X-ray data. Structures involving atomic disorder were simplified by removing the disordered atoms with lower site occupancy and assigning full

occupancy to the remaining atoms. Multiple unit cells were used for each structure, such that the total number of formula units in each simulation cell was 24. For geometry and cell optimizations, all structures were calculated using the PBE functional,[29] GTH pseudopotential[30] with the DZVP Gaussian basis set,[31] and 600 Ry plane wave density cutoff and 40 Ry relative cutoff as implemented in the QS module of the CP2K package.[32] The convergence of the total energy with respect to the plane wave basis set was checked in the range of 200 - 1000 Ry, with intervals of 100 Ry. The relatively high and safe value of 600 Ry was chosen in order to avoid inconsistencies due to different cell sizes with respect to the plane wave basis set.

The formation energies, ΔE_{elec} (PBE), of **1** - **9** were calculated according to the equations shown in Figure 5 and afterwards normalized per formula unit of (di)lithium tartrate. The electronic energies at 0 K of the isolated molecules of lithium acetate, tartaric acid and acetic acid were calculated with the same Gaussian basis set and plane wave density cutoff as the extended phases **1** - **9**. Similar methods were used to calculate the formation energies of **2** - **9** including dispersion correction, ΔE_{elec} (PBE+D), using the density functional B97-D.[33] The Zero Point Vibrational Energies, ZPVE, of phases **2** - **6** were evaluated (at the Γ-point only) within the harmonic approximation as a sum of contributions from all vibrational modes of the system. Thermal populations, E_{vib} (298.15 K), were evaluated according to the classical approximation. Calculation of the formation energies including vibrational contributions, ΔE_{tot} (PBE+V), of **2** - **6** was performed by adding both ZPVE and E_{vib} (298.15 K) to ΔE_{elec} (PBE). Calculation of thermal contributions for structures **7** - **9** was not possible due to the high computational cost involved.

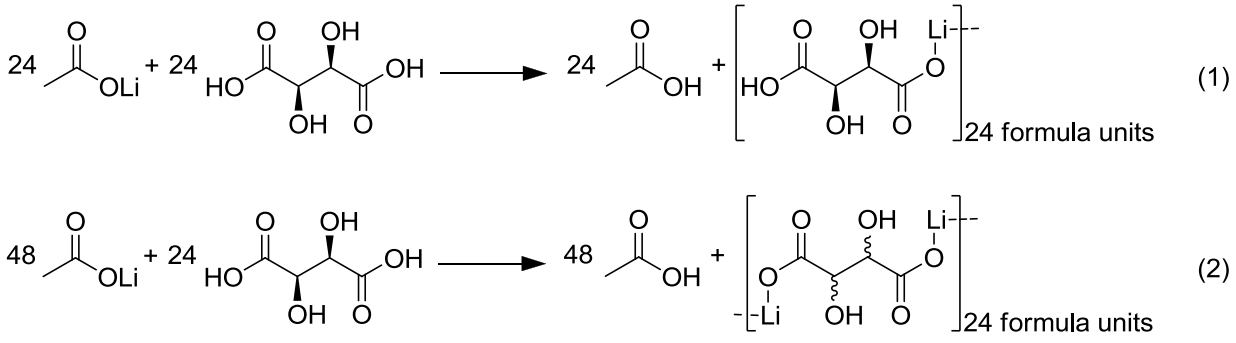

*Figure 5. Chemical equations used to calculate the formation energies of lithium hydrogen L-tartrate **1** (1) and dilithium tartrates **2** - **5** (2).*

3.3. Results

3.3.1. *Structures of new anhydrous lithium tartrates*

The single crystal structures of nine anhydrous lithium tartrates, **1** - **9**, were determined by single crystal X-ray diffraction methods. A summary of the crystal data can be found in Table 1 (**1** - **5**) and Table 2 (**6** - **9**).

	1	**2**	**3**	**4**	**5**
formula	$LiH(L\text{-}C_4H_4O_6)$	$Li_2(L\text{-}C_4H_4O_6)$	$Li_2(L\text{-}C_4H_4O_6)$	$Li_2(meso\text{-}C_4H_4O_6)$	$Li_2(D,L\text{-}C_4H_4O_6)$
crystal size (mm)	0.10 × 0.07 × 0.02	0.5 × 0.4 × 0.3	0.06 × 0.06 × 0.01	0.22 × 0.05 × 0.03	0.08 × 0.05 × 0.015
crystal system	monoclinic	orthorhombic	orthorhombic	monoclinic	monoclinic
space group	$P2_1$	$P2_12_12_1$	$C222_1$	$P2_1/c$	$C2/c$
T (K)	120(2)	120(2)	120(2)	120(2)	120(2)
a (Å)	5.0643(2)	5.0455(3)	5.5800(6)	6.0522(9)	15.988(10)
b (Å)	8.3299(3)	14.9300(12)	9.1055(6)	5.3351(8)	5.0193(14)
c (Å)	7.4469(3)	16.1053(12)	12.0180(11)	9.8636(14)	15.020(8)
α (°)	90	90	90	90	90
β (°)	107.585(2)	90	90	100.474(9)	101.50(5)
γ (°)	90	90	90	90	90
V (Å^3)	299.47(2)	1213.0(2)	610.62(10)	313.18(8)	1181.1(10)
asym. unit	$C_4H_5Li_1O_6$	$C_8H_8Li_4O_{12}$	$C_2H_2Li_1O_3$	$C_2H_2Li_1O_3$	$C_4H_4Li_2O_6$
Z	2	8	4	2	8
d_{calc} (g cm^{-3})	1.730	1.774	1.762	1.717	1.821
μ (mm^{-1})	0.165	0.164	0.162	0.158	0.168
refl. collected	4170	2396	3280	3246	4525
unique refl.	1332	2104	696	713	1212
observed data (I > 2σ(I))	1267	1694	578	543	854
parameters	117	241	61	62	131
R_{int}	0.0355	0.039	0.0750	0.0554	0.0411
R_1	0.0326	0.0402	0.0462	0.0810	0.0673
wR_2 (I > 2σ(I))	0.0683	0.1005	0.1193	0.1736	0.1886
R_1 (all data)	0.0356	0.0517	0.0644	0.1059	0.093
wR_2 (all data)	0.0704	0.1049	0.1337	0.1906	0.2069
GOF	1.109	0.946	0.916	1.014	1.062

*Table 1. Summary of crystal data for lithium tartrates **1** - **5**.*

	6	**7**	**8**	**9**
formula	Li_2(*meso*-$C_4H_4O_6$)	Li_2(*meso*-$C_4H_4O_6$)	Li_2(D,L-$C_4H_4O_6$)	Li_2(L-$C_4H_4O_6$)
crystal size (mm)	0.4 × 0.2 × 0.03	0.15 × 0.15 × 0.02	0.5 × 0.4 × 0.4	0.8 × 0.3 × 0.2
crystal system	monoclinic	monoclinic	monoclinic	monoclinic
space group	$P2_1/c$	Cc	$P2_1/c$	$C2$
T (K)	120(2)	120(2)	120(2)	120(2)
a (Å)	6.4777(5)	9.6880(5)	12.0809(15)	15.153(6)
b (Å)	5.0082(4)	5.3821(2)	4.9703(6)	5.0136(8)
c (Å)	8.9897(8)	11.4090(6)	9.4471(11)	10.376(4)
α (°)	90	90	90	90
β (°)	95.679(8)	93.959(5)	91.241(11)	131.89(6)
γ (°)	90	90	90	90
V (Å^3)	290.21(4)	593.47(5)	567.12(12)	586.8(3)
asym. unit	C_2 H_2 Li O_3	C_4 H_4 Li_2 O_6	C_4 H_4 Li_2 O_6	C_4 H_4 Li_2 O_6
Z	2	4	4	4
d_{calc} (g cm^{-3})	1.853	1.813	1.897	1.833
μ (mm^{-1})	0.171	0.167	0.175	0.169
refl. collected	1215	2956	1885	1316
unique refl.	669	1344	1885	1092
observed data (I > 2σ(I))	538	1240	1478	1074
parameters	58	115	116	115
R_{int}	0.0296	0.0269	0.0 (merged data)	0.0077
R_1	0.0459	0.0343	0.0495	0.0221
wR_2 (I > 2σ(I))	0.1149	0.0749	0.1238	0.0578
R_1 (all data)	0.0612	0.0386	0.0617	0.0225
wR_2 (all data)	0.1320	0.0778	0.1288	0.0581
GOF	1.041	1.061	0.976	1.045

*Table 2. Summary of crystal data for lithium tartrates **6** - **9**.*

3.3.1.1. Single crystal structure of lithium hydrogen L-tartrate in $P2_1$, LiH(L-$C_4H_4O_6$), **1**

The asymmetric unit of **1** consists of one crystallographically independent lithium atom and one crystallographically independent tartrate ligand, which remains protonated on one carboxylate oxygen atom (Figure 6).

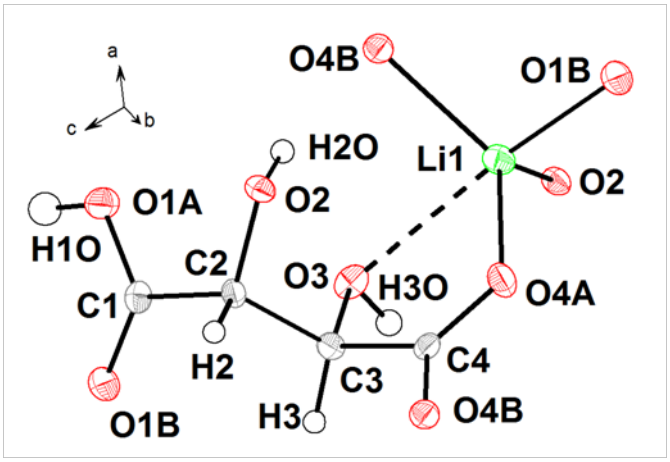

*Figure 6. Ortep extended asymmetric unit of LiH(L-$C_4H_4O_6$), **1**. The long Li-OH distance is shown as a dashed line. C, H, Li and O are coloured grey, white, green and red, respectively. Thermal ellipsoids are given at 50 % probability (20 % probability for hydrogen).*

The tartaric acid ligand coordinates to four lithium atoms *via* the deprotonated carboxylate oxygen group and a hydroxyl oxygen atom, with Li-O distances of 1.934(3) Å - 2.030(3) Å. According to IUPAC nomenclature,[34] it may be classed as μ_4, κ^4: it binds to four different lithium atoms through one hydroxyl oxygen and three unprotonated carboxylic oxygens. The lithium coordination environment is a distorted tetrahedron (O-Li-O angles 97.2(2)° - 119.1(2)°). The remaining ligand hydroxyl oxygen, O3, lies close to a LiO_4 tetrahedron (Li-O distance 2.469(3) Å). The directionality of its thermal ellipsoid indicates some interaction with the lithium may occur, however, bond valence calculations[35] estimate that this oxygen contributes to less than 7 % of the total bonding to the lithium. The tartaric acid carbon skeleton is near-planar with a torsion angle of 178.71(13)°.

The resulting structure is an array of isolated LiO_4 nodes linked in three dimensions by tartaric acid ligands making an I^0O^3 network (Figure 7). Four hydrogen bonds per formula unit may contribute to the overall stability of the system. The use of a single enantiomer of tartaric acid imparts chirality to the structure.

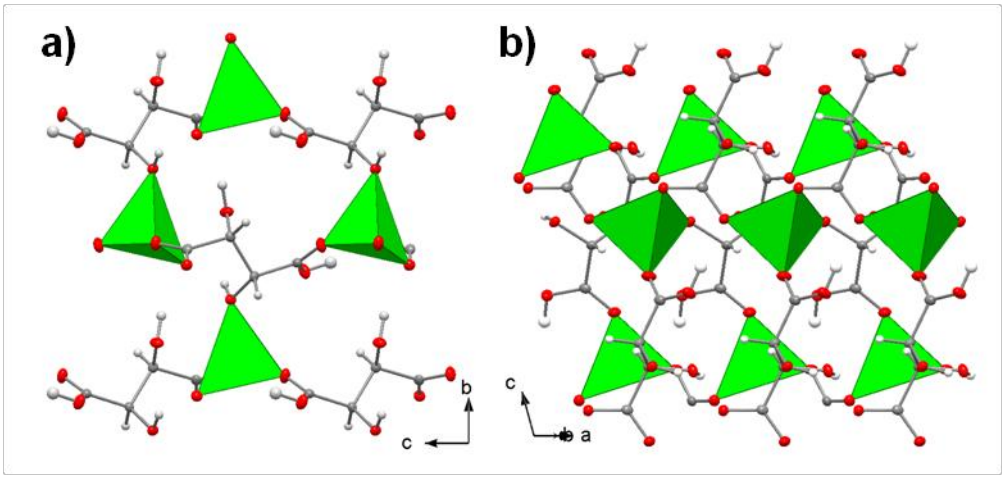

*Figure 7. Structure of LiH(L-$C_4H_4O_6$), **1**: a) viewed down the a-axis, and b) viewed down [1 $\bar{1}$ 0]. C, H and O atoms and LiO_4 tetrahedra are coloured grey, white, red and green, respectively.*

3.3.1.2. Single crystal structure of dilithium L-tartrate in $P2_12_12_1$, $Li_2(L\text{-}C_4H_4O_6)$, **2**

The asymmetric unit of **2** consists of two crystallographically independent tartaric acid ligands and four lithium atoms (Figure 8). Each lithium atom is coordinated by four oxygen atoms in a distorted tetrahedral manner. The tartrate carboxylate groups each bond to three lithium atoms, and the tartrate hydroxyl oxygen atoms bond to one lithium atom each. Li-O bond distances are in the range 1.890(6) Å - 1.970(4) Å. Even in a dense system of such complexity, this wide range is rather surprising. However, as might be expected from electrostatic arguments, the lowest and highest values are for carboxylate and hydroxyl oxygen atoms, respectively. Bond angles within the tetrahedra also vary considerably, from 94.5(3) ° to 121.7(3)°. The carbon skeletons of the tartaric acid moieties are almost planar; torsion angles are 175.5(2)° - 179.0(3)°. Both tartaric acid ligands, although crystallographically independent, may be classed as μ_8, κ^6; that is, they bind to eight different lithium atoms through all six oxygen atoms.

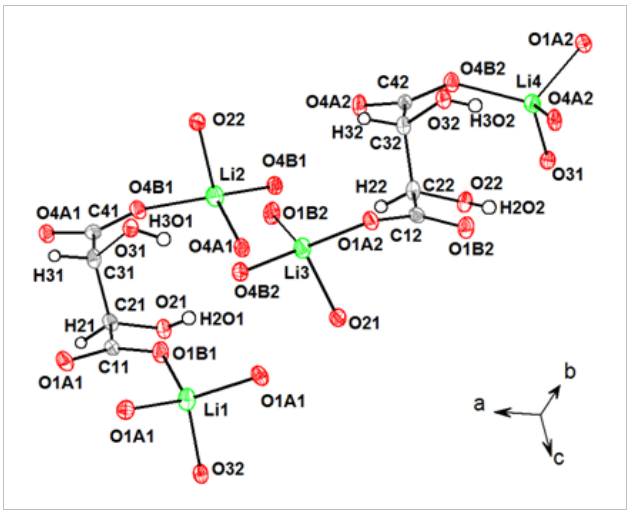

Figure 8. Ortep extended asymmetric unit of $Li_2(L\text{-}C_4H_4O_6)$, ***2****. C, H, Li and O are coloured grey, white, green and red, respectively. Thermal ellipsoids are given at 50 % probability (20 % probability for hydrogen).*

The resulting arrangement is chains of corner-sharing distorted LiO_4 tetrahedra bridged *via* the carboxylate groups of the tartaric acid ligands, which are arranged in a herringbone array to form a 2-D sheet (Figure 9a). The apical positions on the tetrahedra are occupied by hydroxyl oxygen atoms of the ligands in sheets above and below, which link the sheets to form a 3-D, I^1O^2 framework (Figure 9b). The structure is chiral due to the use of a single chiral enantiomer of tartaric acid, which did not racemize under the reaction conditions.

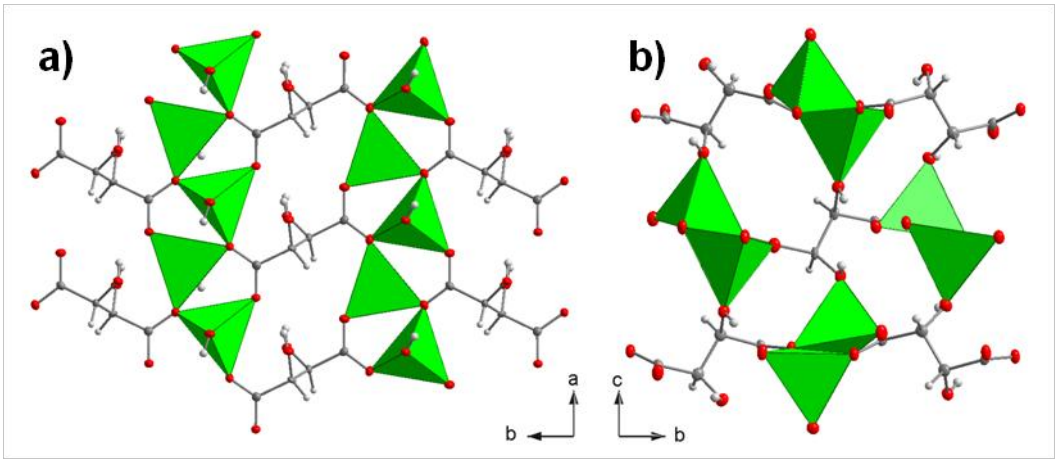

Figure 9. Structure of $Li_2(L\text{-}C_4H_4O_6)$, ***2****: a) viewed down the c-axis, showing chains of LiO_4 tetrahedra bridged by a 2-D herringbone array of tartaric acid ligands, and b) viewed down the chains of corner-sharing LiO_4 tetrahedra with sheets horizontal. C, H and O atoms and LiO_4 tetrahedra are coloured grey, white, red and green, respectively.*

3.3.1.3. Single crystal structure of dilithium L-tartrate in $C222_1$, $Li_2(L\text{-}C_4H_4O_6)$, **3**

The asymmetric unit of **3** consists of half of one tartaric acid ligand and one lithium atom (Figure 10). The lithium atom is coordinated by four oxygen atoms in a severely distorted tetrahedron, with bond distances 1.918(6) Å - 1.956(6) Å and bond angles 84.6(3)° - 121.7(3)°. The smallest angle is between the chelating oxygen atoms, which also have the two longest Li-O bond distances. This is not uncommon for oxygen atoms which chelate lithium. Each tartaric acid ligand coordinates to six lithium atoms in a μ_6, κ^6 fashion with two lithium atoms chelated between the hydroxyl oxygen and one carboxylate oxygen.

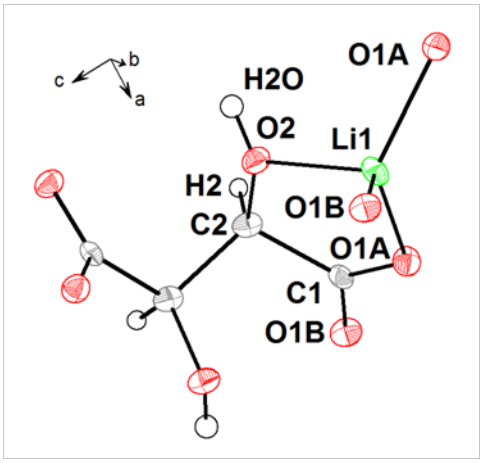

*Figure 10. Ortep extended asymmetric unit of $Li_2(L\text{-}C_4H_4O_6)$, **3**. Unlabelled atoms correspond to those necessary to complete one tartaric acid ligand. C, H, Li and O are coloured grey, white, green and red, respectively. Thermal ellipsoids are given at 50 % probability (20 % probability for hydrogen).*

The resulting structure is an I^1O^2, 3-D framework comprised of chains of corner-sharing LiO_4 tetrahedra connected by tartaric acid ligands (Figure 11). There is no obvious 2-D substructure of the type seen in **2**. However, due to the use of a single enantiomer of tartaric acid, the compound is chiral, like **2**.

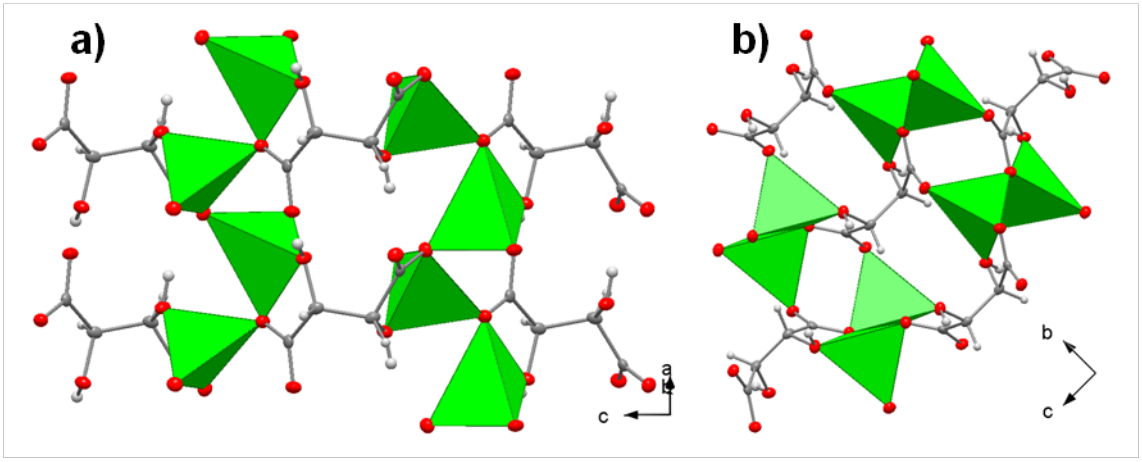

*Figure 11. Structure of $Li_2(L\text{-}C_4H_4O_6)$, **3**: a) viewed down [1 0 $\bar{1}$], showing chains of corner-sharing tetrahedra, and b) viewed down the chains of corner-sharing LiO_4 tetrahedra. C, H and O atoms and LiO_4 tetrahedra are coloured grey, white, red and green, respectively.*

3.3.1.4. Single crystal structure of dilithium *meso*-tartrate in *C*2/*c*, $Li_2(meso\text{-}C_4H_4O_6)$, **4**

The asymmetric unit of **4** consists of half of one tartaric acid ligand and one crystallographically independent lithium atom (Figure 12). The central tartaric acid carbon atoms and their associated hydrogen atoms exhibit disorder between two positions (C2, H2 and C20, H20), with a site occupancy ratio 78.5 : 21.5. The two halves of the tartaric acid moiety are related by inversion symmetry. In a similar manner to **3**, each tartaric acid ligand coordinates to six lithium atoms in a μ_6, κ^6 fashion. At each end of the ligand, separate lithium atoms are coordinated by each of the carboxylate oxygen atoms in a monodentate fashion and another is chelated by neighbouring hydroxyl and carboxylate oxygen atoms. It should be noted that the thermal displacement parameters for the hydroxyl oxygen O2 are unusually large in the direction perpendicular to the ring of chelation to lithium. Modelling the hydroxyl group as two distinct sites, corresponding with the disordered carbon atoms C2 and C20, resulted in an unstable refinement. However, it may not be unreasonable to suggest that this oxygen has substantial freedom to vibrate, or that the two sites are so close to each other as to be indistinguishable.

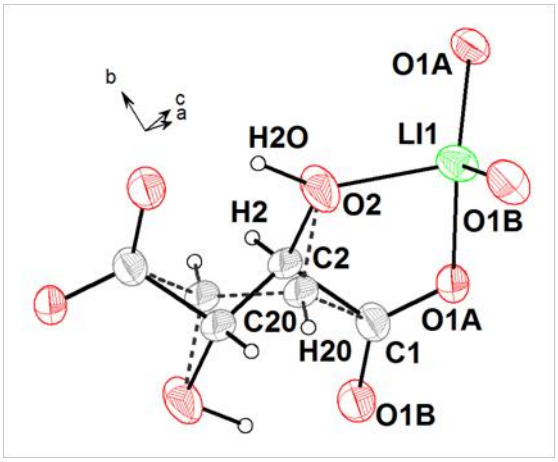

Figure 12. Ortep extended asymmetric unit of Li_2(meso-$C_4H_4O_6$), ***4****. Unlabelled atoms correspond to atoms related by inversion symmetry necessary to complete one tartaric acid ligand. Dashed grey bonds correspond to those of the disordered tartaric acid ligand with lower site occupancy (C20, H20). C, H, Li and O are coloured grey, white, green and red, respectively. Thermal ellipsoids are given at 50 % probability (20 % probability for hydrogen).*

Each lithium atom is coordinated by four oxygen atoms from three different tartaric acid ligands, with Li-O bond distances 1.882(6) Å - 1.966(7) Å. It is noted that the minimum and maximum Li-O bond distances are to the singly-coordinating carboxylate oxygen and the hydroxyl oxygen, respectively. Bond angles within the distorted LiO_4 tetrahedron range from 81.7(2)° to 121.9(3)°. In a similar manner to **3**, the smallest angle is between the chelating oxygen atoms, which also have the two longest Li-O bond distances.

The resulting structure is an array of parallel chains of corner-sharing LiO_4 tetrahedra (Figure 13a), connected by tartaric acid ligands to form a 3-D, I^1O^2 framework (Figure 13b). Like **3**, there is no obvious 2-D substructure. However, the compound is achiral, which is a result of the use of the *meso*-tartaric acid ligand.

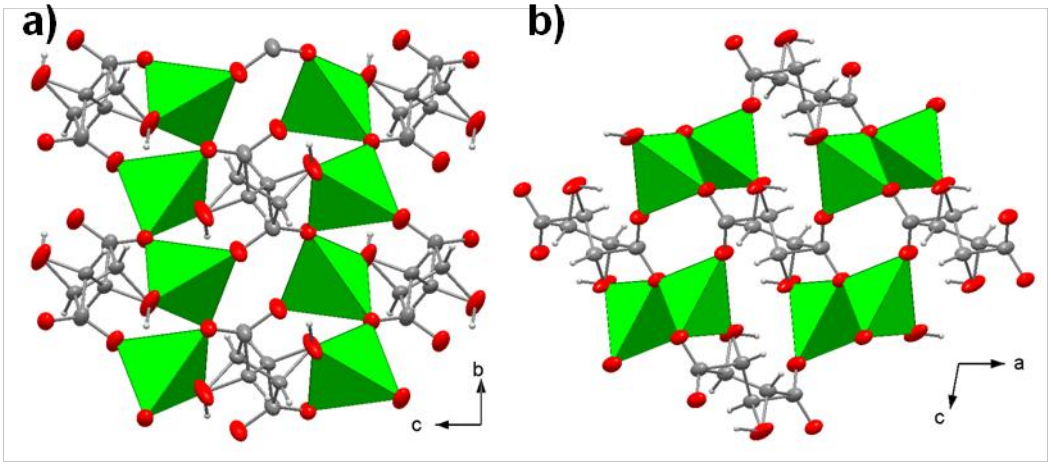

*Figure 13. Structure of $Li_2(meso\text{-}C_4H_4O_6)$, **4**: a) viewed down the a-axis, showing chains of LiO_4 tetrahedra bridged by tartaric acid ligands, and b) viewed down the chains of corner-sharing LiO_4 tetrahedra. C, H and O atoms and LiO_4 tetrahedra are coloured grey, white, red and green, respectively. Note that all disordered atoms, including those with lower site occupancies, are shown.*

3.3.1.5. Single crystal structure of dilithium D,L-tartrate in *C*2/*c*, $Li_2(D,L\text{-}C_4H_4O_6)$, **5**

The asymmetric unit of **5** consists of one tartaric acid ligand and two crystallographically independent lithium atoms (Figure 14). The carbon chain and one carboxylate oxygen atom exhibit disorder between two positions with a site occupancy ratio of 88:12. In a similar manner to **2**, the tartaric acid ligand coordinates to eight lithium atoms in a μ_8, κ^6 fashion: at each end of the ligand, one carboxylate oxygen atom and the hydroxyl oxygen atom coordinate to one lithium atom each and the other carboxylate oxygen atom bridges between two crystallographically independent lithium atoms. Li-O bond distances are 1.908(6) Å - 1.959(7) Å. The lowest of these values is for the disordered oxygen atom position of lower site occupancy. Each lithium atom is coordinated by four oxygen atoms in a distorted tetrahedron (bond angles 87.7(9)° - 124.1(9)°).

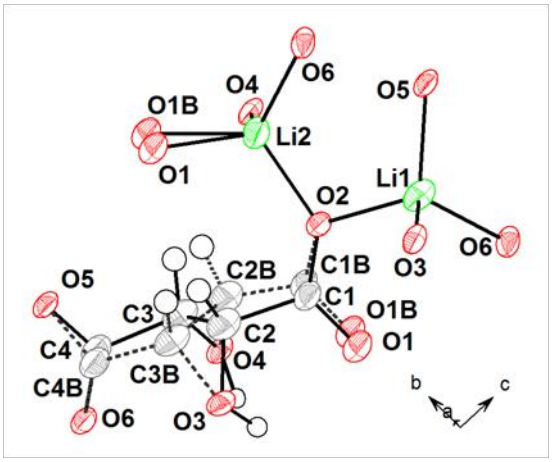

*Figure 14. Ortep extended asymmetric unit of $Li_2(D,L\text{-}C_4H_4O_6)$, **5**. Dashed grey bonds correspond to those of the disordered tartaric acid ligand with lower site occupancy (C1B-C4B, O1B). C, H, Li and O are coloured grey, white, green and red, respectively. Hydrogen atoms not labelled for clarity. Thermal ellipsoids are given at 50 % probability (20 % probability for hydrogen).*

The overall structure of **5** is very similar to that of **2**, in which corner-sharing LiO_4 tetrahedra form 1D chains bridged by tartaric acid moieties in a 2-D herringbone array (Figure 15a). The hydroxyl oxygen atoms link the sheets by filling the apical positions on the LiO_4 tetrahedra, giving rise to a 3-D I^1O^2 framework (Figure 15b). In contrast to the structure of **2**, there is only one crystallographically independent sheet, which, due to the presence of glide plane symmetry in Space Group *C*2/*c*, contains both L- and D- tartaric acid isomers in a 1 : 1 ratio. This results in a structure that, whilst being made up of chiral building blocks, is itself achiral.

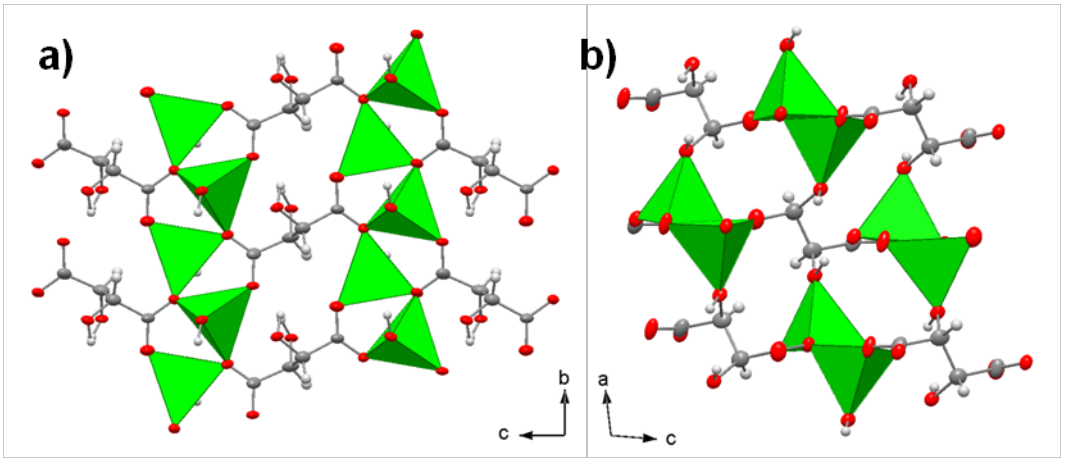

*Figure 15. Structure of $Li_2(D,L\text{-}C_4H_4O_6)$, **5**: a) viewed down the a-axis, showing chains of LiO_4 tetrahedra bridged by a 2-D herringbone array of tartaric acid ligands, and b) viewed down the chains of corner-sharing LiO_4 tetrahedra with sheets horizontal. C, H and O atoms and LiO_4 tetrahedra are coloured grey, white, red and green, respectively. The disordered atoms with lower occupancy are not shown for clarity.*

3.3.1.6. Single crystal structure of dilithium *meso*-tartrate in $P2_1/c$, $Li_2(meso\text{-}C_4H_4O_6)$, **6**

The asymmetric unit of **6** consists of one lithium atom and half of a tartaric acid ligand, which is completed by equivalent atoms generated by inversion symmetry (Figure 16). Each lithium atom is coordinated by four oxygen atoms in a tetrahedral manner. The tartrate carboxylate groups each bond to three lithium atoms, and the tartrate hydroxyl oxygen atoms bond to one lithium atom each. Li-O bond distances are in the range 1.908(4) Å - 1.958(4) Å, a smaller distribution than other similar structures. Bond angles within the tetrahedron vary a little more, from 101.8(2)° to 118.9(2)°. By symmetry, the carbon skeleton of the tartaric acid moiety has a torsion angle of 180°. The ligand may be classed as μ_8, κ^6; that is, it binds to eight different lithium atoms through all six oxygen atoms.

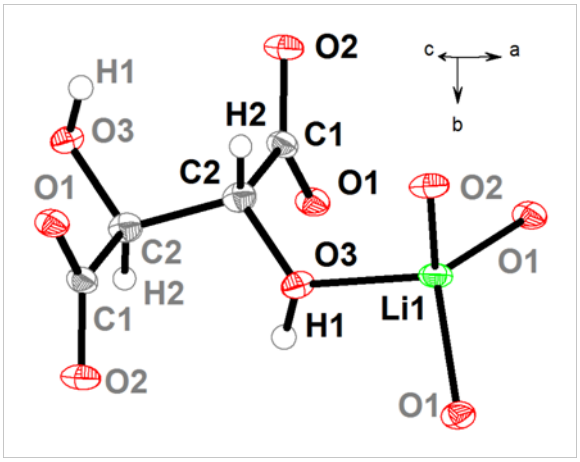

*Figure 16. Ortep extended asymmetric unit of $Li_2(meso\text{-}C_4H_4O_6)$, **6**, showing atoms needed to complete one tartaric acid ligand and the Li coordination sphere (grey labels). C, H, Li and O are coloured grey, white, green and red, respectively. Thermal ellipsoids are given at 50 % probability (20 % probability for hydrogen).*

The resulting arrangement is chains of corner-sharing distorted LiO_4 tetrahedra bridged *via* the carboxylate groups of the tartaric acid ligands, which are arranged in a herringbone array to form a 2-D sheet, as in phases **2**, **5** and **8** (Figure 17a). The apical positions on the tetrahedra are occupied by hydroxyl oxygen atoms of the ligands in sheets above and below, which link the sheets to form a 3-D, I^1O^2 framework (Figure 17b).

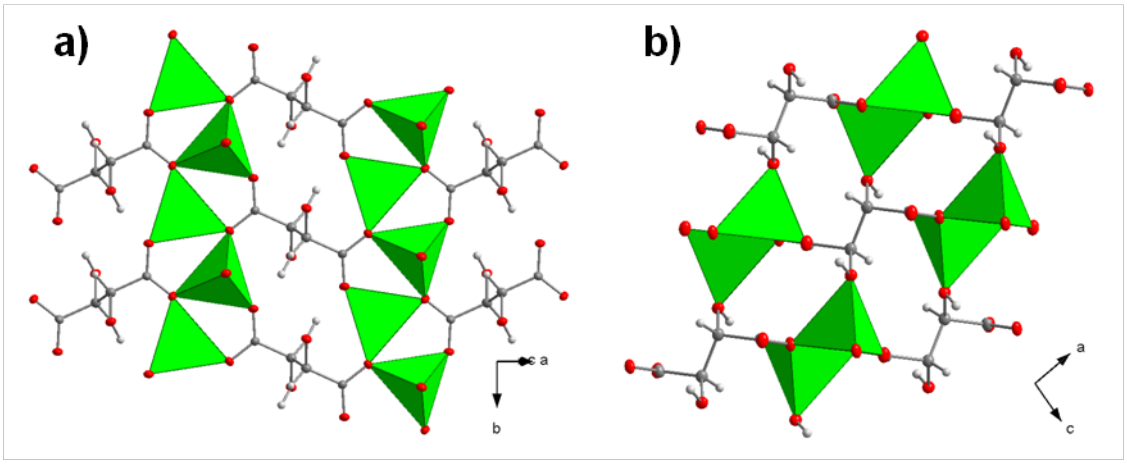

*Figure 17. Structure of $Li_2(meso\text{-}C_4H_4O_6)$, **6**: a) viewed down [1 0 $\bar{1}$], showing chains of LiO_4 tetrahedra bridged by a 2-D herringbone array of tartaric acid ligands, and b) viewed down the chains of corner-sharing LiO_4 tetrahedra with sheets horizontal. C, H and O atoms and LiO_4 tetrahedra are coloured grey, white, red and green, respectively.*

3.3.1.7. Single crystal structure of dilithium *meso*-tartrate in *Cc*, $Li_2(meso\text{-}C_4H_4O_6)$, **7**

The asymmetric unit of **7** consists of one complete tartaric acid ligand and two crystallographically independent lithium atoms (Figure 18). In a similar manner to **3** and **4**, each tartaric acid ligand coordinates to six lithium atoms in a μ_6, κ^6 fashion. At each end of the ligand, separate lithium atoms are coordinated by each of the carboxylate oxygen atoms in a monodentate fashion and another is chelated by neighbouring hydroxyl and carboxylate oxygen atoms. The lithium environments are distorted tetrahedra, with Li - O distances in the range 1.911(4) Å - 2.014(4) Å and bond angles 82.10(2)° - 126.5(2)°. The two smallest angles involve the chelating oxygen atoms. The tartaric acid torsion angle is unusually small (62.0(2)°), resulting in *gauche* carboxylate groups.

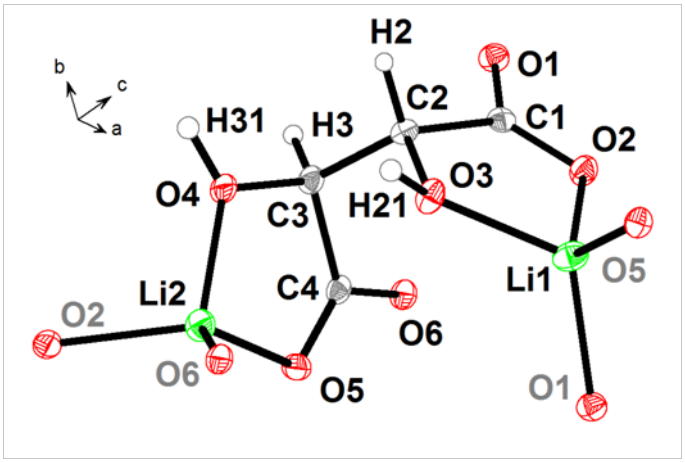

*Figure 18. Ortep extended asymmetric unit of $Li_2(meso\text{-}C_4H_4O_6)$, **7**, showing atoms necessary to complete the coordination sphere of Li (grey labels). C, H, Li and O are coloured grey, white, green and red, respectively. Thermal ellipsoids are given at 50 % probability (20 % probability for hydrogen).*

The resulting structure is again chains of corner-sharing LiO_4 tetrahedra, connected by tartaric acid ligands to form a 3-D, I^1O^2 framework (Figure 19). The chains of tetrahedra are arranged in layers in the *ab*-plane, in which the chains are parallel. However, unlike all the other dilithium tartrates, the chains in adjacent layers run in different directions, making an angle of approximately 58°.

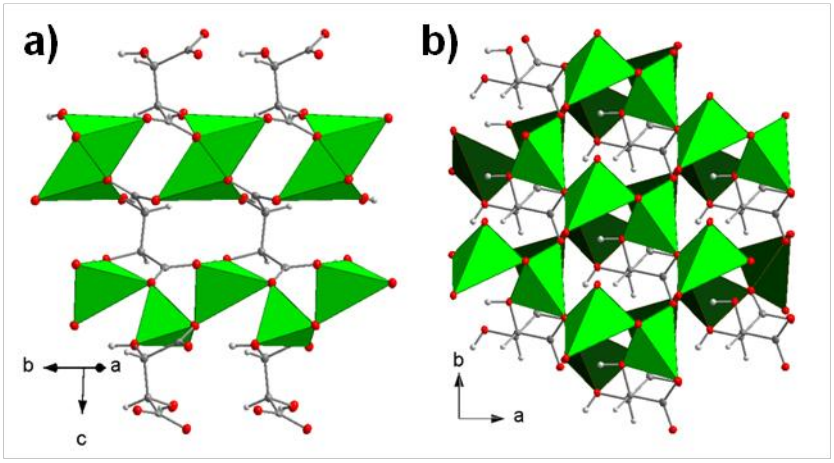

*Figure 19. Structure of $Li_2(meso\text{-}C_4H_4O_6)$, **7**: a) viewed down [1 1 0], showing chains of LiO_4 tetrahedra bridged by tartaric acid ligands (chains in the upper layer run into the picture), and b) viewed down the c-axis, showing the relative orientations of the inorganic chains (shaded darker in the layer below). C, H and O atoms and LiO_4 tetrahedra are coloured grey, white, red and green, respectively.*

3.3.1.8. Single crystal structure of dilithium D,L-tartrate in $P2_1/c$, $Li_2(D,L\text{-}C_4H_4O_6)$, **8**

The asymmetric unit of **8** consists of one complete tartaric acid ligand and two lithium atoms (Figure 20). The lithium atoms are coordinated by four oxygen atoms in a distorted tetrahedron, with bond distances 1.908(4) Å - 2.001(4) Å and bond angles 99.9(2)° - 124.6(2)°. The ligand has a near-linear torsion angle of 172.7(2)° and, as in phase **6**, it coordinates to eight lithium atoms in a μ_8, κ^6 fashion.

The resulting structure is an I^1O^2, 3-D framework comprised of chains of corner-sharing LiO_4 tetrahedra connected by tartaric acid ligands in 2-D herringbone arrays and capped by the hydroxyl groups of ligands above and below (Figure 21). The presence of glide plane symmetry results in both L- and D-tartaric acid enantiomers being present in the structure in equal proportions, therefore the structure overall is achiral.

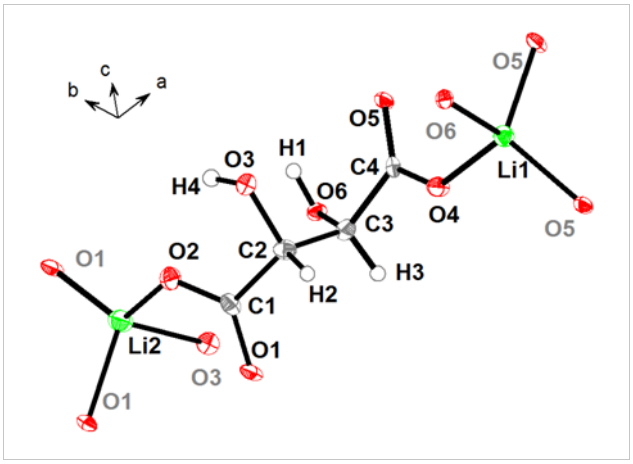

*Figure 20. Ortep extended asymmetric unit of $Li_2(D,L\text{-}C_4H_4O_6)$, **8**, showing atoms necessary to complete the coordination sphere of Li (grey labels). C, H, Li and O are coloured grey, white, green and red, respectively. Thermal ellipsoids are given at 50 % probability (20 % probability for hydrogen).*

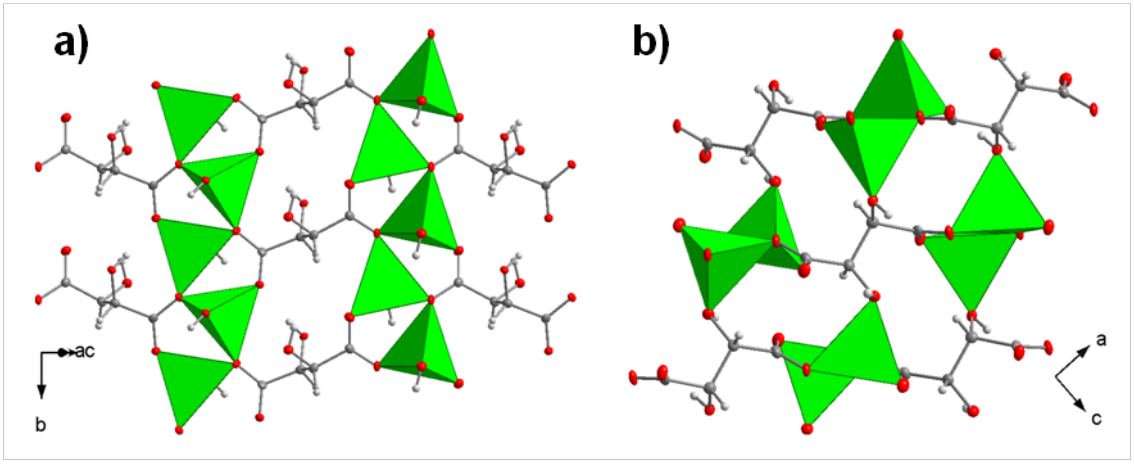

*Figure 21. Structure of $Li_2(D,L\text{-}C_4H_4O_6)$, **8**: a) viewed down [1 0 $\bar{1}$], showing chains of LiO_4 tetrahedra bridged by a 2-D herringbone array of tartaric acid ligands, and b) viewed down the chains of corner-sharing LiO_4 tetrahedra with sheets horizontal. C, H and O atoms and LiO_4 tetrahedra are coloured grey, white, red and green, respectively.*

3.3.1.9. Single crystal structure of dilithium L-tartrate in *C*2, $Li_2(L\text{-}C_4H_4O_6)$, **9**

The asymmetric unit of **9** consists of two halves of tartaric acid ligands and two crystallographically independent lithium atoms (Figure 22). Two crystallographically distinct tartaric acid moieties are completed by symmetric generations of the corresponding atoms. In a similar manner to **2**, **5**, **6** and **8** each ligand coordinates to eight lithium atoms in a μ_8, κ^6 fashion: at each end of the ligand, one carboxylate oxygen atom and the hydroxyl oxygen

atom coordinate to one lithium atom each and the other carboxylate oxygen atom bridges between two crystallographically identical lithium atoms. Li-O bond distances are 1.887(3) Å - 1.986(3) Å. Each lithium atom is coordinated by four oxygen atoms in a distorted tetrahedron (bond angles 101.76(13)° - 122.43(13)°). In contrast to **2**, **5**, **6** and **8**, the tartaric acid moieties have an almost eclipsed conformation, with torsion angles of 138.6(2)° and 140.6(2)°.

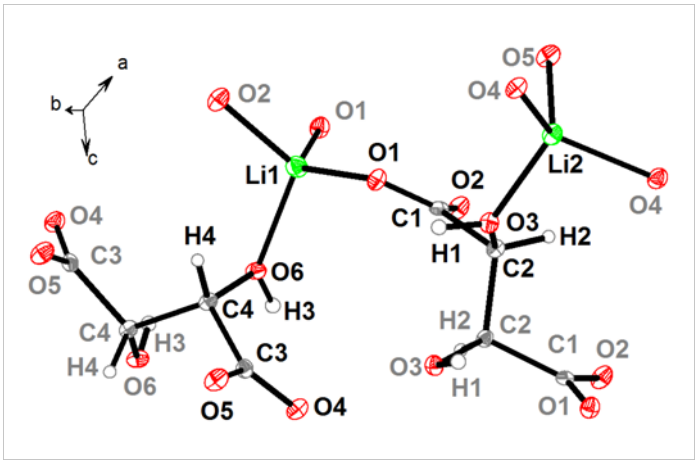

*Figure 22. Ortep extended asymmetric unit of $Li_2(L\text{-}C_4H_4O_6)$, **9**, showing atoms necessary to complete the lithium coordination spheres and ligand moieties (grey labels). C, H, Li and O are coloured grey, white, green and red, respectively. Thermal ellipsoids are given at 50 % probability (20 % probability for hydrogen).*

The overall structure of **9** consists of corner-sharing LiO_4 tetrahedra in 1D chains, bridged by tartaric acid moieties in a 2-D array (Figure 23a). There are two crystallographically distinct arrays, each containing a single ligand and lithium atom. The structure of each array is almost identical, with hydrogen bonding occurring within sheets between neighbouring hydroxyl groups and carboxylate oxygen atoms. Notably, when viewed along the *a*-axis, the hydroxyl groups in adjacent arrays point in opposite directions. In a similar manner to similar to **2**, **5**, **6** and **8**, the hydroxyl oxygen atoms link the sheets by filling the apical positions on the LiO_4 tetrahedra, giving rise to a 3-D, I^1O^2 framework (Figure 23b).

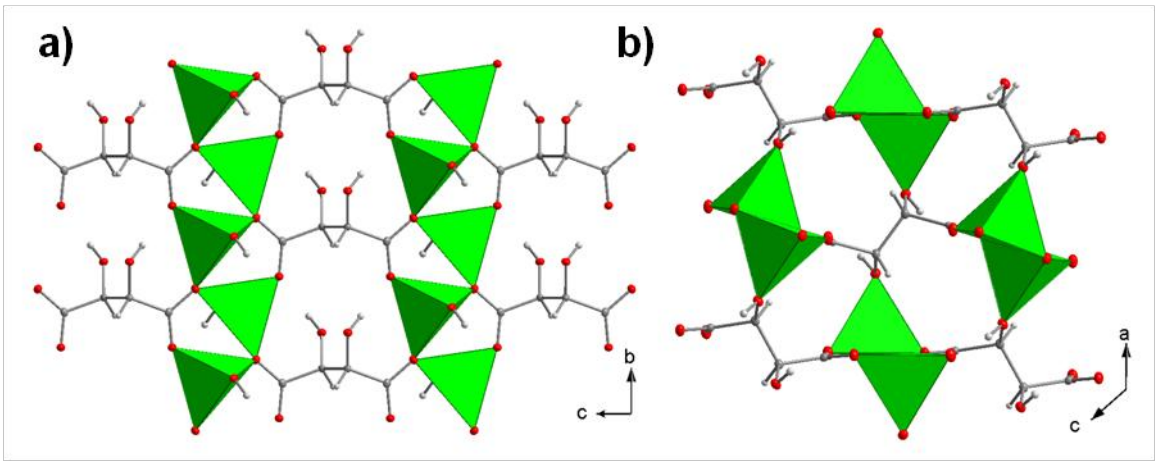

*Figure 23. Structure of $Li_2(L\text{-}C_4H_4O_6)$, **9**: a) viewed down the a-axis, showing chains of LiO_4 tetrahedra bridged by a 2-D array of tartaric acid ligands, and b) viewed down the chains of corner-sharing LiO_4 tetrahedra with sheets horizontal. C, H and O atoms and LiO_4 tetrahedra are coloured grey, white, red and green, respectively.*

3.3.2. *Structures of new hydrated dilithium tartrates*

The structures of hydrated dilithium tartrates **10** and **11** were determined by single crystal X-ray diffraction. A summary of the crystal data can be seen in Table 3.

	10 $Li_2(D,L\text{-tart})\cdot 2H_2O$	**11** $Li_2(meso\text{-tart})\cdot 0.5H_2O$
crystal size (mm)	0.90 × 0.4 × 0.2	0.36 × 0.22 × 0.03
crystal system	triclinic	orthorhombic
space group	*P*1	$C222_1$
T (K)	120(2)	120(2)
a (Å)	6.1037(4)	5.5637(5)
b (Å)	7.3350(7)	9.30007(8)
c (Å)	9.0294(8)	24.992(2)
α (°)	103.450(8)	90
β (°)	90.701(7)	90
γ (°)	100.790(7)	90
V (Å^3)	385.55(6)	1293.24(19)
asym. unit	$C_4 H_8 Li_2 O_8$	$C_4 H_6 Li_2 O_{6.5}$
Z	1	8
d_{calc} (g cm^{-3})	1.705	1.756
μ (mm^{-1})	0.164	0.164
refl. collected	5451	2222
unique refl.	1842	1462
observed data (I > 2σ(I))	1394	1282
parameters	145	123
R_{int}	0.0307	0.0249
R_1	0.0335	0.0391
wR_2 (I > 2σ(I))	0.0812	0.0737
R_1 (all data)	0.0477	0.0489
wR_2 (all data)	0.0849	0.0784
GOF	0.973	1.036

*Table 3. Summary of crystal data for hydrated dilithium tartrates **10** and **11**.*

3.3.2.1. Structure of dilithium D,L-tartrate dihydrate in *P*1, $Li_2(D,L\text{-}C_4H_4O_6)(H_2O)_2$, **10**

The asymmetric unit of **10** consists of one crystallographically independent chiral tartrate ligand, two lithium atoms and two coordinating water molecules (Figure 24). Each ligand binds to four lithium atoms via five oxygen atoms (μ_4, κ^5). Chelation (O1A, O2, O3, O4A), bridging (O4A) and monodentate (O4B) binding modes are observed. The remaining carboxylate oxygen O1B acts as a hydrogen bond acceptor from nearby hydroxyl group and water molecule. The ligand has a near-linear C_4 torsion angle of 174.79(11)°, however the carboxylate groups are rotated by 79.3° with respect to one another. Li1 is five-coordinate, with Li-O bond lengths from 1.999(3) Å to 2.193(3) Å and O-Li-O angles 74.50(9)° - 158.89(14)°. The coordination environment of Li2 is a distorted tetrahedron (Li-O distances

1.856(3) Å - 1.971(3) Å, O-Li-O angles 84.99(10)° - 119.23(13)°). In both cases, the most acute angle is unsurprisingly between the chelating oxygens (O3 and O4A, O1A and O2, respectively). Aside from **1**, which has one long Li-O bond in its coordination sphere, **10** is the only new lithium tartrate compound containing five-coordinate lithium.

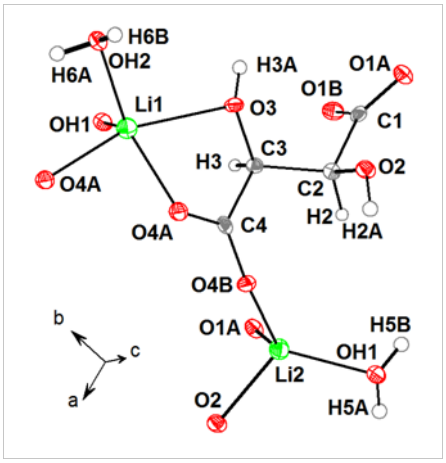

*Figure 24. Ortep extended asymmetric unit of Li_2(D,L-tart)·2H_2O, **10**, showing atoms necessary to complete the lithium coordination spheres. C, H, Li and O are coloured grey, white, green and red, respectively. Thermal ellipsoids are given at 50 % probability (20 % probability for hydrogen).*

Overall, the resulting structure is of Li-O tetramers (carboxylate oxygen O4A bridges between adjacent Li1 atoms; water oxygen OH1 links Li1 to Li2), connected by the ligands to form 2D sheets (Figure 25a). Due to the presence of inversion symmetry, each sheet contains equal amounts of L- and D-tartaric acid moieties therefore the structure is overall achiral. There is extensive hydrogen bonding within and between the sheets (Figure 25b).

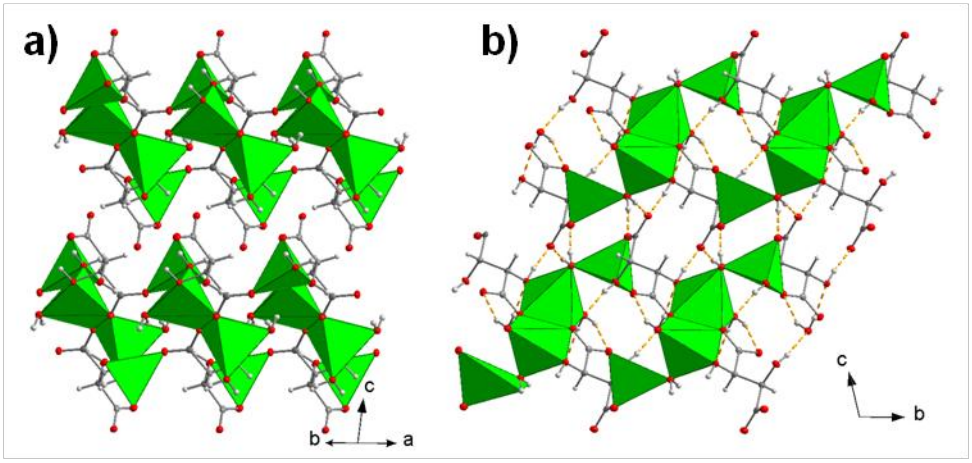

Figure 25. Extended structure of dilithium D,L-tartrate dihydrate, ***10****, showing the stacking of two layers a) viewed down [2 3 1], and b) with hydrogen bonding, viewed down the a-axis. C, H and O atoms and LiO_4 tetrahedra are coloured grey, white, red and green, respectively and hydrogen bonds are shown as dashed orange lines.*

3.3.2.2. Structure of dilithium *meso*-tartrate hemihydrate in $C222_1$, $Li_2(meso\text{-}C_4H_4O_6)(H_2O)_{0.5}$, **11**

The asymmetric unit of **11** consists of one *meso*-tartaric acid ligand, two lithium atoms and half of a water molecule, which resides on a special position (Figure 26). The ligand oxygen atoms coordinate to five lithium atoms (μ_5, κ^6), two through α-chelation and three in a monodentate fashion. It has a *gauche* conformation, similar to **2** (C_4 torsion angle 64.6(2)°). The lithium coordination environments are distorted tetrahedra (Li-O distances 1.919(4) Å - 1.998(4) Å, bond angles 82.99(15)° - 129.9(2)°). Li1 is coordinated solely by ligand oxygens O1-3; these tetrahedra share corners to form chains in the *a*-direction in a similar way to the anhydrous dilithium *meso*-tartrates **4**, **6** and **7**.

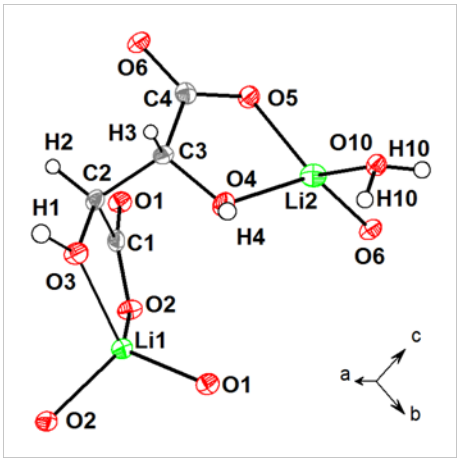

*Figure 26. Ortep extended asymmetric unit of $Li_2(meso\text{-}C_4H_4O_6)(H_2O)_{0.5}$, **11**, showing atoms necessary to complete the lithium coordination spheres. C, H, Li and O are coloured grey, white, green and red, respectively. Thermal ellipsoids are given at 50 % probability (20 % probability for hydrogen).*

The resulting structure is a 3-D I^1O^2 framework, which has inorganic chains interspersed by lines of water-bridged lithium dimers (Figure 27). Both ligand hydroxyl groups and the water molecule act as hydrogen bond donors in an extensive system, the acceptors being the carboxylate oxygens O1 and O6 that each coordinate to just one lithium atom.

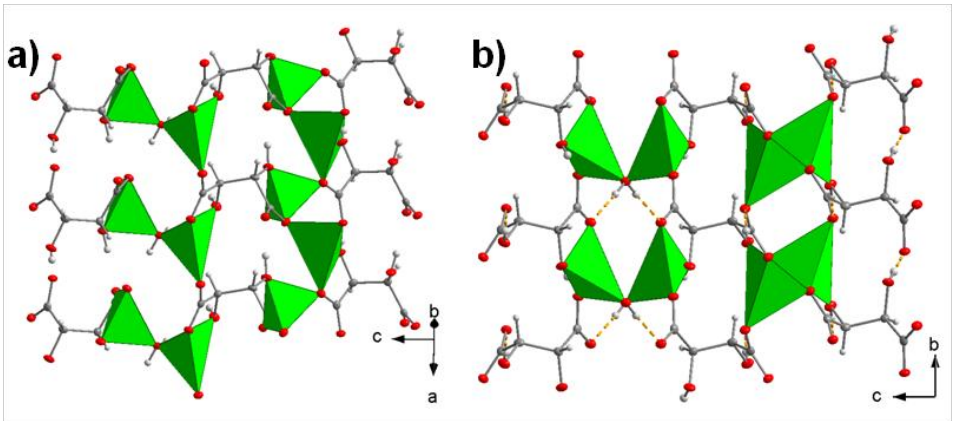

*Figure 27. Structure of $Li_2(meso\text{-}C_4H_4O_6)(H_2O)_{0.5}$, **11**: a) viewed down [1 1 0], showing one chain of LiO_4 tetrahedra and three water-bridged lithium dimers, and b) viewed down the chains of corner-sharing LiO_4 tetrahedra showing hydrogen bonding. C, H and O atoms and LiO_4 tetrahedra are coloured grey, white, red and green, respectively and hydrogen bonds are shown as dashed orange lines.*

3.3.2.3. Comparison of new hydrated lithium tartrates

The structural differences between the new hydrated phases **10** and **11** are even greater than the differences between the dilithium tartrates **2** - **9** (see Section 3.3.3). This is due to the presence of coordinating water molecules, which replace tartrate oxygen atoms in the lithium coordination sphere, reducing metal-ligand connectivity to different extents in each structure. A comparison between the hydrated structures is shown in Table 4.

	10 $Li_2(D,L\text{-tart})(H_2O)_2$	**11** $Li_2(\textit{meso}\text{-tart})(H_2O)_{0.5}$
Space group	*P*1	$C222_1$
d_{calc} (g cm^{-3})	1.705	1.756
Ligand binding	μ_4, κ^5	μ_5, κ^6
Li coordination	tetrahedral, 5-fold	distorted tetrahedral
C_4 torsion angle (°)	174.79(11)	64.6(2)
Connectivity	I^0O^2	I^1O^2
Inorganic substructure	Li tetramers	Li chains + Li dimers
Hydrogen bonding	within and between sheets	ligand-ligand + water-ligand

*Table 4. Summary of the structural features of hydrated dilithium tartrates **10** and **11**.*

Due to the incorporation of water in their structures, the hydrated phases **10** and **11** have lower densities (1.705 g cm^{-3} and 1.756 g cm^{-3}, respectively) than most dilithium tartrates **2** - **9**, and the number of lithium atoms coordinated by each ligand, denoted by μ, is reduced to 4 and 5, respectively. The effect of water binding to lithium is also to distort the coordination sphere, resulting in 5-fold coordination in **10**, and to reduce the inorganic connectivity, forming isolated tetramers in **10** and and dimers in **11**. Torsion angles remain similar to those preferred by the D,L-tartaric and *meso*-tartaric parent acids, which exhibit linear and *gauche* carboxylate groups, respectively.[36] Unsurprisingly, given the number of hydroxyl groups and water molecules in each structure, both contain many hydrogen bonds.

The hydrated phases **10** and **11** were produced in reactions at room temperature using similar hydrated solvent systems to those used in phase behaviour experiments (Section 3.3.6), which also yielded anhydrous phases **2** and **7** and another known hydrated phase, $LiH(L\text{-tart})\cdot H_2O$. This, and the fact that the ligand conformations of the parent acids are maintained, suggests that under low temperature conditions, kinetic control dominates, and the interplay between different phases, both hydrated and anhydrous, is complex. Interestingly, the structure of **11** is suggestive of a phase intermediate between more hydrated phases and anhydrous phases: it contains both chains of LiO_4 tetrahedra and water-bridged Li_2O_7 dimers. Not only that, but

the sample containing single crystals of **11** was dehydrated in air to form a phase-pure sample of **7**, confirming the similarity of the two structures.

3.3.3. *Comparisons of the structures of anhydrous dilithium tartrates*

A large number of structures of lithium tartrate has been uncovered, which includes several ligand-originated isomers and polymorphs of anhydrous dilithium tartrate. This is suggestive of a diverse phase space and relatively accessible energy landscape for these inorganic-organic frameworks, which is of great interest for the discovery of others and the manipulation of their properties. In particular, there is great structural diversity in the anhydrous, I^1O^2 dilithium tartrates **2** - **9**. A summary of the salient features of these compounds, which all have identical elemental composition, $Li_2(C_4H_4O_6)$, can be seen in Table 5 (L-tartrates), Table 6 (*meso*-tartrates) and Table 7 (D,L-tartrates). Due to their difference in chemical composition, **1**, **10** and **11** are omitted from this discussion.

	2	**3**	**9**
Formula	$Li_2(L\text{-}C_4H_4O_6)$	$Li_2(L\text{-}C_4H_4O_6)$	$Li_2(L\text{-}C_4H_4O_6)$
Space group	$P2_12_12_1$	$C222_1$	$C2$
d_{calc} (g cm^{-3})	1.774	1.762	1.833
H-bond unitary graph set	**C(5)C(5)C(6)C(6)S(5)**	**C(5)[R^2_2(12)]**	**C(5) [R^2_2(12)] C(5) [R^2_2(12)]**
C_4 torsion angles (°)	175.5(2) - 179.0(3)	150.7(4)	138.6(2) - 140.6(2)
Ligand binding	μ_8, κ^6, mono-dentate	μ_6, κ^6, chelating	μ_8, κ^6, mono-dentate
Average Li-O bond valence sum	1.10	1.13	1.14
Li-O distances (Å)	1.890(6) - 1.970(4)	1.918(6) - 1.956(6)	1.887(3) - 1.986(3)
δ_{tet} O-Li-O (°)	6.65	12.62	5.92
O-Li-O angles (°)	94.5(3) - 121.7(3)	84.6(2) - 121.7(3)	101.76(13) - 122.43(13)
Substructure	herring-bone sheets	parallel chains	parallel sheets
Chirality	chiral	chiral	chiral
Polarity	apolar	apolar	polar

*Table 5. Comparison of the structures of dilithium L-tartrates **2**, **3** and **9**.*

	4	**6**	**7**
Formula	Li_2(*meso*-$C_4H_4O_6$)	Li_2(*meso*-$C_4H_4O_6$)	Li_2(*meso*-$C_4H_4O_6$)
Space group	$P2_1/c$	$P2_1/c$	Cc
d_{calc} (g cm^{-3})	1.717	1.853	1.813
H-bond unitary graph set	**S(6)**	**C(5)[R^2_2(12)]**	**C(5)C(5)**
C_4 torsion angles (°)	180	180	62.0(2)
Ligand binding	μ_6, κ^6, chelating	μ_8, κ^6, mono-dentate	μ_6, κ^6, chelating
Average Li-O bond valence sum	1.15	1.13	1.06
Li-O distances (Å)	1.882(6) - 1.966(7)	1.908(4) - 1.958(4)	1.911(4) - 2.014(4)
δ_{tet} O-Li-O (°)	13.34	5.01	14.86
O-Li-O angles (°)	81.7(2) - 121.9(3)	101.8(2) - 118.9(2)	82.1(2) - 126.5(2)
Substructure	parallel chains	herring-bone sheets	crossed sheets
Chirality	achiral	achiral	achiral
Polarity	apolar	apolar	polar

*Table 6. Comparison of the structures of dilithium meso-tartrates **4**, **6** and **7**.*

	5	**8**
Formula	Li_2(D,L-$C_4H_4O_6$)	Li_2(D,L-$C_4H_4O_6$)
Space group	$C2/c$	$P2_1/c$
d_{calc} (g cm^{-3})	1.821	1.897
H-bond unitary graph set	**C(5)C(6)**	**C(5)C(5)S(5)**
C_4 torsion angles (°)	171.8(9) - 175.6(9)	172.7(2)
Ligand binding	μ_8, κ^6, mono-dentate	μ_8, κ^6, mono-dentate
Average Li-O bond valence sum	1.12	1.10
Li-O distances (Å)	1.908(6) - 1.959(7)	1.908(4) - 2.001(4)
δ_{tet} O-Li-O (°)	4.93	6.64
O-Li-O angles (°)	87.7(9) - 124.1(9)	99.9(2) - 124.6(2)
Substructure	herring-bone sheets	herring-bone sheets
Chirality	achiral	achiral
Polarity	apolar	apolar

*Table 7. Comparison of the structures of dilithium D,L-tartrates **5** and **8**.*

Whilst all structures **2** - **9** have the same elemental composition, they can be sub-divided into groups of polymorphs, which contain the same ligand isomer, as suggested by Table 5 -Table 7. When structures from different polymorph groups are compared, they may be considered "ligand originated isomers", as shown in Figure 1.

The chirality, or lack thereof, of the ligand dictates which space groups the dilithium tartates may adopt. Structures **2**, **3** and **9**, containing chiral L-tartaric acid, all take non-centrosymmetric, chiral space groups, and these may be apolar ($P2_12_12_1$ and $C222_1$) or polar ($C2$). The others, containing racemic D,L- or *meso*-tartaric acid, take achiral space groups, although in principle chiral systems may be permitted in this case. The majority of these are centrosymmetric and apolar ($P2_1/c$ and $C2/c$), but **7** adopts the polar space group Cc, which is non-centrosymmetric.

Densities vary by up to 10 %, the lowest being 1.717 g cm^{-1} (**4**) and the highest 1.897 g cm^{-1} (**8**). This could cause large differences in the dispersion forces within the crystal structures, which have been found to increase with increasing density in porous frameworks, thereby affecting their relative energies and fine structure.[37] Hydrogen bonds may also play a major role in phase behaviour, as their energies can be up to 25 kJ mol^{-1},[34] far greater than the thermal energy at ambient temperature, RT (where R is the molar gas constant, 8.3145 J mol^{-1} K^{-1}). The wide range of hydrogen bonding motifs observed and their effect on the infrared spectra of the dilithium tartrates are described in detail in Section 3.3.4.

Distortions of both the ligand and the metal coordination from their ideal geometries may have an adverse affect on structural energies. The torsion angle of the ligand C_4 carbon backbone varies between *gauche* (**7**) and linear (**2**, **4** - **6** and **8**), with two structures having close to eclipsed functional groups (**3**, 150.7(4)°, and **9**, 138.6(2)° - 140.6(2)°). In all cases, each ligand uses all six oxygen atoms in binding to lithium (resulting in the notation κ^6), but differences in the binding modes to lithium mean that each ligand coordinates to either six (μ_6, chelating mode) or eight lithium atoms (μ_8, mono-dentate mode).

The lithium atoms in **2** - **9** all have distorted tetrahedral coordination spheres, in which Li-O distances and O-Li-O angles vary widely. The most useful parameters for comparing these distortions are the average bond valence sum,[35] which takes into account all the Li-O distances, and the root mean squared deviation from the ideal tetrahedral angle, δ_{tet}.[38] The higher the bond valence sum, the closer the ligand oxygen atoms are to lithium and the stronger the Li-O bonding is. The range 1.06 (**7**) - 1.15 (**4**) is within the distribution expected for monovalent lithium, and is above 1 due to the low temperatures used in the single crystal structure determination studies, which reduce thermal vibrations and cause contraction of the overall structure. Values for δ_{tet} fall into two categories, corresponding to those structures featuring mono-dentate binding (4.93° - 6.65°) and those featuring chelation (12.62° - 14.68°).

Structures featuring chelation have higher values due to the small bite angle between oxygen atoms from the same ligand. The range of bond valence and δ_{tet} values may be attributed to the different crystal packing observed in each structure; the limited flexibility of the ligands limit the extent to which the ideal tetrahedral geometry can be reached. Overall, the combinations of different ligand conformations and metal binding modes result in four recognisable substructures: herringbone sheets (**2**, **5**, **6** and **8**), parallel sheets (**9**), crossed sheets (**7**) and other parallel chains (**3** and **4**).

3.3.4. *Hydrogen bonding analysis of dilithium tartrates*

One of the main structural differences in the dilithium tartrates is the range of hydrogen bonding motifs, from isolated intra-ligand hydrogen bonds in **4** to rings, one-dimensional chains and two-dimensional hydrogen bonding networks in others. This section describes an attempt to formalise this variation, made in order to discuss the differences and relate them to other features, such as energetics.

Graph set theory has been widely used in analysis of the intermolecular interactions of organic molecules, polymorphs and cocrystals, following the work of Etter, Bernstein and others.[39] It is a formalisation of the hydrogen bonding patterns observed between molecules, by consideration of the interactions between the hydrogen bond donor and acceptor groups, and their repetition within the crystal structure. All hydrogen bonding patterns can be ascribed to one of four designators: chains (**C**), rings (**R**), intramolecular patterns (**S**) and other finite patterns (**D**). The designator is augmented by a subscript, **d**, the number of hydrogen bond donors, and a superscript, **a**, the number of acceptors, in the pattern. Finally, the number of atoms in the pattern, **n**, called the degree of the pattern, is given in parentheses. The overall graph set descriptor is therefore $\mathbf{G^a_d(n)}$, where **G** represents one of the four designators.

Non-covalent interactions such as hydrogen bonding are known to be much weaker than coordination bonding, which is the most important type of interaction in determining the connectivity of inorganic-organic frameworks. Hydrogen bonding, despite being known to be important in directing the structures and properties of inorganic-organic frameworks,[3c, 40] has therefore not yet been studied systematically in their structural analysis. The issue that an inorganic-organic framework poses to graph set analysis is the definition of a molecule: the entire framework can be thought of as one molecule because the ligand units are linked covalently to each other. Therefore any hydrogen bond within the structure is essentially

intramolecular and could be denoted "**S**", i.e. self-hydrogen bonding. For analysis of inorganic-organic framework structures we therefore propose to use each ligand as the individual units to be linked by hydrogen bonds, rather than each 'molecule'. This has the advantage of considering hydrogen bonding as separate from the coordination bonding of the main framework, and so their relative contributions to the energy of each structure can be separated. By way of example, any hydrogen bonding motif denoted **S** in an inorganic-organic framework must be between functional groups on the same ligand moiety, i.e. it is an intra-ligand hydrogen bond.

3.3.4.1. Hydrogen bond analysis of dilithium L-tartrates

A summary of the main features of the hydrogen bonding networks of dilithium L-tartrates is shown in Table 8.

	2	**3**	**9**
Formula	$Li_2(L\text{-}C_4H_4O_6)$	$Li_2(L\text{-}C_4H_4O_6)$	$Li_2(L\text{-}C_4H_4O_6)$
Space group	$P2_12_12_1$	$C222_1$	$C2$
Inter-ligand H-bonds per ligand	2	2	2
Intra-ligand H-bonds per ligand	0.5	0	0
H-bond dimensionality	1	1	1
H-bond unitary graph set	**C(5)C(5)C(6)C(6)S(5)**	**C(5) [$R^2_2(12)$]**	**C(5)[$R^2_2(12)$] C(5)[$R^2_2(12)$]**
Other notable graph sets	**N_2: $R^1_2(7)$, $R^1_2(7)$, $C^2_1(7)$; N_3: $R^2_2(7)$**	-	-
D-A distances (Å)	2.602(3) - 2.959(3)	2.699(3)	2.724(2) - 2.785(2)
H-A distances (Å)	1.96(4) - 2.57(4)	1.82(5)	1.84(2) - 1.94(2)
D-H··A angles (°)	112(3) - 177(4)	173(4)	163(2) - 170(2)

*Table 8. Summary of the hydrogen bonding in dilithium L-tartrates **2**, **3** and **9**.*

The structure of **2** contains five different hydrogen bonds, four of which occur between crystallographically identical ligands in the *a*-direction, and one of which is intra-ligand. The inter-ligand hydrogen bonds give rise to unitary graph sets **C(5)** and **C(6)**; when combined they form rings involving a single carboxylate acceptor (binary graph set **$R^1_2(7)$**) (Figure 28).

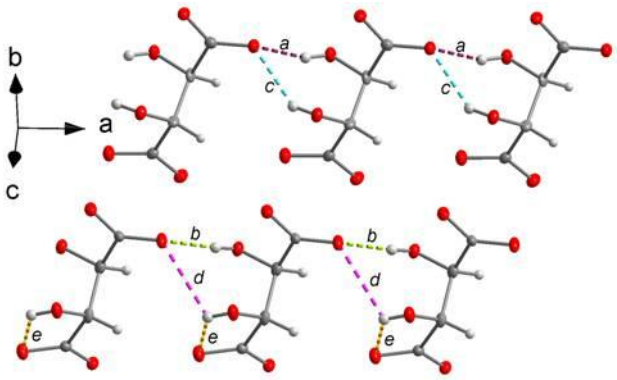

*Figure 28. Hydrogen bonding in $Li_2(L\text{-}C_4H_4O_6)$, **2**, omitting Li atoms for clarity. Hydrogen bonds shown as labelled dashed coloured lines: a and b, c and d, and e give rise to the descriptors **C(5)**, **C(6)** and **S(5)**, respectively.*

There is one crystallographically independent hydrogen bond in **3**, between hydroxyl group O2/H2O and carboxylate oxygen O1B. Combined along the *a*-axis they result a chain of rings, with the graph set **C(5)[R^2_2(12)]** (Figure 29).

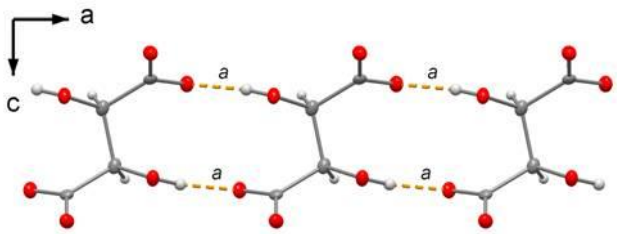

*Figure 29. Hydrogen bonding in $Li_2(L\text{-}C_4H_4O_6)$, **3**, omitting Li atoms for clarity. Hydrogen bonds shown as labelled dashed orange lines.*

Graph set analysis of the hydrogen bonding network in **9** confirms the presence of chains of rings running along the *b*-axis (**N_1**: **C(5)[R^2_2(12)]C(5)[R^2_2(12)]**) (Figure 30).

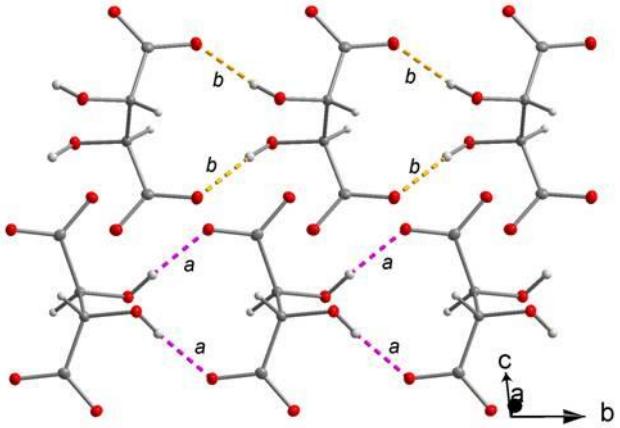

*Figure 30. Hydrogen bonding in $Li_2(L\text{-}C_4H_4O_6)$, **9**, omitting Li atoms for clarity. Hydrogen bonds shown as labelled dashed coloured lines: a and b are crystallographically distinct.*

3.3.4.2. Hydrogen bond analysis of dilithium *meso*-tartrates

A summary of the main features of the hydrogen bonding networks of dilithium *meso*-tartrates is shown in Table 9.

	4	**6**	**7**
Formula	Li_2(*meso*-$C_4H_4O_6$)	Li_2(*meso*-$C_4H_4O_6$)	Li_2(*meso*-$C_4H_4O_6$)
Space group	$P2_1/c$	$P2_1/c$	Cc
Inter-ligand H-bonds per ligand	0	2	2
Intra-ligand H-bonds per ligand	2	0	0
H-bond dimensionality	0	1	2
H-bond unitary graph set	**S(6)**	**C(5)[R^2_2(12)]**	**C(5)C(5)**
Other notable graph sets	**N_2: R^1_2(7)**	-	**N_2: C^2_2(12), C^2_2(12), R^4_4(24)**
D-A distances (Å)	2.625(4)	2.707(2)	2.613(2) - 2.672(2)
H-A distances (Å)	1.67(6)	1.83(3)	1.72(3) - 1.74(3)
D-H··A angles (°)	146(5)	167(3)	175(3) - 176(2)

*Table 9. Summary of the hydrogen bonding in dilithium meso-tartrates **4**, **6** and **7**.*

There is one hydrogen bond in the structure of **4**, which occurs between carboxylate oxygen O1B and the hydroxyl group in the β-position of the same ligand, O2/O2O. They form intra-ligand six-membered rings, giving rise to the graph set **S(6)** (Figure 31).

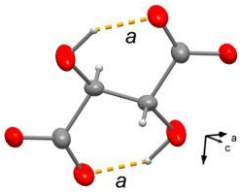

*Figure 31. Hydrogen bonding in $Li_2(meso\text{-}C_4H_4O_6)$, **4**, omitting Li atoms for clarity. Hydrogen bonds shown as labelled dashed orange lines.*

Each hydroxyl group in **4** forms a hydrogen bond with a carboxylate oxygen of a nearby ligand within the same 2-D herringbone array. The presence of a crystallographic centre of symmetry gives rise to chains of rings along the *b*-axis, resulting in the unitary graph set **C(5)[R^2_2(12)]** (Figure 32).

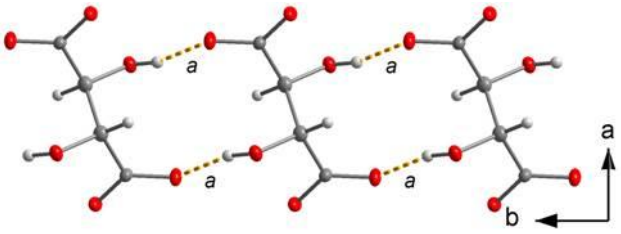

*Figure 32. Hydrogen bonding in $Li_2(meso\text{-}C_4H_4O_6)$, **6**, omitting Li atoms for clarity. Hydrogen bonds shown as labelled dashed orange lines.*

Each hydroxyl group in **7** forms a hydrogen bond with a carboxylate oxygen atom from a ligand nearby, resulting in the unitary graph set **C(5)C(5)** and a binary graph set that includes **C^2_2(12)** chains and an infinite range of rings in 2-D, of which **R^4_4(24)** has the lowest degree (Figure 33).

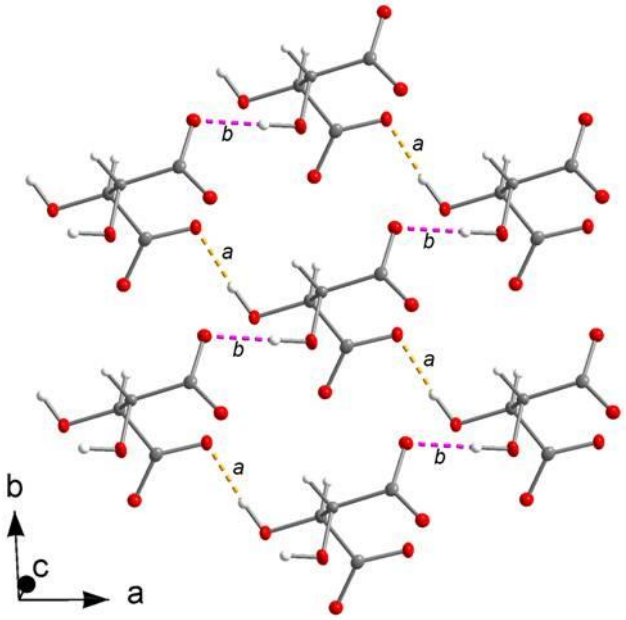

*Figure 33. Hydrogen bonding in one layer of $Li_2(meso\text{-}C_4H_4O_6)$, **7**, omitting Li atoms for clarity. Hydrogen bonds shown as labelled dashed coloured lines: a and b are crystallographically distinct.*

3.3.4.3. Hydrogen bond analysis of dilithium D,L-tartrates

A summary of the main features of hydrogen bonding networks of dilithium D,L-tartrates is shown in Table 10.

	5	**8**
Formula	$Li_2(D,L\text{-}C_4H_4O_6)$	$Li_2(D,L\text{-}C_4H_4O_6)$
Space group	*C*2/*c*	$P2_1/c$
Inter-ligand H-bonds per ligand	2	2
Intra-ligand H-bonds per ligand	0	1
H-bond dimensionality	1	2
H-bond unitary graph set	**C(5)C(6)**	**C(5)C(5)S(5)**
Other notable graph sets	$\mathbf{R^1_2(7)}$	$\mathbf{N_2}$: $\mathbf{C^2_2(12)}$, $\mathbf{C^2_2(12)}$, $\mathbf{R^4_4(24)}$, $\mathbf{C^2_1(4)}$
D-A distances (Å)	2.786(4) - 2.804(4)	2.625(2) - 3.091(2)
H-A distances (Å)	1.87(3) - 2.08(3)	1.862(12) - 2.56(3)
D-H··A angles (°)	134(2) - 168(3)	122(3) - 170(3)

*Table 10. Summary of the hydrogen bonding in dilithium D,L-tartrates **5** and **8**.*

There are two distinct hydrogen bonds in **5**, both of which involve carboxylate oxygen O5 as the inter-ligand acceptor. The separate hydrogen bonds give rise to **C(5)** and **C(6)** chains in the *b*-direction; combined, they result in a seven-membered ring, $\mathbf{R^1_2(7)}$ (Figure 34).

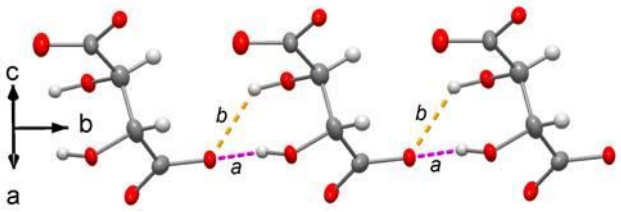

*Figure 34. Hydrogen bonding in one layer of $Li_2(D,L\text{-}C_4H_4O_6)$, **5**, omitting Li atoms for clarity. Hydrogen bonds shown as labelled dashed coloured lines: a and b give rise to the descriptors **C(5)** and **C(6)**, respectively.*

There are three distinct hydrogen bonds in the structure of **8**, the strongest likely to be between the hydroxyl oxygen O6 and neighbouring carboxylate oxygen O4 (D-A distance 2.696(2) Å, D-H..A angle 170(3)°). The hydroxyl group O3/H4 participates in a bifurcated hydrogen bond, donating to both O1 and O2 in inter- and intra-ligand fashion, respectively. The inter-ligand hydrogen bonds result in chains, which run perpendicular to each other, giving rise to a 2-D network and the unitary graph set **C(5)C(5)S(5)**. Notably, the different hydrogen bond motifs also combine to give binary graph sets $\mathbf{R^4_4(24)}$ and $\mathbf{C^2_1(4)}$ (Figure 35).

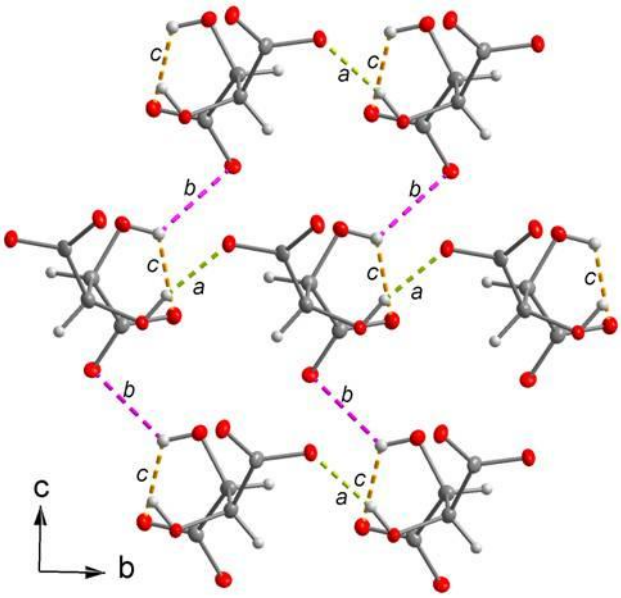

*Figure 35. Hydrogen bonding in $Li_2(D,L\text{-}C_4H_4O_6)$, **8**, omitting Li atoms for clarity. Hydrogen bonds shown as labelled dashed coloured lines: a and b, and c give rise to the descriptors **C(5)** and **S(5)**, respectively.*

3.3.4.4. Strength of hydrogen bonding and relation to infrared absorption

Hydrogen bonding is expected to lower the energy of any given structure, relative to an identical one in which hydrogen bonding does not occur. The IUPAC definition of a hydrogen bond states that "with a few exceptions, usually involving fluorine, the associated energies are less than 20 - 25 kJ mol^{-1}.[34] Therefore, where the energy differences between polymorphs are of a similar magnitude, hydrogen bonding could have a profound effect on their relative energies. Indeed, it performs a significant role in directing the packing structure of materials, including organic polymorphs and co-crystals[1a, 41] and inorganic-organic frameworks.[40] In general, stronger hydrogen bonds have shorter hydrogen-acceptor distances, H..A, and more linear hydrogen bond angles, D-H..A. This corresponds to the top left of a plot of hydrogen bond angle vs. hydrogen-acceptor distance (Figure 36).

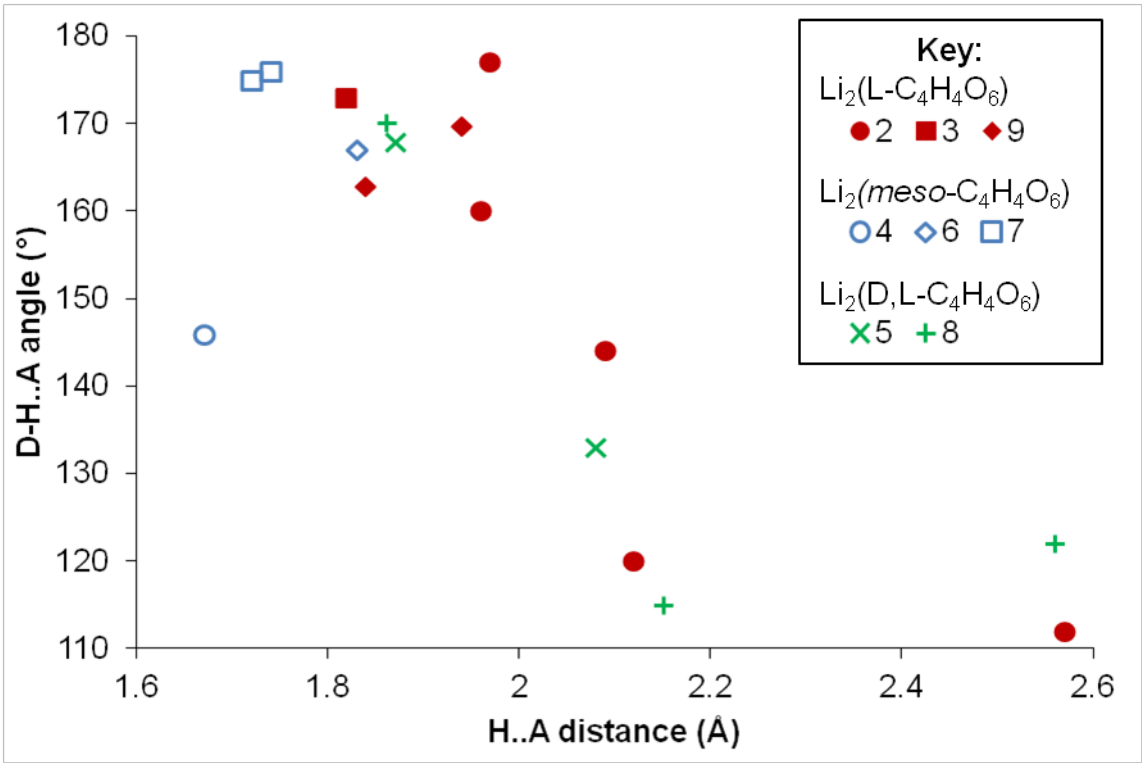

*Figure 36. Plot of hydrogen bond angle vs. hydrogen-acceptor distance for dilithium tartrates **2** - **9**. Data are coloured by ligand isomer (see key for details).*

In addition to lowering a structure's energy, participation as a hydrogen bonding donor also causes a decrease in hydroxyl group O-H bond strength by withdrawal of electron density from the O-H σ-bonding orbital. The stronger the hydrogen bond, the greater the perturbation in bond strength.[42] This effect can clearly be seen in the infrared spectra of the dilithium

tartrates, where the stretching frequencies for hydroxyl groups participating in hydrogen bonding are shifted to lower wavenumbers (Figure 37). Most notably, the O-H stretching frequencies of **3**, **6** and **7** are shifted to the lowest frequencies, suggesting that the contribution to energy lowering from hydrogen bonding will be most apparent in these phases. They also appear in the top left corner of Figure 36. In contrast, **2**, **5** and **8**, which appear in the bottom right corner of Figure 36, have O-H stretching frequencies that are relatively unperturbed by hydrogen bonding. **9** exhibits two overlapping sharp peaks with intermediate shifts, due to its two well-defined and similar hydrogen bond environments. Differences in peak intensities and can be explained by variation in the strength of IR absorption of each material, experimental changes between collections of different ATR-FTIR spectra and the data normalisation used. In general, peak broadening is due to the perturbation of O-H bond strength by hydrogen bonding, but it may also be due to additional variations in local structure within each material.

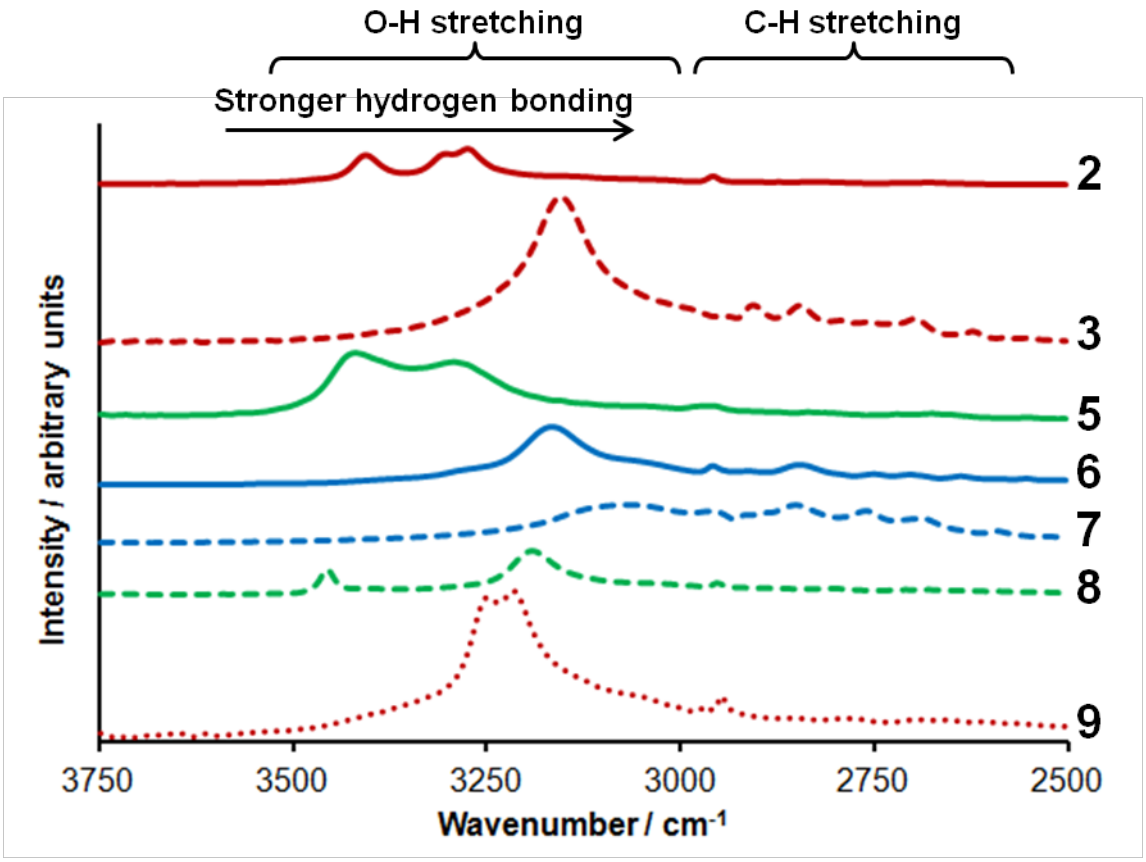

*Figure 37. Fourier-transform infrared spectra of dilithium L-tartrates **2**, **3** and **5-9** in the region corresponding to stretching modes of bonds to hydrogen, showing perturbations in O-H stretching frequency due to hydrogen bonding.*

Based on the relative shift in frequency of the O-H stretches, the FTIR peaks were assigned to different hydroxyl groups within each crystal structure, with those exhibiting stronger hydrogen bonding being assigned peaks with larger shifts. With only a few exceptions due to peak overlap and bifurcated hydrogen bonds, the assignments were straightforward (Table 11). The frequency shift of each peak, δ_{OH}, was calculated relative to the least shifted FTIR stretch, 3456 cm^{-1}, of **8**. Average values of δ_{OH} were calculated as a measure of the relative contribution hydrogen bonding might have on the energy of each structure: the larger δ_{OH}, the more effect expected.

	Donor atom	H-bond label	H..A distance (Å)	D-A distance (Å)	D-H..A angle (°)	FTIR peak (cm^{-1})	Relative frequency shift, δ_{OH} (cm^{-1})	Average δ_{OH} (cm^{-1})
2	O2	*a*	1.96	2.744	160	3275[1]	181	141.5
	O6	*b*	1.97	2.762	177	3275[1]	181	
	O3	*c*	2.09	2.774	144	3302[2]	154	
	O7[3]	*d*	2.57	2.959	112	3406	50	
		e	2.12	2.602	120			
3	O2	*a*	1.82	2.699	173	3155[4]	301	301
4	O2	*a*	1.67	2.625	146	--	--	--
5	O4	*a*	1.87	2.786	168	3294[5]	162	98
	O3	*b*	2.08	2.8	133	3422[5]	34	
6	O3	*a*	1.83	2.707	167	3167	289	289
7	O4	*a*	1.72	2.613	175	3067[1, 5]	389	389
	O3	*b*	1.74	2.672	176	3067[1, 5]	389	
8	O6	*a*	1.862	2.697	170	3194[5]	262	131
	O3[3]	*b*	2.56	3.091	122	3456[6]	0	
		c	2.15	2.625	115			
9	O3	*a*	1.84	2.724	162.8	3217	239	221.5
	O6	*b*	1.94	2.7852	169.7	3252	204	

*Table 11. Individual hydrogen bond parameters and FTIR assignments for O-H stretches in the dilithium tartrates **2** - **9**. Notes: (1) significant peak overlap, (2) shoulder peak, (3) bifurcated hydrogen bond, (4) strong absorption, (5) broad absorption, (6) sharp absorption.*

3.3.5. *Energetics of dilithium tartrates*

The relative energies of lithium tartrates **1** - **9** were calculated using density functional theory, with additional calculations performed for **2** - **9** to take into account additional dispersion

correction and for **2** - **6** to include zero point vibrational energy, ZPVE, and thermal vibrational energy at 298.15 K. The values for **2** - **9** are shown in Table 12. Due to the considerable computational cost involved, vibrational contributions were not calculated for **7** - **9**.

	2	**3**	**4**	**5**	**6**	**7**	**8**	**9**
Ligand isomer	L-	L-	*meso-*	D,L-	*meso-*	*meso-*	D,L-	L-
Space group	$P2_12_12_1$	$C222_1$	$P2_1/c$	$C2/c$	$P2_1/c$	Cc	$P2_1/c$	$C2$
ΔE_{elec}**(PBE)** [1] **(kJ mol^{-1})**	3.85	0	1.84	4.53	-8.67	-6.21	2.56	-0.06
ΔE_{elec}**(PBE+D)** [1] **(kJ mol^{-1})**	-1.24	0	11.59	-2	-19.29	-11.68	-13.62	-7.95
ΔE_{tot}**(PBE+V)** [1] **(kJ mol^{-1})**	14.37	0	2.04	6.56	-5.94	--	--	--

*Table 12. Calculated energies of the dilithium tartrates **2** - **9**. Note: (1) Relative to that of **3**.*

The range of energies calculated using the PBE functional alone, ΔE_{elec}(PBE), is 13.2 kJ mol^{-1}. This is less than half the range of energies calculated when a dispersion correction, ΔE_{elec}(PBE+D), is included, 30.88 kJ mol^{-1}. In addition, the relative order of the energies of **2** - **9** changes, giving good agreement with their experimental phase behaviour (Section 3.3.6). The difference between the two schemes is due to additional weighting given in ΔE_{elec}(PBE+D) to both short- and long-range intermolecular interactions, including hydrogen bonding (discussed in Section 3.3.5.1), which increases the variance of energies observed. Inclusion of ZPVE and thermal vibrational energy without dispersion correction, ΔE_{tot}(PBE+V), results in **3** - **6** remaining within a similar energy range. However, the relative energy of **2** increases dramatically from 3.85 kJ mol^{-1} to 14.37 kJ mol^{-1} and is discussed in Section 3.3.5.2. Incidentally, the relative energy of the monolithiated compound, **1**, is 143.51 kJ mol^{-1} higher than that of **3**. This indicates that the formation of **1** is less energetically favourable than the dilithium tartrates; the major factor is likely to be the weaker electrostatic interactions in **1** (the ligand has only one negative charge).

3.3.5.1. Structure - energy relationships in dilithium tartrates **2** - **9**

The phase behaviour (Section 3.3.6) of the lithium tartrates is explained well by ΔE_{elec}(PBE+D) but poorly by ΔE_{elec}(PBE), indicating that the additional dispersion correction plays a significant and important role in calculation of the structures' energies. This is perhaps unsurprising, as the number and types of covalent bonds (e.g. C-C, C-H, C-O,

Li-O) that dominate the frameworks' absolute energies are essentially the same for each of the isomers **2** - **9**, whilst features that affect dispersion interactions, such as packing density, hydrogen bonding, metal-ligand coordination geometry and ligand conformations vary considerably across the series (Table 13).

	2	**3**	**4**	**5**	**6**	**7**	**8**	**9**
Ligand isomer	L-	L-	*meso-*	D,L-	*meso-*	*meso-*	D,L-	L-
Space group	$P2_12_12_1$	$C222_1$	$P2_1/c$	$C2/c$	$P2_1/c$	Cc	$P2_1/c$	$C2$
ΔE_{elec} (PBE+D) (kJ mol^{-1})[1]	-1.24	0	11.59	-2.00	-19.29	-11.68	-13.62	-7.95
Density (g cm^{-3})	1.77	1.76	1.72	1.82	1.85	1.81	1.90	1.83
Average FTIR δ_{OH} (cm^{-1})[2]	141.5	301.0	--	98.0	289.0	389.0	131.0	221.5
Average Li-O bond valence sum	1.10	1.13	1.15	1.12	1.13	1.06	1.10	1.14
Average O-Li-O deviation, δ_{tet} (°)	6.65	12.62	13.34	4.93	5.01	14.86	6.64	5.92
Average C_4 torsion angle (°)	177	151	180	174	180	173	62	139

*Table 13. Calculated relative energies of dilithium tartrates **2** - **9**, including dispersion correction, and related structural parameters. Notes: (1) Relative to that of **3**, (2) Relative to the least-shifted peak position in **8**.*

The best correlation of ΔE_{elec}(PBE+D) with a single structural feature is with density (Figure 38). In structures of identical elemental composition, increased density should result in stronger long-range intermolecular interactions, which reduce the relative energy. This seems to be the case for **2** - **9**, however, there is still some variance unaccounted for, as indicated by the residual factor $R^2 = 0.7669$.

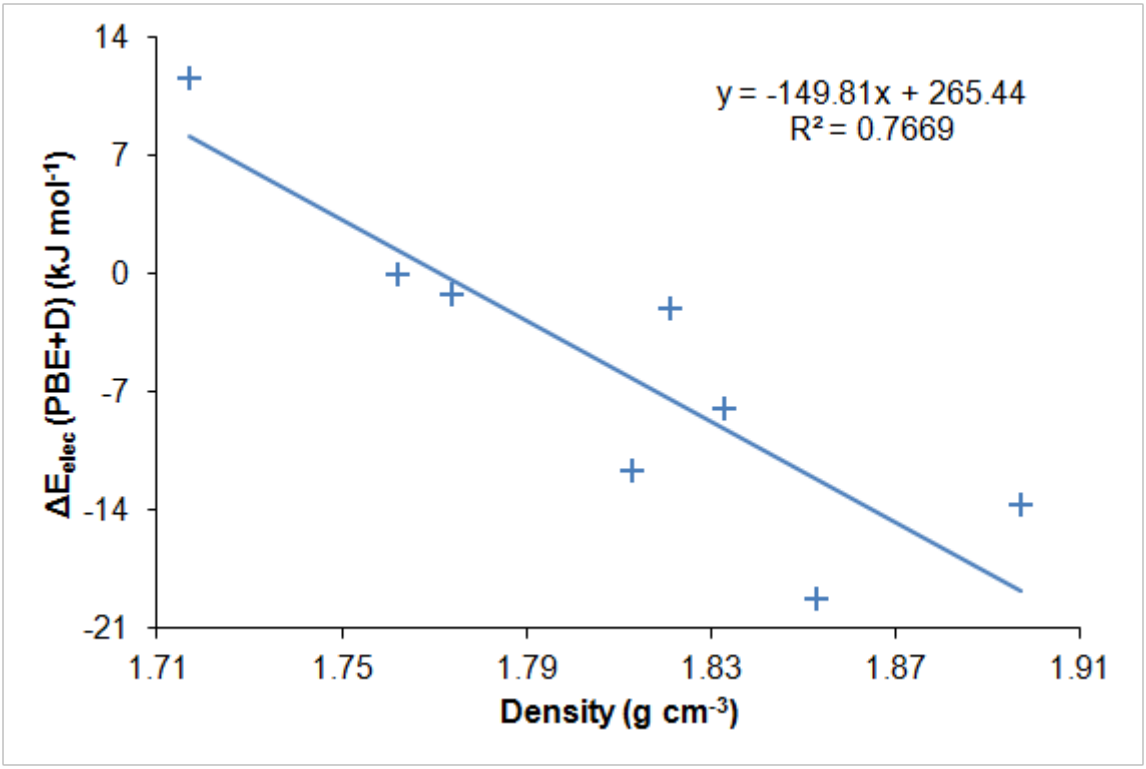

*Figure 38. Correlation between ΔE_{elec} (PBE+D) and crystal density of dilithium tartrates **2** - **9**, showing the equation of the line of best fit and its corresponding residual factor.*

No other factor shown in Table 13 correlates well on its own with ΔE_{elec}(PBE+D), indicating that hydrogen bonding (as described by the O-H peak shift in the FTIR spectrum), metal-ligand coordination geometry and ligand conformation affect relative energies in a minor way, if at all. The variation in average Li-O bond valence sum is very small, ranging from 1.06 (**7**) to 1.15 (**4**), therefore it has negligible effect on the energy. Variations in LiO_4 distortion (described by deviation from the ideal tetrahedral angle, δ_{tet}) are difficult to relate to ΔE_{elec}(PBE+D), as they depend on ligand geometry and metal-ligand binding modes, which in turn affect Li-O bond strength and the overall structure topology. The δ_{tet} values of the dilithium tartrates can be divided into two distinct categories: phases exhibiting mono-dentate binding, **2**, **5**, **6**, **8** and **9**, have values between 4.93° and 6.65°. Those exhibiting chelation, **3**, **4** and **7**, have higher values, from 12.62° - 14.86°, due to the chelation bite angle being below 90°. No significant correlation with ΔE_{elec}(PBE+D) was found in either case. Ligand conformation is also hard to relate to ΔE_{elec}(PBE+D), due to the non-linear dependence of energy on torsion angles and the difference in conformational preference between chiral and *meso*-tartrate isomers. In addition, conformational preference in the

tartaric acids has recently been shown to be dependent primarily on the available number and stability of intramolecular hydrogen bonds, rather than any other electronic effect.[36]

Hydrogen bonding, the effect of which is modelled better by ΔE_{elec}(PBE+D) than by ΔE_{elec}(PBE), appears to have no correlation with relative energies on its own. However, closer inspection of Figure 38 reveals that structures with energies much lower than modelled by density alone, **6** and **7**, exhibit shorter, more linear hydrogen bonding, and those with energies higher than expected, **5** and **8**, exhibit weaker hydrogen bonding.

In order to determine whether this was a real effect, multiple linear regression analysis was performed simultaneously on average values of the FTIR O-H stretching frequency shift, δ_{OH}, and the crystallographic densities of **2**, **3** and **5** - **9**, to optimise the fit to equations of type

$$\Delta E_{elec,i}(PBE + D) = a.\rho_i + b.\delta_{OH,ave,i} + c$$

where a, b and c are refined constants, and ρ and $\delta_{OH,\,ave}$ are the density in g cm^{-3} and average value of δ_{OH} in cm^{-1}, respectively, of structure i (i = 2, 3, 5 - 9).

Incorporation of $\delta_{OH,\,ave}$ improved the residual statistics from R^2 = 0.7295 (omitting data for **4**, for which an FTIR spectrum could not be obtained) to R^2 = 0.8135, demonstrating that hydrogen bonding does indeed have a small effect on the relative structural energies of the dilithium tartrates and plays a role that is secondary to density. Final values for a, b and c were -141.77 kJ cm^3 mol^{-1} g^{-1}, -0.03669 kJ mol^{-1} cm and 258.5955 kJ mol^{-1}, respectively. A plot of the calculated values versus fitted values is shown in Figure 39. The variance not accounted for may be due to additional, more subtle, structural factors and inadequacies in the models used, such as omission of crystallographic disorder in calculated structures, and indirect measurement of hydrogen bond strength using FTIR O-H peak shifts.

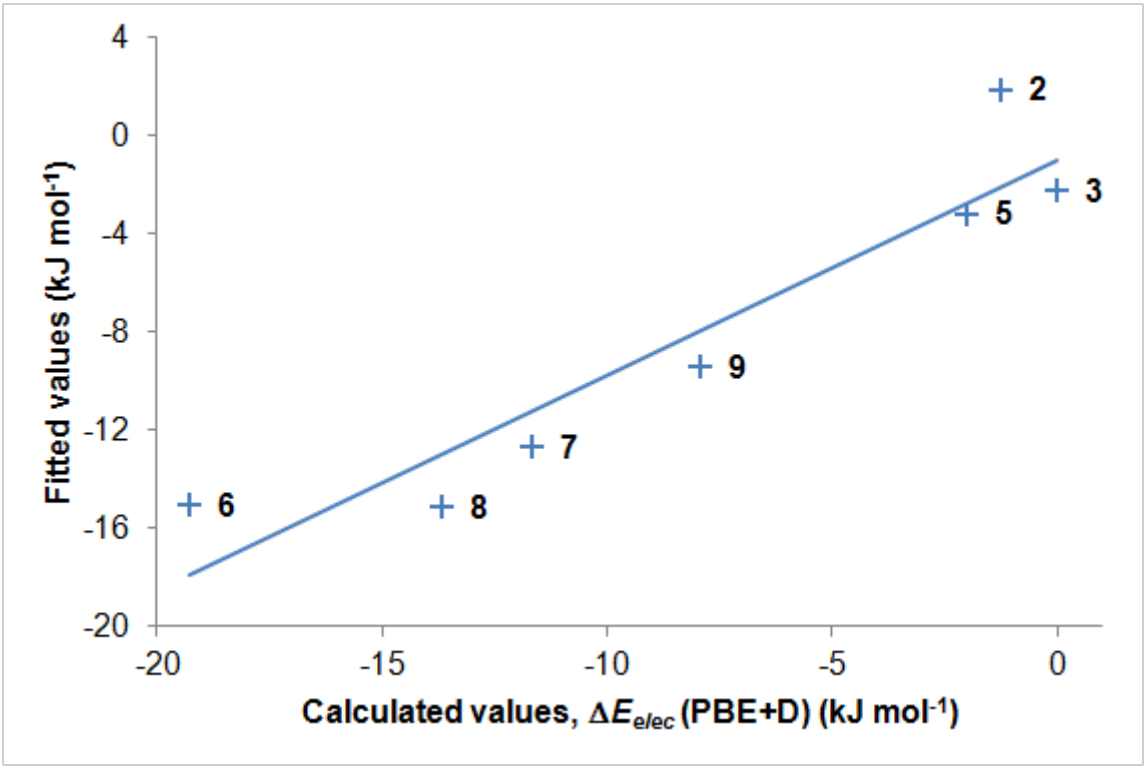

*Figure 39. Calculated energies versus values fitted by multiple linear regression of the density and LiO_4 angular distortion, $\delta_{OH,\,ave}$, of dilithium tartrates **2**, **3** and **5** - **9**.*

3.3.5.2. Comparison between vibrational contributions of polymorphs **2** and **3**

The difference in ZPVE between polymorphs **2** and **3**, 15.37 kJ mol^{-1}, suggests that they have different topologies, in agreement with X-ray diffraction data. To gain further insight into this difference, analysis of the normal modes of each structure was performed and compared with experimental FTIR spectra.

Both experimental and calculated datasets differ between **2** and **3** in the region below 720 cm^{-1}, which corresponds to heavy atom motion, and above 3000 cm^{-1}, which corresponds to hydrogen atom motion (Figure 40). In general, the normal modes of **2** occur at higher frequency than those of **3**, giving rise to higher ZPVE in **2**. In the high frequency region of **2**, calculations show two clear bands corresponding to O-H stretches at 3295.06 cm^{-1} and 3455.07 cm^{-1} (corresponding to 3275 cm^{-1} and 3406 cm^{-1} in the experimental spectrum). The O-H stretches associated with **3** are lower in frequency (3114.72 cm^{-1} and 3149.78 cm^{-1}) and differ by only 35.06 cm^{-1} and so appear as one broad peak (3155 cm^{-1}) in the experimental FTIR spectrum. In contrast to both **2** and **3**, the calculated O-H stretches of the isolated L-tartaric acid molecule occur at higher frequencies (3536.46 and 3587.68 cm^{-1}). This

provides further confirmation that the hydroxyl group protons in **2** and **3** are involved in hydrogen bonding, as found in Section 3.3.4.4.

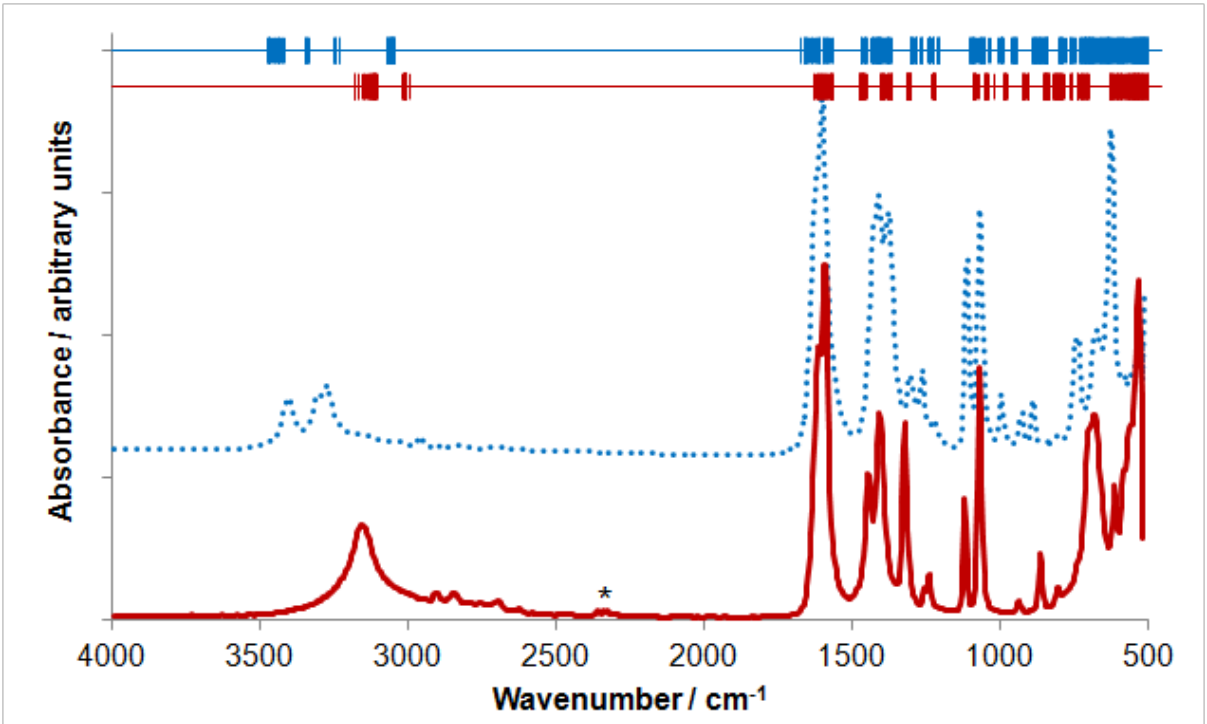

*Figure 40. Experimental FTIR spectra of dilithium L-tartrate polymorphs **2** and **3**, shown as red and blue dotted lines, respectively, alongside their calculated normal mode frequencies, shown in blue and red, respectively. The asterisk marks absorption due to atmospheric CO_2.*

The difference between the ZPVE energies of the O-H modes in **2** and **3**, 2.90 kJ mol^{-1}, contributes only a minor fraction of the total ZPVE difference. This implies that the major part of the destabilization of **2** relative to **3** at 0 K lies in the ZPVE arising from degrees of freedom that involve framework backbone heavy atoms. Differences in fine structural features, such as crystal packing, ligand conformation and metal-ligand binding may be responsible for this.

3.3.6. *Phase behaviour of lithium tartrates*

The phase behaviour of the lithium tartrates has been investigated as a function of temperature, solvent water fraction and ligand isomer. The products of reactions under various conditions chosen were identified and their relative amounts deduced by powder X-ray diffraction. A summary of the crystalline phases, particle morphologies and yields can be seen in Table 14. Two different solvent systems were chosen. Kinetic conditions were achieved in pure ethanol due to the insolubility of the products in this solvent, which limited

re-dissolution of phases once they were formed. Water:ethanol solvent mixtures, optimized to eliminate immediate precipitation, gave conditions closer to thermodynamic equilibrium, enabling slower crystallization and re-dissolution due to enhanced solubility.

Ligand isomer	Solvent	Synthesis temperature (°C)						
		25	60	100	125	150	180	200
L-	ethanol	**3** *powder [94 %]*	**3, 2** *powder [94 %]*	**2, 3** *needles [86 %]*	**2, 3** *needles [85 %]*	**2, (3)** *plates, powder [82 %]*	**2, (3)** *needles [82 %]*	**2** *needles [88 %]*
L-	water / ethanol	$LiH(L\text{-}tart)\cdot H_2O$ + **2** *plates*	**2, 9** *plates [60 %]*	**2, 9** *plates [52 %]*	**2, 9** *plates, rods [54 %]*	**2, 9** *plates, rods [52 %]*	**2, 9, 6** *polycr. [59 %]*	**2, 9, 6** *polycr. [56 %]*
meso-	ethanol	?	**7, 6** *powder, blocks [77 %]*	**7, 6** *powder, rods [57 %]*	**7, 6** *powder, rods [54 %]*	**7, (4, 6)** *powder, rods [77 %]*	**7, 6, (4)** *powder, needles [85 %]*	**6, 7, (4)** *needles, powder [80 %]*
meso-	water / ethanol	**7**, (+ ?) *polycr.*	**7** *plates [59 %]*	**6** *blocks [56 %]*	**6** *rods [77 %]*	**6** *rods [77 %]*	**6** *rods [73 %]*	**6** *rods, polycr. [68 %]*
D,L-	ethanol	?	$H_2(D,L\text{-}tart)$ + ?	$H_2(D,L\text{-}tart)$ + ?	$H_2(D,L\text{-}tart)$ + ?	**5, 8** *rods [84 %]*	**5, 8** *rods [90 %]*	**5, 8** *powder, needles [90 %]*
D,L-	water / ethanol	$LiH(L\text{-}tart)\cdot H_2O$ *plates*	**8, (5)** *rods, plates [17 %]*	**8** *rods [19 %]*	**8** *rods [20 %]*	**8** *rods [20 %]*	**8, 6** *rods, polycr. [22 %]*	**6** *polycr. [31 %]*

Table 14. Phase behaviour (? = unknown phase; tart = $C_4H_4O_6^{2-}$), morphologies ("polycr." indicates polycrystalline material) and yields of solely dilithium products of lithium tartrates with respect to temperature, solvent system and ligand isomer. Major phases are listed in order of abundance, with minor phases in parentheses.

3.3.6.1. General observations of lithium tartrates phase behaviour

Overall, all the anhydrous dilithium tartrates, **2** - **9**, were obtained by using various reaction conditions, along with one known hydrated phase, $LiH(L\text{-}C_4H_4O_6)\cdot H_2O$, and some unknown phases. Of the anhydrous dilithium tartrate phases, all but the highest energy phase, **4**, can be obtained in phase-pure form. This indicates that by variation of temperature and solvent composition, fine control, both kinetic and thermodynamic, can be exerted over phase behaviour for each ligand isomer in this structurally diverse system.

Non-aqueous conditions generally resulted in mixed phases and poorer crystal growth, confirming kinetic conditions were achieved. In the case of D,L-tartrate, no known lithiated product was produced in ethanol below 150 °C, due to the high lattice energy and low solubility of the reagent acid. However, non-aqueous conditions do enable the formation of **3**, **4** and **5**, which are not readily accessible when water is present. On the other hand, hydrated solvent conditions generally lead to better-defined morphologies, lower energy phases, purer products and lower yields. This is due to the increased solubility of the products, and confirms that conditions closer to thermodynamic equilibrium were achieved.

3.3.6.2. Phase behaviour of lithium *meso*-tartrates

Non-aqueous conditions result in a mixture of *meso*-tartrate phases at all elevated temperatures, with an increasing fraction of **6** and formation of small amounts of **4** at high temperatures. The observation of **4**, the energy of which is more than 20 kJ mol^{-1} greater than those of **6** and **7**, suggests that inter-conversion between phases does not occur and that formation of each phase occurs *via* a different reaction pathway. At lower temperatures **7** has the lowest activation energy, but **6** and **4** become increasingly accessible as temperature increases (Figure 41, red lines). Hydrated conditions result in pure lithium *meso*-tartrate phases at all elevated temperatures. The product at 25 °C and 60 °C is the polar phase in space group *Cc*, **7**, which forms as thick plates. This suggests that **7** is a kinetic phase and at low temperatures there is insufficient kinetic energy to overcome the activation barrier from **7** to **6**. At higher temperatures **7** is converted entirely to the lowest energy lithium tartrate phase, **6**, which forms as rods in $P2_1/c$ (Figure 41, blue line).

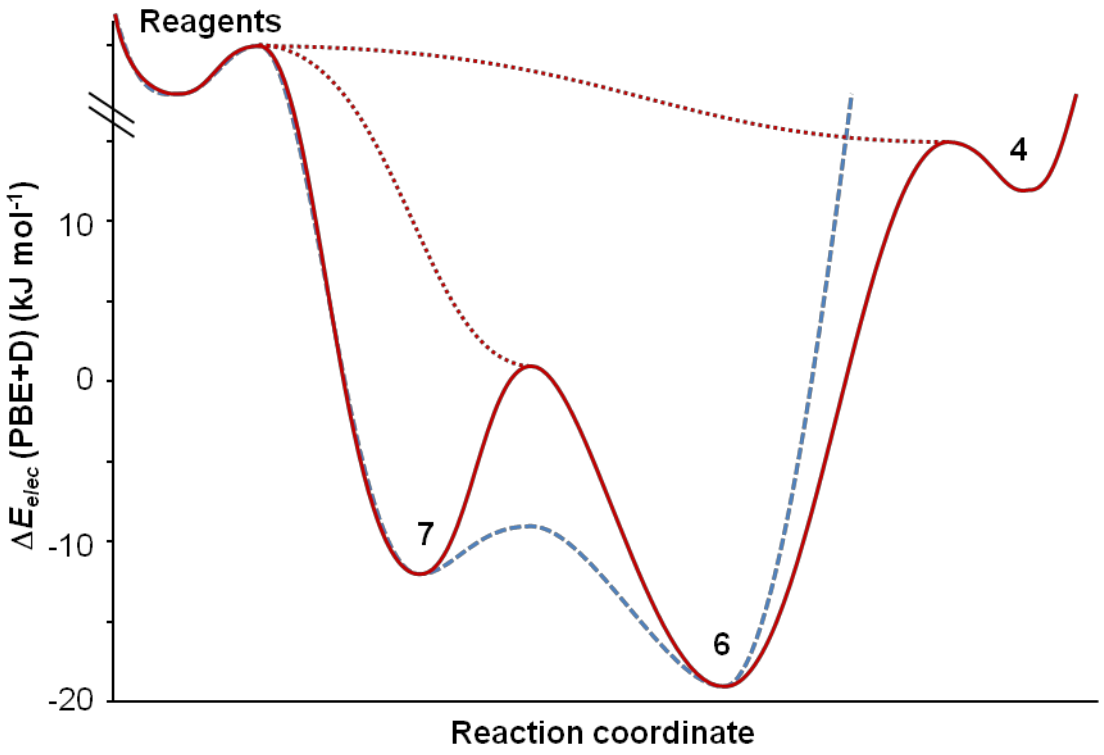

Figure 41. Formation energetics of lithium meso-tartrates, showing behaviour in non-aqueous and mixed solvent media as red and blue lines, respectively. Dotted lines represent alternative kinetic pathways, for which activation energies decrease with temperature. The relative heights of barriers between phases indicate their activation energies but they do not necessarily correspond to absolute values.

3.3.6.3. Phase behaviour of lithium L-tartrates

In non-aqueous conditions, **3** and **2** form as a pure phases at room temperature and 200°C, respectively. A mixture of the two phases forms in-between these extremes, with the proportion of **2** increasing with temperature. This suggests that the activation energy for formation of **2** in non-aqueous conditions decreases with temperature, as was found for *meso*-tartrates **4** and **6**. The lowest energy L-tartrate, **9** could not be obtained in ethanol, suggesting that **2** and **3** are kinetic phases and the activation energy for the formation of **9** is prohibitively high (Figure 42, red lines).

In water-containing solvent the hydrated phase, $LiH(L\text{-}C_4H_4O_6)\cdot H_2O$, forms at room temperature. At elevated temperatures it is not present, suggesting it is a kinetic phase and an increasing entropic contribution to the structures' free energy helps to drive off coordinated water, forming anhydrous phases. **2** and **9** form at all other temperatures, but the activation

energy between **2** and **9** must be high enough to prevent complete conversion taking place within the timescale of the reaction, which was three days (Figure 42, blue line). In a separate reaction at 150 °C, more complete conversion was achieved by increasing the reaction time and the fraction of water in the solvent (Section 3.2.1.9). This resulted in a purer sample of **9**, albeit with approximately 20 % **2**, confirming that it is the lowest energy L-tartrate phase.

At 180 °C and 200 °C in hydrated solvent conditions, Li_2(*meso*-tartrate), **6**, forms from the L-tartaric acid starting material. This is indicative of in-situ ligand isomerisation, which is enabled by the high temperature and availability of water for substitution reactions, and has been seen previously in other inorganic-organic framework syntheses.[43] The mother liquor in these reactions was discoloured, indicating that the organic ligand had not only undergone isomerisation but had also began to decompose. Furthermore, the morphology of the reaction products was polycrystalline, indicative of the new impurities in the reaction mixture. The formation of **6** following ligand isomerisation is well in agreement with calculated energies, which indicate it is the global energy minimum structure.

In hydrated conditions, **3** is not observed, implying that it is indeed a kinetic phase favoured by non-aqueous conditions, like **4** and **7** in the *meso*-tartrate system. These three phases exhibit ligands in chelation binding to Li, suggesting that in the absence of competition from water this is the preferred state of precursors in ethanol, which leads to kinetic products.

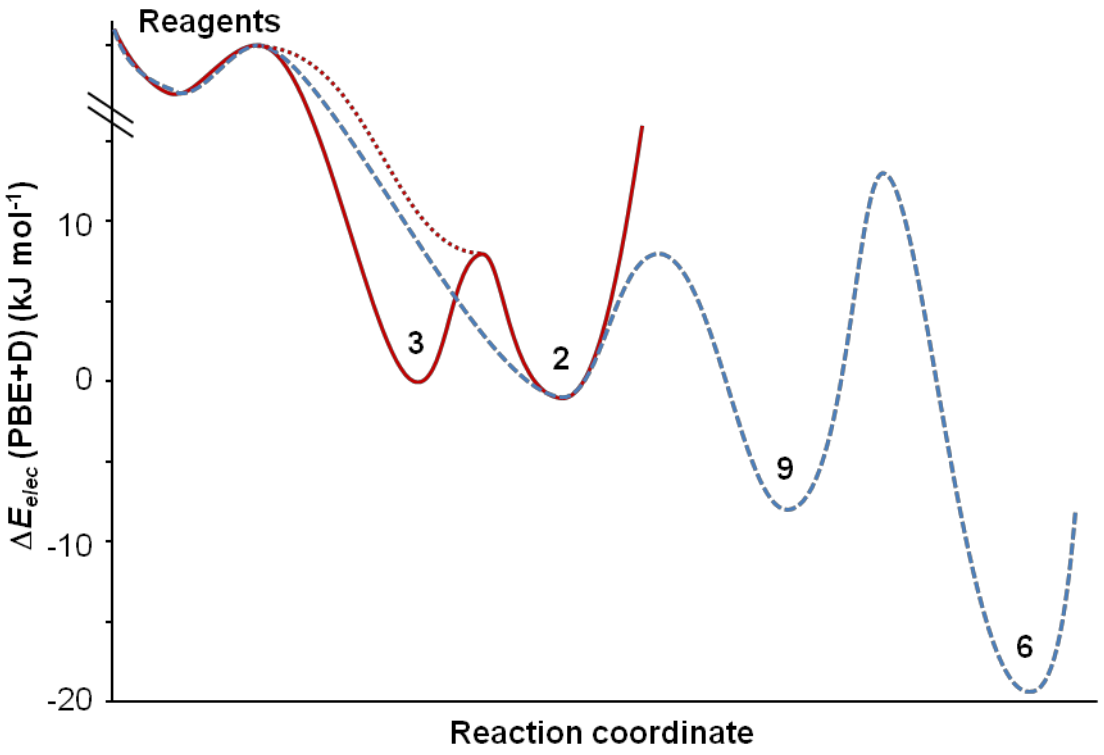

Figure 42. Formation energetics of lithium L-tartrates, showing behaviour in non-aqueous and mixed solvent media as red and blue lines, respectively. The dotted line represents an alternative kinetic pathway, for which activation energy decreases with temperature. The relative heights of barriers between phases indicate their activation energies but they do not necessarily correspond to absolute values.

3.3.6.4. Phase behaviour of lithium D,L-tartrates

Reactions involving D,L-tartaric acid in non-aqueous conditions lead to no known lithiated products at temperatures below 150 °C, due to the high lattice energy and low solubility of D,L-tartaric acid. Between 150 °C and 200 °C, the product is a mixture of **5** and **8**, indicating that kinetic conditions were achieved and the barrier for inter-conversion between the phases is prohibitively high (Figure 43, red lines).

In hydrated conditions, LiH(L-$C_4H_4O_6$)·H_2O forms at room temperature as seen in the L-tartaric acid system, presumably as a racemic conglomerate of L- and D- enantiomorphs (powder X-ray diffraction cannot distinguish between the two forms). At temperatures between 60 °C and 180 °C, the phase in $P2_1/c$, **8**, is the major phase. PXRD analysis of the 60 °C product shows the presence of **5** as a trace phase; the diffraction peaks arising from this structure are relatively weak. That fact that **8** is the major phase across this temperature

range is in agreement with calculations, which show that it is the most stable D,L-tartrate phase (Figure 43, blue line). Furthermore, spontaneous resolution of dilithium D- and L-tartrate forms from D,L-tartaric acid does not occur, because the energy of D,L- phase **8** is below that of any of the enantiomorphic chiral phases **2**, **3** and **9**. However, as was seen in the L-tartaric acid system, at 180 °C and 200 °C the ligand undergoes *in-situ* isomerisation. This enables the formation of **6**, which is the global energy minimum structure.

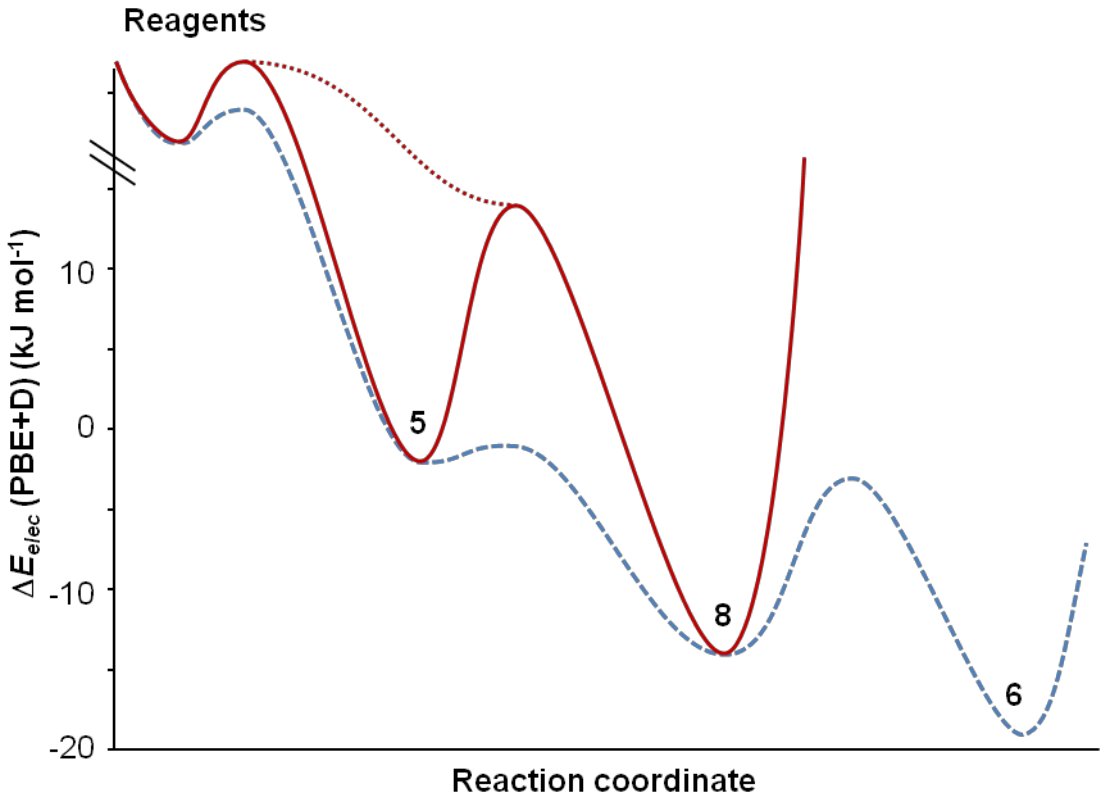

Figure 43. Formation energetics of lithium D,L-tartrates, showing behaviour in non-aqueous and mixed solvent media as red and blue lines, respectively. The dotted line represents an alternative kinetic pathway and the relative heights of barriers between phases indicate their activation energies but do not necessarily correspond to absolute values.

3.4. Conclusions

Eleven new crystal structures of lithium tartrate frameworks have been determined by single crystal X-ray diffraction, including one lithium hydrogen tartrate (**1**), eight anhydrous dilithium tartrates (**2** - **9**) and two hydrated dilithium tartrates, involving three different ligand isomers: L-, *meso*- and D,L-tartaric acid. Despite identical elemental composition and I^1O^2 connectivity, **2** - **9** exhibit a range of structural features, such as density, hydrogen bonding, ligand conformation and metal binding modes. Their various hydrogen bonding patterns were categorized by modified graph set analysis and their strengths were found to relate well to shifts observed in O-H stretching frequency in FTIR spectra.

The relative energies of the isomeric dilithium tartrate phases **2** - **9** were calculated using density functional theory, with and without dispersion correction and vibrational contributions (including ZPVE and thermal vibrations at room temperature). Trends in various structural features were investigated to rationalise the variation in calculated energies, with crystallographic density and hydrogen bonding strength found to be important. In addition, the large increase in energy difference between chiral polymorphs **2** and **3** when vibrational contributions were added was found to be primarily due to ZPVE of heavy atom modes, rather than light atom modes such as O-H stretches.

The phase behaviour of each ligand isomer was investigated as a function of solvent water content and temperature, and found to be well-described by thermodynamic (calculated relative energies) and kinetic effects (solvent effects and structural features). Fine control could be exerted over the phase behaviour, with all but the highest energy structure, **4**, being obtained in bulk form. Spontaneous resolution of the racemic D,L-tartaric acid into chiral dilithium tartrates did not occur, because the energies of chiral dilithium tartrate products **2**, **3** and **9** are all above the lowest energy racemic phase, **8**. However, under high temperature thermodynamic conditions, ligand isomerisation of both chiral L- and racemic D,L-tartaric acids was found to occur, giving rise to the global minimum energy phase, **6**, irrespective of starting isomer.

3.5. Future work

The high energy *meso*-tartrate phase **4** could not be obtained in phase-pure form for analysis other than single crystal X-ray diffraction. If it could be synthesized it would be useful to confirm the observations made in this work, particularly with regards to the effect of hydrogen bonding on O-H stretching frequency and relative energy. Efforts are ongoing to synthesize **4** by mechanochemical methods for this purpose. It is thought that this technique, described in Chapter 4, may enable kinetic stabilization of **4** in powder form due to the relatively dry conditions in the mill, which may favour intra-molecular hydrogen bonding and lithium chelation exhibited by **4**.

In this structurally diverse family of inorganic-organic frameworks, it would also be interesting to examine the effect of structure on physical properties. Mechanical property measurements, in collaboration with Dr. Jin-Chong Tan and Dr. Monica Kosa, are currently being performed on lithium L-tartrate **2** and lithium D,L-tartrate **8** using nanoindentation on single crystals. These phases are particularly useful due to their orthorhombic and pseudo-orthorhombic symmetry, which allows full determination of the complete elastic constant tensor and thus determination of other mechanical properties such as bulk modulus.

Initial computational molecular dynamics simulations, in collaboration with Dr. Monica Kosa, also indicate that these materials are promising candidates for new solid electrolytes. When a lithium vacancy is created *in-silico*, hopping of the lithium atoms between sites along the inorganic chain is observed. However, there are a number of synthetic issues that must be overcome in order to make the lithium tartrates useful for this application in reality. These include how to create lithium vacancies using low-temperature synthesis methods (see Chapter 5), and how to reduce the activation energy of lithium hopping. Unfortunately, the simulation temperature at which mobility is observed is above the limit of thermal stability of these materials, and may be due to the inherently high strength of Li-O bonding in the crystal structure.

The variety of crystallographic space groups adopted by the new lithium tartrates suggests that measurement of their dielectric properties may uncover interesting behaviour. Although the strong ferroelectric effect in Rochelle salt, $KNa(L\text{-}C_4H_4O_6)\cdot 4H_2O$, is thought to be due to ordering of the water protons rather than the ligand itself, the chiral lithium L-tartrates **2**, **3** and **9**, and the polar *meso*-tartrate phase, **7**, may yet display such properties, owing to their

inherently non-centrosymmetric nature. The anhydrous phases would also have the advantage of stability at higher temperatures than analogous hydrated systems, although switching polarisation may be more difficult in such frameworks in which the ligand orientation is fixed by coordination bonding.

Other anhydrous alkali metal tartrates, such as sodium and potassium, have not been investigated to a similar extent as the lithium tartrates. Therefore it would be interesting to investigate them to see what structural variations occur with larger monovalent cations, as has been investigated in the alkaline earth tartrates.[12]

Some of the results reported in this chapter were published in the article "Structural Diversity and Energetics in Anhydrous Lithium Tartrates: Experimental and Computational Studies of Novel Chiral Polymorphs and Their Racemic and Meso Analogues", in Crystal Growth and Design, Volume 11, Pages 221 -230, January 2011.[44] This article described structures **1** - **5**, and compared their calculated energies, with and without vibrational contributions. A similar article containing the remaining results is currently in preparation and will be submitted for publication in the near future.[45]

3.6. References

(1) (a) Nangia, A. *Acc. Chem. Res.* **2008**, *41*, (5), 595-604. (b) Issa, N.; Karamertzanis, P. G.; Welch, G. W. A.; Price, S. L. *Cryst. Growth Des.* **2009**, *9*, (1), 442-453.

(2) Makal, T. A.; Yakovenko, A. A.; Zhou, H. C. *J. Phys. Chem. Lett.* **2011**, *2*, (14), 1682-1689.

(3) (a) Bowden, T. A.; Milton, H. L.; Slawin, A. M. Z.; Lightfoot, P. *Dalton Trans.* **2003**, (5), 936-939. (b) Prakasha Reddy, J.; Foxman, B. M. *J. Mol. Struct.* **2008**, *890*, (1-3), 227-231. (c) Tan, J.-C.; Merrill, C. A.; Orton, J. B.; Cheetham, A. K. *Acta Mater* **2009**, *57*, (12), 3481-3496. (d) Videnova-Adrabinska, V.; Nowak, A. M.; Wilk, M.; Janczak, J.; Baran, J. *J. Mol. Struct.* **2011**, *996*, (1-3), 53-63.

(4) (a) Gandara, F.; de la Pena-O'Shea, V. A.; Illas, F.; Snejko, N.; Praserpio, D. M.; Gutierrez-Puebla, E.; Monge, M. A. *Inorg. Chem.* **2009**, *48*, (11), 4707-4713. (b) Kukovec, B. M.; Venter, G. A.; Oliver, C. L. *Cryst. Growth Des.* **2012**, *12*, (1), 456-465.

(5) Bailey, A. J.; Lee, C.; Feller, R. K.; Orton, J. B.; Mellot-Draznieks, C.; Slater, B.; Harrison, W. T. A.; Simoncic, P.; Navrotsky, A.; Grossel, M. C.; Cheetham, A. K. *Angew. Chem.-Int. Edit.* **2008**, *47*, (45), 8634-8637.

(6) (a) Harvey, H. G.; Slater, B.; Attfield, M. P. *Chem.-Eur. J.* **2004**, *10*, (13), 3270-3278. (b) Bernini, M. C.; de la Pena-O'Shea, V. A.; Iglesias, M.; Snejko, N.; Gutierrez-Puebla, E.; Brusau, E. V.; Narda, G. E.; Illas, F.; Monge, M. A. *Inorg. Chem.* **2010**, *49*, (11), 5063-5071.

(7) Beevers, C. A.; Hughes, W. *Nature* **1940**, *146*, 96-96.

(8) Valasek, J. *Phys. Rev.* **1921**, *17*, (4), 475-481.

(9) (a) Yanes, A. C.; Lopez, T.; Stockel, J.; Peraza, J. F.; Torres, M. E. *J. Mater. Sci.* **1996**, *31*, (10), 2683-2686. (b) Torres, M. E.; Lopez, T.; Peraza, J.; Stockel, J.; Yanes, A. C.; Gonzalez-Silgo, C.; Ruiz-Perez, C.; Lorenzo-Luis, P. A. *J. Appl. Phys* **1998**, *84*, (10), 5729-5732. (c) Kamba, S.; Kulda, J.; Petricek, V.; McIntyre, G.; Kiat, J. P. *J. Phys.-Condes. Matter* **2002**, *14*, (15), 4045-4055. (d) Torres, M. E.; Lopez, T.; Stockel, J.; Solans, X.; Garcia-Valles, M.; Rodriguez-Castellon, E.; Gonzalez-Silgo, C. *J. Solid State Chem.* **2002**, *163*, (2), 491-497. (e) Arora, S. K.; Patel, V.; Amin, B.; Kothari, A. *B. Mater Sci.* **2004**, *27*, (2), 141-147. (f) Dabhi, R. M.; Parekh, B. B.; Joshi, M. J. *Indian J Phys* **2005**, *79*, (5), 503-507. (g) Kumar, S.; Kaur, B.; Kotru, P. N.; Bamzai, K. K. *Ferroelectrics* **2006**, *332*, 167-185. (h) Kotru, P. N.; Want, B.; Ahmad, F. *Mat. Sci. Eng. A-Struct.* **2007**, *443*, (1-2). (i) Kumar, S.; Kaur, B.; Kotru, P. N.; Bamzai, K. K. *Ferroelectrics* **2007**, *350*, 5-21. (j) Want, B.; Ahmad, F.; Kotru, P. N. *J. Mater. Sci.* **2007**, *42*, (22), 9324-9330. (k) Want, B.; Ahmad, F.; Kotru, P. N. *Cryst. Res. Technol.* **2007**, *42*, (8), 822-828. (l) Firdous, A.; Quasim, I.; Ahmad, M. M.; Kotru, P. N. *B. Mater Sci.* **2010**, *33*, (4), 377-382.

(10) (a) Coronado, E.; Galan-Mascaros, J. R.; Gomez-Garcia, C. J.; Murcia-Martinez, A. *Chem.-Eur. J.* **2006**, *12*, (13), 3484-3492. (b) Lin, J.-D.; Long, X.-F.; Lin, P.; Du, S.-W. *Cryst. Growth Des.* **2009**.

(11) (a) Seo, J. S.; Whang, D.; Lee, H.; Jun, S. I.; Oh, J.; Jeon, Y. J.; Kim, K. *Nature* **2000**, *404*, (6781), 982-986. (b) Thushari, S.; Cha, J. A. K.; Sung, H. H. Y.; Chui, S. S. Y.; Leung, A. L. F.; Yen, Y. F.; Williams, I. D. *Chem. Commun.* **2005**, (44), 5515-5517. (c) Wu, C. D.; Hu, A.; Zhang, L.; Lin, W. B. *J. Am. Chem. Soc.* **2005**, *127*, (25), 8940-8941. (d) Au-Yeung, A. S. F.; Sung, H. H. Y.; Cha, J. A. K.; Siu, A. W. H.; Chui, S. S. Y.; Williams, I. D. *Inorg. Chem. Commun.* **2006**, *9*, (5), 507-511. (e) Vaidhyanathan, R.; Bradshaw, D.; Rebilly, J. N.; Barrio, J. P.; Gould, J. A.; Berry, N. G.; Rosseinsky, M. J. *Angew. Chem., Int. Ed.* **2006**, *45*, (39), 6495-6499.

(12) (a) Kam, K. C.; Young, K. L. M.; Cheetham, A. K. *Cryst. Growth Des.* **2007**, *7*, (8), 1522-1532. (b) Appelhans, L. N.; Kosa, M.; Radha, A. V.; Simoncic, P.; Navrotsky, A.; Parrinello, M.; Cheetham, A. K. *J. Am. Chem. Soc.* **2009**, *131*, (42), 15375-15386.
(13) Allen, F. *Acta Crystallogr., Sect. B: Struct. Sci.* **2002**, *58*, 380-388.
(14) Cheetham, A. K.; Rao, C. N. R.; Feller, R. K. *Chem. Commun.* **2006**, (46), 4780-4795.
(15) Stouten, P. F. W.; Verwer, P.; Vaneijck, B. P.; Kroon, J. *Acta Crystallogr., Sect. C: Cryst. Struct. Commun.* **1988**, *44*, 1961-1963.
(16) Bott, R. C.; Sagatys, D. S.; Smith, G.; Byriel, K. A.; Kennard, C. H. L. *Polyhedron* **1994**, *13*, (22), 3135-3141.
(17) Gelbrich, T.; Threlfall, T. L.; Huth, S.; Seeger, E.; Hursthouse, M. B. *Z. Anorg. Allg. Chem.* **2004**, *630*, (10), 1451-1458.
(18) Gelbrich, T.; Threlfall, T. L.; Huth, S.; Seeger, E. *Polyhedron* **2006**, *25*, (4), 937-944.
(19) (a) Forster, P. M.; Burbank, A. R.; Livage, C.; Férey, G.; Cheetham, A. K. *Chem. Commun.* **2004**, (4), 368-369. (b) Forster, P. M.; Stock, N.; Cheetham, A. K. *Angew. Chem., Int. Ed.* **2005**, *44*, (46), 7608-7611.
(20) Parr Instrument Company, 211 53rd St., Moline, Illinois 61265 USA.
(21) Hooft, R. W. W. *COLLECT data collection software*, Nonius B.V., **1998**.
(22) Duisenberg, A. J. M. *J. Appl. Crystallogr.* **1992**, *25*, 92-96.
(23) Otwinowski, Z.; Minor, W., In *Methods in Enzymology*, Carter, J., C. W.; Sweet, R. M., Eds. Academic Press: New York, **1997**; Vol. 276: Macromolecular Crystallography, Pt A., pp 307-326.
(24) Sheldrick, G. M. *SADABS: Version 2007/2*, Bruker AXS Inc., Madison, Wisconsin, USA, **2007**.
(25) *APEX2*, 2009.9; Bruker AXS Inc., Madison, Wisconsin, U.S.A., **2009**.
(26) Sheldrick, G. M. *Acta Crystallogr., Sect. A: Found. Crystallogr.* **2008**, *64*, 112-122.
(27) Brandenburg, K.; Putz, H. *Diamond*, 3.2; CRYSTAL IMPACT GbR, Bonn, Germany, **2009**.
(28) Macrae, C. F.; Edgington, P. R.; McCabe, P.; Pidcock, E.; Shields, G. P.; Taylor, R.; Towler, M.; van de Streek, J. *J. Appl. Crystallogr.* **2006**, *39*, 453-457.
(29) Perdew, J. P.; Burke, K.; Ernzerhof, M. *Phys. Rev. Lett.* **1996**, *77*, (18), 3865-3868.
(30) (a) Goedecker, S.; Teter, M.; Hutter, J. *Phys. Rev. B: Condens. Matter. Mater. Phys.* **1996**, *54*, (3), 1703-1710. (b) Krack, M. *Theor. Chem. Acc.* **2005**, *114*, (1-3), 145-152.
(31) VandeVondele, J.; Hutter, J. *J. Chem. Phys.* **2007**, *127*, (11).
(32) (a) Krack, M.; Parrinello, M. *Forschungszentrum Julich, NIC Series* **2004**, *25,* 29. (b) VandeVondele, J.; Krack, M.; Mohamed, F.; Parrinello, M.; Chassaing, T.; Hutter, J. *Comput. Phys. Commun.* **2005**, *167*, (2), 103-128.
(33) Grimme, S. *J. Comput. Chem.* **2006**, *27*, (15), 1787-1799.
(34) *IUPAC. Compendium of Chemical Terminology*. McNaught, A. D.; Wilkinson, A., Ed.; 2nd ed.; Blackwell Scientific Publications: Oxford, **1997**.
(35) Brese, N. E.; O'Keeffe, M. *Acta Crystallogr., Sect. B: Struct. Sci.* **1991**, *47*, 192-197.
(36) Janiak, A.; Rychlewska, U.; Kwit, M.; Stepien, U.; Gawronska, K.; Gawronski, J. *Chemphyschem* **2012**, *13*, (6), 1500-1506.
(37) (a) Chang, B. K.; Bristowe, N. C.; Bristowe, P. D.; Cheetham, A. K. *Phys. Chem. Chem. Phys.* **2012**, *14*, (19), 7059-7064. (b) Galvelis, R.; Slater, B.; Cheetham, A. K.; Mellot-Draznieks, C. *CrystEngComm* **2012**, *14*, (2), 374-378.
(38) Harding, M. *Acta Crystallographica Section D* **2000**, *56*, (7), 857-867.
(39) (a) Etter, M. C.; Macdonald, J. C.; Bernstein, J. *Acta Crystallogr. Sect. B-Struct. Commun.* **1990**, *46*, 256-262. (b) Bernstein, J.; Davis, R. E.; Shimoni, L.; Chang, N. L. *Angew. Chem.-Int. Edit.* **1995**, *34*, (15), 1555-1573.

(40) (a) Burke, N. J.; Burrows, A. D.; Mahon, M. F.; Pritchard, L. S. *CrystEngComm* **2003**, *5*, 355-357. (b) Jain, P.; Ramachandran, V.; Clark, R. J.; Zhou, H. D.; Toby, B. H.; Dalal, N. S.; Kroto, H. W.; Cheetham, A. K. *J. Am. Chem. Soc.* **2009**, *131*, (38), 13625-+. (c) Besara, T.; Jain, P.; Dalal, N. S.; Kuhns, P. L.; Reyes, A. P.; Kroto, H. W.; Cheetham, A. K. *Proc. Natl. Acad. Sci. U. S. A.* **2011**, *108*, (17), 6828-6832.

(41) Karamertzanis, P. G.; Day, G. M.; Welch, G. W. A.; Kendrick, J.; Leusen, F. J. J.; Neumann, M. A.; Price, S. L. *J. Chem. Phys.* **2008**, *128*, (24), 17.

(42) Steiner, T. *Angew. Chem.-Int. Edit.* **2002**, *41*, (1), 48-76.

(43) (a) Brown, K. A.; Martin, D. P.; LaDuca, R. L. *CrystEngComm* **2008**, *10*, (10), 1305-1308. (b) Wang, J.; Lin, Z. J.; Ou, Y. C.; Shen, Y.; Herchel, R.; Tong, M. L. *Chem.-Eur. J.* **2008**, *14*, (24), 7218-7235. (c) Farnum, G. A.; Martin, D. P.; Sposato, L. K.; Supkowski, R. M.; LaDuca, R. L. *Inorg. Chim. Acta* **2010**, *363*, (1), 250-256. (d) Banisafar, A.; LaDuca, R. L. *Inorg. Chim. Acta* **2011**, *373*, (1), 295-300.

(44) Yeung, H. H.-M.; Kosa, M.; Parrinello, M.; Forster, P. M.; Cheetham, A. K. *Cryst. Growth Des.* **2011**, *11*, (1), 221-230.

(45) Yeung, H. H. M. et al., manuscript in preparation

Chapter 4. Isostructural compounds and multi-component ligand solid solutions in the lithium succinate family

4.1. Introduction

4.1.1. *Isoreticular inorganic-organic frameworks*

MOF-5 is perhaps the most archetypal porous inorganic-organic framework, made of Zn_4O subunits connected by a 3-D array of 1,4-benzenedicarboxylate linkers.[1] Isoreticular materials can readily be made by substitution of the linkers by others of different length, with the overall framework topology remaining unchanged (Figure 1).[2] Other systems, such as zeolitic imidazolate frameworks, exhibit similar substitutions in which ligand substituents vary in chemical functionality or steric bulk, resulting in dramatic changes in pore geometry.[3] Indeed, different substituents can direct the formation of different framework topologies.[4] This has been one of major driving forces behind research into porous inorganic-organic frameworks, as it allows the pore volume, surfaces, and hence gas sorption properties to be tuned by varying the ligand. The resulting materials show remarkable diversity in both density and their interactions with guest molecules, offering potential in applications such as gas storage,[3, 5] catalysis,[6] sensors[7] and separations.[8]

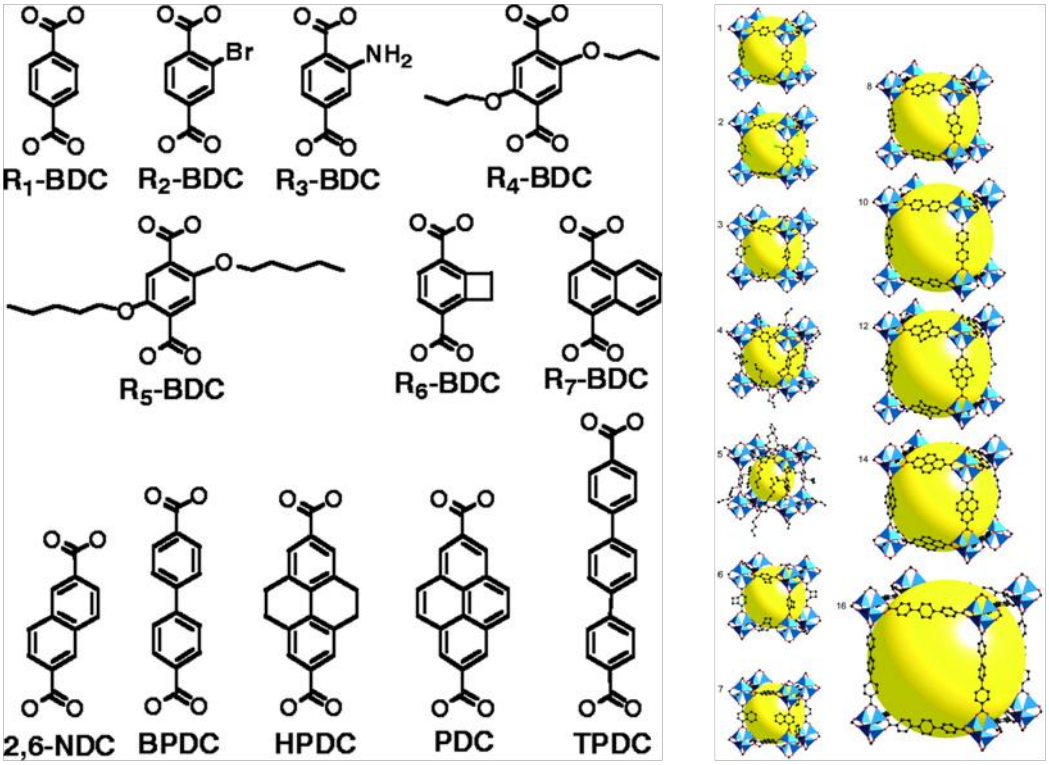

Figure 1. Ligands used in the synthesis of isoreticular materials IRMOF-1 to -16, with corresponding crystal structures shown right (omitting interpenetrated frameworks). Reproduced with permission,[2] copyright 2002 AAAS.

Isoreticular non-porous inorganic-organic frameworks are less prevalent in the literature, due to the lack of similar observations of ligand substitution in densely-packed materials. Isostructural compounds featuring different metal ions are common, due to similarities in size and preferred coordination geometry of certain transition metals[9] and alkaline earth metals.[10] Ligand substitution is less common, but can occur when the structure allows incorporation of longer ligands *via* increased separation of inorganic chains or layers. This is apparent in the increase in inter-chain distance from manganese adipate, $Mn(C_6H_8O_4)$, to manganese pimelate, $Mn(C_7H_{10}O_4)$,[11] and from cobalt glutarate, $Co(C_5H_6O_4)$,[12] to cobalt pimelate, $Co(C_7H_{10}O_4)$,[13] due to one and two additional (CH_2) units in the ligand alkyl chain, respectively. The separation between LiO antifluorite layers pillared by rigid ligands in the I^2O^1 framework[14] lithium (1,4-benzenedicarboxylate), $Li_2(C_8H_4O_4)$,[15] can be increased by replacing the ligand with napthalenedicarboxylate, ($C_{14}H_8O_4^{2-}$), which incorporates an extra conjugated benzene ring.[16] This has the additional beneficial effect of increasing the thermal stability from 500 °C to 610 °C.

Ligand substitution has not previously been reported in non-porous frameworks with 3-D inorganic connectivity, probably due to the supposed rigidity of the inorganic substructure and the absence of free space into which substituted ligands may be placed. The results presented in this chapter show that ligand substitution is in fact possible in lithium succinate, $Li_2(suc)$ (suc = $C_4H_4O_4^{2-}$), a non-porous framework with dimensionality I^3O^0. Flexibility of the ligand site allows complete substitution of the succinate moiety by ligands of a similar length (Figure 2), resulting in topologically similar structures with lattice parameters that depend on the ligand substituents involved.

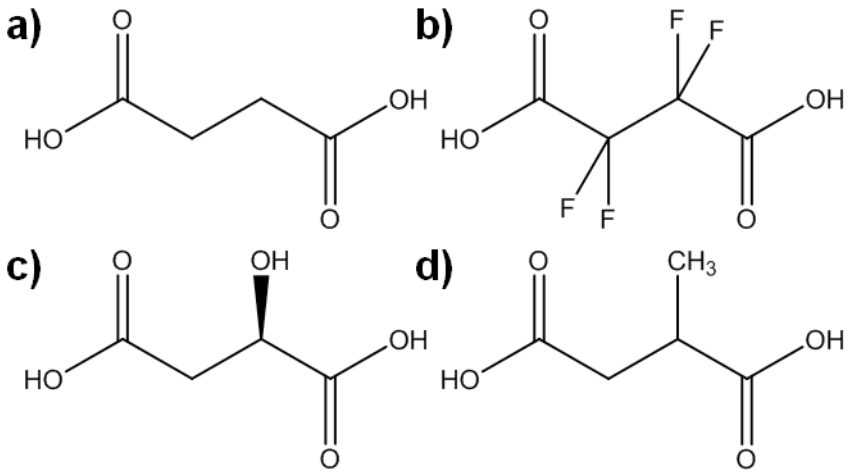

Figure 2. Molecular structures of selected C_4-ligands: a) succinic acid, b) tetrafluorosuccinic acid, c) L-malic acid, and d) methylsuccinic acid.

4.1.2. *Ligand substitution in inorganic-organic frameworks*

Metal or cation substitution is commonly used in metal alloys, metal oxides and other purely inorganic materials to tailor a wide range of properties such as mechanical strength,[17] hydrogen storage[18], ferroelectricity,[19] photocatalysis,[20] superconductivity,[21] phosphorescence,[22] ionic conductivity,[23] ion-exchange, molecular sieving and catalysis.[24] In such materials, generally speaking, the metal atoms are substituted, with charge balance achieved by incorporation of anionic (e.g. oxygen vacancies in $LaGaO_3$)[25] or cationic defects (e.g. interstitial protons or alkali metal cations in zeolites)[24] in the structure when necessary. Solid solutions are substituted materials in which the parent compounds are isostructural and there are often no phase transitions across the entire range of compositions between them. Such systems commonly adhere to Vegard's law, which is the empirical observation that cell parameters vary linearly with composition.[26] While the focus of most work in the area of inorganic-organic frameworks concerns well-ordered materials, disordered mixed-component MOFs have recently gained attention due to their ability to combine or enhance the interesting and useful properties of the constituent parts in a single crystalline phase.[27] Two broad classes of solid solution are recognised in hybrid framework materials: (i) systems in which the solid solution involves two different cations, e.g. $Ca_{1-x}Sr_x$(tartrate) in Figure 3,[10] and (ii) those in which two different ligands are present, e.g. $Al(OH)(bdc)_{1-x}(abdc)_x$ [(bdc) = benzene-1,4-dicarboxylate; (abdc) = 2-aminobenzene-1,4-dicarboxylate].[28] Due to geometrical considerations, examples of the former are likely to be quite common, but the latter has hitherto only been observed in porous or low-dimensional frameworks.[27a, 28-29]

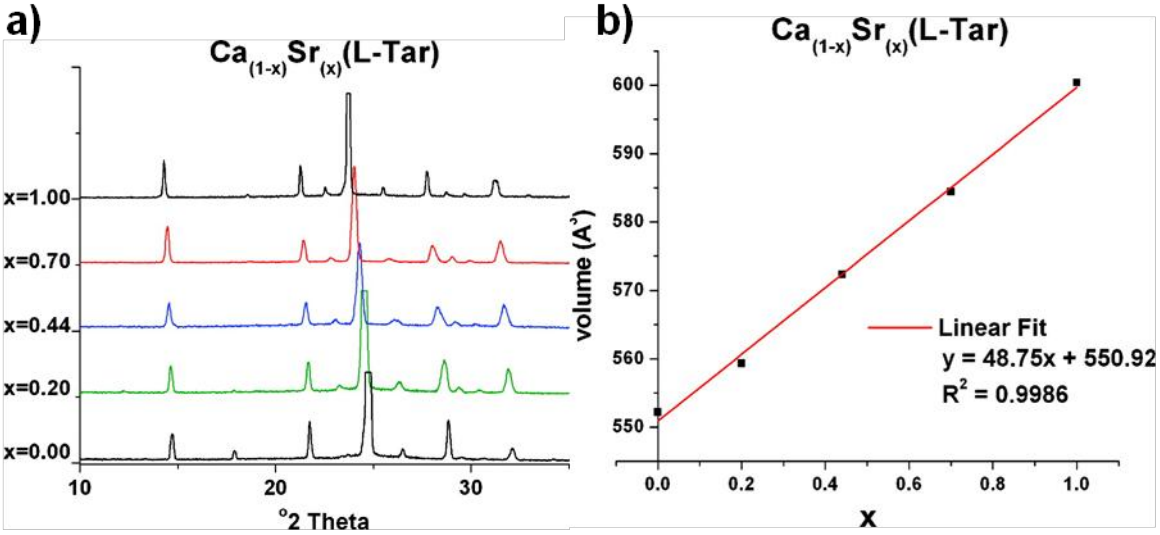

Figure 3. Mixed metal solid solutions in $Ca_{1-x}Sr_x$(L-tartrate): a) powder X-ray diffraction patterns showing variation in peak position with composition, and b) volume (calculated by Rietveld refinement) vs. composition (determined by ICP). Reproduced with permission,[10] copyright 2009 ACS.

Porous isoreticular MOFs based on the ubiquitous MOF-5 were shown by Deng *et al*. to incorporate many chemical functional groups in one crystalline phase by mixing ligands with different substituents.[27a] These so-called "multivariate MOFs" were synthesized using the same conditions as for the single-ligand phases but varying the ratios of different ligand precursor acids. Whilst in some cases this resulted in properties more than the linear sums of the pure components, for example 400 % better selectivity for carbon dioxide over carbon monoxide, control over stoichiometry was limited. A similar methodology was used by Marx *et al*., termed the "MIXMOF" concept, in investigation of the MIL-53(Al) structure.[28] Whilst the presence of varying amounts of both ligands was clearly shown by MAS-NMR and FTIR, powder X-ray diffraction could not conclusively demonstrate control over solid solution behaviour due to the peak broadening and overlap between phases of almost identical cell parameters. Synthesis of mixed-ligand variants of MOF-5 and demonstration of the dependence of catalyst loading[29e] and catalytic activity[29b] on ligand content were shown by the same group. A mixed-ligand phase of MIL-101(Fe) was post-synthetically modified by Taylor-Pashow *et al*., in order to include an optical contrast agent and an anticancer drug.[29a] However, problems were again encountered in confirmation of phase homogeneity.

The lattice metrics of perhalo-cobalt bipy (bipy = 4,4'-bipyridine) coordination polymers were demonstrated by Adams *et al*. to be finely controlled by variation in chloride : bromide

ratio.[29c] Although strictly speaking, the ligand varied in this case is not organic, the study shows a clear continuous variation in powder X-ray diffraction patterns and good stoichiometry control using either mechanochemistry or thermal elimination of HBr or HCl from the corresponding acid salt. Another successful attempt to control the stoichiometry in a mixed-ligand system was performed by Fukushima *et al*. when combining the interdigitated structures CID-5 and CID-6 (CID = coordination polymer with an interdigitated structure), which differ in the pendant ligand functional group (nitro- and methoxy-, respectively).[29d] Whilst a clear continuum of powder X-ray diffraction patterns is shown across the series, they admit that "the key for successful preparation of solid solutions in this system is that the unit cell parameters… are not markedly different, and there would be little stress in the crystal, even if the two types of ligand are mixed with arbitrary ratios".[29d] This leaves some doubt about the conclusions of the powder X-ray diffraction analysis, since peak overlap from phases with different compositions could mask biphasic behaviour, and it also suggests a limitation in the types of inorganic-organic systems available for manipulation by solid-solutions.

The results presented in this chapter demonstrate that ligand solid solutions are in fact possible between inorganic-organic frameworks with very different cell parameters. High resolution synchrotron powder X-ray diffraction was used to show a linear change in unit cell volume between the parent compounds Li_2(suc) and lithium tetrafluorosuccinate, Li_2(flu), which have cell volumes of 1330 $Å^3$ and 1424 $Å^3$, respectively. In addition, the ternary system between Li_2(suc), lithium L-malate, Li_2(mal), and lithium methylsuccinate, Li_2(met), and the binary system between Li_2(mal) and lithium fumarate, Li_2(fum), also display noticeable variation in lattice parameters. What is remarkable is that all compounds involved are non-porous, I^3O^0 frameworks involving a range of substituent functional groups.

4.1.3. *Lithium succinate*

The structure of Li_2(suc) was reported by Klapper and Kuppers in 1973.[30] It is a three-dimensional I^3O^0 inorganic-organic framework in which the ligand bridges the edge- and corner-sharing LiO_4 tetrahedra (Figure 4a). It adopts the centrosymmetric space group *R*$\bar{3}$, and has small, inaccessible cavities that can be seen when viewed down the *c*-axis (Figure 4b).

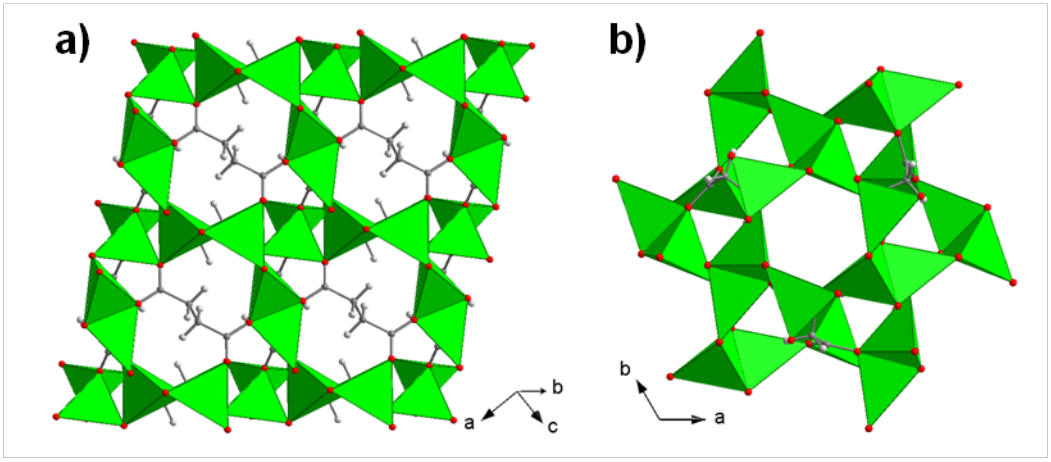

Figure 4. Structure of lithium succinate, a) showing the connectivity between the organic and inorganic parts, and b) showing the inaccessible cavities viewed down the c-axis. C, H and O atoms and LiO_4 tetrahedra are shown in grey, white, red and green, respectively.

Calculation of pore volume in PLATON[31] reveals that the cavities in Li_2(suc) take up just 2% of the crystal structure, which is too small to accommodate any small molecules and so there are no pathways for diffusion of species such as lithium cations through voids in the framework. This indicates that Li_2(suc) is probably an ionic insulator. Due to its wide band gap, Li_2(suc) is also an electronic insulator. Whilst low electronic conductivity is desirable in order to function effectively as a potential solid electrolyte, the ionic conductivity must be increased. However, the presence of the flexible ligand, a relatively open structure lacking solvent molecules and extended Li-O-Li connectivity make it a candidate material for manipulation to make a solid electrolyte. Further promise for this application arises from the work of Augustsson *et al.*, who suggested that Li_2(suc) may already occur in lithium batteries.[32] Soft X-ray spectroscopy was used to identify the constituents of the solid electrolyte interphase in electrochemically cycled cells and gave evidence for formation of Li_2(suc) as well as other lithium carboxylate species.

The flexible nature of succinic acid may give some chance to increase ionic conductivity through distortion of the Li_2(suc) framework structure, which could assist the passage of lithium ions from one site to the next. Furthermore, this work shows that flexibility of the ligand site in Li_2(suc) also allows substitution of the succinate moiety by related ligands (Figure 2), which may help to alter the structure for enhancement of lithium transport properties. In addition, variable amounts of different ligands can be present in the same crystalline phase in solid solution, giving further opportunity to optimise the structure and resulting properties.

4.1.4. *Mechanosynthesis as a way to create disorder in non-porous inorganic-organic frameworks*

Forming a mixed-ligand solid solution in a dense, non-porous hybrid framework is a non-trivial task because of the apparent lack of space for bulky substituents. However, if the composition of a mixed-ligand system can be controlled, precise tuning of the framework architecture and optimisation of the material's properties should be possible. This requires the framework to be flexible and spacious enough to accommodate new moieties and the reactivity, solubility and geometry of the different components to be similar, allowing them to combine homogeneously with the desired stoichiometry. In solution, ligands with different functionality also react at varying rates and show different preferences for forming a given hybrid framework structure, resulting in a lack of direct control of the product stoichiometry and homogeneity as discussed above.

Mechanochemistry is one possible solution that was investigated in order to gain control over product stoichiometry and homogeneity. It involves grinding solid reagents within a mill, together with one or more ball-bearings that exert the mechanical force required to drive a chemical reaction. When small quantities of a liquid are used to aid synthesis kinetics, it is known as liquid-assisted grinding,[33] and it has been widely used in the synthesis of organic cocrystals.[34] Due to the self-contained reaction conditions and absence of significant volumes of solvent, mechanochemistry can lead to near-quantitative yields and was shown by Adams *et al*. to give fine control over the stoichiometry of a mixed-ligand inorganic-organic framework system.[29c] More recently, liquid-assisted grinding has been shown to be a facile way to synthesize inorganic-organic frameworks, such as zeolitic imidazolate frameworks[33b] and solvent-free mechanochemical conditions can be used to amorphize the same materials.[35] We expect that the relatively dry conditions in the grinding process, along with the constant breaking and reforming of particulates (presumably by breaking and reforming of chemical coordination bonds), may enable kinetic stabilisation of disordered mixed ligand phases with high homogeneity.

4.1.5. *Mechanical properties of inorganic-organic frameworks*

Knowledge of the mechanical properties of inorganic-organic frameworks is essential for successful applications, due to the various mechanical stresses that may act on the materials in devices and technologies.[36] For example, MOFs must be robust enough to withstand hydrostatic compression in gas sorption applications and thermal expansion in high

temperature catalysis in order to avoid structural distortion and degradation in their properties.[37] Stiffness, shear modulus and adhesion strength are critical in applications such as actuator and sensor coatings, in which the material's response to cyclic stresses must not vary with time.[38] However, the mechanical properties of inorganic-organic frameworks have only recently begun to be explored. In the few studies available, both experimental (nanoindentation, atomic force microscopy, high pressure X-ray crystallography etc.) and computational approaches (density functional theory and molecular dynamics) have been used to probe intrinsic structure-property relationships in both porous and non-porous hybrid frameworks. In porous hybrids, elastic properties have been found to depend on density, solvent-accessible volume and host-guest interactions[39] and are highly anisotropic due to the directionality of rigid organic linkers.[40] In additional, short-range ligand-ligand interactions[39] and cation-dependent rigidity of ligand-metal-ligand units[41] are responsible for stiffening in topologically similar porous frameworks.

The densely packed framework systems studied previously have been isolated materials[42] or polymorphs with different structures.[43] Both have the limitation that the frameworks' mechanical properties can only be investigated as a comparison between structural elements of individual systems, rather than trends across different ones. In addition, whilst the trends within each system may be clear, a general picture of the relative influence of different structural features on mechanical properties is not. For example, in the copper phosphonoacetate polymorphs studied by Tan *et al.*, elastic moduli are largest along crystallographic directions dominated by the inorganic chains or sheets, and smallest where organic connectivity dominates.[43] In cerium oxalate formate, $Ce(C_2O_4)(HCO_2)$, it is the rigid organic oxalate moieties that impart more stiffness than the inorganic chains or more compliant formate ligands (Figure 5).[42a] In contrast, in the experimental and computational study of zinc phosphate phosphonoacetate hydrate, $Zn_3(PO_4)(O_2CCH_2PO_3)(H_2O)$, the mechanical properties are best related to the orientation of the small, elliptical cavity within the structure.[42b] These studies show that mechanical properties of different inorganic-organic frameworks are complex and highly dependent on the intricacies of the structure in question. Further studies are necessary to expand understanding and to form a general picture of mechanical properties of inorganic-organic frameworks.

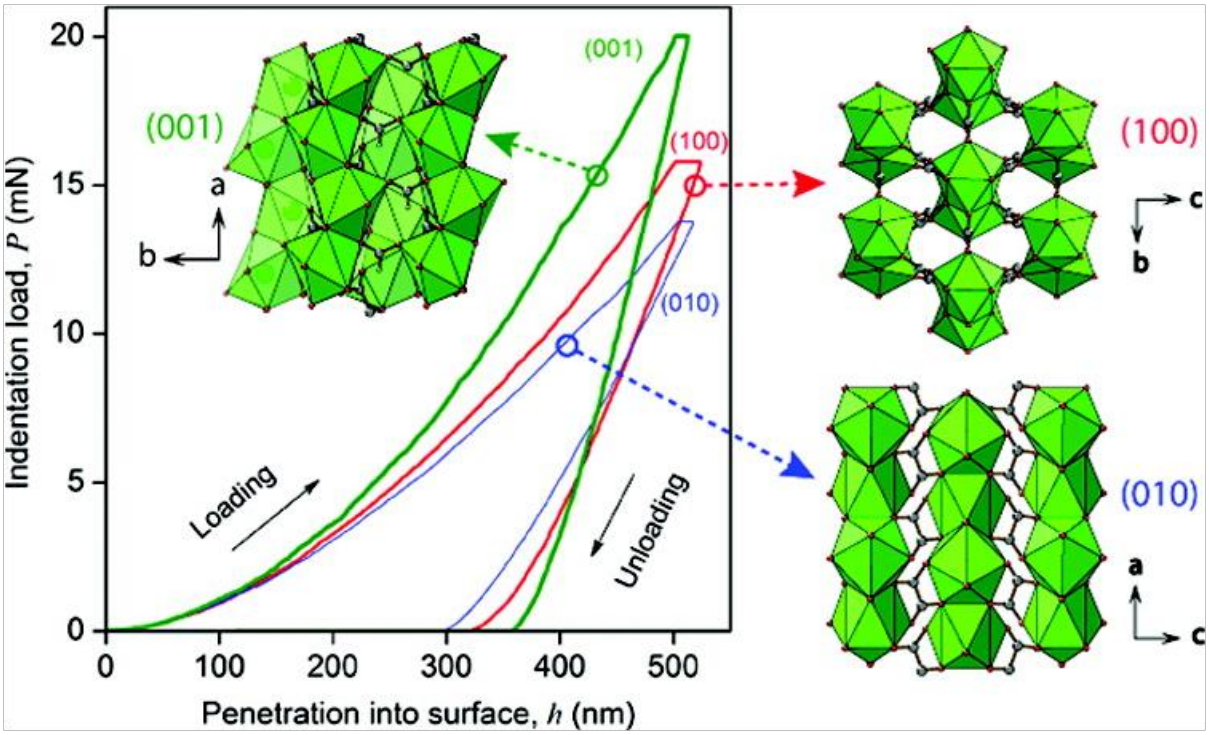

Figure 5. Load-displacement (P-h) curves obtained from the three main crystallographic orientations of $Ce(C_2O_4)(HCO_2)$ and their corresponding structural representations. Reproduced with permission,[42a] copyright 2009 ACS.

The family of frameworks investigated in this chapter provides an ideal opportunity to extend understanding of mechanical properties of inorganic-organic frameworks. All the frameworks have the same topology and 3-D inorganic connectivity, and so trends in mechanical properties can be examined solely as a function of local structure, such as inter-ligand interactions and Li-O bond strength, because the bulk structural features are essentially constant.

4.2. Experimental

4.2.1. *Synthesis*

All reagents, tetrafluorosuccinic acid (99 %, TCI), L-malic acid (99 %, Fisher), succinic acid (99 %, Sigma), R-methylsuccinate (>97.0 %, TCI), lithium acetate dihydrate (98 %, Acros), lithium oxide (99.5 % metals basis, VWR) and lithium hydroxide monohydrate (99 %, Fisher), were bought and used as received. Methanol and absolute ethanol (both Fisher) and in-house deionised water were used as solvents. Crystallizations were performed in 4 - 20 ml PTFE-capped borosilicate glass vials. Mechanochemical reactions were performed using a Retsch Mixer Mill MM400[44] equipped with stainless steel jars manufactured in-house. In these reactions an excess of 10 wt.% lithium oxide of was used to compensate for a decrease in gross lithium content due to its hygroscopic nature. Solvothermal reactions were carried out in 23 ml PTFE-lined stainless steel autoclaves purchased from Parr Instrument Company.[45]

4.2.1.1. Synthesis of lithium succinate, $Li_2(suc)$, $Li_2(C_4H_4O_4)$

Succinic acid (1 mmol) was dissolved in water:ethanol (1:9, 5 ml), lithium acetate dihydrate (2 mmol) was dissolved in water ethanol (1:4, 5 ml) and the solutions combined in a PTFE-capped borosilicate glass vial at 70 °C. After 8 days, colourless blocks had formed on the vial sides. The product, $Li_2(suc)$ (47 mg, 36 %), was filtered, washed in methanol and dried in air at 70 °C overnight. Elemental analysis: C 36.90 %, H 3.04 %, N 0.0 % (calculated for $C_4H_4Li_2O_4$: C 36.97 %, H 3.10 %, N 0.0 %).

4.2.1.2. Synthesis of lithium tetrafluorosuccinate, $Li_2(flu)$, $Li_2(C_4F_4O_4)$

Tetrafluorosuccinic acid (0.5 mmol) and lithium hydroxide monohydrate (1.0 mmol) were dissolved in water (0.4 ml) and the solution was placed in a PTFE-capped borosilicate glass vial at 70 °C. After 12 days, colourless blocks had formed on the vial sides. The product, $Li_2(flu)$ (82 mg, 81 %) was filtered, washed in methanol and dried in air at 70 °C overnight. Elemental analysis: C 23.55 %, H 0.12 %, N 0.0 % (calculated for $C_4F_4Li_2O_4$: C 23.79 %, H 0.0 %, N 0.0 %).

4.2.1.3. Synthesis of lithium L-malate, $Li_2(mal)$, $Li_2(C_4H_4O_5)$

L-malic acid (1 mmol) was dissolved in water:ethanol (1:9, 5 ml), lithium acetate dihydrate (2 mmol) was dissolved in water ethanol (1:4, 5 ml) and the solutions combined in a

PTFE-capped borosilicate glass vial at 70 °C. After 8 days, colourless blocks had formed on the vial sides. The product, $Li_2(mal)$ (56 mg, 38 %), was filtered, washed in methanol and dried in air at 70 °C overnight. Elemental analysis: C 32.99 %, H 2.64 %, N 0.0 % (calculated for $C_4H_4Li_2O_5$: C 32.92 %, H 2.76 %, N 0.0 %).

4.2.1.4. Synthesis of lithium methylsuccinate, $Li_2(met)$, $Li_2(C_5H_6O_4)$

R-methylsuccinic acid (1 mmol) and lithium hydroxide monohydrate (2 mmol) were dissolved in water (0.4 ml) and the resulting solution was filtered through cotton wool into a PTFE-lined stainless steel autoclave. It was heated at 150 °C for one week, after which it was cooled to room temperature and immediately opened. The product, a colourless precipitate covered in a dark brown film, was observed to contain triangular crystals suitable for single crystal X-ray diffraction studies. A bulk sample was synthesized as follows: a solution of R-methylsuccinic acid (1 mmol) in ethanol (5 ml) was combined with a solution of lithium acetate dihydrate (2 mmol) in ethanol (5 ml) in a PTFE-lined stainless steel autoclave. It was heated at 150 °C for three days, after which it was cooled naturally to room temperature and the resulting white powder (102 mg, 71 %) was filtered, washed in ethanol and dried at 60 °C in air overnight. Elemental analysis: C 39.18 %, H 4.40 %, N 0.0 % (calculated for $C_5H_6Li_2O_4$: C 41.71 %, H 4.20 %, N 0.0 %), suggesting some residual water in the sample.

4.2.1.5. Synthesis of $Li_2(suc)_{1-x}(flu)_x$

A series of compounds with nominal composition (from reactant ratios) $Li_2(suc)_{1-x}(flu)_x$ [x = 0, 0.2… 1] was synthesized by mechanochemical methods. Typically, lithium oxide (1.1 mmol), succinic acid and tetrafluorosuccinic acid (combined amount 1 mmol) were placed in a stainless steel grinding jar with two 8 mm diameter stainless steel balls. The mixture was ground for 30 minutes in the mixer mill at 25 Hz, yielding a grey powder (80-95 %), which was dried at 100 °C overnight.

4.2.1.6. Synthesis of $Li_2(suc)_x(mal)_y(met)_z$

A series of compounds, with nominal composition $(Li_2(suc)_x(mal)_y(met)_z$ [$x + y + z = 1$; x, y, z = 0.0, 0.2, 0.33, 0.4, 0.5, 0.6, 0.8, 1.0] was synthesized by mechanochemical combination of stoichiometric amounts of the pure end-members, which were synthesized by solvothermal methods. Typically, lithium acetate dihydrate (2.0 mmol) was dissolved in ethanol (5 ml) and combined with a solution of the desired acid (1.0 mmol) in ethanol (5 ml). The resulting mixture was heated at 150 °C for three days, before cooling to room temperature, filtering,

washing (ethanol) and drying in air at 70 °C overnight, to yield white powder (50-80 % yield). The end-members were placed according to the desired stoichiometry in a stainless steel grinding jar with two 8 mm diameter stainless steel balls. The mixture was ground for 30 minutes in the mixer mill at 25 Hz, yielding a fine white powder (85-95 %).

4.2.1.7. Thermal transformation of lithium L-malate to lithium $(L\text{-malate})_{1-x}(fumarate)_x$

Single crystals of lithium L-malate (100 mg), prepared using the procedure described in Section 4.2.1.3, were heated to 320 °C in a box furnace for 22 hours, before cooling slowly to room temperature with the furnace closed. Upon examination, the original material had cracked into smaller crystals (87.3 mg), but the crystal quality was retained. Suitable crystals were selected for single crystal X-ray diffraction studies, which showed its composition to be $Li_2(L\text{-malate})_{0.23}(fumarate)_{0.77}$. Similar heat treatments were performed at different temperatures and times, yielding single crystals with different ligand ratios, which were used for single crystal X-ray diffraction.

4.2.2. *Single crystal X-ray diffraction*

Crystal structure determination by X-ray diffraction was performed as described in Chapter 2.

4.2.3. *High resolution synchrotron powder X-ray diffraction*

High resolution synchrotron X-ray powder diffraction was performed using beamline I11 at the Diamond Light Source as described in Chapter 2.

4.2.3.1. Rietveld refinement of $Li_2(suc)_{1-x}(flu)_x$

Rietveld refinement was performed using the single crystal structure of $Li_2(flu)$ as a starting point to obtain accurate cell parameters, atomic positions and isotropic displacement parameters. The background function was modelled by a shifted Chebyshev function of 16-24 terms, which was refined in later cycles. Peak profiles were modelled using GSAS profile function 2, with U, V, W, X, Y and Lorentzian anisotropic broadening coefficient, X_e, the refined parameters. Hydrogen atoms were inserted at 1/1.4 the C-F distances and their position shifts and isotropic displacement parameters constrained to match those of the corresponding C atom. The H and F site occupancies were constrained to add up to unity, initially fixed at the nominal fractions and then refined in later cycles. Atomic positions and isotropic displacement parameters of all non-hydrogen atoms were refined.

4.2.3.2. Le Bail refinement of $Li_2(suc)_x(mal)_y(met)_z$

Le Bail fitting was used to obtain accurate lattice parameters for all phases in the ternary system $Li_2(suc)_x(mal)_y(met)_z$. The background function was modelled by a shifted Chebyshev function of 20 terms, which was refined in later cycles. Peak profiles were modelled using GSAS profile function 2, with U, V, W, X, Y and Lorentzian anisotropic broadening coefficient, X_e, the refined parameters. Cell parameters were refined using those of $Li_2(suc)$ as a starting point.

4.2.4. *Solid state magic angle spinning nuclear magnetic resonance spectroscopy*

^{13}C-[^{1}H]-cross polarization magic angle spinning nuclear magnetic resonance, CPMAS NMR, spectra were measured by Dr. Thomas Koester on a Bruker Avance spectrometer at resonance frequencies of 100.70 MHz and 400.42 MHz, for ^{13}C and ^{1}H, respectively. All CPMAS spectra were obtained using a spinning speed of 5000 Hz and proton decoupling with a 4 mm NMR probe. For the variable contact time experiments, contact times between 250 μs and 7 ms were used. For the CPMAS spectra of the compounds in the $Li_2(suc)_x(mal)_y(met)_z$ system, contact times of 1.0 ms were used. Typically, 512 or 1024 free induction decays were accumulated with a repetition time of 10 s.

4.2.5. *Solution nuclear magnetic resonance spectroscopy*

Li_2(L-malate)$_{0.23}$(fumarate)$_{0.77}$ (30 mg) was dissolved in D_2O (0.75 ml) and filtered through cotton wool into a 5 mm Wilmad 528-PP NMR tube. ^{13}C and ^{1}H Spectra were run by the NMR service at the University of Cambridge Chemical Laboratory.

4.2.6. *Scanning electron microscopy*

Scanning electron micrographs were taken using a JEOL 6340F FEGSEM under high vacuum with secondary electron imaging. Powder samples were placed in a thin layer on carbon tape, which was attached to an aluminium stub. The sample was sputtered with gold for 1-2 minutes under an argon atmosphere to reduce charging effects in the microscope.

4.2.7. *Nanoindentation*

Nanoindentation was performed at ambient temperature by Dr. Wei Li using an MTS NanoIndenter® XP.[46] Two types of diamond indenter tips were used: 1) A sharp three sided pyramidal Berkovich tip (tip radius ~100 nm) was used to determine the elastic modulus (*E*)

and hardness (H), and 2) a blunt spherical tip (tip radius ~10 μm) was used to extract the elastic-plastic transition and to study the creep behaviour.[43]

The nanoindentation experiments were performed on 0 1 $\bar{1}$-type facets of each framework, using both a quasi-static (load-controlled) module and a continuous stiffness measurement (CSM) module. Measurement of the E and H, and elastic-plastic transition properties were performed under the CSM mode by superimposing a 2 nm sinusoidal displacement at 45 Hz onto the primary loading with Berkovich and spherical tips, respectively. Loading and unloading strain rates of 0.05 s^{-1} were used and the indenters were held for 30 s prior to unloading in order to minimize the influence of creep. Creep experiments were performed using a spherical tip under quasi-static mode with fixed load of 60 mN, and the indenter was held for 1200 s in order to maximize creep effects.

The E and H were calculated as a function of surface penetration depth (h) using the dynamic CSM mode. This was accomplished by continuous monitoring of the change of the elastic contact stiffness (S) determined from gradient of the load-displacement curves, followed by extraction of the reduced modulus (E_r):[47]

$$E_r = \frac{\sqrt{\pi}}{2\beta}\frac{S}{\sqrt{A_c}}$$

where A_c is the contact area under load (based on the calibrated tip area function) and β is a constant that depends on the geometry of the indenter (β = 1.034 for a Berkovich tip). The method proposed by Oliver and Pharr[48] to extract E from E_r assumes isotropic elastic properties, which is normally not the case for single crystals. To account for the effects of anisotropy in single crystals, it has been shown[47a, 49] that the modulus obtained from nanoindentation of a single crystal is more appropriately represented as an ‘‘indentation modulus”, given by:

$$\frac{1}{E_r} = \frac{1-v_i^2}{E_i} + \frac{1-v_s^2}{E_s}$$

where v is the Poisson’s ratio and the subscripts i and s refer to the indenter and test material, respectively. The indenter properties used in this study were E_i = 1141 GPa, and v_i = 0.07. In this work, the elastic moduli from the 0, 1, $\bar{1}$ facets of Li_2(suc), Li_2(flu) and Li_2(mal) were calculated using v_s = 0.3.

The hardness of a material is defined as its resistance to local plastic deformation. Thus, indentation hardness, H, can be determined from the indentation load, P, divided by the contact area, A_c:

$$H = \frac{P}{A_c}$$

where A_c is a function of the contact depth, h_c, and can be determined by the following equation:

$$A_c(h_c) = C_0 h_c^2 + C_1 h_c + C_2 h_c^{1/2} + C_3 h_c^{1/4} + \cdots + C_8 h_c^{1/128}$$

where C_0 - C_8 are constants. It may be noted that if it is assumed that a Berkovich indenter has a perfect tip, only C_0 is used. However, for imperfect tips, higher-order terms have to be taken into account and these are obtained from the tip-area function curve fit for a given tip.

The contact depth is estimated from the load-displacement data using the equation:

$$h_c = h_{max} - 0.75\frac{P}{S}$$

where h_{max} is the maximum indentation depth and $0.75(P/S)$ denotes the extent of elastic recovery (h_e).

The yield stress, σ_y, was estimated from the plot of indentation stress, $\sigma = P / A$, versus indentation strain, $\varepsilon = a / R$(where a = contact radius and R = tip radius), by extrapolation of the elastic and plastic regions. Linear regression on the selected data was used to fit straight lines in the two regions, the intersection of which gave a value for σ_y.

4.3. Results

4.3.1. *Parent compounds*

The structures of three new compounds- lithium tetrafluorosuccinate, Li_2(flu), lithium L-malate, Li_2(mal), and lithium methylsuccinate, Li_2(met) -have been determined by single crystal X-ray diffraction at 120(2) K. The structure of lithium succinate, Li_2(suc), in the achiral space group *R*$\bar{3}$ previously reported at ambient temperature,[30] was also re-determined at 120(2) K for better comparison of its atomic structure with the others. Li_2(flu) and Li_2(met) are found to be isostructural with Li_2(suc). Li_2(mal) is almost isostructural with Li_2(suc), having the same inorganic connectivity, but it takes the chiral space group *R*3 and the whole ligand features in the asymmetric unit. Variations in the unit cell, ligand conformation and lithium coordination sphere have been explained by the effects of the different ligand substituents on the structure. It was found that the major variations are a result of the steric size, hydrogen bonding propensity and electronegativity of the ligand substituents. Relevant details of the structure determinations are shown in Table 1.

4.3.1.1. Single crystal structure of lithium succinate, Li_2(suc), $Li_2(C_4H_4O_4)$, at 120 K

The single crystal structure of Li_2(suc) has been previously reported at ambient temperature and it was found to change little with decreasing temperature in this study.[30] For the purposes of comparison with other materials, the relevant features of the structure at 120(2) K, some of which were given less importance in the original publication, are discussed here.

The asymmetric unit of Li_2(suc) consists of half of one ligand and one lithium atom (Figure 6). Each ligand carboxylate group binds to four lithium atoms: O1 bridges between two corner-sharing lithium atoms and O2 bridges between two edge-sharing ones. Each oxygen atom exhibits both *syn* and *anti* lithium binding conformations (Figure 7).[50] The carboxylate groups are almost perpendicular to the C_4 backbone (O1-C1-C2-C2 91.75(14)°) and, due to inversion symmetry, the ligand C_4 backbone torsion angle is 180°. The lithium atom coordination environment is a distorted tetrahedron, with Li-O distances ranging from 1.939(2) Å to 1.960(2) Å and angles between 87.86(8)° and 123.77(11)°. This gives rise to a bond valence sum[51] of 1.08 and a root mean squared angle deviation from the ideal tetrahedral angle, δ_{tet},[52] of 10.89°. Overall, the structure is an I^3O^0 framework, with small cavities that can be seen when viewed down the *c*-axis, as shown in Figure 4.

	Lithium succinate	Lithium tetrafluorosuccinate	Lithium L-malate	Lithium methylsuccinate
crystal size (mm)	0.4 × 0.35 × 0.3	0.15 × 0.1 × 0.1	0.3 × 0.3 × 0.3	0.15 × 0.15 × 0.03
crystal system	trigonal	trigonal	trigonal	trigonal
space group	*R*3	*R*3	*R*3	*R*3
T (K)	120(2)	120(2)	120(2)	120(2)
a (Å)	12.0600(8)	12.4291(5)	11.8771(11)	12.1272(13)
b (Å)	12.0600(8)	12.4291(5)	11.8771(11)	12.1272(13)
c (Å)	10.5752(5)	10.6013(4)	10.7193(10)	10.8023(12)
α (°)	90	90	90	90
β (°)	90	90	90	90
γ (°)	120	120	120	120
V (Å^3)	1332.03(14)	1418.3(10)	1309.5(2)	1375.8(3)
asym. unit	C_2 H_2 Li O_2	C_2 F_2 Li O_2	C_4 H_4 Li_2 O_5	$C_{2.5}$ H_3 Li O_2
Z	9	9	9	9
d_{calc} (g cm^{-3})	1.458	2.128	1.666	1.564
λ (Å)	0.71073	0.71073	1.54180	1.54180
μ (mm^{-1})	0.124	0.245	1.302	1.100
refl. collected	2102	1121	2219	818
unique refl.	710	716	1093	550
observed data (I > 2σ(I))	609	557	1060	492
parameters	54	64	111	70
R_{int}	0.0217	0.0179	0.0173	0.0259
R_1	0.0330	0.0453	0.0412	0.0541
wR_2 (I > 2σ(I))	0.0836	0.0751	0.1134	0.1420
R_1 (all data)	0.0410	0.0563	0.0419	0.0593
wR_2 (all data)	0.0914	0.0858	0.1140	0.1465
GOF	1.056	1.060	1.088	1.073

Table 1. Single crystal structure determination parameters for lithium succinate, lithium tetrafluorosuccinate, lithium L-malate and lithium methylsuccinate.

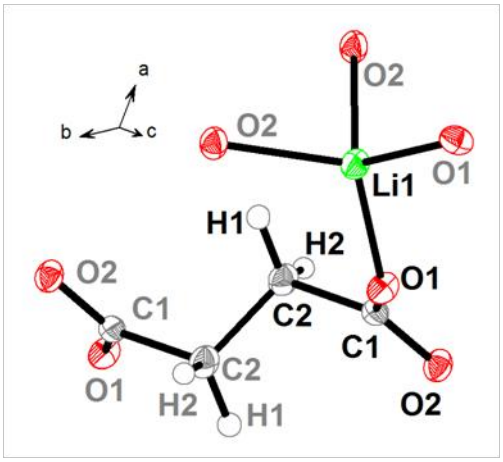

Figure 6. Ortep extended asymmetric unit of lithium succinate, showing atoms necessary to complete one ligand and the coordination environment of the lithium atom. C, H, Li and O atoms are shown in grey, white, green and red, respectively. Additional atoms are labelled in grey.

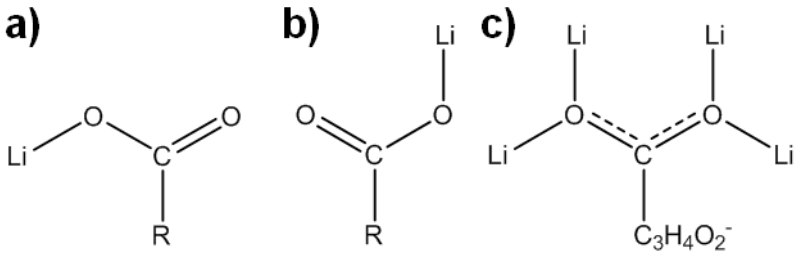

Figure 7. Common binding modes between lithium and carboxylate groups: a) anti conformer, b) syn conformer, and c) binding in lithium succinate. R represents the remaining ligand functionality.

4.3.1.2. Single crystal structure of lithium tetrafluorosuccinate, Li_2(flu), $Li_2(C_4F_4O_4)$

The asymmetric unit of Li_2(flu) contains half of one tetrafluorosuccinate ligand and one lithium atom (Figure 8). As in Li_2(suc), the ligand carboxylate groups are essentially perpendicular to the carbon chain (O1-C1-C2-C2 torsion angle 89.9(2)°) and, due to crystallographic symmetry the ligand C1-C2-C3-C4 torsion angle is 180°. The lithium atom coordination tetrahedron is more distorted than in Li_2(suc), with Li - O distances ranging from 1.951(4) Å to 2.020(4) Å and angles between 87.71(14)° and 128.8(2)°. This gives rise to a reduced bond valence sum, 0.99, and an increased δ_{tet}, 12.90°.

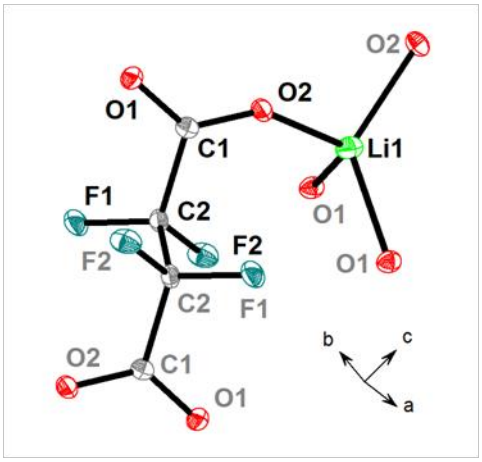

Figure 8. Ortep extended asymmetric unit of lithium tetrafluorosuccinate, showing atoms necessary to complete one ligand and the coordination environment of the lithium atom. C, F, Li and O atoms are shown in grey, turquoise, green and red, respectively. Additional atoms are labelled in grey.

Perfluorination is known to alter the conformational behaviour and non-bonding and bonding interactions of ligands,[53] and so it is common for perfluorinated ligands to form entirely different framework structures to their hydrogenated counterparts. Notably, the lowest energy conformation of tetrafluorosuccinic acid, H_2(flu) was calculated by Friscic *et al.* as having an angle of 80° between planes of the carboxylate groups and the carbon chain.[53b] In contrast, this is close to the metastable conformation of succinic acid, H_2(suc) (70°), for which the most stable conformation has a corresponding angle of 180°.[53b] Therefore, it may be somewhat unexpected that H_2(flu) forms a phase isostructural with its hydrogenated counterpart. However, in the lithium-based framework Li_2(suc) the relevant angle, 88.6(2)°, is closer to that preferred by the fluorinated ligand, making it easier for this architecture to incorporate the tetrafluorosuccinate moiety.

4.3.1.3. Single crystal structure of lithium L-malate, Li_2(mal), $Li_2(C_4H_4O_5)$

The single crystal structure of Li_2(mal) is almost isostructural with Li_2(suc); however, the asymmetric unit consists of one whole ligand and two lithium atoms (Figure 9). In addition, the presence of the single enantiomer of L-malic acid, which did not racemize *in-situ*, confirms that the resulting structure is chiral and adopts the space group *R*3, unlike the other parent phases which adopt $R\bar{3}$. The ligand hydroxyl group is disordered between two chirally equivalent positions, O5A (82.7(9) % occupancy) points into the cavity and O5B (17.3(9) %) is located closer to the inorganic framework. As in Li_2(suc), the C_4 torsion angle of Li_2(mal) is almost linear (C1-C2-C3-C4 179.8(3)°), but the carboxylate groups deviate slightly from

perpendicular, particularly away from the hydroxyl group of major occupancy (O1-C1-C2-C3 93.5(3)°; C2-C3-C4-O3 73.1(3)°). The lithium coordination spheres of Li_2(mal) are distorted tetrahedra, with bond distances and O-Li-O angles in the ranges 1.919(5) - 1.969(6) Å and 88.2(2) - 127.1(3)°, respectively. This gives rise to an average bond valence sum of 1.09, almost identical to that of Li_2(suc), and a slightly lower δ_{tet}, 10.59°.

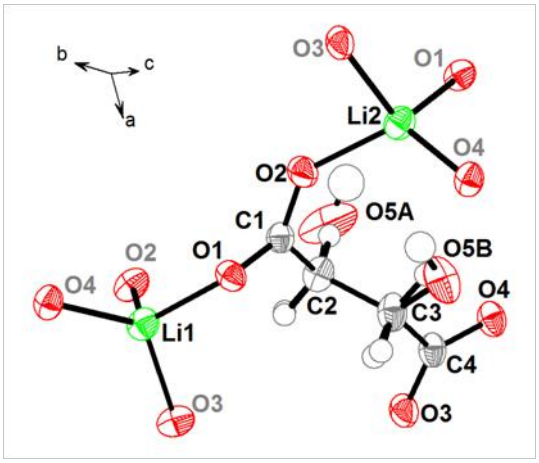

Figure 9. Ortep extended asymmetric unit of lithium L-malate, showing atoms necessary to complete the lithium coordination environments (grey labels) and disordered OH groups (O5A, O5B). C, H, Li and O atoms are shown in grey, white, green and red, respectively. Labels for H atoms are omitted for clarity.

The hydroxyl group of major occupancy, O5A, acts a hydrogen bond donor and acceptor to the hydroxyl groups of two nearby ligands (D-A distance 2.984(6) Å). This results in a trimer of hydrogen bonded species, shown in Figure 10, which causes a contraction in the *a*- and *b*-axes and thus a reduction in the cell volume compared to Li_2(suc).

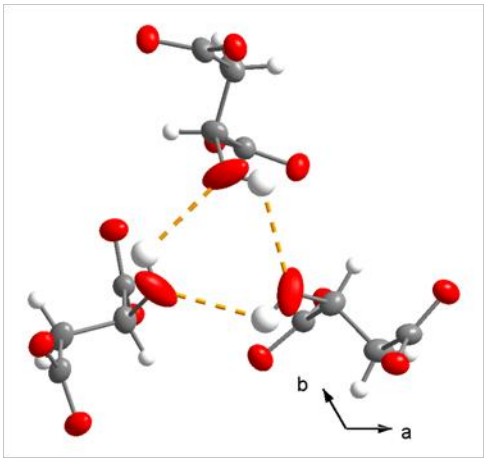

Figure 10. Trimer of L-malate ligands in lithium L-malate, showing hydrogen bonding of the major hydroxyl groups both within and between ligands. C, H and O atoms are shown in grey, light grey and red, respectively. Hydrogen bonds are shown as dashed orange lines.

4.3.1.4. Single crystal structure of lithium methylsuccinate, $Li_2(met)$, $Li_2(C_5H_6O_4)$

The asymmetric unit of $Li_2(met)$ consists of half of one methylsuccinate ligand and one lithium atom (Figure 11). The ligand in this case is severely disordered: the carbon backbone takes two possible conformations (C1-C2A/B-C2A/B-C1, 70(2)% and C1-C2C/D-C2C/D-C1, 30(2) %), with two equally occupied possible positions for the methyl group in each case (C3A and C3B, respectively). The lithium coordination tetrahedron is very distorted, although less so than $Li_2(flu)$, with Li-O bond distances in the range 1.956(4) Å - 1.999(5) Å and O-Li-O angles between 88.3(2)° and 123.7(2)°. This gives rise to bond valence sum of 1.02 and a δ_{tet} of 11.09°. Due to crystallographic symmetry the ligand C_4 torsion angle is linear (C1-C2-C3-C4 180°), but the torsion angle between the carboxylate groups and the ligand backbone is reduced severely (O2-C1-C2A-C2A 63.8(10)°). In order to accommodate this, the CH protons lie almost coplanar with the carboxylate groups.

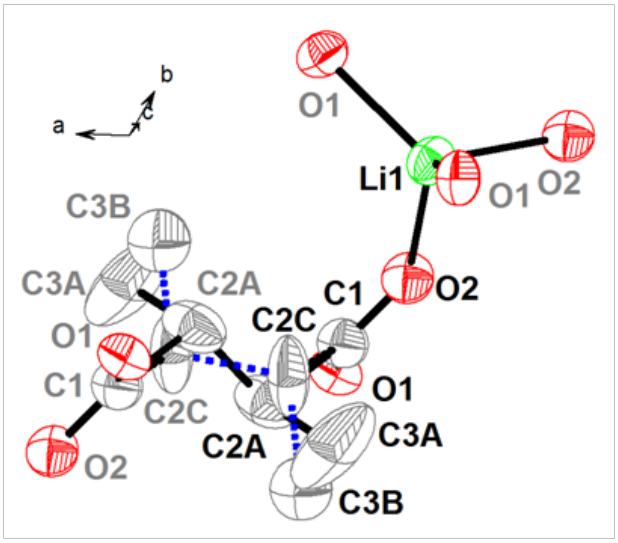

Figure 11. Ortep extended asymmetric unit of lithium methylsuccinate, showing atoms necessary to complete one ligand and the Li coordination sphere (grey labels). H atoms not shown for clarity; the disordered atoms with minor occupancy are linked with blue dashed lines. C, O and Li coloured grey, red and green.

The stereochemistry observed in Li_2(met) indicates the ligand has racemized during synthesis. This means that there are six possible locations of the methyl substituent in the framework cavity (instead of the three main positions in chiral Li_2(mal)). Only half of the six positions are occupied, but without hydrogen bonding to counteract the repulsion between groups, the result is a large increase in cell volume compared to Li_2(suc), particularly along the *c*-axis. Synthesis of this material required temperatures above 150°C, which previously resulted in isomerisation of lithium tartrates (see Chapter 3). This suggests that without racemisation the framework structure could not form, perhaps due to the increased strain involved if three methyl groups were forced into as close proximity as the hydroxyl groups in Li_2(mal). This is indicative of an upper limit on the effective substituent size that can be accommodated by this structure type, and is apparent in the lower crystal data quality obtained compared to the other structures. This can be explained largely by the crystal's poor diffraction at small *d*-spacing, resulting in low completeness, higher residual factors and a low data : parameter ratio.

4.3.1.5. Comparison of structures

As discussed above, there are many variations in the crystal structures of Li_2(suc), Li_2(flu), Li_2(mal) and Li_2(met), which are compared in Figure 12 and Table 2.

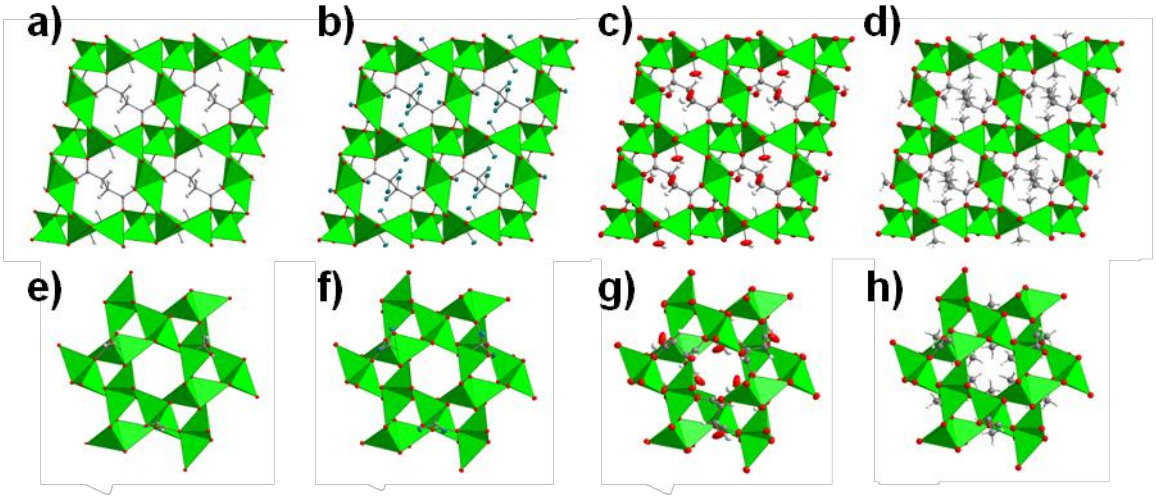

Figure 12. Comparison of ligand-substituted structures (from left to right: lithium succinate, lithium tetrafluorosuccinate, lithium L-malate and lithium methylsuccinate), (a-d) showing connectivity between organic and inorganic parts, and (e-h) showing occupancy of the solvent inaccessible cavity in the c-direction. C, H, F and O atoms and LiO_4 tetrahedra are shown in grey, white, turquoise, red and green, respectively. Only the sites of major ligand occupancy are shown for lithium L-malate and lithium methylsuccinate.

	Lithium succinate	Lithium tetrafluorosuccinate	Lithium L-malate	Lithium methylsuccinate
Unit cell volume ($Å^3$)	1332.03(14)	1418.3(10)	1309.5(2)	1375.8(3)
a* / *c	1.14	1.17	1.11	1.12
C-C-CO_2^- torsion angle (°)	91.75(14)	89.9(2)	C1: 93.5(3) C4: 73.1(3)	63.8(10)
Average Li-O bond distance (Å)	1.949(9)	1.99(3)	1.95(2)	1.97(2)
Bond valence sum	1.08	0.99	Li1: 1.09 Li2: 1.09	1.02
RMS O-Li-O deviation, δ_{tet} (°)	10.89	12.90	10.59	11.09

Table 2. Selected features of the single crystal structures of lithium succinate, lithium tetrafluorosuccinate, lithium L-malate and lithium methylsuccinate.

The unit cell volume varies in these compounds by over 8 %, from Li_2(mal) (1309.5(2) $Å^3$) to Li_2(flu) (1418.2(1) $Å^3$). In Li_2(mal) the effect of hydrogen bonding between hydroxyl groups is to contract the *a*- and *b*-axes relative to Li_2(suc), with resulting decreases in both *a* / *c* and unit cell volume. In contrast, Li_2(flu) exhibits an increase in both *a* / *c* and unit cell volume relative to Li_2(suc). When viewed down the *c*-axis (Figure 12f), no inter-ligand interaction between F atoms is observed in the *ab*-plane; in fact, the shortest inter-ligand F-F distance

occurs in the *c*-direction (2.8106(16) Å). Therefore, the expansion in a / c and the unit cell must only be a result of the expansion of the LiO_4 tetrahedra, caused by the electronegative effect of four F substituents per ligand, which withdraw negative charge away from the carboxylate groups, reducing their electrostatic attraction to lithium cations. In Li_2(met), the unit cell expansion is a result of steric interactions between methyl substituents within the framework cavity. The disorder among methyl group positions allows them to reduce clashing in the *ab* plane to some extent, and in fact a / c is reduced slightly compared to Li_2(suc). The structure is still highly strained, however, as shown by the small torsion angle between carboxylate oxygens and the ligand carbon backbone (63.8(10)°).

In all the structures the lithium coordination environment is a distorted tetrahedron. Bond valence sums vary from 0.99 in Li_2(flu) to 1.09 in Li_2(mal), and correlate with variation in the bond lengths. The bond valence sum of Li_2(met) is almost as low as Li_2(flu); in this case it is due to the strain caused by inter-ligand repulsion rather than an electronegativity effect. There is little variation in δ_{tet} among the structures, apart from an increase for Li_2(flu). This extra distortion may be caused by the relative conformational rigidity of the fluorinated ligand, and is enabled by its longer Li-O bonds. Reduction in bond valence sum and increase in δ_{tet} could have a positive effect on lithium mobility in these structures, because of the related weakening of Li-O bond strength. This would enable more facile breaking of coordination bonds as lithium cations move through the framework, and thus a reduction in activation energy for lithium transport.

4.3.1.6. Effect of substituent on thermal stability

Thermogravimetric analysis shows that Li_2(suc) is the most thermally stable structure, followed by Li_2(met), Li_2(flu) and Li_2(mal) in that order (Figure 13). Li_2(suc) shows a sharp one-step decomposition between 410 °C and 470 °C, with 57 % remaining mass, corresponding to lithium carbonate (Li_2CO_3 calculated 56 %), which was confirmed by FTIR analysis of the residue (see Appendix). Li_2(met) decomposes in two sharp steps, at 360 °C and 480 °C, leaving 50 % residue at 700 °C (Li_2CO_3 calculated 51 %). Li_2(flu) exhibits a sharp one-step mass loss at 320 °C - 420 °C, leaving 20 % mass. FTIR analysis shows no significant peaks above the fingerprint region, indicating the product may be lithium fluoride (LiF calculated 26 %). Li_2(mal) begins to decompose around 250 °C, first with a slow loss of 12 %, which corresponds to elimination of water across the ligand (H_2O calculated 12 %, see Section 4.3.3). The main framework decomposition occurs in between those of Li_2(flu) and

Li_2(suc) at 400 °C, leaving 51 % residue at 700 °C (Li_2CO_3 calculated 50 %, confirmed by FTIR).

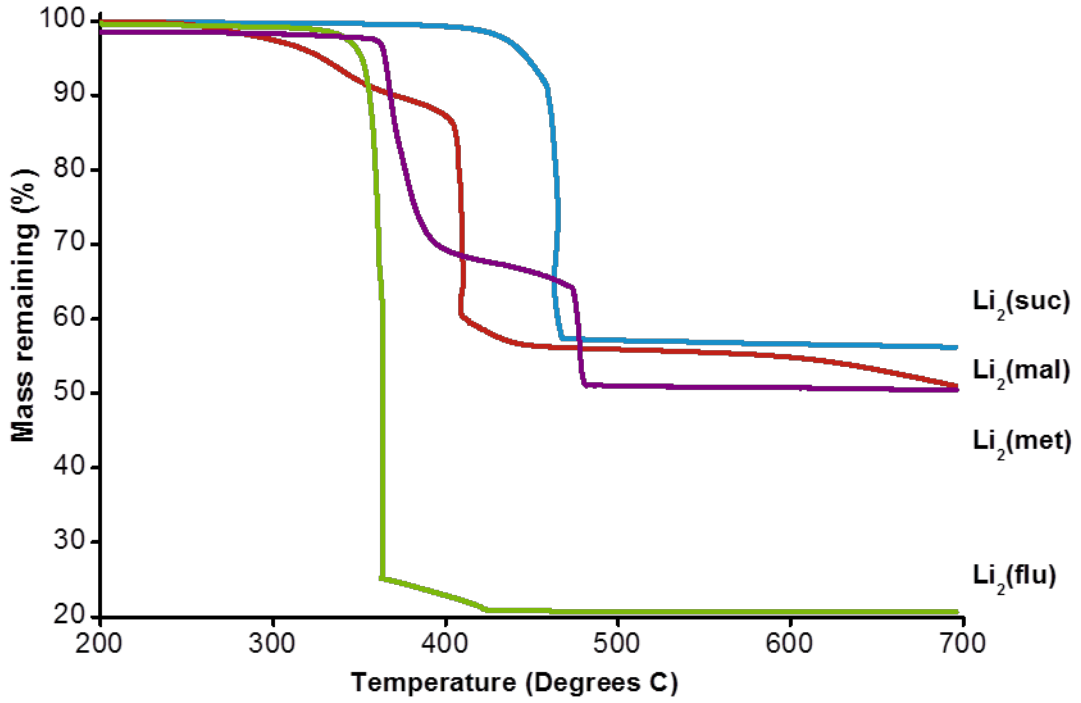

Figure 13. Thermogravimetric analysis of lithium succinate, lithium tetrafluorosuccinate, lithium L-malate and lithium methylsuccinate, shown in blue, green, red and purple, respectively.

Li_2(suc) is by far the most stable compound. The major mass loss in Li_2(flu) is at 320 °C, around 90 °C earlier than Li_2(suc), indicating that its decomposition is thermodynamically much more favourable. The reason for this is unclear: the enthalpy of formation of 2×LiF is only marginally more negative than $Li_2(CO_3)$, but the gaseous products in the case the decomposition of Li_2(flu) are unknown, neither is its enthalpy of formation. Li_2(met), which has a similar bond valence sum (1.02) to Li_2(flu) (0.99) is only marginally more stable and decomposes above 360 °C, but these values still compare favourably with isolated succinic acid, which has been found to decompose from 190 °C.[54] Li_2(mal) decomposes at lower temperature due to the hydroxyl functionality, which can be eliminated along with a proton to give off water before the framework as a whole collapses. This dehydration is investigated in more detail in Section 4.3.3.

4.3.1.7. Ligand substituent effects on mechanical properties

Nanoindentation of 0, 1, $\bar{1}$-type crystal facets (Figure 14) gave load-displacement curves for each of Li_2(suc), Li_2(flu) and Li_2(mal), shown in Figure 15. Due to the morphology of the crystals, no other facets were available for measurements and so it was not possible to obtain a complete picture of the frameworks' anisotropic mechanical behaviour. However, since the compounds investigated in this work are isostructural (or almost isostructural in the case of Li_2(mal)), values obtained on the same crystallographic facets should yield qualitative, if not quantitative, insight into the mechanical effects of different ligands. The calculated values for elastic modulus, E, hardness, H, and yield stress, σ_y, of each structure are shown in Table 3, along with relevant parameters describing their packing. Single crystals of Li_2(met) of sufficient size or quality for nanoindentation could not be grown.

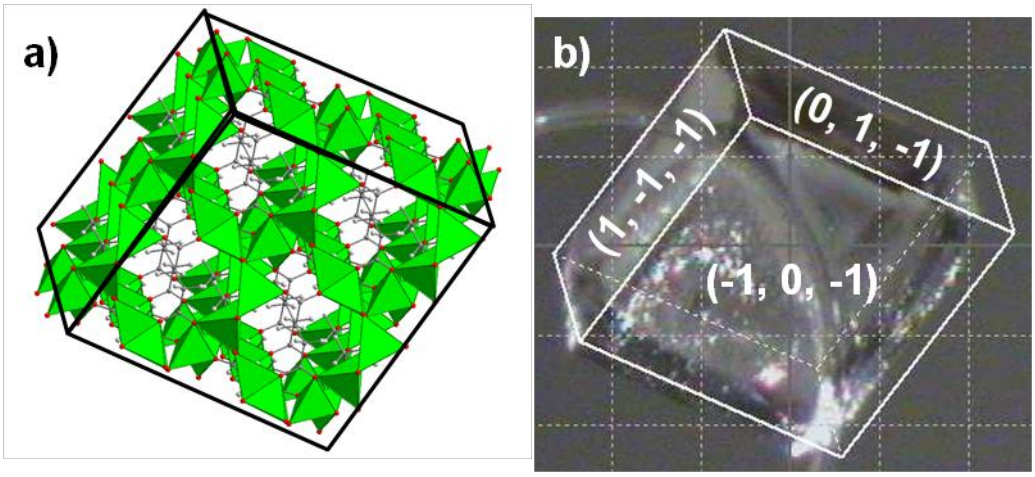

Figure 14. Face indexation of a typical crystal used for nanoindentation: a) the crystal structure of lithium succinate, the orientation of which corresponds to b) a photograph of a single crystal on an X-ray diffractometer goniometer loop, with crystal facets labelled.

	Lithium succinate	**Lithium tetrafluorosuccinate**	**Lithium L-malate**
Elastic modulus, *E* (GPa)	20.3(6)	33.2(10)	29.8(7)
Hardness, *H* (GPa)	1.65(6)	2.35(7)	2.28(6)
Yield stress, σ_y (GPa)	1.116(15)	0.860(13)	1.62(2)
Packing index (%)	73.5	82.7	79.8
Void space per unit cell (Å^3)	352.99(4)	245.37(2)	264.52(4)

Table 3. Mechanical properties measured by nanoindentation, packing indices (calculated using PLATON[31]) and void space per unit cell for lithium succinate, lithium tetrafluorosuccinate and lithium L-malate. Only the major part of the disordered L-malate ligand was used for the calculation of its packing index.

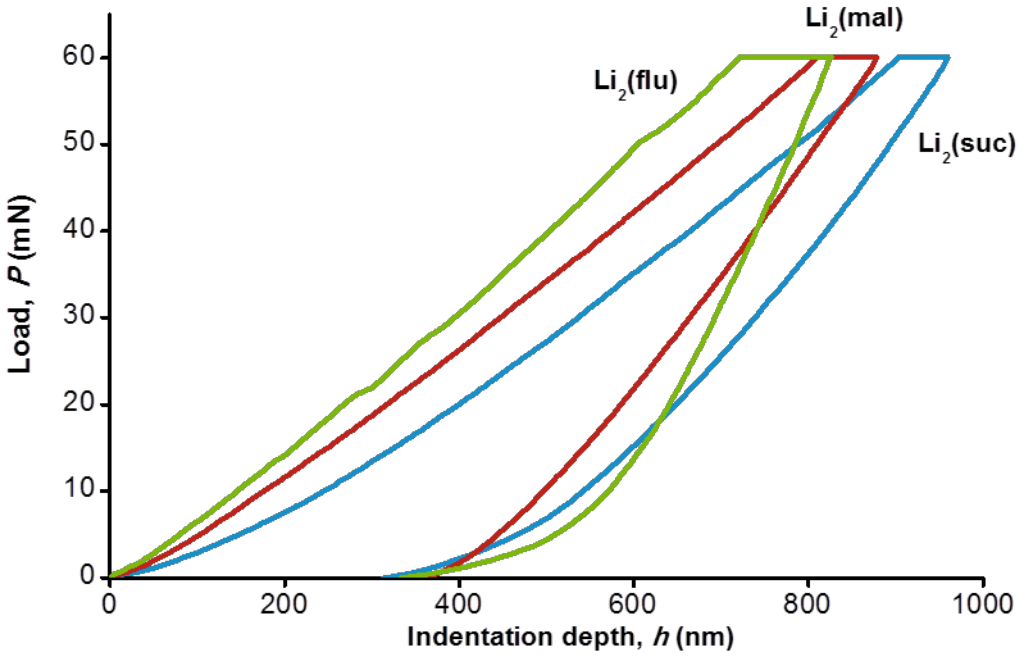

Figure 15. Typical load, P, vs. indentation depth, h, curves for 0, 1, 1 facets of lithium succinate (blue), lithium tetrafluorosuccinate (green) and lithium L-malate (red).

All three structures have lower values of *E* than most other non-porous inorganic-organic frameworks,[36, 42-43] due to the relative compliance of the monovalent, ionic lithium coordination sphere and the flexibility associated with the succinate ligand, compared to rigid linkers previously studied, such as oxalic acid.[42a] The fluorine- and hydroxyl-substituted ligands cause an increase in *E* compared to Li_2(suc) (Figure 16), resulting in values of 33.2(10) GPa and 29.8(7) GPa for Li_2(flu) and Li_2(mal), respectively. This correlates with increased packing index and decreased void space, which increase the effect of short-range inter-ligand interactions within the crystal structure.

Values for *H* follow a similar trend to *E*, whereby Li_2(flu) and Li_2(mal) are harder than Li_2(suc), again largely due to the increased inter-ligand dispersion forces. However, within experimental error at all indentation depths, Li_2(flu) and Li_2(mal) have identical values for *H* (Figure 17), indicating that dispersion forces are not the only important factor in the case of resistance to plastic deformation. It is likely that hydrogen bonding in Li_2(mal) increases its hardness, whilst weakening of Li-O bonds in Li_2(flu) reduces the pressure needed for plastic deformation to the extent that they have equal hardnesses.

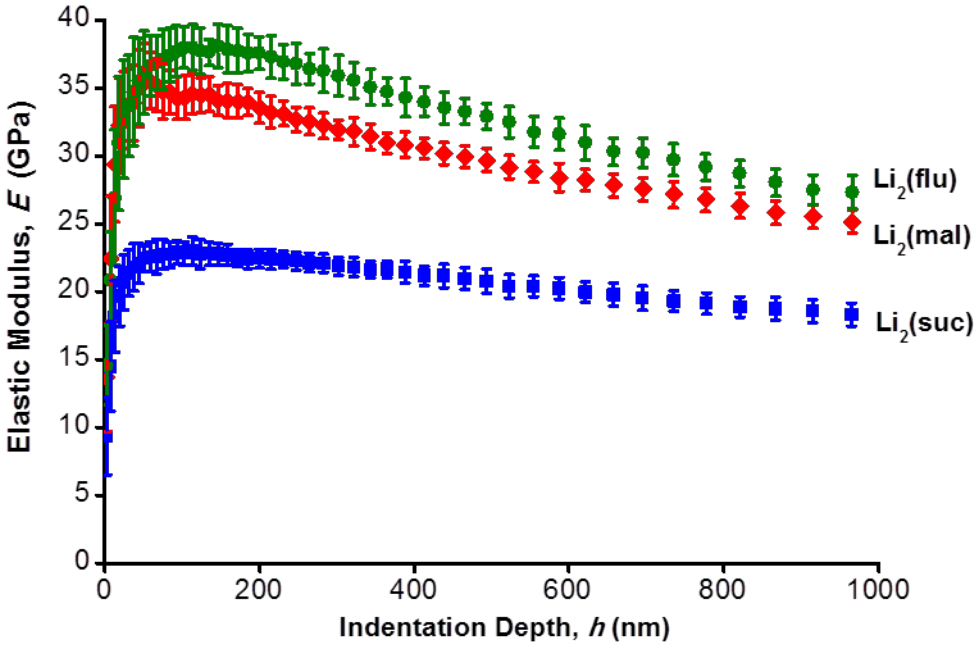

Figure 16. Plot of elastic modulus, E, vs. indentation depth, h, showing standard deviations for Li_2(suc) (blue squares), Li_2(mal) (red diamonds) and Li_2(flu) (green circles).

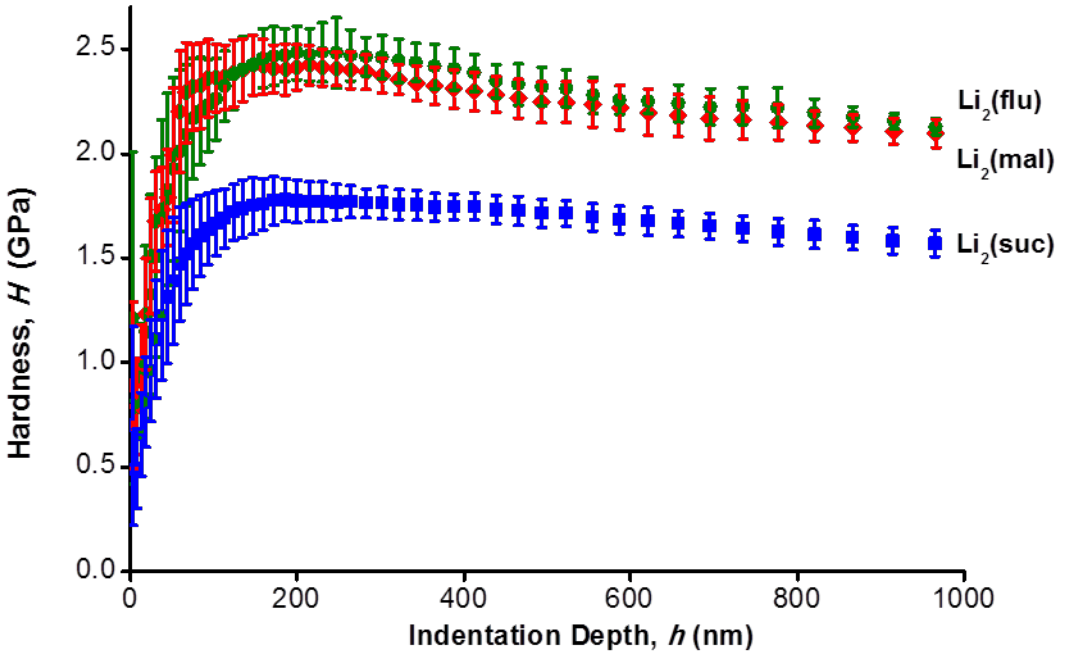

Figure 17. Plot of hardness, H, vs. indentation depth, h, showing standard deviations for Li_2(suc) (blue squares), Li_2(mal) (red diamonds) and Li_2(flu) (green circles).

The plot of indentation stress, σ, versus strain, ε, illustrates the transition between regions of elastic behaviour at low ε and plastic behaviour at higher ε (Figure 18). The intersection of lines extrapolated from the two regions gives an estimate of the yield stress, σ_y, of each material. Values of ε at the yield point are less reliable because they depend heavily on the variable contact delay at low ε. Values for σ_y exhibit a trend different to those of *E* and *H*, and seem to relate closely to framework bonding, rather than packing density or inter-ligand dispersion interactions. Li_2(flu) has the lowest Li-O bond strength (see Section 4.3.1.5) and correspondingly has the lowest σ_y (0.860(13) GPa); very little stress is needed to break the framework bonds to cause plastic deformation. Li_2(suc) and Li_2(mal) have similar Li-O bonding, but the additional hydrogen bonding in Li_2(mal) enables it to withstand higher stress before yielding (σ_y = 1.62(2) GPa). It therefore has the highest value of σ_y, with Li_2(suc) (σ_y = 1.116(15) GPa) midway between it and Li_2(flu).

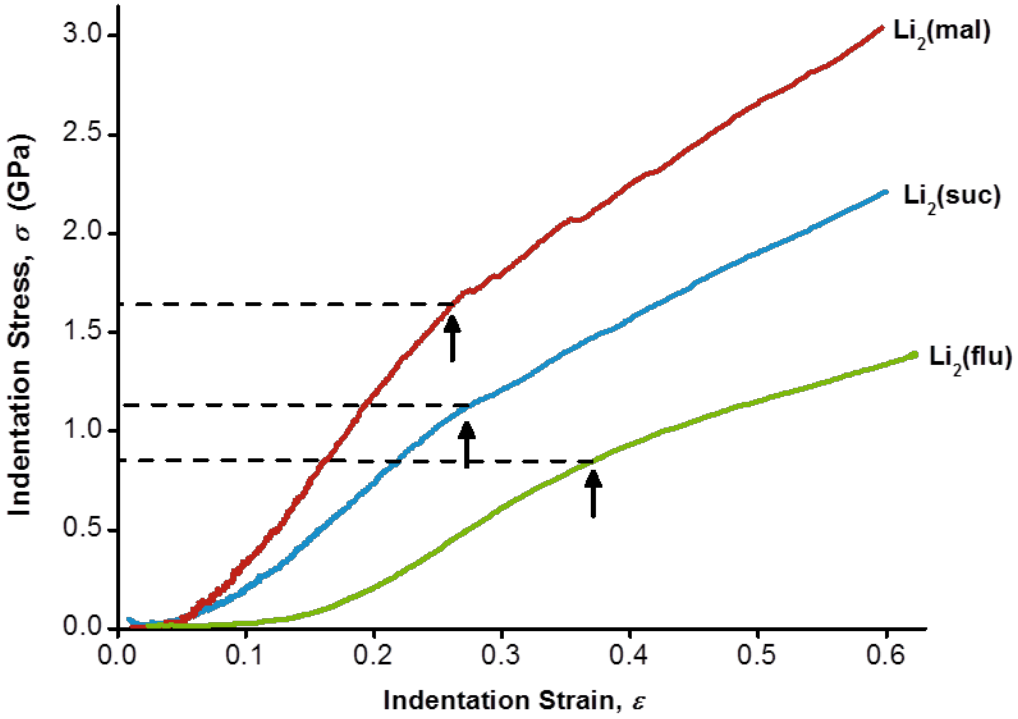

Figure 18. Plot of indentation stress, σ, vs. strain, ε, for Li_2(suc) (blue), Li_2(mal) (red) and Li_2(flu) (green). Arrows mark the yield stresses, σ_y, at which elastic behaviour at low ε turns into plastic deformation upon increasing ε.

Creep in all systems is very low: even after 20 minutes of constant loading, the increase in indentation depth, *h*, is negligible (Figure 19). This contrasts with behaviour of the layered copper phosphonoacetate framework CuPA-2, which was found to exhibit strongly

anisotropic creep due to the directionality of interlayer hydrogen bonding.[43] The negligible creep in $Li_2(suc)$, $Li_2(flu)$ and $Li_2(mal)$ can be ascribed to the 3-D inorganic connectivity, for which there exists no particularly weakly-bound orientation.

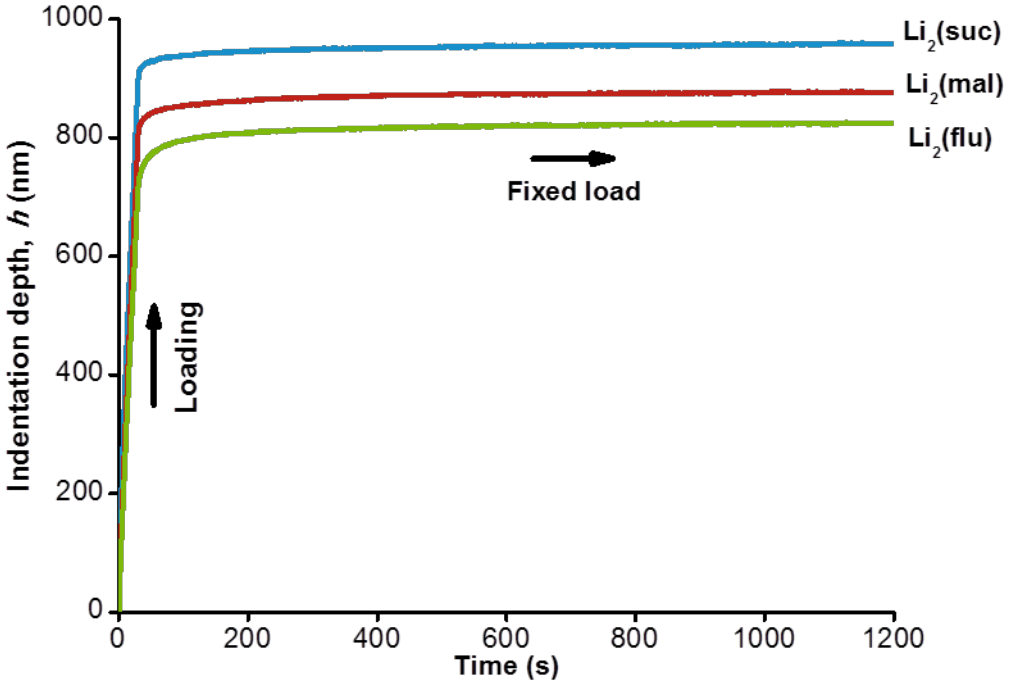

Figure 19. Creep behaviour under constant load of lithium succinate, lithium tetrafluorosuccinate and lithium L-malate (blue, green and red lines, respectively).

4.3.2. *Mixed-ligand compounds*

Solid solution behaviour of ligand substitution has been achieved in non-porous inorganic-organic frameworks using mechanochemical synthesis and confirmed by high-resolution powder X-ray diffraction and solid-state NMR analysis methods. The binary system $Li_2(suc)_{1-x}(flu)_x$ exhibits a seven percent increase in unit cell volume, V, with increasing x, which is apparent in the large peak position shifts of the high-resolution powder X-ray diffraction. Similar variation is seen with increasing z in the ternary system $Li_2(suc)_x(mal)_y(met)_z$ [where $x + y + z = 1$]. In contrast, V remains almost constant upon variation of x and y when z is unchanged. $Li_2(suc)_{1-x}(flu)_x$ exhibits single phase behaviour and good homogeneity, confirmed by SEM, and smooth variation in FTIR and TGA data. Solid-state NMR methods confirm that the ligands in both systems remain intact during synthesis and, in the case of $Li_2(suc)_{0.5}(flu)_{0.5}$, exist in close proximity on the atomic scale, further confirming its single phase nature.

4.3.2.1. Cell variations in $Li_2(suc)_{1-x}(flu)_x$

The mixed-ligand inorganic-organic framework system $Li_2(suc)_{1-x}(flu)_x$ was synthesized by mechanochemical methods and analysed by high resolution synchrotron powder X-ray diffraction and solid state NMR methods. Both these and other complementary techniques show that $Li_2(suc)_{1-x}(flu)_x$ exhibits solid solution behaviour, with substantial changes in cell parameters across the series.

The high-resolution synchrotron powder X-ray diffraction data clearly shows single-phase behaviour for all samples in $Li_2(suc)_{1-x}(flu)_x$, demonstrating ligand mixing and homogeneity in each phase. Peak positions show a change in cell parameters across the series (Figure 20). In general, the peaks move to lower 2θ with increasing (flu) content, ***x***, indicating an increase in cell parameters. However, peaks with a strong l-component initially shift towards higher 2θ before increasing slightly. Unlike in previous studies, the cell parameters of the end-members are markedly different and so there is no overlap between their respective peaks. Rietveld refinement was used to determine accurate cell parameters and atomic structure for all samples in $Li_2(suc)_{1-x}(flu)_x$, and relevant parameters are shown in Table 4. A representative plot, showing the observed, calculated and difference data for $Li_2(suc)_{0.5}(flu)_{0.5}$ is shown in Figure 21.

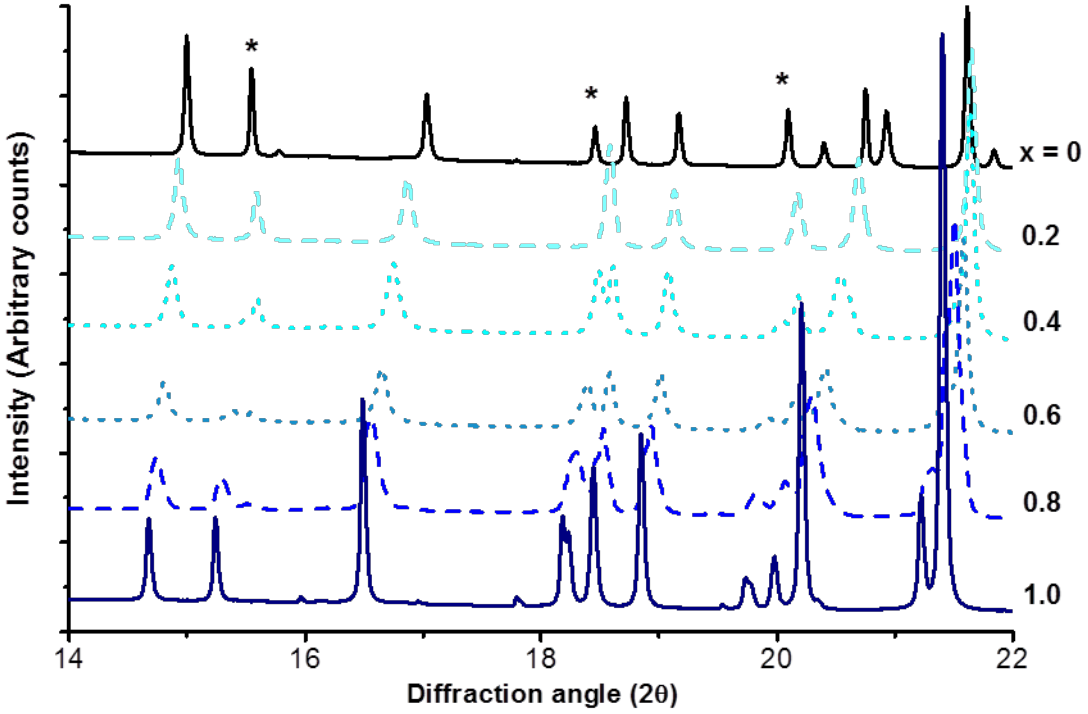

Figure 20. High resolution synchrotron powder X-ray diffraction data for $Li_2(suc)_{1-x}(flu)_x$ [x = 0, 0.2,.. 0.8, 1.0]. Asterisks mark selected peaks with significant l-component.

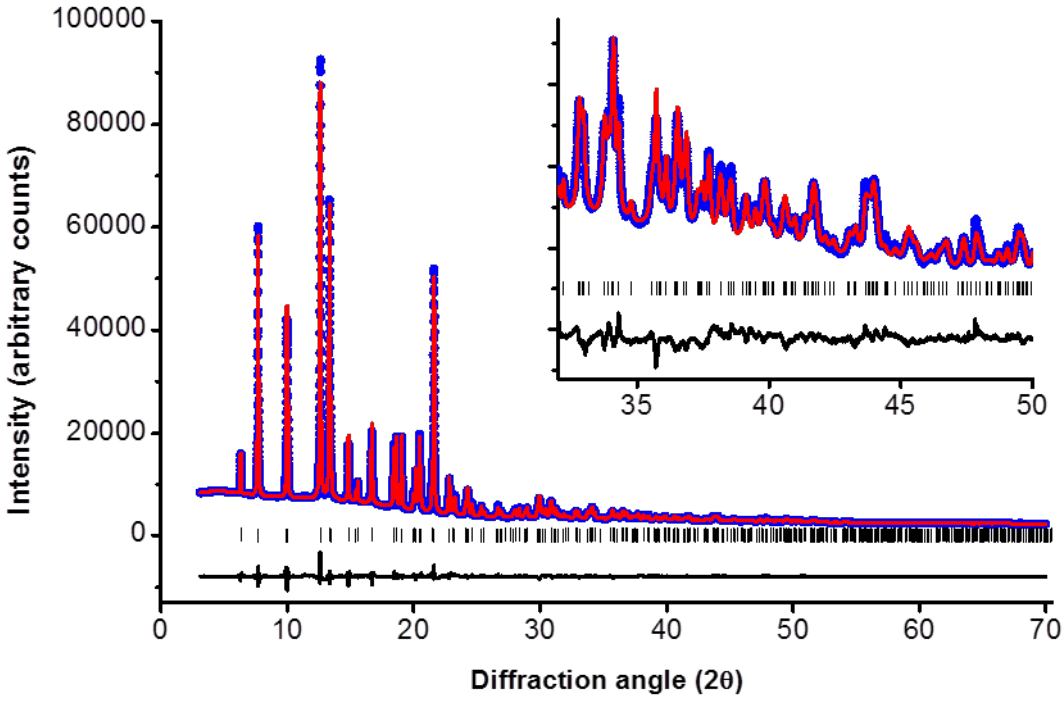

Figure 21. Rietveld refinement of $Li_2(suc)_{0.5}(flu)_{0.5}$, showing markers indicating the positions of expected peaks and high angle data (inset). Observed, calculated and difference data are shown as blue circles, and red and black lines, respectively.

x (nominal)	0	0.2	0.4	0.5	0.6	0.8[1]	1
a, *b* (Å)	12.02432(5)	12.15801(7)	12.2565(11)	12.29591(10)	12.33097(11)	12.39354(7)	12.44896(1)
c (Å)	10.62274(5)	10.54769(6)	10.51906(7)	10.52236(6)	10.53058(7)	10.56924(5)	10.60883(4)
α, β (°)	90	90	90	90	90	90	90
γ (°)	120	120	120	120	120	120	120
Unit cell volume (Å^3)	1330.113(12)	1350.247(15)	1368.49(3)	1377.73(3)	1386.68(3)	1405.94(2)	1423.848(10)
F_{occ}	0	0.1984(14)	0.3821(13)	0.4819(12)	0.5623(14)	0.7751(14)	1
wR_p	0.0356	0.0213	0.0248	0.0221	0.0221	0.0261	0.0312
R_p	0.0213	0.0149	0.0169	0.0148	0.0153	0.0185	0.0204
χ^2	5.32	2.502	2.719	2.439	24.06	0.3711	5.276
Variables	50	59	58	60	58	61	61
U	53.8	83.88	131.4	138	167	115.2	27.65
V	-6.323	-13.06	-18.46	-44.32	-51.58	-14.35	3.74
W	1.403	3.358	4.664	6.791	7.732	4.675	1.016
Y	8.521	33.93	53.88	56.95	59.79	15.44	-
X_e	9.15	-19.34	-34.08	-30.45	-30.21	-7.565	1.997
zero	-1.38396	-1.27654	-1.07726	-1.24142	-1.28665	0.0221	-1.2095
X	-	1.653	-	-	-	3.159	2.421

Table 4. Rietveld refinement parameters for powder X-ray diffraction data of $Li_2(suc)_{1-x}(flu)_x$. Note 1) A different wavelength was used for this sample (0.82715 Å, c.f. 0.826124 Å).

A plot of cell parameters against *x* shows an increase in *a*-axis length and a small initial decrease in *c*-axis length (Figure 22). The linear dependence of *V* with *x* may be expected from Vegard's law,[55] which although more commonly applied to metal alloys[26] was originally developed through the study of similarly ionic compounds. The fact that the cell axes do not display linear behaviour may be due to anisotropic stress accommodation within the framework structure.

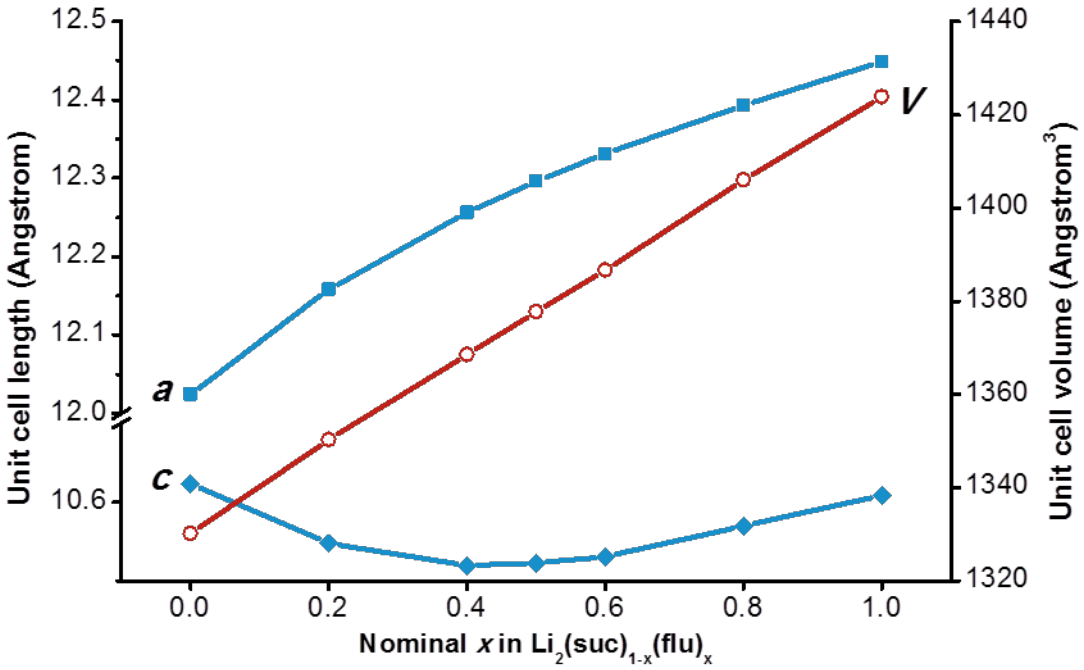

Figure 22. Cell parameter variations in $Li_2(suc)_{1-x}(flu)_x$: a- and c-axis lengths are shown by blue squares and diamonds, respectively, and cell volume, V, is shown by red circles. Error bars lie within the data markers.

Refinement of fluorine site occupancy, F_{occ}, reveals that variation in ligand ratio is well controlled by mechanosynthesis (Figure 23). In all samples featuring mixed ligands, F_{occ} is slightly lower than expected. This may be due to incomplete reaction or lower than expected starting material purity, but more likely it is an artefact of the refinement model, in which positions of succinate H atoms were constrained to vary with those of tetrafluorosuccinate F atoms. The H atoms could therefore easily account for some electron density associated in reality with F atoms, reducing the apparent occupancy of the F site.

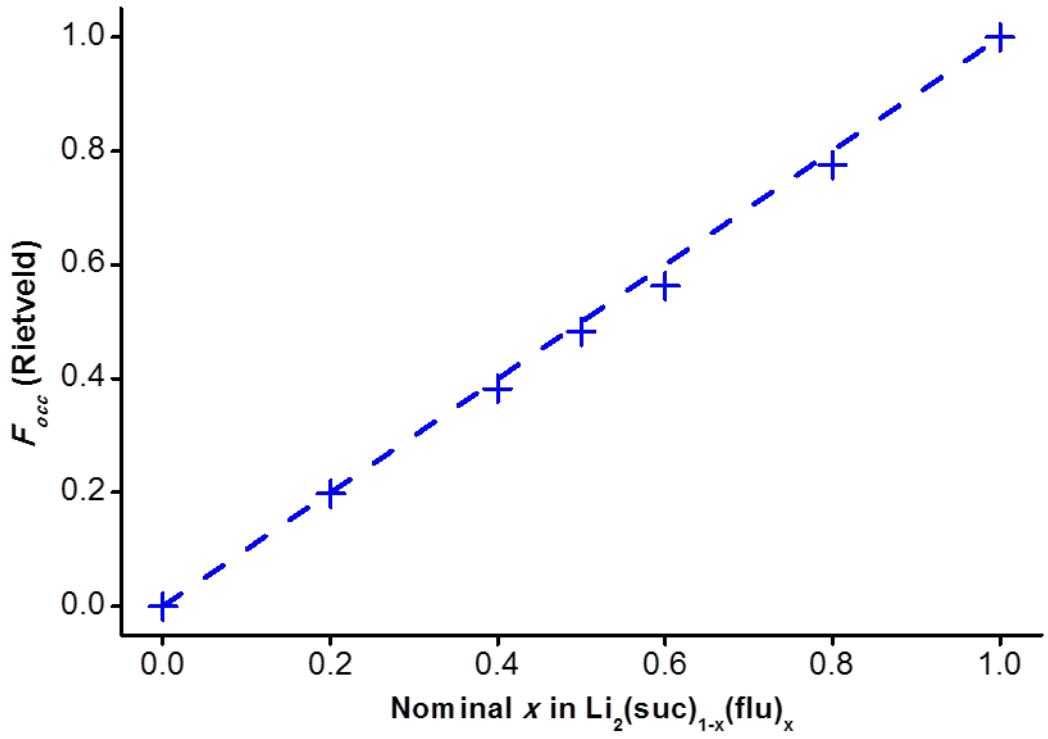

Figure 23. Plot of fluorine site occupancy from Rietveld refinement, F_{occ}, vs. nominal (flu) content from reactant ratio, x. The straight line, x = y, represents the ideal stoichiometry.

4.3.2.2. Confirmation of homogeneity by solid state NMR

Explicit confirmation of the homogeneous presence of both ligands in the 1:1 mixed phase was obtained in a ^{13}C cross-polarisation MAS-NMR experiment, in which the build-up of peaks was measured as a function of contact time (Figure 24 and Figure 25). At the shortest contact time, only the peaks for (suc) carbons are observed, due to their spatial proximity to the coupled protons. The alkyl carbon (36 ppm) reaches maximum intensity first, followed by the carboxylate carbon (183 ppm), as expected from their relative distances from the alkyl protons (1.0 Å and 2.1 Å, respectively, see Figure 26). At longer contact times cross-polarization to nearby ligands can occur, and so the signal for the (flu) carboxylate carbon, which is 3.7 Å away from the nearest proton, is clearly observed at 168 ppm. Critically, the ^{13}C cross-polarisation spectrum of the precursor tetrafluorosuccinic acid does not contain any significant peaks, due to the absence of any alkyl protons and the very weak coupling between the acid proton and other carbons (Figure 27). Therefore the ^{13}C (flu) signal in the 1:1 mixed phase must arise because of coupling to (suc) protons in close proximity to (flu) ligands, indicating that the ligands are neighbours in the same crystalline phase.

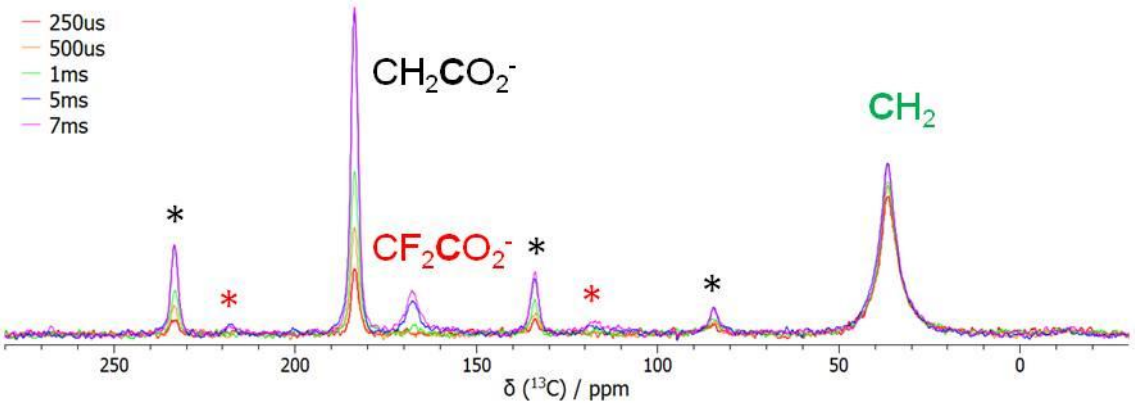

Figure 24. Cross polarisation MAS-NMR of ^{13}C cross-polarisation MAS-NMR spectra of $Li_2(suc)_{0.5}(flu)_{0.5}$ as a function of contact time. Asterisks indicate spinning sidebands; the CF_2 peak from tetrafluorosuccinate ligands is not observed due to lack of ^{19}F decoupling. Figure courtesy of Dr. Thomas Koester.

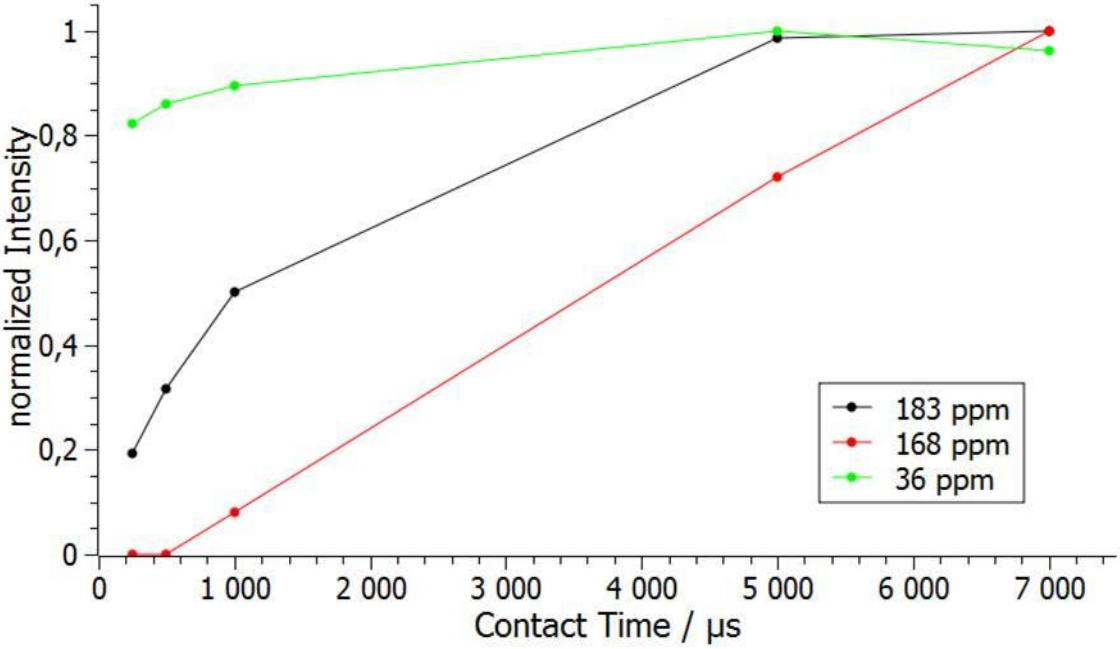

Figure 25. Build-up curves of ^{13}C cross-polarisation MAS-NMR peaks in $Li_2(suc)_{0.5}(flu)_{0.5}$, showing the lag of the (flu) CF_2COO peak due to much weaker dipolar coupling with the protons in succinate ligands. Figure courtesy of Dr. Thomas Koester.

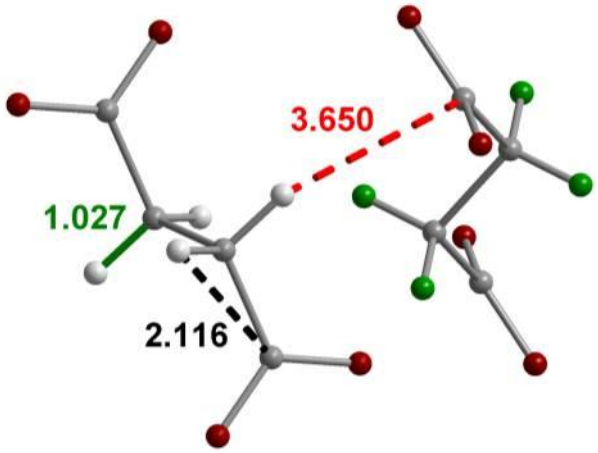

Figure 26. Closest through-space carbon-hydrogen distances in $Li_2(suc)_{0.5}(flu)_{0.5}$, showing an intra-ligand alkyl C-H bond (green), an intra-ligand carboxylate C - alkyl H distance (black dashed line) and an inter-ligand C-H distance (red dashed line). C, H, F and O atoms are coloured grey, white, green and red, respectively.

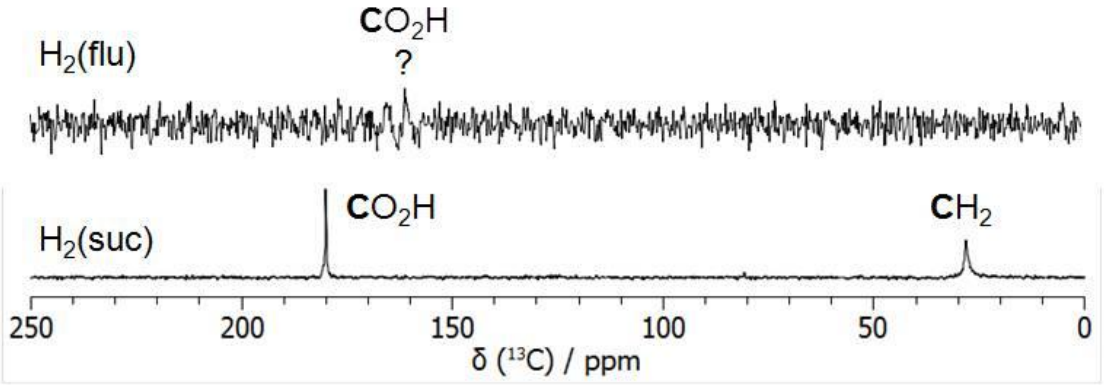

Figure 27. ^{13}C cross polarisation MAS-NMR of tetrafluorosuccinic acid and succinic acid, indicating the lack of peaks in the spectrum of the fluorinated ligand. Figure courtesy of Dr. Thomas Koester.

4.3.2.3. Complementary analysis of $Li_2(suc)_{1-x}(flu)_x$

Elemental analysis of the carbon and hydrogen content shows a continuous variation in ligand content and is in close agreement with expected compositions, confirming that the integrity of both hydrogenated and fluorinated ligands was maintained during the synthesis (Figure 28). Interestingly, in contrast to the Rietveld refinement of F site occupancy, all samples display slightly lower than expected hydrogen content, although they are all within the commonly accepted 0.2 wt.% error of expected values of the microanalysis technique. Similar microanalysis was not available to determine fluorine content directly.

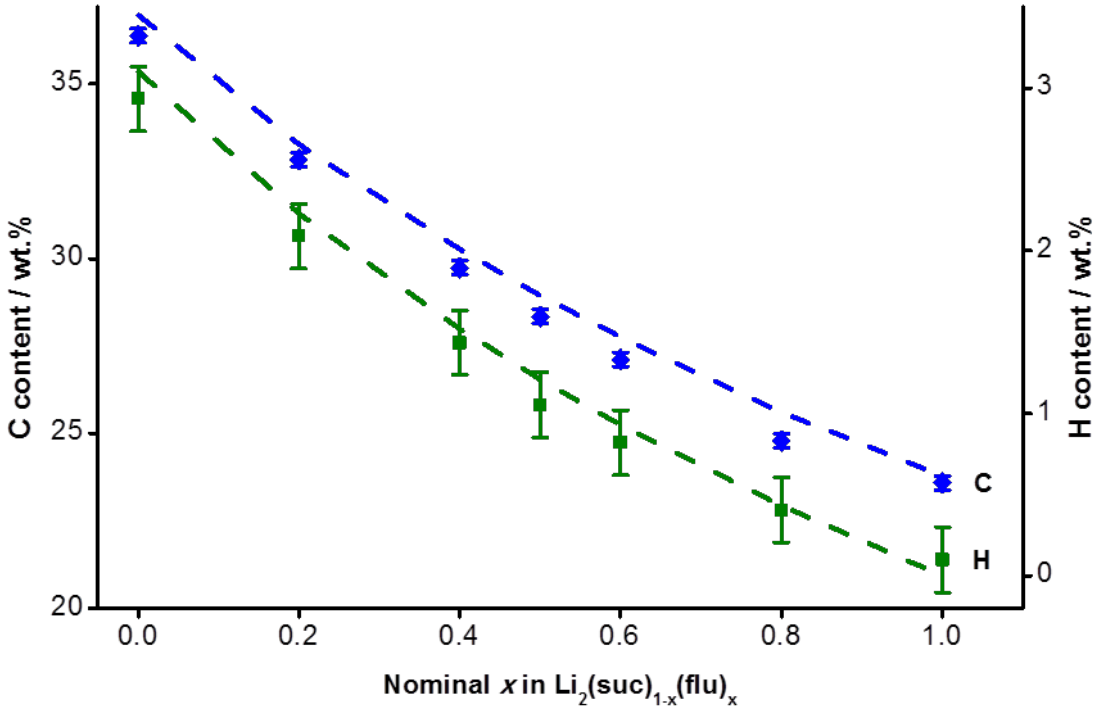

Figure 28. C and H microanalysis of $Li_2(suc)_x(flu)_{1-x}$. Blue diamonds and dotted line indicate observed and calculated values, respectively, for C, and green squares and dotted line indicate observed and calculated values, respectively, for H. Error bars shown at 0.2 wt.%.

Scanning electron microscopy micrographs confirm homogeneity on a scale at least below 100 nm in each sample. Particle morphology is found to change gradually across the series, between large agglomerates of smaller particles where $x = 0$ and smaller agglomerates of larger particles where $x = 1$. (Figure 29).

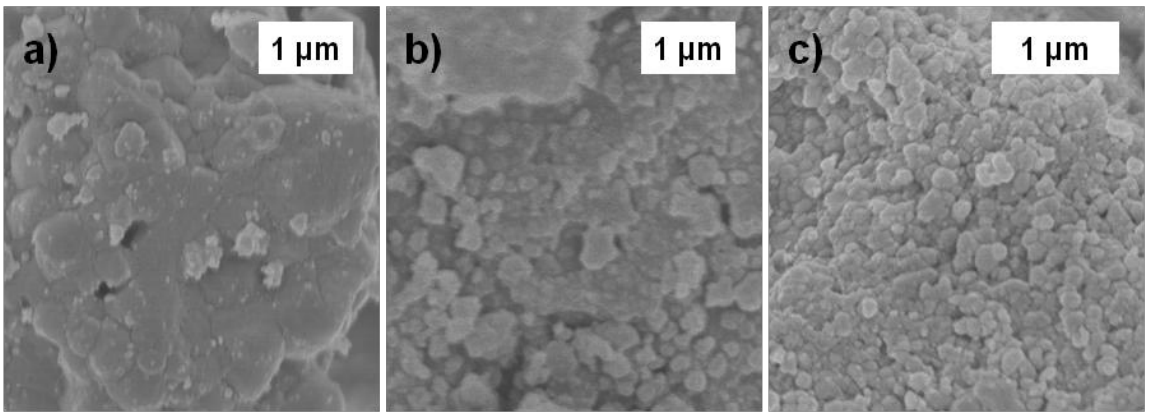

Figure 29. SEM micrographs of $Li_2(suc)_x(flu)_{1-x}$, where a) x = 0, b) x = 0.5 and c) x = 1.0. Scales are indicated by bars of 1 µm length.

Fourier-transform infrared spectra confirm the presence of both hydrogenated and fluorinated ligands, with the ratio of the peaks from the different ligands, particularly in the C=O stretching region, varying smoothly as expected with ligand fraction (Figure 30). Interestingly, the peak corresponding to the tetrafluorosuccinate carboxylate antisymmetric stretching mode shifts to higher frequency as x decreases from $x = 1$. Equally, the equivalent peak from the succinate ligand also shifts to higher frequency as x increases from $x = 0$. Both changes may be due to the perturbation of local structure around each ligand, which forces the tetrafluorosuccinate ligand into a progressively smaller environment and the succinate ligand into a progressively more spacious environment. In both cases, the effect of perturbation from the ligands' equilibrium environments (i.e. in the parent compounds) is to raise the energy of the stretching vibration.

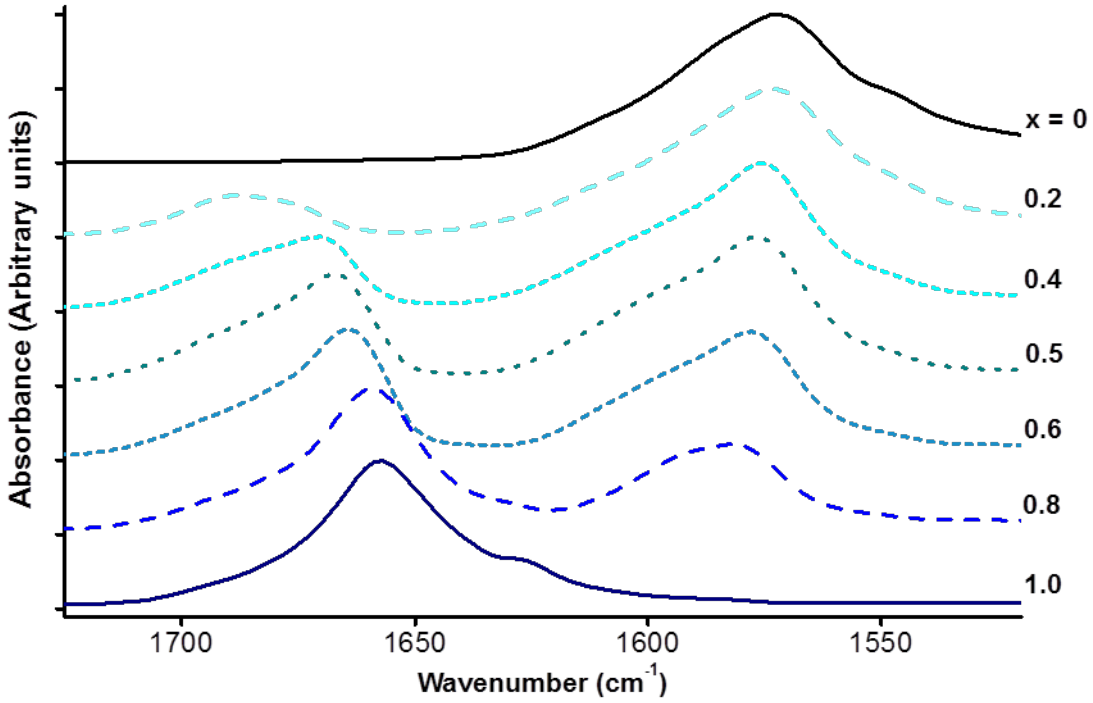

Figure 30. Infrared spectra of $Li_2(suc)_{1-x}(flu)_x$ in the C=O stretching region, showing the change in absorbance and shift in band positions of the carboxylate antisymmetric stretches.

Thermogravimetric analysis shows a gradual decrease in thermal stability as the fraction of fluorinated ligand increases from $x = 0$ to $x = 0.5$, with the main mass loss occurring in a single, broad step for each compound (Figure 31). This is due to the increasing thermodynamic driving force for decomposition, as discussed with the parent compounds. For samples in which the major ligand is tetrafluorosuccinate, between $x = 0.5$ and $x = 1$, thermal decomposition occurs in one sharp step at approximately constant temperature.

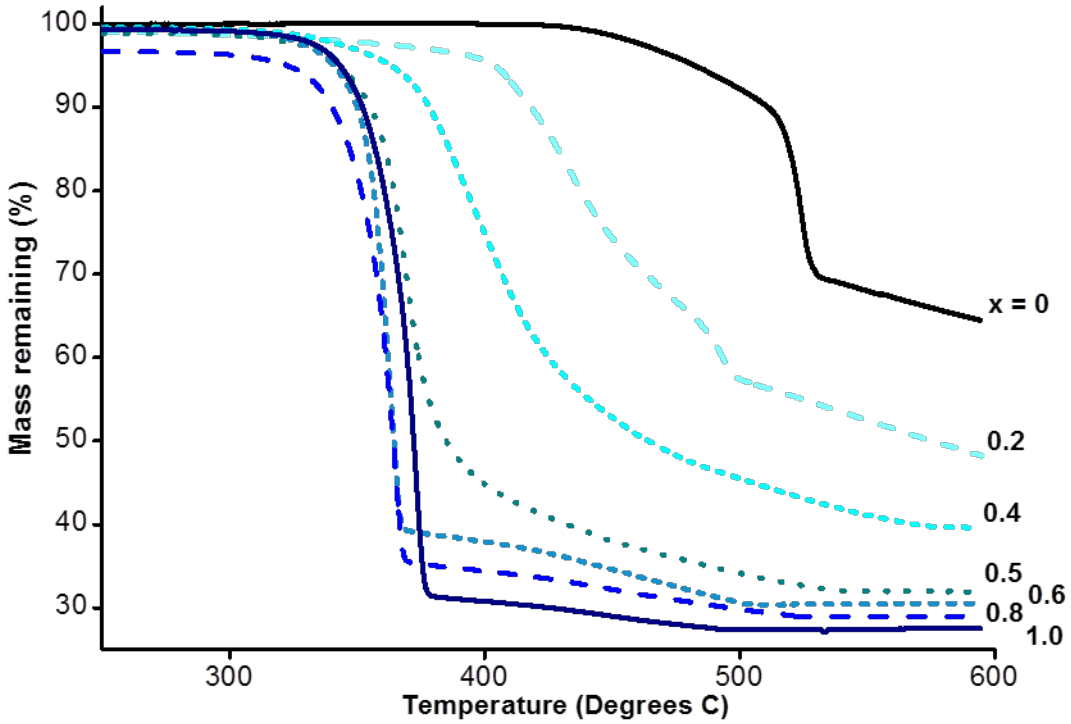

Figure 31. Thermogravimetric analysis of $Li_2(suc)_x(flu)_{1-x}$, showing decreasing thermal stability with increasing x up to x = 0.5.

4.3.2.4. Cell variations in $Li_2(suc)_x(mal)_y(met)_z$

The diffraction patterns of $Li_2(suc)_x(mal)_y(met)_z$ exhibited significantly broader peaks than $Li_2(suc)_{1-x}(flu)_x$, leading to the data not being of high enough quality for Rietveld refinement of atomic positions. Le Bail analysis was therefore used to determine accurate cell parameters for each phase (see Appendix for refinement parameters). A representative refinement of the ternary phase $Li_2(suc)_{1/3}(mal)_{1/3}(met)_{1/3}$ is shown in Figure 32.

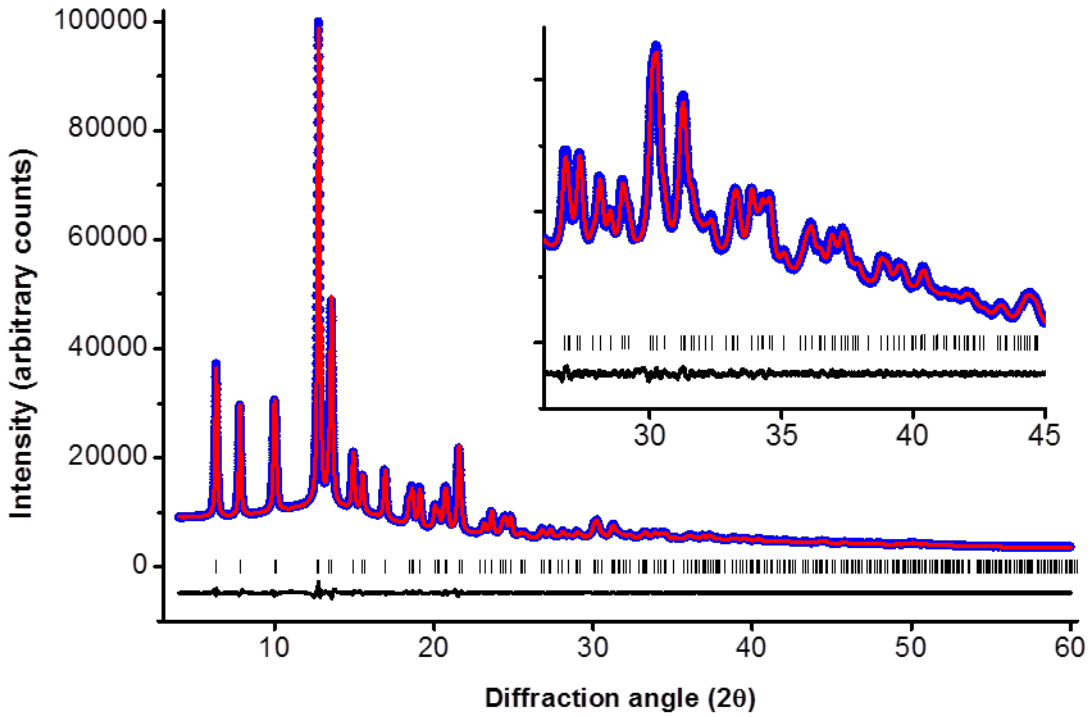

Figure 32. Le Bail refinement of $Li_2(suc)_{1/3}(mal)_{1/3}(met)_{1/3}$, showing expected peak positions and high angle data (inset). Observed, calculated and difference data are shown in blue, red and black, respectively.

In the binary solid solution $Li_2(suc)_x(met)_z$, V does not vary linearly with z, but has curved behaviour that can be fitted to a polynomial of order 3 (Figure 33). The a / c ratio reaches a minimum when z = 0.5, due to the steric bulk of the methyl groups, which interact with the other framework components, causing an increase in the strain along the c-axis. Between z = 0.5 and z = 0.8, the average number methyl groups in each cavity is closer to two, and so steric interactions between them begin to dominate, causing an expansion of the ab-plane.

In the binary system $Li_2(mal)_x(met)_z$, variation of V is more linear (Figure 34). The a / c ratio displays different behaviour, reaching a maximum at low z then decreasing. This is thought to be a result of disruption to the hydrogen bonding trimer described in Section 4.3.1.3, which causes contraction of the a-axis in pure $Li_2(mal)$. As soon as one hydroxyl group is replaced by a methyl group, two out of three hydrogen bonding interactions are removed, causing a rapid expansion of the ab-plane and an increase in the a / c ratio. As z increases further, inter-ligand interactions happen increasingly in the c direction due to the disorder among methyl group positions, allowing them to fill space in the cavity not accessible to the hydroxyl groups of the chiral L-malate ligand, which must remain in the a/b plane due to the single enantiomeric configuration present. This results in a gradual decrease in the a / c ratio.

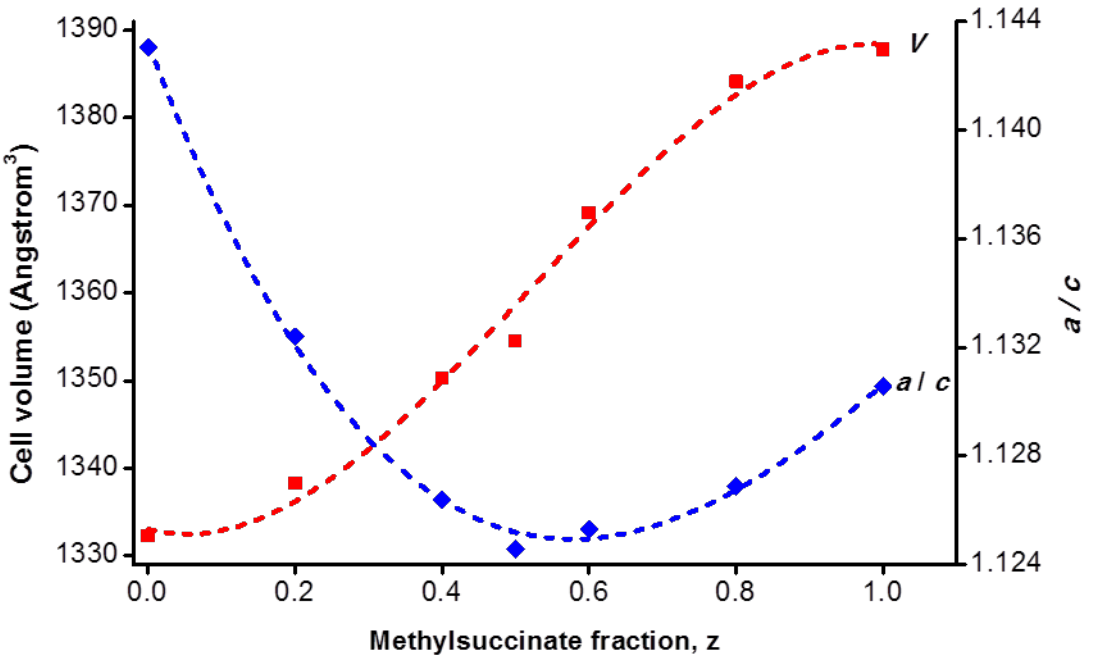

Figure 33. Variation in cell volume, V (red squares), and a / c ratio (blue diamonds) in $Li_2(suc)_x(met)_z$. Error bars lie within data markers.

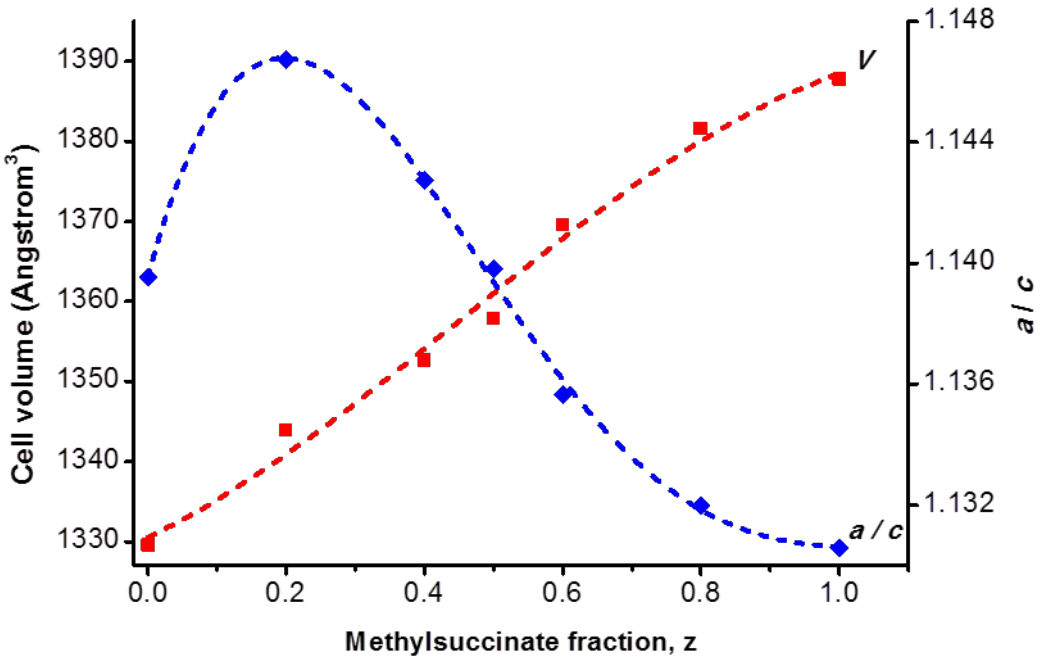

Figure 34. Variation in cell volume, V (red squares), and a / c ratio (blue diamonds) in $Li_2(mal)_x(met)_z$. Error bars lie within data markers.

The binary system $Li_2(suc)_x(mal)_y$ shows much less variation than $Li_2(suc)_x(met)_z$ and $Li_2(mal)_y(met)_z$ in both V and a / c (Figure 35). Both reach maxima around $x = 0.5$, due to the steric repulsion between hydroxyl groups in the *ab*-plane. Only at high values of x does hydrogen bonding counteract this, when on average more than two OH groups occupy the cavity within the crystal structure. It should be noted that the vertical axes in Figure 35 are less than half the scale of the other binary systems, showing that the effect of hydroxyl groups is much smaller than that of steric repulsion between methyl groups.

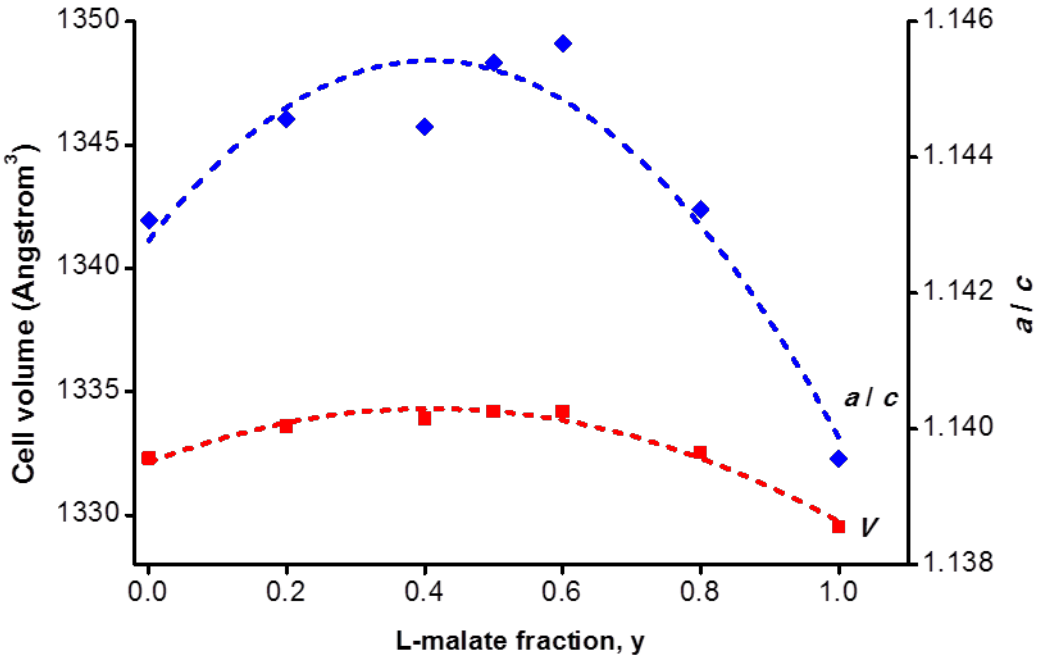

Figure 35. Variation in cell volume, V (red squares), and a / c ratio (blue diamonds) in $Li_2(suc)_x(mal)_y$. Error bars lie within data markers.

Overall, in the ternary phase diagram of $Li_2(suc)_x(mal)_y(met)_z$ the most striking variation is seen in V, which is almost invariant where the sum $(x + y)$ is constant but it increases dramatically as a function of methylsuccinate fraction, z (Figure 36). The ratio of the cell parameters, a / c, varies less systematically than V, depending on the specific interactions between substituents in each case (Figure 37). The behaviour is made more complicated by the disorder among methyl groups, but the highest values of a / c tend to be at low z and intermediate y due to the steric interactions in the *ab*-plane in these phases.

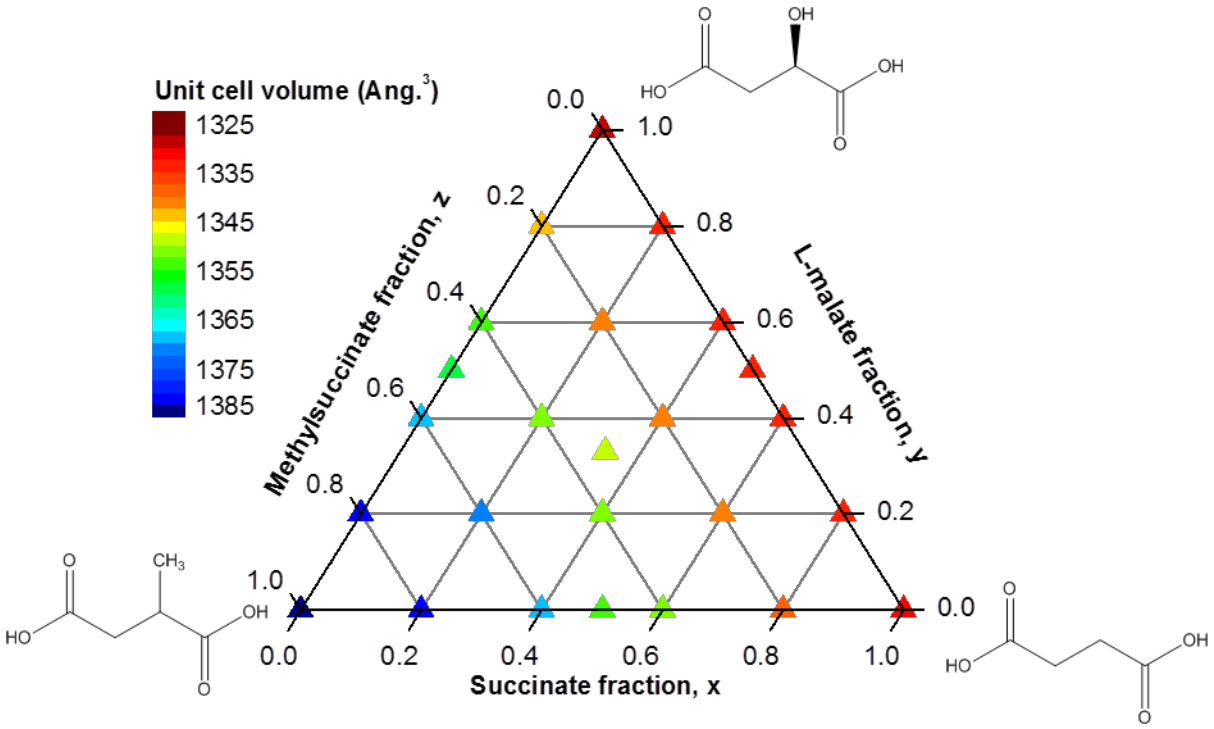

Figure 36. Plot of unit cell volume vs. composition for the ternary solid solution $Li_2(suc)_x(mal)_y(met)_z$, showing ligands corresponding to the pure end-members.

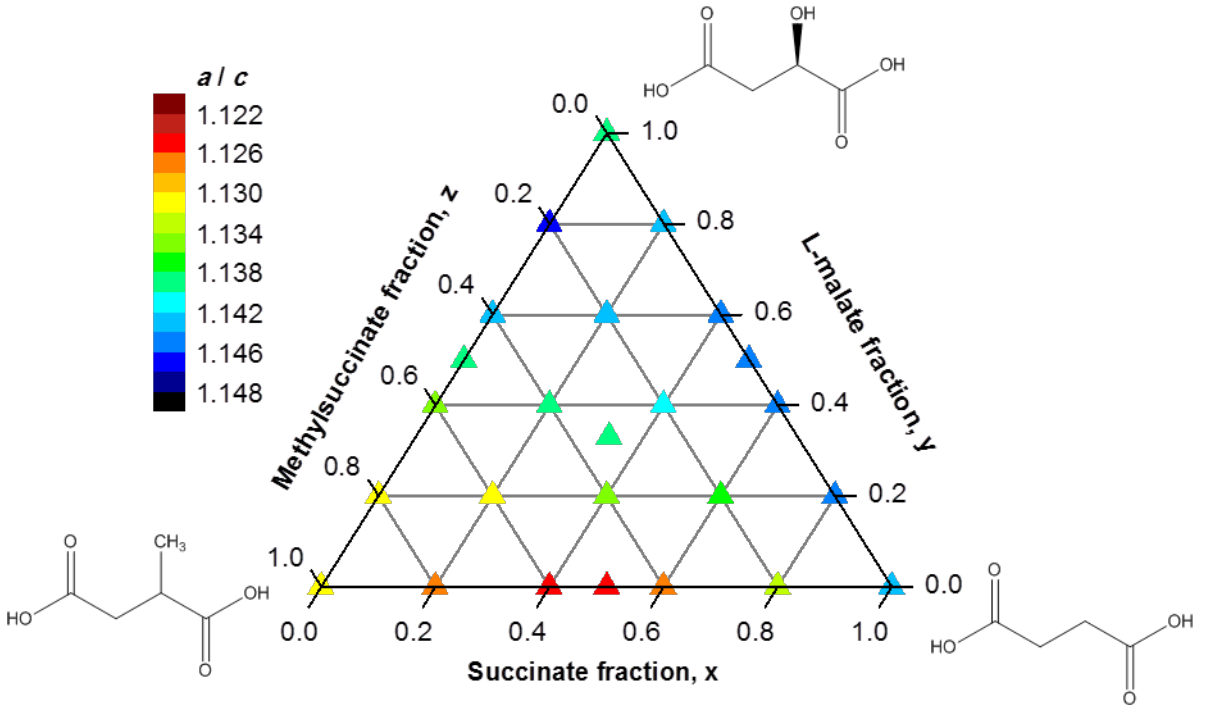

Figure 37. Plot of cell parameter ratio, a / c, vs. composition for the ternary solid solution $Li_2(suc)_x(mal)_y(met)_z$, showing ligands corresponding to the pure end-members.

One final observation of $Li_2(suc)_x(mal)_y(met)_z$ is that the parent phase $Li_2(mal)$ is chiral, adopting the space group *R*3, whereas the others adopt *R*$\bar{3}$. Strictly speaking, it is therefore

not isostructural and mixed-ligand phases of compositions containing the L-malate ligand are not solid solutions. However, the phases are topologically similar, the only major difference being a hydroxyl substituent that breaks the centric symmetry. Therefore we may call these materials "topologically similar disordered mixed-ligand phases". The mixing of chiral and achiral parent phases is, to the best of the author's knowledge, unreported in any type of material, although solid solutions of molecules with opposite chirality have been studied previously.[56] This leads to the questions, "at what composition does the achiral phase become chiral, i.e. can you consider an isolated chiral molecule in an achiral bulk phase as a point defect, not contributing to its overall chirality? If so, at what concentration does the effect of chiral molecules translate into bulk chirality?"

4.3.2.5. Confirmation of ternary phase components by solid state NMR

Solid state NMR again provided confirmation that the expected ligands were present in the mixed-ligand phases $Li_2(suc)_x(mal)_y(met)_z$. The ^{13}C spectra obtained (Figure 38) show clear differences between the pure compounds, with the peaks in regions 175 ppm - 190 ppm, 70 ppm, 30 ppm - 45 ppm, 25 ppm and 20 ppm assigned to $\underline{C}O_2^-$, $\underline{C}HOH$, $\underline{C}H_2$, $\underline{C}H$ and $\underline{C}H_3$, respectively. The spectra of binary mixed-ligand phases are linear combinations of the spectra of the end-members, whilst the ternary phase $Li_2(suc)_{1/3}(mal)_{1/3}(met)_{1/3}$ shows all the peaks from all three ligands.

It should be noted that this does not provide conclusive evidence for homogeneous ligand mixing, as was the case in $Li_2(suc)_{0.5}(flu)_{0.5}$. If a similar cross-polarization experiment had been performed on $Li_2(suc)_{1/3}(mal)_{1/3}(met)_{1/3}$, the presence of protons on all ligands, rather than just (suc), would have made interpretation of the results ambiguous. However, the NMR confirms that the ligands remained intact and, coupled with accurate cell-parameter determination by high-resolution powder X-ray diffraction data, points firmly towards homogeneous, disordered mixed-ligand behaviour in this ternary phase diagram.

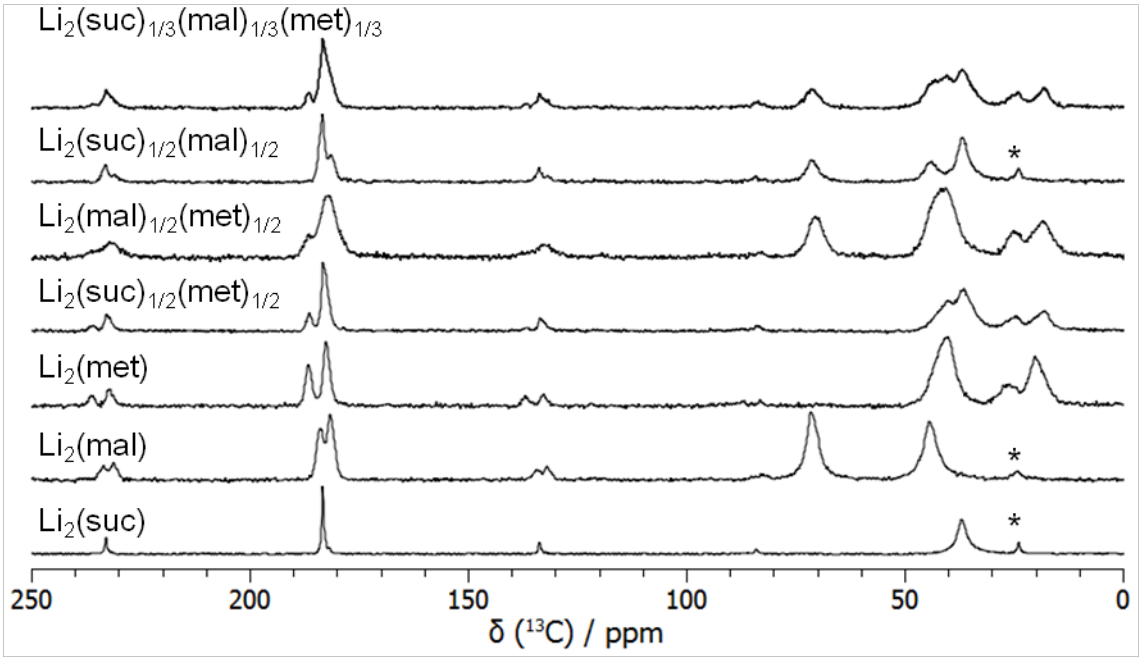

Figure 38. Solid state MAS-NMR ^{13}C spectra of pure compounds lithium succinate, lithium L-malate and lithium methylsuccinate, and their binary and ternary mixed-ligand phases. Asterisks mark peaks from the methyl group of lithium acetate impurity (masked in samples containing (met). Figure courtesy of Dr. Thomas Koester.

4.3.3. *Topotactic dehydration of lithium L-malate*

The observation in the thermogravimetric analysis of $Li_2(mal)$ that around 12 % mass loss occurs before the main framework decomposition temperature suggests that water (12 wt.% calculated) was being eliminated from the ligand. Further investigation by single crystal X-ray diffraction, NMR and FTIR shows that upon heating above 320 °C, the L-malate ligand dehydrates in a single-crystal to single-crystal process to form the fumarate ligand, $(fum)^{2-} = C_4H_2O_4^{2-}$, which has a *trans* C=C double bond (Figure 39). The resulting material is a solid solution of malate and fumarate ligands with composition $Li_2(mal)_{1-x}(fum)_x$, where x can be controlled by variation of the heat treatment up to approximately $x = 0.8$. Complete topotactic dehydration of the ligand is not possible due to framework decomposition above 350 °C.

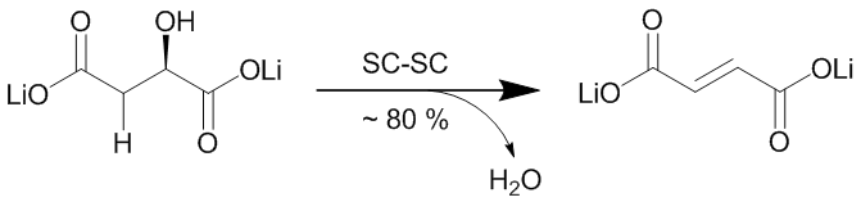

Figure 39. Chemdraw schematic of the topochemical dehydration of lithium L-malate.

Notably, the fumarate ligand's *cis* isomer, maleic acid, was not formed due to the ligand's orientation with carboxylates *trans* to one another held fixed by the inorganic $(LiO_2)_\infty$ network. In addition, synthesis of lithium-based fumarate frameworks using conventional solution methods did not result in the formation of a I^3O^0 structure similar to Li_2(suc). Instead, the pure ligand compound Li_2(fum) is found to take a denser form, with I^1O^2 architecture (see Chapter 5). This indicates that topotactic dehydration is a potential route to form structures that are not accessible using other synthetic methods.

4.3.3.1. Single crystal structure of Li_2(L-malate)$_{0.23}$(fumarate)$_{0.77}$

The crystal structure of $Li_2(mal)_{0.23}(fum)_{0.77}$ was determined by single crystal X-ray diffraction methods at 120 K. Relevant details are shown in Table 5.

$Li_2(mal)_{0.23}(fum)_{0.77}$ is isostructural to Li_2(mal), but contains disorder in the ligand whereby the fumarate ligand ($C_4H_2O_4^{2-}$) has replaced most of the L-malate ligand. The asymmetric unit contains two lithium atoms and one ligand moiety, with site occupancies 0.228(8) and 0.772(8) for L-malate and fumarate, respectively (Figure 40).

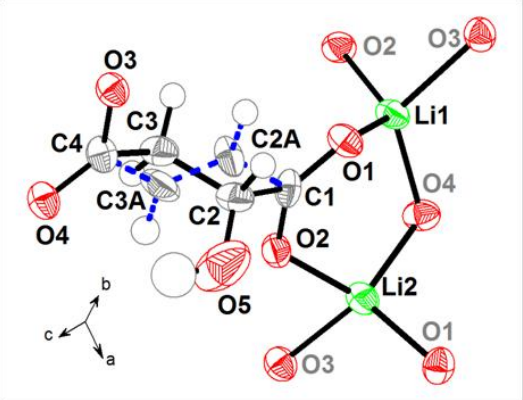

Figure 40. Ortep extended asymmetric unit of Li_2(L-malate)$_{0.23}$(fumarate)$_{0.77}$, showing the atoms needed to complete the lithium coordination sphere (grey labels). The C-C and C-H bonds of the fumarate ligand are shown as dashed blue lines. C, H, Li and O atoms are coloured grey, white, green and red, respectively.

	$Li_2(L\text{-malate})_{0.23}(fumarate)_{0.77}$
crystal size (mm^3)	0.2 × 0.2 × 0.2
crystal system	trigonal
space group	R 3
T (K)	120(2)
a (Å)	11.7600(6)
b (Å)	11.7600(6)
c (Å)	11.0689(7)
α (°)	90
β (°)	90
γ (°)	120
V ($Å^3$)	1325.71(13)
asym. unit	$C_4 H_{2.44} Li_2 O_{4.22}$
Z	9
d_{calc} ($g\,cm^{-3}$)	1.487
λ (Å)	0.71073
μ (mm^{-1})	0.128
reflections collected	2127
unique reflections	1273
observed data (I > 2σ(I))	994
parameters	113
R_{int}	0.0184
R_1	0.0425
wR_2 (I > 2σ(I))	0.1084
R_1 (all data)	0.0588
wR_2 (all data)	0.1236
GOF	1.042

Table 5. Single crystal structure determination parameters for $Li_2(mal)_{0.23}(fum)_{0.77}$.

The lithium coordination spheres are distorted tetrahedra (bond distances 1.917(12) Å - 2.005(12) Å, angles 88.9(4)° - 122.8(5)°) with bond valence sums 1.09 and 1.07 for Li1 and Li2, respectively. δ_{tet}, 10.15°, is reduced slightly compared with Li_2(mal), but the average Li-O bond distance is the same (1.95(3) Å). The ligand bond distances are reasonable for C-C and C-O, with the caveat of restraints in the L-malate distances in the structure refinement, which were necessary due to its low occupancy. Notably, the distance between the central fumarate carbons C2A and C3A, which was refined freely, is shorter than the others at 1.273(6) Å, corresponding to a C=C double bond. The fumarate ligand is close to planar: the angles between the planes of the carbon backbone and carboxylate groups are 7.4(12)° and 4.9(12)° for O2-C1-C2A-C3A and O3-C4-C3A-C2A, respectively.

The overall structure closely resembles $Li_2(mal)$ (Figure 41), although there are some changes in the unit cell parameters, which are discussed in Section 4.3.3.4.

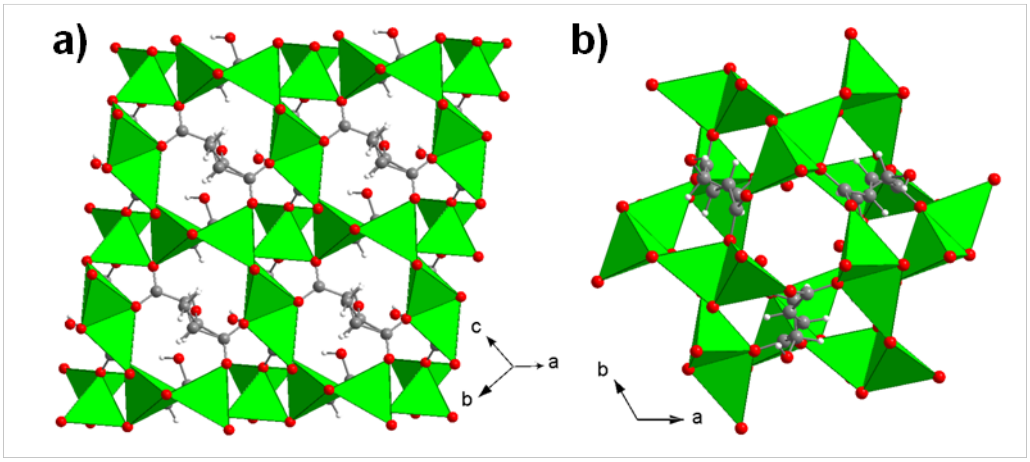

Figure 41. Extended structure of $Li_2(L\text{-}mal)_{0.23}(fum)_{0.77}$, a) showing the connectivity between organic and inorganic parts, and b) viewed down the c-axis. Both ligands are shown for completeness. C, H and O atoms and LiO_4 tetrahedra are shown in grey, white, red and green, respectively.

4.3.3.2. Confirmation of mixed ligand composition by solution NMR

The presence of both L-malate and fumarate ligands in the bulk sample of $Li_2(mal)_{0.23}(fum)_{0.77}$ was confirmed by ^1H (Figure 42) and ^{13}C solution NMR (Figure 43). Peaks were assigned as follows: L-malate ^{13}C δ = 42.481 ppm ($\underline{C}H_2$), 70.251 ppm ($\underline{C}HOH$), 179.766 ppm ($\underline{C}O_2$-βOH), 180.951 ppm ($\underline{C}O_2$-αOH); ^1H δ = 1.766 ppm (O$\underline{H}$), 2.22 ppm and 2.52 ppm (both dd, C$\underline{H}_2$), 4.155 ppm (dd, C$\underline{H}$). Fumarate ^{13}C δ = 135.239 ppm ($\underline{C}H$), 174.631 ppm ($\underline{C}O_2$); ^1H δ = 6.372 ppm (s, C$\underline{H}$).

It is worth noting that the observed chemical shift of the fumarate proton is δ = 6.372 ppm, which is close to the expected chemical shift of δ = 6.31 ppm, simulated using ChemDraw.[57] In contrast, the simulated chemical shift of maleic acid, the *cis* isomer of fumaric acid, is higher: δ = 6.49 ppm. This gives further confirmation that the *trans* isomer, fumaric acid, is the only product, pointing towards a topochemical reaction mechanism rather than one involving more substantial structural rearrangement.

The areas under the ^1H peaks were integrated to give an estimate of the fumarate fraction, *x*, in the sample, which was calculated as 0.81, in close agreement with the value obtained by single crystal X-ray diffraction, 0.77.

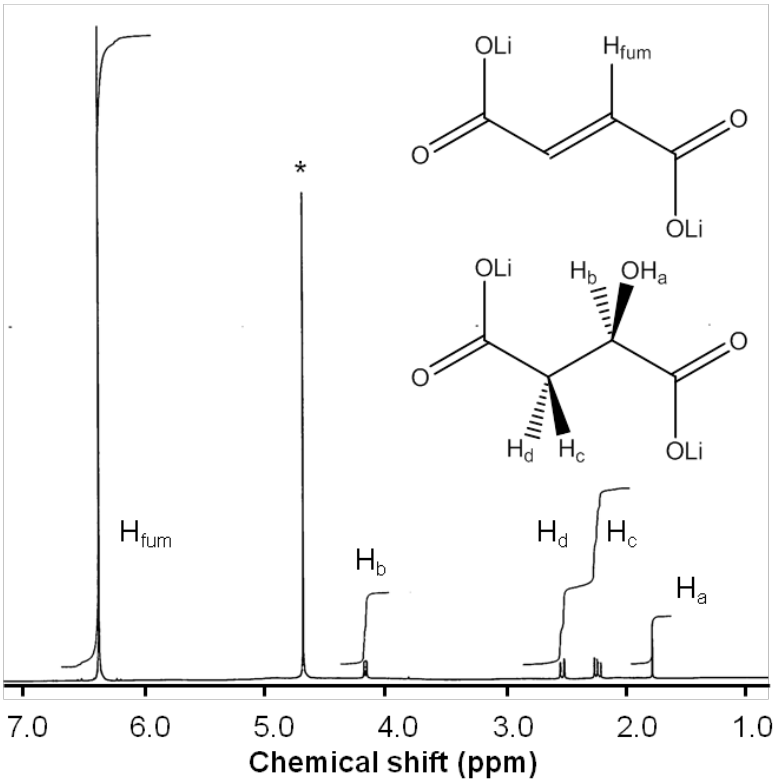

Figure 42. ^{1}H NMR spectra of $Li_2(mal)_{0.23}(fum)_{0.77}$ dissolved in D_2O, showing peak assignments and relative peak intensities. The asterisk marks an HOD impurity peak.

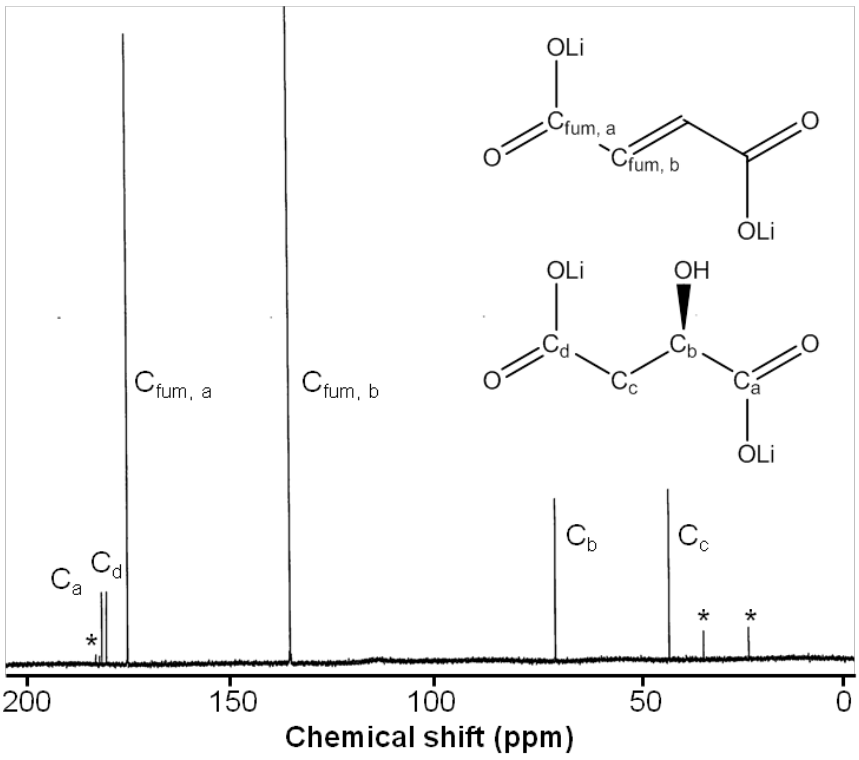

Figure 43. ^{13}C NMR spectrum of $Li_2(mal)_{0.23}(fum)_{0.77}$ dissolved in D_2O, showing peak assignments according to the ligand structures. Asterisks mark malic acid impurity peaks.

4.3.3.3. Confirmation of ligand transformation by FTIR

Comparison of the infrared spectra of Li_2(mal) and Li_2(L-mal)$_{0.23}$(fum)$_{0.77}$ reveal a reduction in the intensity of the bands corresponding to the malate O-H stretch (3440 cm^{-1}) and C-OH stretch (1070 cm^{-1}), and the appearance of a band at 970 cm^{-1} due to the formation of the fumarate *trans* C=C double bond (Figure 44).

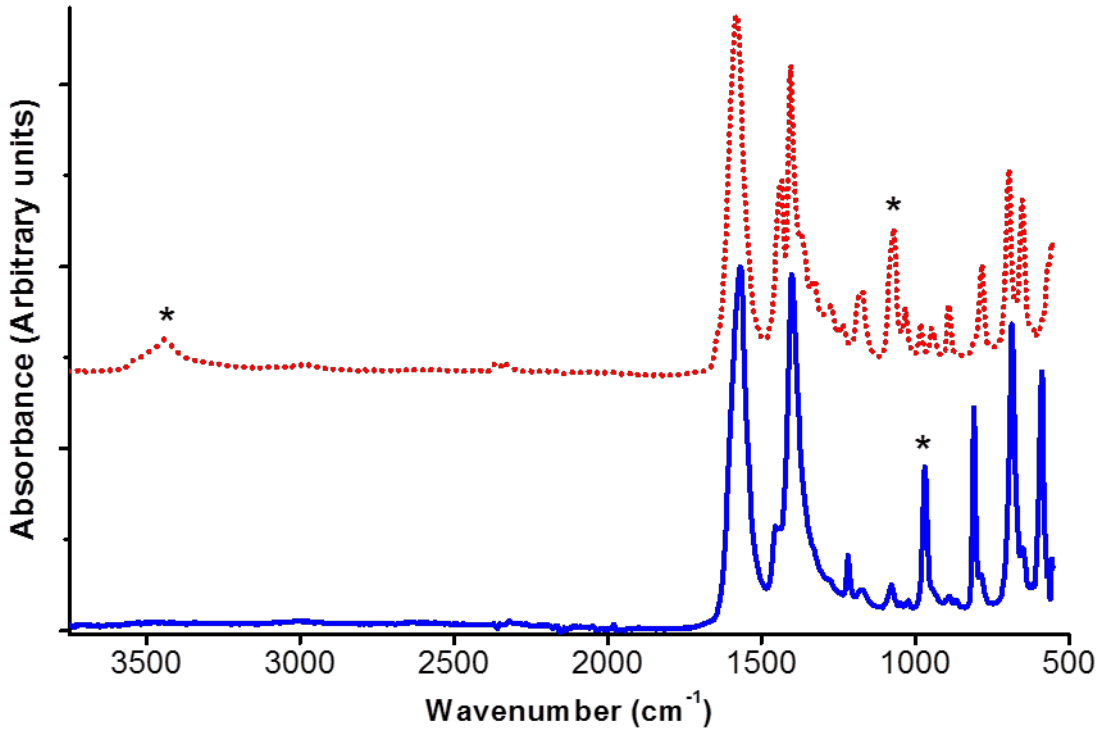

Figure 44. Fourier-transform infrared spectra of Li_2(mal) (red dotted line) and Li_2(L-mal)$_{0.23}$(fum)$_{0.77}$ (blue solid line). Asterisks mark the malate O-H and C-OH stretching bands and fumarate trans HC=CH out of plane deformation band at 3440 cm^{-1}, 1070 cm^{-1} and 970 cm^{-1}, respectively.

4.3.3.4. Variation in cell parameter as a function of fumarate fraction, *x*

Further structure determination was performed on crystals of Li_2(mal) exposed to different heat treatments, in order to observe changes in the unit cell as a function of fumarate fraction, *x*. The results are shown in Table 6.

Heat treatment	none	320 °C 10 hours	320 °C 22 hours	350 °C 20 hours
Fumarate fraction, *x*	0	0.575(12)	0.772(8)	0.800(14)
a / Å	11.8771(11)	11.8093(10)	11.7600(6)	11.7253(15)
c / Å	10.7193(10)	10.9615(11)	11.0689(7)	11.126(2)
V / Å^3	1309.5(2)	1323.9(2)	1325.71(13)	1324.7(4)
d_{calc} (g cm^{-3})	1.666	1.531	1.487	1.484
R_1	0.0412	0.0513	0.0425	0.0847

Table 6. Cell parameter and fumarate fraction variation in $Li_2(L\text{-mal})_{1-x}(fum)_x$ as a function of heat treatment.

The most striking change from the original structure is an increase in unit cell volume with fumarate fraction, *x*. This expansion is highly anisotropic: whilst the *c*-axis increases in length by around 4 %, the *a*-axis actually decreases by 1 %. This may be due to the rigidity of the planar fumarate ligand, which forces the inorganic part of the framework to distort, rather than the loss of hydroxyl groups (which would instead cause expansion in the *ab*-plane). Accompanying this change is a decrease in density of around 10 %, as a result of the loss of over three H_2O units per four ligands in the structure as well as the cell expansion. Attempts to reach complete conversion to pure lithium fumarate by increasing the heating temperature to 350 °C were unsuccessful. Crystal quality of the resulting product was poor, as demonstrated by the refinement indicator $R_1 = 0.0847$, and around 20 % of the malate ligand remained. In addition, powder X-ray diffraction analysis of the bulk product showed formation of trace Li_2CO_3, indicative of framework decomposition.

4.4. Conclusions

The crystal structures of four new non-porous lithium-based inorganic-organic frameworks, lithium tetrafluorosuccinate and lithium methylsuccinate, and lithium L-malate and lithium (L malate)$_{0.23}$(fumarate)$_{0.77}$, have been determined and found to be isostructural and almost isostructural, respectively, with lithium succinate, which has 3-D inorganic connectivity. The atomic structures and cell parameters are found to vary with different ligand substituents, whilst the overall framework topology remains constant. The effect of ligand substitution on the mechanical properties and thermal stability was investigated in detail. Methylation of the succinate ligand results in a highly strained structure, in which both Li-O bonds and the unit cell volume expand relative to lithium succinate and in which thermal stability is reduced. Fluorination results in cell expansion, decreased yield stress and even lower thermal stability, due to elongation of Li-O framework bonds. However, the fluorinated structure has the highest elastic modulus and hardness due to increased packing density and ligand rigidity. Incorporation of a chiral hydroxyl group on the ligand results in a similar increase in elastic modulus and hardness, due to the combination of packing density and inter-ligand hydrogen bonding. In this case, however, the unit cell volume is lower than lithium succinate due to contraction caused by the hydrogen bonding.

Binary and ternary mixed-ligand non-porous inorganic-organic frameworks have been synthesized for the first time. Mechanochemical reactions between the pure end-members lithium succinate, lithium tetrafluorosuccinate, lithium L-malate and lithium methylsuccinate yielded single phase, homogeneous materials, whose composition was confirmed by high-resolution powder X-ray diffraction and solid state NMR experiments. The effect of composition on atomic structure and cell parameters were investigated by Rietveld and Le Bail refinement and found to vary with ligand substituent. In the binary solid solution lithium (succinate)$_{1-x}$(tetrafluorosuccinate)$_x$, cell volume varies linearly with x and exhibits an overall increase of 7 %, which enables good differentiation between X-ray diffraction peaks and thus confirmation of single-phase behaviour. Analysis of the solid state MAS-NMR ^{13}C cross-polarisation build-up curves for the phase with composition $x = 0.5$ also confirms the proximity of hydrogenated and fluorinated ligands on the atomic scale. In the ternary mixed-ligand system lithium (succinate)$_x$(L-malate)$_y$(methylsuccinate)$_z$, cell volume varies linearly with z but is essentially unchanged when $x + y = constant$. Interestingly, the presence of the chiral L-malate ligand breaks the centric symmetric of the bulk phase, involving a transition

from space group $R\bar{3}$ to $R3$. This means that the phases are not strictly solid solutions, but may be called "topologically similar" disordered mixed-ligand phases.

Topochemical dehydration was observed upon heating lithium L-malate up to 320 °C. The resulting structure, a disordered mixed-ligand phase with composition lithium $(\text{L-malate})_{1-x}(\text{fumarate})_x$, was investigated by single crystal X-ray diffraction and found to exhibit anisotropic expansion with increasing x. The composition of the product was confirmed by solution NMR and FTIR, but thermal decomposition of the framework at higher temperatures gives rise to a ligand transformation limit of $x \approx 0.8$.

Overall, it has been demonstrated for the first time that ligand solid solutions and "topologically similar" disordered mixed-ligand phases can be formed in 3-D non-porous inorganic-organic frameworks, both by mechanosynthesis and by topotactic dehydration. This represents a novel way to introduce disorder into what are commonly regarded as very rigid, ordered, crystalline systems. Although no lithium conductivity was observed in the samples tested from this work, it nonetheless demonstrates the potential to induce ligand-based disorder into the structure, which may have potential in controlling the structures and properties of other inorganic-organic framework systems. It is apparent that modifying the chemical functionality on framework ligands can induce changes in various structural elements, such as cell parameters, metal coordination and ligand conformation. This could offer a profound enhancement of the control of physical properties of functional inorganic-organic frameworks, such as their electronic, magnetic and optical properties.

4.5. Future work

4.5.1. *Parent compounds*

The single crystal structure of lithium methylsuccinate consists of both enantiomeric isomers of the ligand, due to *in-situ* isomerisation. This leads to the question of whether or not the same structure can be formed directly from the racemic acid, which may require a lower synthesis temperature because there are already equal quantities of each enantiomer present. In addition, it could enable a more ordered structure to be formed, and perhaps better crystallization. This would have an effect on the local structure, which could be investigated by examining changes in features such as the Li bond valence sum and root mean squared O-Li-O angle. If crystals of sufficient size could be grown, it would also be interesting to investigate the effect of the purely bulky methyl substituent on the mechanical properties of Li_2(met). This would provide a useful comparison to those with mechanical properties already measured by nanoindentation, Li_2(suc), Li_2(flu) and Li_2(mal), but without hydrogen bonding or elongated Li-O bonding.

4.5.2. *Mixed-ligand compounds*

It would be interesting to investigate non-porous inorganic-organic frameworks based on metals other than lithium for substitutional behaviour on the ligand sublattice, as a way to gain fine control over their physical properties. As described in Section 4.1.1, the effects of ligand substitution on porous frameworks are beginning to be investigated, but this is an as yet unexplored concept in non-porous frameworks. Tuning of the organic and inorganic structural elements could have interesting consequences for properties such as magnetism, ferroelectric behaviour, luminescence and electrical conductivity. It may be also be advantageous to develop synthesis methods that allow ligand solid solution behaviour in samples with morphologies other than fine powders obtained by mechanochemical synthesis, such as thin films and single crystals, which would enable the use of a wider range of measurement techniques.

The observation of mixed-ligand phases in which the parent compounds contain both achiral and chiral ligands, such as $Li_2(suc)_x(mal)_y(met)_z$, raises questions about the chirality of the bulk materials, since they are technically not solid solutions. Of particular interest is the effect of low concentrations of chiral ligands in a bulk achiral phase, and the effect of increasing the concentration of localised chiral point defects on the overall chirality. One

possible means to study this would be solid-state circular dichroism, which gives a characteristic signal depending on the chirality of the material studied and has previously been used to confirm the chirality of inorganic-organic frameworks.[58]

4.5.3. *Topotactic dehydration*

Formation of ligand solid solutions via topotactic thermal dehydration may be one way to control stoichiometry in single crystals, and as such should be investigated further. In the case of lithium (L malate)$_{1-x}$(fumarate)$_x$, control over x with thermal treatment conditions must be mapped out more thoroughly. It may also be possible to increase the limit of x by altering treatment conditions, such as using an inert atmosphere or vacuum to reduce framework decomposition and to increase the entropic driving force associated with water loss.

Topotactic thermal ligand dehydration may be a way not only to induce solid solution behaviour, but also to increase the porosity or functionality of porous inorganic-organic frameworks. Further treatment of the unsaturated framework ligand after heat treatment, such as addition of HX (where X is any anionic functional group) over the C=C double bond, could introduce new chemical functionality into framework architectures that may not readily form such structures directly.

4.6. References

(1) Li, H.; Eddaoudi, M.; O'Keeffe, M.; Yaghi, O. M. *Nature* **1999**, *402*, (6759), 276-279.
(2) Eddaoudi, M.; Kim, J.; Rosi, N.; Vodak, D.; Wachter, J.; O'Keeffe, M.; Yaghi, O. M. *Science* **2002**, *295*, (5554), 469-472.
(3) Phan, A.; Doonan, C. J.; Uribe-Romo, F. J.; Knobler, C. B.; O'Keeffe, M.; Yaghi, O. M. *Acc. Chem. Res.* **2010**, *43*, (1), 58-67.
(4) Hayashi, H.; Cote, A. P.; Furukawa, H.; O'Keeffe, M.; Yaghi, O. M. *Nat. Mater.* **2007**, *6*, (7), 501-506.
(5) Rosi, N. L.; Eckert, J.; Eddaoudi, M.; Vodak, D. T.; Kim, J.; O'Keeffe, M.; Yaghi, O. M. *Science* **2003**, *300*, (5622), 1127-1129.
(6) Wu, C. D.; Hu, A.; Zhang, L.; Lin, W. B. *J. Am. Chem. Soc.* **2005**, *127*, (25), 8940-8941.
(7) (a) Liu, Y. Y.; Zhang, J.; Xu, F.; Sun, L. X.; Zhang, T.; You, W. S.; Zhao, Y.; Zeng, J. L.; Cao, Z.; Yang, D. W. *Cryst. Growth Des.* **2008**, *8*, (9), 3127-3129. (b) Horike, S.; Shimomura, S.; Kitagawa, S. *Nat. Chem.* **2009**, *1*, (9), 695-704.
(8) Saint Remi, J. C.; Remy, T.; Van Hunskerken, V.; van de Perre, S.; Duerinck, T.; Maes, M.; De Vos, D.; Gobechiya, E.; Kirschhock, C. E. A.; Baron, G. V.; Denayer, J. F. M. *Chemsuschem* **2011**, *4*, (8), 1074-1077.
(9) (a) Kim, Y. J.; Jung, D. Y.; Hong, K. P.; Demazeau, G. *Solid State Sci.* **2001**, *3*, (8), 837-846. (b) Culp, J. T.; Fanucci, G. E.; Watson, B. C.; Morgan, A. N.; Backov, R.; Ohnuki, H.; Meisel, M. W.; Talham, D. R. *J. Solid State Chem.* **2001**, *159*, (2), 362-370. (c) Coronado, E.; Galan-Mascaros, J. R.; Gomez-Garcia, C. J.; Murcia-Martinez, A. *Chem.-Eur. J.* **2006**, *12*, (13), 3484-3492. (d) Beghidja, A.; Rabu, P.; Rogez, G.; Welter, R. *Chem.-Eur. J.* **2006**, *12*, (29), 7627-7638. (e) Furman, J. D.; Burwood, R. P.; Tang, M.; Mikhailovsky, A. A.; Cheetham, A. K. *J. Mater. Chem.* **2011**, *21*, (18), 6595-6601. (f) Saines, P. J.; Yeung, H. H.-M.; Hester, J. R.; Lennie, A. R.; Cheetham, A. K. *Dalton Trans.* **2011**, *40*, (24), 6401-6410.
(10) Appelhans, L. N.; Kosa, M.; Radha, A. V.; Simoncic, P.; Navrotsky, A.; Parrinello, M.; Cheetham, A. K. *J. Am. Chem. Soc.* **2009**, *131*, (42), 15375-15386.
(11) Saines, P. J.; Jain, P.; Cheetham, A. K. *Chem. Sci.* **2011**, *2*, (10), 1929-1939.
(12) Lee, E.; Kim, Y.; Jung, D. Y. *Inorg. Chem.* **2002**, *41*, (3), 501-506.
(13) Livage, C.; Egger, C.; Nogues, M.; Férey, G. *Comptes Rendus Acad. Sci. Ser. II C* **2001**, *4*, (3), 221-226.
(14) Cheetham, A. K.; Rao, C. N. R.; Feller, R. K. *Chem. Commun.* **2006**, (46), 4780-4795.
(15) Kaduk, J. A. *Acta Crystallogr., Sect. B: Struct. Sci.* **2000**, *56*, 474-485.
(16) Banerjee, D.; Kim, S. J.; Parise, J. B. *Cryst. Growth Des.* **2009**, *9*, (5), 2500-2503.
(17) (a) Appel, F.; Wagner, R. *Mater. Sci. Eng. R-Rep.* **1998**, *22*, (5), 187-268. (b) Fahrenholtz, W. G.; Hilmas, G. E.; Talmy, I. G.; Zaykoski, J. A. *J. Am. Ceram. Soc.* **2007**, *90*, (5), 1347-1364.
(18) Schlapbach, L.; Zuttel, A. *Nature* **2001**, *414*, (6861), 353-358.
(19) (a) Damjanovic, D. *Rep. Prog. Phys.* **1998**, *61*, (9), 1267-1324. (b) Catalan, G.; Scott, J. F. *Adv. Mater.* **2009**, *21*, (24), 2463-2485.
(20) (a) Osterloh, F. E. *Chem. Mater.* **2008**, *20*, (1), 35-54. (b) Kudo, A.; Miseki, Y. *Chem. Soc. Rev.* **2009**, *38*, (1), 253-278.
(21) Murakami, M.; Sakai, N.; Higuchi, T.; Yoo, S. I. *Supercond. Sci. Technol.* **1996**, *9*, (12), 1015-1032.
(22) Hoppe, H. A. *Angew. Chem.-Int. Edit.* **2009**, *48*, (20), 3572-3582.

(23) (a) Iwahara, H.; Uchida, H.; Ono, K.; Ogaki, K. *J. Electrochem. Soc.* **1988**, *135*, (2), 529-533. (b) Stramare, S.; Thangadurai, V.; Weppner, W. *Chem. Mater.* **2003**, *15*, (21), 3974-3990.
(24) (a) Corma, A. *Chem. Rev.* **1995**, *95*, (3), 559-614. (b) Cheetham, A. K.; Férey, G.; Loiseau, T. *Angew. Chem.-Int. Edit.* **1999**, *38*, (22), 3268-3292.
(25) Ishihara, T.; Matsuda, H.; Takita, Y. *J. Am. Chem. Soc.* **1994**, *116*, (9), 3801-3803.
(26) Denton, A. R.; Ashcroft, N. W. *Phys. Rev. A* **1991**, *43*, (6), 3161-3164.
(27) (a) Deng, H. X.; Doonan, C. J.; Furukawa, H.; Ferreira, R. B.; Towne, J.; Knobler, C. B.; Wang, B.; Yaghi, O. M. *Science* **2010**, *327*, (5967), 846-850. (b) Burrows, A. D. *CrystEngComm* **2011**, *13*, (11), 3623-3642.
(28) Marx, S.; Kleist, W.; Huang, J.; Maciejewski, M.; Baiker, A. *Dalton Trans.* **2010**, *39*, (16), 3795-3798.
(29) (a) Taylor-Pashow, K. M. L.; Della Rocca, J.; Xie, Z. G.; Tran, S.; Lin, W. B. *J. Am. Chem. Soc.* **2009**, *131*, (40), 14261. (b) Kleist, W.; Jutz, F.; Maciejewski, M.; Baiker, A. *Eur. J. Inorg. Chem.* **2009**, (24), 3552-3561. (c) Adams, C. J.; Haddow, M. F.; Lusi, M.; Orpen, A. G. *Proc. Natl. Acad. Sci. U. S. A.* **2010**, *107*, (37), 16033-16038. (d) Fukushima, T.; Horike, S.; Inubushi, Y.; Nakagawa, K.; Kubota, Y.; Takata, M.; Kitagawa, S. *Angew. Chem.-Int. Edit.* **2010**, *49*, (28), 4820-4824. (e) Kleist, W.; Maciejewski, M.; Baiker, A. *Thermochim. Acta* **2010**, *499*, (1-2), 71-78.
(30) Klapper, H.; Kuppers, H. *Acta Crystallogr. Sect. B-Struct. Commun.* **1973**, *B29*, 21-26.
(31) Spek, A. L. *Acta Crystallogr. Sect. D-Biol. Crystallogr.* **2009**, *65*, 148-155.
(32) Augustsson, A.; Herstedt, M.; Guo, J. H.; Edstrom, K.; Zhuang, G. V.; Ross, P. N.; Rubensson, J. E.; Nordgren, J. *Phys. Chem. Chem. Phys.* **2004**, *6*, (16), 4185-4189.
(33) (a) Friscic, T.; Fabian, L. *CrystEngComm* **2009**, *11*, (5), 743-745. (b) Beldon, P. J.; Fabian, L.; Stein, R. S.; Thirumurugan, A.; Cheetham, A. K.; Friscic, T. *Angew. Chem.-Int. Edit.* **2010**, *49*, (50), 9640-9643.
(34) Friscic, T.; Jones, W. *Cryst. Growth Des.* **2009**, *9*, (3), 1621-1637.
(35) Bennett, T. D.; Cao, S.; Tan, J.-C.; Keen, D. A.; Bithell, E. G.; Beldon, P. J.; Friscic, T.; Cheetham, A. K. *J. Am. Chem. Soc.* **2011**, *133*, (37), 14546-14549.
(36) Tan, J.-C.; Cheetham, A. K. *Chem. Soc. Rev.* **2011**, *40*, (2), 1059-1080.
(37) Chapman, K. W.; Halder, G. J.; Chupas, P. J. *J. Am. Chem. Soc.* **2009**, *131*, (48), 17546-17547.
(38) Ameloot, R.; Stappers, L.; Fransaer, J.; Alaerts, L.; Sels, B. F.; De Vos, D. E. *Chem. Mater.* **2009**, *21*, (13), 2580-2582.
(39) Tan, J.-C.; Bennett, T. D.; Cheetham, A. K. *Proc. Natl. Acad. Sci. U. S. A.* **2010**, *107*, (22), 9938-9943.
(40) Bahr, D. F.; Reid, J. A.; Mook, W. M.; Bauer, C. A.; Stumpf, R.; Skulan, A. J.; Moody, N. R.; Simmons, B. A.; Shindel, M. M.; Allendorf, M. D. *Phys. Rev. B* **2007**, *76*, (18).
(41) Bennett, T. D.; Tan, J.-C.; Moggach, S. A.; Galvelis, R.; Mellot-Draznieks, C.; Reisner, B. A.; Thirumurugan, A.; Allan, D. R.; Cheetham, A. K. *Chem.-Eur. J.* **2010**, *16*, (35), 10684-10690.
(42) (a) Tan, J.-C.; Furman, J. D.; Cheetham, A. K. *J. Am. Chem. Soc.* **2009**, *131*, (40), 14252-14254. (b) Kosa, M.; Tan, J.-C.; Merrill, C. A.; Krack, M.; Cheetham, A. K.; Parrinello, M. *Chemphyschem* **2010**, *11*, (11), 2332-2336.
(43) Tan, J.-C.; Merrill, C. A.; Orton, J. B.; Cheetham, A. K. *Acta Mater* **2009**, *57*, (12), 3481-3496.
(44) Retsch Ltd., 3 California Drive, Castleford, West Yorkshire, WF10 5QH, UK.
(45) Parr Instrument Company, 211 53rd St., Moline, Illinois 61265 USA.
(46) MTS Corp., 14000 Technology Drive, Eden Prairie, MN USA 55344

(47) (a) Lilleodden, E. T.; Zimmerman, J. A.; Foiles, S. M.; Nix, W. D. *J. Mech. Phys. Solids* **2003**, *51*, (5), 901-920. (b) Kumar, P.; Kiran, M. *Nanoscale Res. Lett.* **2010**, *5*, (7), 1085-1092.
(48) (a) Oliver, W. C.; Pharr, G. M. *J. Mater. Res.* **1992**, *7*, (6), 1564-1583. (b) Oliver, W. C.; Pharr, G. M. *J. Mater. Res.* **2004**, *19*, (1), 3-20.
(49) (a) Vlassak, J. J.; Nix, W. D. *J. Mech. Phys. Solids* **1994**, *42*, (8), 1223-1245. (b) Bei, H.; George, E. P.; Pharr, G. M. *Scr. Mater.* **2004**, *51*, (9), 875-879. (c) Fischer-Cripps, A. C., *Introduction to Contact Mechanics*. Ling, F. F., Ed.; 2nd ed.; Springer: New South Wales, **2007**.
(50) Carrell, C. J.; Carrell, H. L.; Erlebacher, J.; Glusker, J. P. *J. Am. Chem. Soc.* **1988**, *110*, (26), 8651-8656.
(51) Brese, N. E.; O'Keeffe, M. *Acta Crystallogr., Sect. B: Struct. Sci.* **1991**, *47*, 192-197.
(52) Harding, M. *Acta Crystallographica Section D* **2000**, *56*, (7), 857-867.
(53) (a) Hulvey, Z.; Furman, J. D.; Turner, S. A.; Tang, M.; Cheetham, A. K. *Cryst. Growth Des.* **2010**, *10*, (5), 2041-2043. (b) Friscic, T.; Reid, D. G.; Day, G. M.; Duer, M. J.; Jones, W. *Cryst. Growth Des.* **2011**, *11*, (4), 972-981.
(54) Allan, J. R.; Carson, B. R.; Gerrard, D. L.; Hoey, S. *Thermochim. Acta* **1990**, *158*, (1), 91-97.
(55) Vegard, L. *Z. Phys.* **1921**, *5*, 17-26.
(56) Lajzerowicz, J.; Chion, B. *J. Chem. Phys.* **1981**, *74*, (6), 3500-3509.
(57) Cousins, K. R. *J. Am. Chem. Soc.* **2011**, *133*, (21), 8388-8388.
(58) (a) Fielden, J.; Quasdorf, K.; Ellern, A.; Kogerler, P. *Eur. J. Inorg. Chem.* **2009**, (6), 717-720. (b) Liu, L.; Huang, S. P.; Yang, G. D.; Zhang, H.; Wang, X. L.; Fu, Z. Y.; Dai, J. C. *Cryst. Growth Des.* **2010**, *10*, (2), 930-936. (c) Liang, X. Q.; Jia, J. T.; Wu, T.; Li, D. P.; Liu, L.; Tsolmon; Zhu, G. S. *CrystEngComm* **2010**, *12*, (11), 3499-3501.

Chapter 5. Structure control, electrochemical behaviour and ionic transport in lithium-based frameworks

5.1. Introduction

This chapter considers the diverse structures of lithium-based inorganic-organic frameworks, and investigates the factors affecting their structures and properties, particularly for lithium battery applications. The rise of lithium ion batteries in the last two decades as the principle means of energy storage for small-scale, portable electronic devices is underpinned by the large electrode potential and low mass of lithium, which result in batteries with higher energy density than any other system. This has meant that mass energy storage for clean electric vehicles, renewable sources and grid applications is starting to become a reality. However, significant issues remain that must be overcome for them to make a significant difference. Safety and longevity are of prime concern, alongside increases in energy and power density, in order to make them viable on a large scale in the long term.[1]

The other notable potential application of lithium-containing frameworks is in gas sorption. Incorporation of lithium, which has high charge density, is beneficial to both the interaction of framework walls with small molecules and the gravimetric storage capacity of the material.[2] Thus, lithium-containing MOFs are promising candidates for hydrogen storage,[2a, 3] carbon dioxide sequestration[4] and sensing applications.[2b]

Fundamentally, the physical properties of any material are a result of the chemistry and structure of its component atoms and molecules. In order to design better materials, an understanding of the relationship between structure and properties is vital, as is knowledge of how to manipulate and synthesize materials with desirable properties. In this chapter, four new lithium-based inorganic-organic framework structures are reported that contain a variety of ligands and topologies. Non-porous, anhydrous structures in particular were targeted due to the lower chemical and thermal stability of compounds containing water or other small solvent molecules.[5] The diversity of the new compounds is discussed alongside other known lithium-based inorganic-organic frameworks, and trends in their structures are examined. The results of electrochemical cycling and conductivity measurements on some of these materials are discussed, exploring their potential as anode materials and solid electrolytes in lithium batteries.

5.1.1. *Structure control in lithium-based inorganic-organic frameworks*

The coordination sphere of lithium, and indeed of other *s*-block cations, is less rigid than those of many transition metals, which adopt certain geometries determined by crystal field

stabilisation effects. Therefore, the architectures of lithium-based inorganic-organic frameworks are determined less by the geometry of secondary building units, SBUs, and more by ligand conformation and other crystal packing effects. In addition, lithium is extremely hydrophilic and coordination by water and other small molecules can result in reduced connectivity and lower thermal stability in inorganic-organic frameworks.[5] These factors certainly have a significant effect on the structures of lithium-based frameworks, and so their control and possible design will require a different approach to that applied to transition metal-based inorganic-organic frameworks.

In their recent review on *s*-block metal coordination networks (CNs), Banerjee *et al*. summarized the structures of some lithium-based frameworks,[6] but omitted a number of important examples. They did, however, note that "the structural chemistry of lithium CNs is dominated by the metal's tendency to favour tetrahedral coordination with carboxylate oxygen atoms and by network topologies that depend strongly on the nature of organic linkers".[6] In addition, they observed that lithium ions are often coordinated by polar solvents, and that connectivity between LiO_4 units ranges from isolated to layered edge-linked tetrahedra. Fromm[7] made similar comments in a previous review, adding that structures "can be governed by the capacity of the ligand to bridge between metal ions, i.e. its steric demand as well as its number and position of donor sites".[7] However, very few examples were described, and the author's scope was limited to examples of specific interest to organometallic chemistry.

The compounds and analysis described in this chapter offer new insight into the overall structural trends of lithium-based inorganic-organic frameworks, which may help to design structures with properties tailored towards specific applications, such as lithium batteries and gas storage. In particular, a much wider diversity than previously observed has been uncovered in lithium dicarboxylates, involving structures with connectivities spanning all I^mO^n combinations, as defined by Cheetham *et al*.[8] Trends have been investigated in the structures of 49 lithium dicarboxylate frameworks, including those previously reported and 18 reported for the first time in this thesis. Three classes of ligands were identified: those with linear, bent or flexible conformations (Figure 1), which affect the type of structure produced, as does the metal:ligand ratio and the degree of solvation.

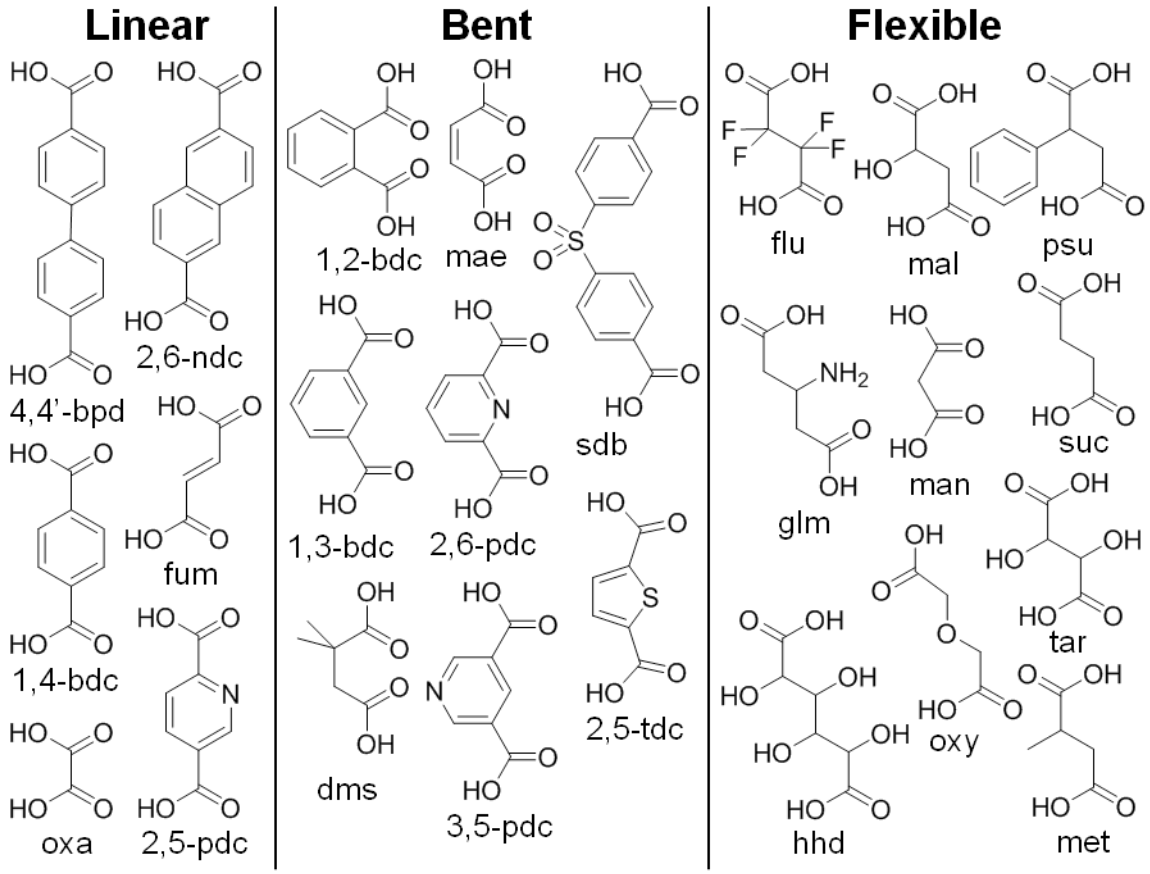

Figure 1. Dicarboxylic acid ligands used in lithium-based inorganic-organic frameworks, grouped by the conformational relationship between carboxylate groups.

5.1.2. *Battery-related properties of lithium-containing inorganic-organic frameworks*

5.1.2.1. Negative electrode behaviour of lithium-containing inorganic-organic materials

Organic materials have been investigated as active components in lithium batteries since the 1960's,[9] with substantial efforts made in the areas of organosulfur compounds, organic radicals and carbonyl compounds, which have recently been subject of a comprehensive review by Liang *et al*.[10] Most of these materials operate at voltages suitable for positive electrodes, and negative electrode materials have been investigated far less frequently due to the already satisfactorily high capacity of metallic lithium. However, use of metallic lithium in lithium batteries creates serious problems due to the formation of dendrites upon charging, which eventually lead to short-circuiting.[11] This fatal problem can be avoided by replacing lithium with carbonaceous materials such as graphite, into which ionic lithium can insert, but they compromise capacity and suffer initial capacity loss and potential safety issues due to operation at potentials lower than the stability window of conventional electrolytes.[12] Development of intermetallic compounds, particularly those based on tin and silicon, which

offer charge densities close to metallic lithium and also tuneable operating potential, has so far been unable to overcome problems associated with large changes in structure and volume upon charging and discharging and high initial capacity loss.[13]

A renewed effort has recently been made to discover materials with low operating potentials that may be high-capacity, high-safety alternatives to existing anode materials.[14] Chen *et al.* reported the redox chemistry of the tetralithium salt of tetrahydroxybenzoquinone, $Li_xC_6O_6$ (where $x = 4$), which can be both reduced to $x = 2$ and oxidised to $x = 6$.[14a, b] This two-way process meant that a symmetric cell could be constructed, which showed reasonable capacity retention of over 100 mA h g^{-1} after 50 cycles. Furthermore, the material could be synthesized from biomass sources, potentially leading the way for more "sustainable" materials to be investigated.

Lithium dicarboxylates have also received attention as anode materials, potentially reacting with up to one extra lithium ion per carboxylate group, which leads to high theoretical capacities (Figure 2). Lithium terephthalate, Li_2(1,4-bdc) chemical formula $Li_2(C_8H_4O_4)$, and lithium *trans-trans*-muconate, $Li_2(C_6H_4O_4)$, are capable of reversibly reacting with two and one lithium ions per formula unit, giving reversible capacities of 300 mA h g^{-1} at 0.8 V and 150 mA h g^{-1} at 1.4 V, respectively.[14c] The charged nature of these materials means that their component ions have low solubility in conventional electrolytes, improving their cyclability compared to small-molecule carbonyl compounds. Their crystal structure of Li_2(1,4-bdc) shows it to be a three-dimensional, I^2O^1 framework,[15] and this may be important in further enhancing stability, which is evident in its maintained activity at 80 °C with polymer electrolytes. In addition, the thermal decomposition of both materials was shown to be far less exothermic than carbonaceous electrodes, resulting in safer cells.

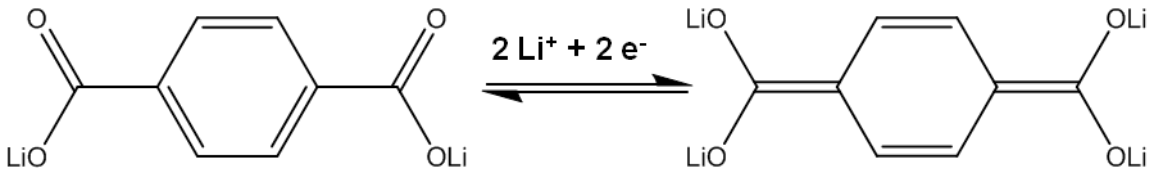

Figure 2. Schematic of the reversible electrochemical reduction of lithium terephthalate.[14c]

This work was extended by Walker *et al.*, who investigated the effect of conjugation length and *cis*/*trans* isomerisation on the dicarboxylates $LiO_2C(CH{=}CH)_nCO_2Li$, where $n = 1 - 4$.[14e] The crystal structures of these materials were not determined, but it was found that compounds featuring *trans* C=C double bonds with $n = 2 - 4$ reversibly react with ~ 1 Li per

formula unit at potentials below 1.5 V that increased with *n*, giving capacities up to 160 mA h g^{-1}. In contrast, the *cis* isomers had similar operating potentials but showed very little reversibility, whilst dilithium fumarate, the *trans* isomer with *n* = 1, was reported to have no activity. The trends in operating potential were explained by increasing conjugation length lowering the energy required for reduction, whilst the inability to react with two Li per formula unit was put down to the proximity of carboxylate groups on the ligand. The lack of reversibility in the *cis* isomers was suggested to be a result of molecular packing, but remained unclear.

The same group investigated lithium 4,4-tolane-dicarboxylate, $Li_2(C_{16}H_8O_4)$ (Figure 3), which has longer conjugation and shows reversible capacity of ~200 mAh g^{-1} at ~0.65 V.[14f] The capacity of this compound changed dramatically depending on whether crystallized from methanol or ethanol, indicating that both morphological and crystallographic effects were important factors in its performance. However, they were unable to obtain any crystal structures of the two structural isomers, so the effect of polymorphism remains unclear. In addition, the mechanism of reduction was investigated using DFT calculations and EPR spectroscopy, but failed to reveal any conclusive insight on the process.

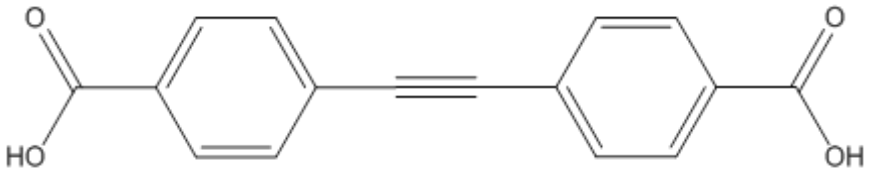

Figure 3. Structure of 4,4-tolane dicarboxylic acid.

It should be noted that other mechanisms for electrode behaviour, such as metal-based redox[16] and guest-based redox,[17] have also been reported in MOFs but despite the promising properties reported to date, the work described above highlights a lack of understanding of the structures and mechanisms involved in the electrochemical behaviour of lithium dicarboxylate materials. It is hoped that the structural diversity and trends in the frameworks described in this chapter may lead to greater understanding of the electrochemical behaviour of lithium dicarboxylates. Electrochemical cycling measurements have been performed on three compounds and the results are presented herein.

5.1.2.2. Ionic conductivity of inorganic-organic frameworks

In the early 2000's, Kitagawa and co-workers investigated the proton conductivity of a number of copper coordination polymers featuring dithiooxamide derivatives, Cu(R_2-dtoa)

(where R = H, C_2H_4OH etc.), under hydrogen gas and humid conditions.[18] The crystal structures of the compounds were not determined, but shown by extended X-ray absorption fine structure analysis to consist of square planar dimeric copper (II) units, whose open site acidity enabled release of protons by coordinated water molecules within the structure. Conductivities of the order of 10^{-5} S cm^{-1} were achieved. A similar approach was used by Jeong *et al.*, who reported conductivity of 1.5×10^{-2} S cm^{-1} in the as-synthesized I^0O^3 framework, Cu_3(1,3,5-benzenetricarboxylate)$_2(H_2O)_3$ (also known as HKUST-1), following sorption of methanol.[19] Conductivity was reduced if the acidic water coordinated to the Cu^{II} centres was replaced with acetonitrile (Figure 4), or if the charge-carrying methanol was replaced by hexane, blocking the proton transfer pathway.

Figure 4. Representation of proton conductivity in HKUST-1, structure shown left, via acidity of water molecules adsorbed at open sites, top right, which is reduced dramatically if an aprotic acetonitrile molecule is coordinated instead (bottom right). Reproduced with permission,[19] copyright 2012 ACS.

Yamada *et al.* reported proton conductivity of 1.3×10^{-3} S cm^{-1} in the I^0O^1 coordination polymer, Fe(oxalate)$(H_2O)_2$.[20] In this case, coordinated water molecules again act as the proton source, but are ordered along the chains of iron oxalate and are not free to diffuse through the structure. Taylor *et al.* showed that the I^0O^2 framework, Zn_3(1,3,5-benzenetriphosphonate)$(H_2O)_2 \cdot 2H_2O$, provides a conduction pathway for protons *via* an ordered array of coordinated and hydrogen-bonded water molecules between the layers.[21] This results in a low activation energy (0.17 eV), but the low acidity of protons on the coordinated water molecules gives rise to reasonably low conductivity (3.5×10^{-5} S cm^{-1}). Shigematsu *et al.* reported control of proton conductivity and activation energy *via* ligand

variation in (1,4-bdc)-based I^1O^2 frameworks Al(OH)[(R-C_6H_3)$(COO)_2$](H_2O), where R = H, NH_2, OH, and Al(OH)[(C_6H_2)$(COOH)_2(COO)_2$](H_2O).[22] The more acidic the pendant group, the higher the conductivity and lower the activation energy, achieving 2.0×10^{-6} S cm^{-1} and 0.21 eV, respectively, for R = $(COOH)_2$.

Attempts to develop conducting inorganic-organic frameworks containing mobile proton sources, rather than bound acidic groups, have met with reasonable success. Okawa *et al*. reported that uptake of water between the layers of the I^0O^2 frameworks, $NH(prol)_3[M^{II}Cr^{II}(oxalate)_3]\cdot n H_2O$ (M = Mn, Fe, Co; prol = 3-hydroxypropyl), results in an increase of six orders of magnitude to 1×10^{-4} S cm^{-1}.[23] They also investigated the effect of chain length on the alkylammonium cation, showing that the more hydrophilic the chains, the higher the conductivity, even at low humidities.[24] Pardo *et al.* showed that in the 3-D, I^0O^3 framework $(NH_4)_4[MnCr_2(oxalate)_6]\cdot 4H_2O$, helical chains of ammonium cations and disordered water molecules give rise to conductivity one order of magnitude higher (1.1×10^{-3} S cm^{-1}).[25]

There have been few attempts to create *anhydrous* inorganic-organic frameworks exhibiting proton conductivity above 100 °C, which would be useful in high-temperature fuel cell applications. Bureekaew *et al*. confined imidazole molecules within two 3-D aluminium-based inorganic-organic frameworks, MIL-53 and Al(OH)(1,4-naphthalenedicarboxylate). The different pore sizes and surfaces resulted in different packing arrangements and therefore different mobilities of the guest charge carriers. The flat, hydrophobic surface of the latter framework resulted in higher conductivity (2.2×10^{-5} S cm^{-1} *vs.* 5.5×10^{-8} S cm^{-1}, at 120 °C). This value was subsequently improved by two orders of magnitude, to 1.7×10^{-3} S cm^{-1} at 150 °C, by replacing imidazole guests with flexible histamine molecules.[26] Hurd *et al*. reported the structure of an I^0O^3 framework, Na_3(2,4,6-trihydroxyl-1,3,5-benzenetrisulfonate), which contains one-dimensional pores lined with sulfonate groups.[27] Triazole was introduced into the channels, and the resulting proton conductivity was concentration-dependant, reaching a maximum at 150 °C of 5×10^{-4} S cm^{-1} for 45 % loading, higher than the pure guest substance itself. In a proof-of-concept experiment, the material was used as a membrane in a working H_2/air cell, giving a high, stable open circuit voltage of 1.18 V at 100 °C.

The only report of lithium ion conduction in an inorganic-organic framework is the functionalisation of the I^1O^2 framework Mg_2(1,4-dioxido-2,5-benzenedicarboxylate) with

lithium isopropoxide and conventional electrolyte molecules by Wiers *et al.* (Figure 5).[28] The isopropoxide anions coordinate to open Mg^{2+} sites, leaving the lithium ions free to move through the 1-D channels solvated by the electrolyte. This results in conductivity of 3.1×10^{-4} S cm^{-1} at 300 K, with an activation energy of just 0.15 eV.

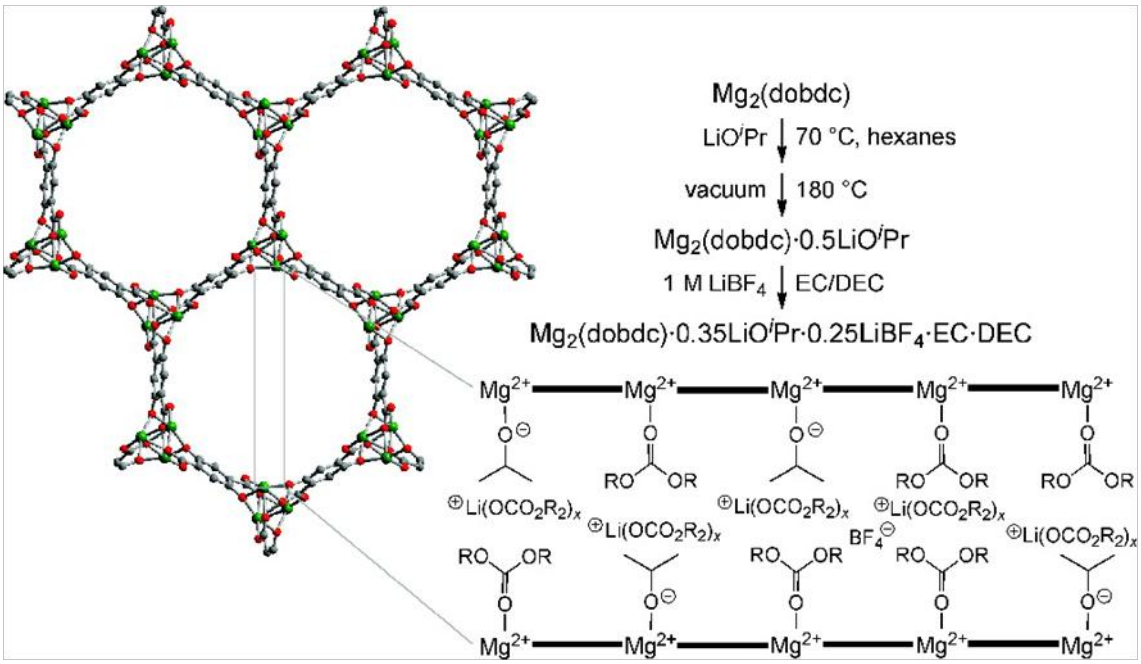

Figure 5. Structure of Mg_2(1,4-dioxido-2,5-benzenedicarboxylate) and its modification to form a solid electrolyte. A representation of a cross-sectional view along a channel is shown bottom right [R = -CH_2CH_2- (EC) or -CH_2CH_3 (DEC)). Reproduced with permission,[28] copyright 2011 ACS.

All the above materials feature guest molecules, either coordinated or mobile within a *porous* framework, which act as charge sources and/or carriers, carrying protons or lithium ions through the structure. In contrast, the new materials described in this thesis are non-porous and generally contain no guest molecules. They would therefore be free of related complications, such as low thermal stability and susceptibility to adsorption or desorption of guest molecules; however, for transport of lithium to occur alternative conduction pathways would have to be present. If reasonable conductivities were achieved in these compounds, they would present the opportunity for a more detailed investigation of the relationship between structure and ionic conductivity. Ionic conductivity measurements have been performed on seven compounds and the results are presented herein.

5.2. Experimental

5.2.1. *Synthesis*

All reagents, 2,2-dimethylsuccinic acid (99 %, Aldrich), lithium hydroxide monohydrate (reagent grade, Fisher), lithium acetate dihydrate (98 %, Acros), fumaric acid (99 %, Sigma), chlorosuccinic acid (96 %, Aldrich), D,L-malic acid (> 99.0 %, Fluka), terephthalic acid (99 %, Acros), lithium oxide (99.5 %, VWR), succinic acid (99 %, Sigma), 3-nitropropionic acid (> 97 %, Sigma) and tetrafluorosuccinic acid (> 97.0 %, TCI) were bought and used as received. Absolute ethanol (analytical reagent grade, Fisher) and in-house deionised water were used as solvents. Crystallizations were performed in 8 - 20 ml PTFE-capped borosilicate glass vials. Solvothermal reactions were carried out in 23 ml PTFE-lined stainless steel autoclaves purchased from Parr Instrument Company.[29] Mechanochemical reactions were performed using a Retsch Mixer Mill MM400[30] equipped with stainless steel jars manufactured in-house. In these reactions an excess of lithium oxide of 10 wt.% was used to compensate for a decrease in gross lithium content due to its hygroscopic nature.

5.2.1.1. Synthesis of dilithium 2,2-dimethylsuccinate, $Li_2(dms)$, $Li_2(C_6H_8O_4)$

2,2-dimethylsuccinic acid (73 mg, 0.5 mmol) and lithium hydroxide monohydrate (42 mg, 1.0 mmol) were dissolved in minimal deionised water in a 8 ml borosilicate glass vial. Ethanol (5 ml) was added, resulting in a cloudy suspension that became clear within minutes. The vial was placed in an oven at 70 °C overnight to yield colourless flat rods, suitable ones of which were selected for single crystal X-ray diffraction. A purer sample was synthesized for further analysis by combining a solution of 2,2-dimethylsuccinic acid (146 mg, 1.0 mmol) in ethanol (5 ml) with a solution of lithium acetate dihydrate (204 mg, 2.0 mmol) in ethanol (5 ml). The mixture was placed in a 23 ml PTFE-lined stainless steel autoclave and heated at 180 °C for 3 days, after which the resulting product, colourless flat plates (101 mg, 62 %), was filtered, washed with ethanol and dried at 60 °C overnight. Elemental analysis: C 45.47 %, H 4.98 %, N 0.0 % (calculated for $Li_2C_6H_8O_4$: C 45.61 %, H 5.10 %, N 0.0 %).

5.2.1.2. Synthesis of dilithium fumarate, $Li_2(fum)$, $Li_2(C_4H_2O_4)$

Fumaric acid (0.5 mmol) and lithium hydroxide monohydrate (1.0 mmol) were dissolved in water (1 ml). Ethanol (3 ml) was added, resulting in a cloudy suspension, which became clear upon addition of the minimal amount of water. The solution was placed in a PTFE-lined

stainless steel autoclave and heated at 180 °C for four days, then cooled to room temperature. Suitable colourless blocky crystals were separated from the discoloured mother liquor for single crystal X-ray diffraction analysis. A bulk sample for further analyses was synthesized as follows: fumaric acid (5.0 mmol) and lithium hydroxide monohydrate (10.0 mmol) were dissolved in water (5 ml) and the resulting solution was filtered through cotton wool into a 12ml borosilicate glass vial. The lid was opened slightly to allow slow evaporation of the solvent and the vial was heated at 60 °C for 16 days. The white crystalline precipitate (450 mg, 70 %) was separated from the mother liquor (pH 6) by filtration, washed with water and dried in air at 60 °C overnight. Elemental analysis: C 37.51 %, H 1.49 %, N 0.0 % (calculated for $Li_2C_4H_2O_4$: C 37.55 %, H 1.58 %, N 0.0 %).

5.2.1.3. Synthesis of lithium hydrogen fumarate, LiH(fum), LiH($C_4H_2O_4$)

Fumaric acid (1.0 mmol), lithium hydroxide monohydrate (1.0 mmol) and water (2 ml) were placed in a 20 ml borosilicate glass vial and the mixture was heated at 70 °C for 30 minutes, resulting in a clear solution. Ethanol (5 ml) was added and the solution again heated at 70 °C for two days. The vial lid was then opened slightly to allow slow evaporation of the solvent. After one week a colourless crystalline precipitate had formed on the vial sides. Suitable crystals were selected for single crystal X-ray diffraction analysis. A bulk sample for further analyses was synthesized as follows: fumaric acid (2.0 mmol), lithium hydroxide monohydrate (2.0 mmol) and water (2 ml) were placed in a 20 ml borosilicate glass vial and the mixture was heated at 60 °C overnight. The lid was then opened slightly to allow slow evaporation of the solvent over one week. The product, colourless crystals (241 mg, 99 %) was washed in ethanol and dried overnight at 60 °C in air. Elemental analysis: C 39.40 %, H 2.46 %, N 0.0 % (calculated for $LiC_4H_3O_4$: C 39.38 %, H 2.48 %, N 0.0 %).

5.2.1.4. Synthesis of lithium hydrogen D,L-malate, LiH(D,L-mal), LiH($C_4H_4O_5$)

Chlorosuccinic acid (1.0 mmol) and lithium hydroxide monohydrate (2.0 mmol) were dissolved in water (2 ml) in a 8 ml borosilicate glass vial and heated to 60 °C for five weeks, after which the vial lid was opened slightly to allow slow evaporation of the solvent and the vial was placed in a mild thermal gradient at room temperature. After five more weeks a colourless crystalline precipitate had developed, which was filtered, washed (ethanol) and dried in air at room temperature. Suitable crystals were selected for single crystal X-ray diffraction analysis, which showed that the ligand had undergone hydrolysis, discussed in Section 5.3.1.5. A bulk sample for further analyses was synthesized as follows: D,L-malic

acid (5.0 mmol) and lithium hydroxide monohydrate (5.0 mmol) were dissolved in water (1 ml) in a 20 ml borosilicate glass vial, which was placed in a 150 °C oven for one week with the lid opened slightly to allow slow evaporation of the solvent. The white crystalline precipitate (600 mg, 86 %) was filtered from the mother liquor and dried in air overnight. Elemental analysis: C 34.04 %, H 3.38 %, N 0.0 % (calculated for $LiC_4H_4O_5$: C 34.31 %, H 3.60 %, N 0.0 %).

5.2.1.5. Mechanochemical synthesis of lithium terephthalate, Li_2(1,4-bdc), $Li_2(C_8H_4O_4)$

Terephthalic acid (1.0 mmol) and lithium oxide (1.1 mmol) were placed in a stainless steel grinding jar with two 8 mm diameter stainless steel balls. The mixture was ground for 30 minutes in the mixer mill at 25 Hz, yielding a grey powder (80 - 95 %), which was dried at 100 °C overnight. Elemental analysis: C 52.58 %, H 2.24 %, N 0.0 % (calculated for $Li_2C_8H_4O_4$: C 53.98 %, H 2.27 %, N 0.0 %), suggesting a small impurity phase was present, confirmed by TGA (see Appendix).

5.2.2. *Single crystal X-ray diffraction*

Single crystal structure determination was performed as described in Chapter 2. Due to both twinning and the fragile sheet-like nature of Li_2(dms), substantial smearing of diffraction peaks could not be avoided. The resulting low quality of the data meant that anisotropic displacement parameters (ADPs) of non-hydrogen atoms could not be refined freely without becoming ‘non-positive definite’. In order to reach a stable refinement, all oxygen atoms were constrained to have the same APD. Lithium atoms, methyl carbon atoms and all other carbon atoms were treated likewise.

5.2.3. *Powder X-ray diffraction*

Powder X-ray diffraction was performed as described in Chapter 2. Data for Li_2(dms) showed substantial preferred orientation in the [001] direction, which corresponds to the direction perpendicular to the layers and the largest crystal facets. Despite other analyses confirming the composition of the sample, many diffraction peaks could not be unambiguously assigned, suggesting some difference to the single crystal structure and the possible presence of impurity phases.

5.2.4. *Electrochemical cycling*

Electrochemical cycling was performed by Dr Brent Melot. Swagelock-type cells were assembled in an argon-filled glove box, using a Li metal disk as the negative electrode and a Whatman GF/D borosilicate glass fibre sheet saturated with LP30 electrolyte ($LiPF_6$ 1 M in ethylene carbonate-dimethyl carbonate 1:1 w/w). Samples were combined with 30 wt. % carbon (Ketjenblack, AkzoNobel) and ball-milled under argon for 8 minutes using a Retsch PM100 mixer mill. Typically, 10-12 mg of the mixed powders was used as the positive electrode per cell. Charge-discharge tests were conducted at 20 °C using a VMP system (Biologic S.A., Claix, France) operating in galvanostatic mode. Cells were typically cycled between 3.0 V and 0.5 V *vs.* Li^+/Li^0 at a rate of 1 Li^+ exchanged per 20 hours.

5.2.5. *Ionic conductivity*

Ionic conductivity was measured by Thomas Pilz on compact pressed powder pellets (diameter 6 mm, thickness 1.3 mm - 2.1 mm), placed between two ion blocking silver electrodes in a quartz tube floated with argon. A Novocontrol Alpha A 4.2 Analyzer was used with the ZG-4 interface in a 2-wire arrangement. Spectra were recorded from 1 Hz to 5 MHz during continuous heating at a rate of 0.5 K min^{-1}, controlled by the WinDeta program.[31] Impedance data was fitted using the WinFit program to give values for bulk conductivity.[32]

5.3. Results

5.3.1. *New lithium-based inorganic-organic frameworks*

The structures of four new lithium frameworks, involving the ligands 2,2-dimethylsuccinate, fumarate and D,L-malate, have been determined by single crystal X-ray diffraction (Table 1).

	Li_2(dms)	**Li_2(fum)**	**LiH(fum)**	**LiH(D,L-mal)**
formula	$Li_2(C_6H_8O_4)$	$Li_2(C_4H_2O_4)$	$LiH(C_4H_2O_4)$	$LiH(C_4H_4O_5)$
crystal size (mm)	0.4 × 0.1 × 0.04	0.9 × 0.35 × 0.05	0.9 × 0.8 × 0.7	0.2 × 0.2 × 0.05
crystal system	triclinic	triclinic	monoclinic	monoclinic
space group	*P*1	*P*1	$P2_1/c$	$C2/c$
T (K)	120(2)	120(2)	120(2)	120(2)
a (Å)	6.2511(6)	3.3392(3)	8.6330(3)	26.025(2)
b (Å)	9.8961(11)	4.9297(3)	8.3281(2)	4.9925(4)
c (Å)	12.225(2)	7.4736(5)	7.7839(3)	8.9158(8)
α (°)	101.862(13)	76.777(5)	90	90
β (°)	102.726(13)	86.619(6)	114.207(5)	102.253(8)
γ (°)	90.012(8)	78.680(6)	90	90
V (Å^3)	721.1(2)	117.421(15)	510.43(3)	1132.04(16)
asym. unit	C_{12} H_{16} Li_4 O_8	C_4 H_2 Li_2 O_4	C_4 H_3 Li O_4	C_4 H_5 Li O_5
Z	4	1	4	8
d_{calc} (g cm^{-3})	1.455	1.809	1.588	1.643
μ (mm^{-1})	0.116	0.155	0.141	0.151
refl. collected	3459	3120	6482	1957
unique refl.	3459	586	1270	1080
observed data (I > 2σ(I))	2384	558	1198	1055
parameters	104	49	91	110
R_{int}	n/a (merged data)	0.0179	0.0154	0.0129
R_1	0.0910	0.0267	0.0292	0.0462
wR_2 (I > 2σ(I))	0.2523	0.0761	0.0867	0.1205
R_1 (all data)	0.1200	0.0277	0.0306	0.0306
wR_2 (all data)	0.2695	0.0775	0.0880	0.1209
GOF	1.009	1.107	1.021	1.092

Table 1. Single crystal structure determinations for dilithium 2,2-dimethylsuccinate, Li_2(dms), dilithium fumarate, Li_2(fum), lithium hydrogen fumarate, LiH(fum), and lithium hydrogen D,L-malate, LiH(D,L-mal).

5.3.1.1. Structure of dilithium 2,2-dimethylsuccinate, Li_2(dms)

The asymmetric unit of dilithium 2,2-dimethylsuccinate, Li_2(dms), consists of four lithium atoms and two ligand moieties (Figure 6). The lithium atoms have distorted tetrahedral coordination, with bond distances 1.887(12) Å - 2.089(10) Å and angles 90.1(5)° - 121.2(6)°. Both Li1 and Li2 are coordinated by oxygen atoms from four different ligand molecules; their bond valence sums are 1.06 and 1.08, respectively. In contrast, the oxygen atoms in the coordination spheres of Li3 and Li4 come from just three different ligand molecules. O8a and O6a belong to carboxylate groups of the same ligand, as do O1a and O3a, forming seven-membered rings involving the carbon skeleton of the ligand and respective lithium atoms. The strain inherent in such rings may be the cause of the lower bond valence sum, 0.98 for both Li3 and Li4, although this value remains in agreement with that expected for a monovalent cation. In contrast, the bond valence sums of Li1 and Li2 are 1.06 and 1.08, respectively.

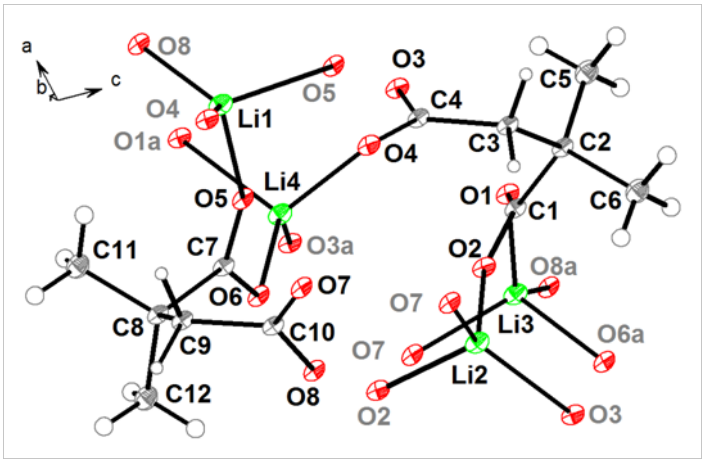

Figure 6. Ortep extended asymmetric unit of dilithium 2,2-dimethylsuccinate, showing atoms necessary to complete the lithium coordination spheres. C, H, Li and O atoms are shown in grey, white, green and red, respectively. Additional atoms are labelled in grey.

The conformations of the ligand carbon skeletons are midway between *gauche* and eclipsed (C1-C4 -37.1(6)°, C7-C10 -34.1(6)°). Each ligand oxygen atom coordinates to two lithium atoms, with O1 and O3, and O6 and O8 sharing lithium atoms as described above, giving rise to the notation μ_7, $\kappa^{4}.^{33}$ Steric interactions dominate over electrostatic repulsion between carboxylate groups, as C4 and C10 point away from the sides of the ligands that contain methyl groups. This separation between hydrophilic carboxylate groups and hydrophobic methyl groups encourages the structure to adopt layers approximately 10 Å thick, which stack

via weak van der Waals forces (Figure 7a). The layers consist of a 2-D network of corner-sharing LiO_4 tetrahedra bridged by carboxylate groups of the ligand molecules, giving the framework I^2O^0 connectivity (Figure 7b). This is apparent in the crystal morphology of the bulk phase, which consists of flat sheets; however, the flat rods obtained for single crystal structure determination point towards the possibility for morphology control using different synthesis conditions. As with other framework structures based on the 2,2-dimethylsuccinate ligand, the methyl groups of the ligand point away from the inorganic network and form a hydrophobic surface either side of the layer, enabling facile exfoliation of nanosheets (see Section 5.3.1.5).[34]

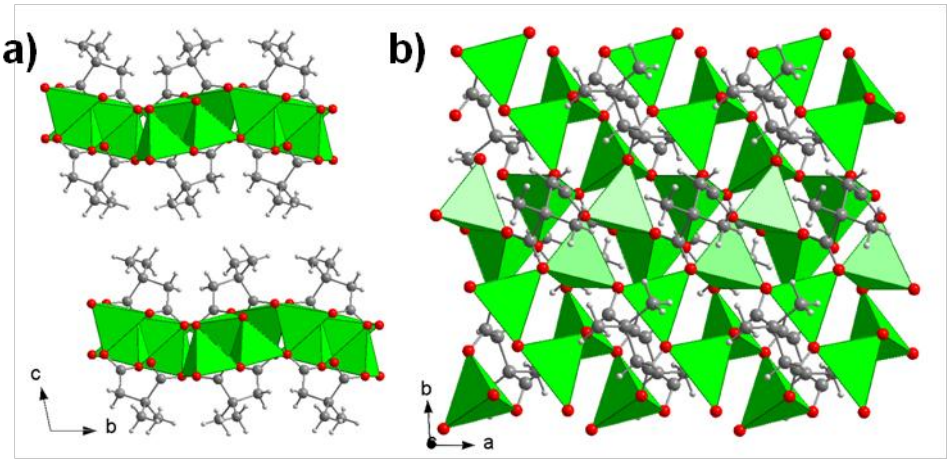

Figure 7. Extended structure of dilithium 2,2-dimethylsuccinate, showing a) two corrugated sheets viewed down the a-axis, and b) the inorganic connectivity in one sheet, viewed down the c-axis. C, H and O atoms and LiO_4 tetrahedra are shown in grey, white, red and green, respectively.

5.3.1.2. Structure of dilithium fumarate, Li_2(fum)

The extended asymmetric unit of dilithium fumarate, Li_2(fum), consists of half of one fumarate ligand and one lithium atom (Figure 8). The ligand is planar and retains the *trans* conformation of the conjugated π-system of the starting material. C-C bond lengths are as expected for single and double carbon-carbon bonds, at 1.5002(11) Å and 1.331(2) Å, respectively. The carboxylate oxygen atoms are essentially co-planar with the carbon skeleton, with O1-C1-C2-C2 and O2-C1-C2-C2 torsion angles -8.34(13)° and 169.90(8)°, respectively. The lithium coordination environment is a distorted tetrahedron. Li-O bond distances are remarkably uniform, between 1.942(2) Å and 1.988(2) Å, but O-Li-O angles vary widely between 89.20(7)° and 119.10(8)°. The bond valence sum is 1.02, in good

agreement with the expected value for monovalent lithium, although a little lower than most other lithium-based inorganic-organic frameworks. This may be a result of the rigidity of the ligand, which limits the extent to which the LiO_4 tetrahedron can relax.

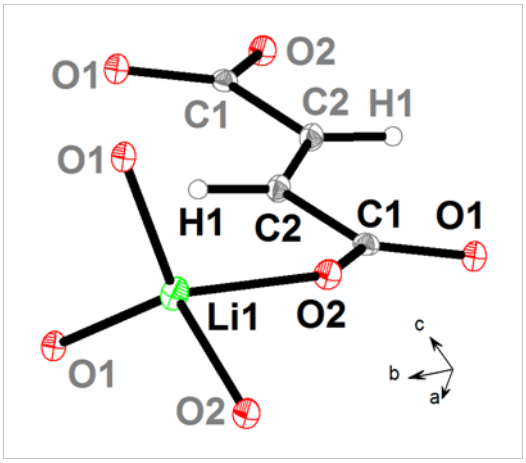

Figure 8. Ortep extended asymmetric unit of dilithium fumarate, showing atoms needed to complete one ligand moiety and the lithium coordination sphere. C, H, Li and O atoms are shown in grey, white, green and red, respectively. Additional atoms are labelled in grey.

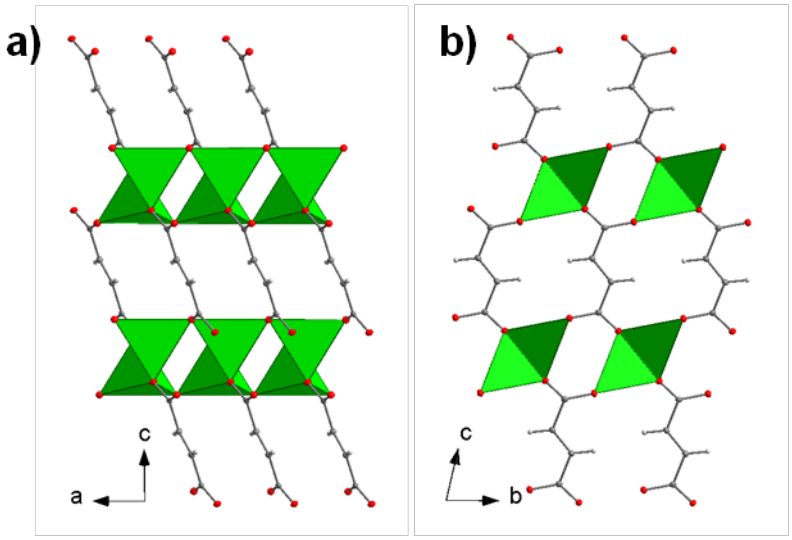

Figure 9. Extended structure of dilithium fumarate, viewed a) down the b-axis, showing ribbons of Li_2O_6 units, and b) viewed down the a-axis. C, H and O atoms and LiO_4 tetrahedra are shown in grey, white, red and green, respectively.

The overall structure can be thought of as dimers of edge-sharing LiO_4 tetrahedra, joined by their corners to form ribbons along the *a*-axis (Figure 9a). Of the ligand oxygen atoms, O2 bridges between lithium atoms in the same dimer, whilst O1 bridges between lithium atoms in adjacent dimers. Each ligand therefore coordinates to eight different lithium atoms through

all four oxygens, and so may be denoted μ_8, κ^4. The ribbons are connected in two dimensions by flat arrays of the fumarate ligand (Figure 9b), giving rise to a 3-dimensional, I^1O^2 structure.

5.3.1.3. Structure of lithium hydrogen fumarate, LiH(fum)

The asymmetric unit of lithium hydrogen fumarate, LiH(fum), consists of one singly protonated fumarate ligand and one lithium atom (Figure 10). The ligand is planar and retains the *trans* conformation found in fumaric acid. One carboxylate oxygen atom, O1, is protonated, leading to distinct single/double bond character and a difference in C-O bond distances within the group (C1-O1 1.3074(11) Å, C1-O2 1.2242(11) Å). The other carboxylate group is fully deprotonated and the negative charge delocalised, as evident from the C-O bond distances of 1.2654(11) Å (C4-O3) and 1.2541(11) Å (C4-O4). The lithium coordination environment is a distorted tetrahedron, with uniform Li-O bond distances 1.910(2) - 1.948(2) Å and O-Li-O bond angles 91.78(7)° - 116.23(8)°. The Li bond valence sum is 1.13, as expected for monovalent lithium.

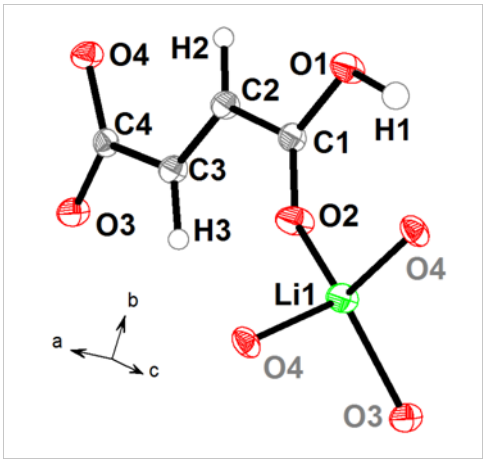

Figure 10. Ortep extended asymmetric unit of lithium hydrogen fumarate, showing atoms necessary to complete the lithium coordination sphere. C, H, Li and O atoms are shown in grey, white, green and red, respectively. Additional atoms are labelled in grey.

The lithium tetrahedra share edges, forming isolated Li_2O_6 dimers, which are connected by aligned ligand moieties in three dimensions to form an I^0O^3 framework (Figure 11). Only three of the four ligand oxygen atoms participate in coordination to lithium; the protonated one, O1, does not, but instead acts as a hydrogen bond donor to O3 on a neighbouring ligand. O2 and O3 coordinate to just one lithium atom each, acting as terminal groups in the Li_2O_6 dimer, whilst O4 forms the bridge between lithium atoms in the same dimer. Overall, the

fumarate ligand coordinates to four lithium atoms through three oxygens, so may be denoted μ_4, κ^3.

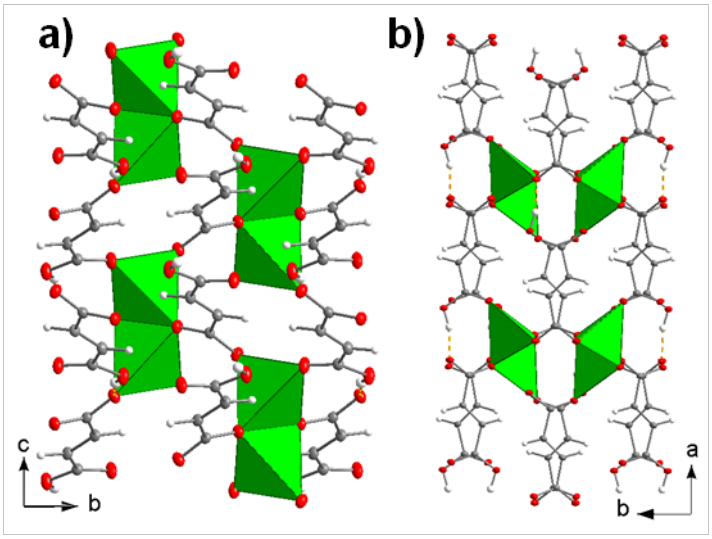

Figure 11. Extended structure of lithium hydrogen fumarate, a) viewed down the a-axis, and b) viewed down the c-axis. C, H and O atoms and LiO_4 tetrahedra are shown in grey, white, red and green, respectively. Hydrogen bonds are shown as dashed orange lines.

5.3.1.4. Structure of lithium hydrogen D,L-malate, LiH(D,L-mal)

The asymmetric unit of lithium hydrogen D,L-malate, LiH(D,L-mal), contains one singly protonated ligand moiety and one lithium atom (Figure 12). The malate ligand carbon backbone is essentially planar, with C1-C2-C3-C4 torsion angle 178.4(15)°. The carboxylate group closest to the hydroxyl group is deprotonated, as is expected from its lower pK_a due to the hydroxyl group's electron withdrawing nature. All three of those oxygen atoms are involved in coordination to Li1, and O2 bridges between adjacent lithium atoms. The protonated carboxylic acid group exhibits disorder between two positions with equal occupancy. The lithium coordination environment is a relatively uniform tetrahedron. Li-O bond distances vary between 1.905(3) Å and 1.954(3) Å, and O-Li-O angles are in the range 103.86(15)° - 118.20°(15). The bond valence sum for Li1 is 1.15, in agreement with that expected for monovalent lithium but slightly on the high side, due to low steric hindrance, ligand flexibility and efficient packing of the ligand moieties. This compares to the previously reported chiral analogue, lithium hydrogen L-malate,[35] which has a bond valence sum of 1.05.

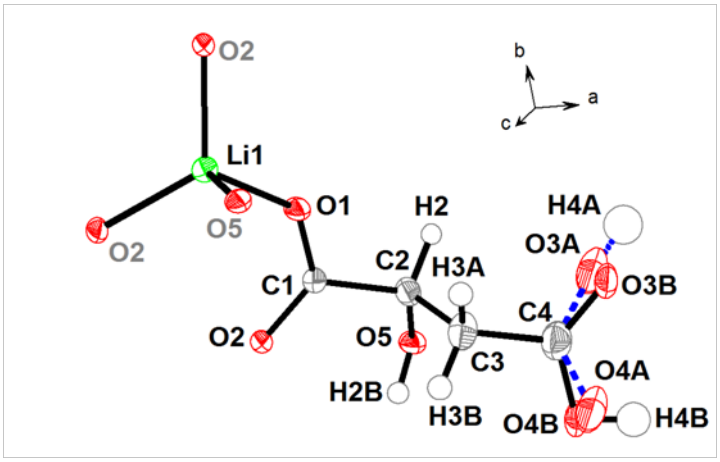

Figure 12. Ortep extended asymmetric unit of lithium hydrogen D,L-malate, showing atoms necessary to complete the lithium coordination sphere. C, H, Li and O atoms are shown in grey, white, green and red, respectively. Additional atoms are labelled in grey and one part of the disordered carboxylic acid moiety is shown with dashed blue bonds.

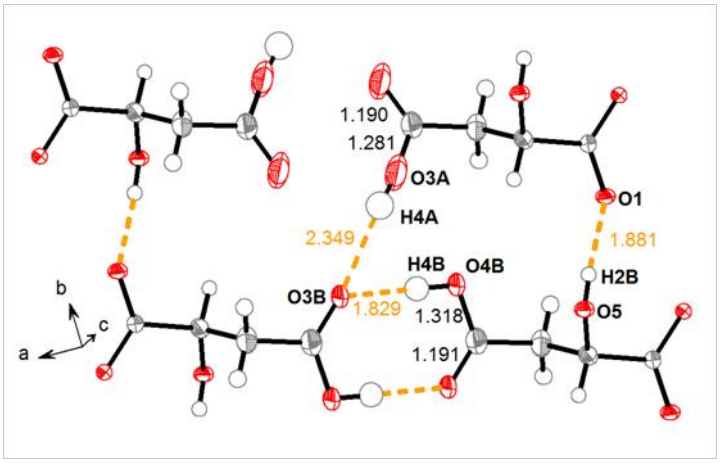

Figure 13. Carboxylate C-O distances and hydrogen bonds (dashed orange lines) in lithium hydrogen D,L-malate. The two parts of the disordered carboxylic acid group are shown on separate ligand moieties.

The carboxylic acid C-O bond distances confirm the presence of single/double bond character and show that the proton should be associated with a different oxygen atom in each part of the disordered group. H4B participates in a hydrogen bonded carboxylic acid dimer with the ligand opposite (graph set notation $\mathbf{R^2_2(8)}$).[36] In contrast, the C4-O3A-H4A angle refines to 168(5)°, pointing H4A more towards an adjacent ligand than the one directly opposite (Figure 13). The ligand hydroxyl group also participates in a strong hydrogen bond with a carboxylate oxygen atom on an adjacent ligand. One caveat with these observations is that due to the poor interaction of protons with X-rays, their positions are often poorly resolved

using X-ray diffraction. Therefore, although the C-O bond distances give confidence that H4A is bound to O3A, some caution should be exercised when discussing its and other protons' positions. It could, for example, also participate in a carboxylic acid dimer like H4B.

The overall structure of LiH(D,L-mal) is of one-dimensional inorganic chains of corner-sharing LiO_4 tetrahedra, connected by the ligand to form two-dimensional I^1O^1 layers (Figure 14a). The layers stack via hydrogen bonds between the protonated ligand carboxylic acid groups (Figure 14b). The chains of tetrahedra are connected in much the same way as in the herringbone sheets of anhydrous lithium tartrates **2**, **5**, **6** and **8** (see Chapter 3):[37] three carboxylate oxygen atoms bind to the lithium atoms within one sheet and a hydroxyl oxygen from a ligand above or below caps each tetrahedron, forming the link between sheets in each 2-D layer. In this case, however, the other end of the ligand remains protonated and therefore does not propagate any "organic" connectivity between the chains in this direction. The ligands either side of a given inorganic chain are a single enantiomer of malic acid, making it chiral. However, due to the space group symmetry, all adjacent chains are of an opposite handedness, therefore the overall structure is achiral.

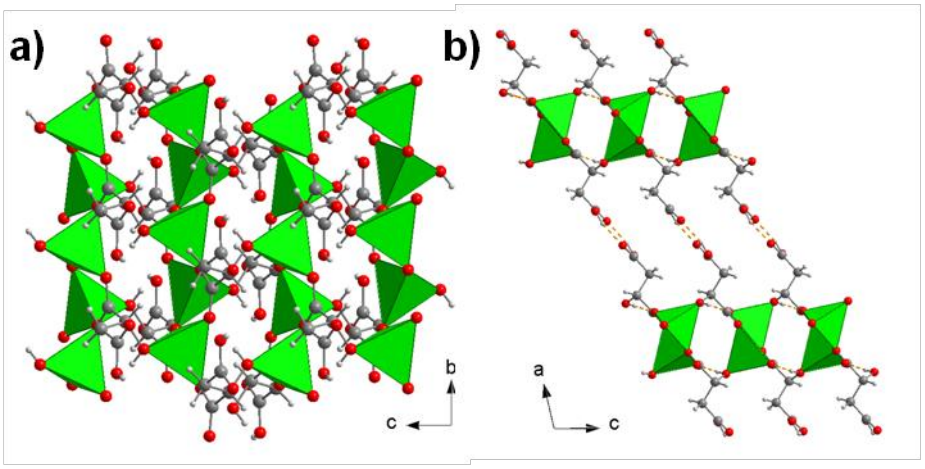

Figure 14. Extended structure of lithium hydrogen D,L-malate, a) viewed down the a-axis, showing an I^1O^1 sheet, and b) viewed down the b-axis, showing hydrogen bonding between the sheets. C, H and O atoms and LiO_4 tetrahedra are shown in grey, white, red and green, respectively. Hydrogen bonds are shown as dashed orange lines. Only one part of the disordered carboxylic acid moiety is shown.

5.3.1.5. Trends in structural features

Various trends, shown in Table 2 and Table 3, can be drawn from the structures described in this section and previous chapters and those reported in other works.[35, 38]

To the best of the author's knowledge, Li_2(dms) is the only lithium-based framework with I^2O^0 connectivity. Recent work within the author's research group has shown that the 2,2-dimethylsuccinate ligand ubiquitously forms such structures, due to the bent conformation of the carbon backbone and the hydrophobic surface provided by the methyl groups.[34] Furthermore, the weak interaction between the layers of Li_2(dms) enables facile exfoliation of nanosheets by simple sonication of single crystals in acetonitrile, which could be advantageous for fabrication of thin films of these materials for applications. Sheets with aspect ratios between approximately 1:200 and 1:400 (thickness:lateral width) were observed using atomic force microscopy by Jin-Chong Tan (Figure 15).

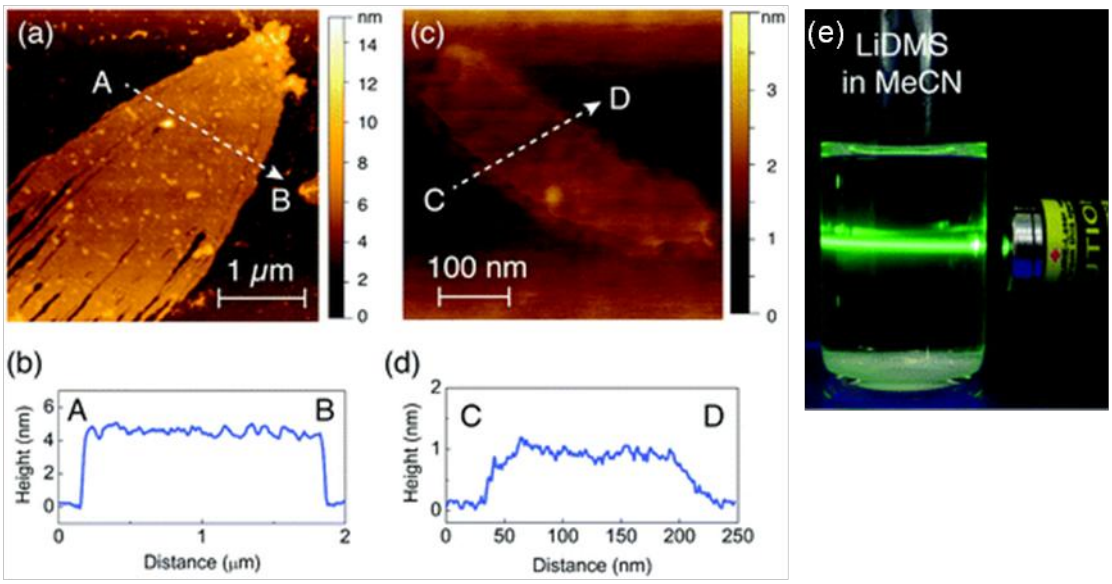

Figure 15. Atomic force microscopy height topography and cross-sectional profiles of Li_2(dms) nanosheets: (a and b) a multilayered film with a thickness of about 5 nm and with a lateral dimension of ~2 × 2 μm^2; (c & d) a single elementary host layer with a thickness of about 1 nm; (e) demonstration of the Tyndall effect in a colloidal suspensions containing exfoliated nanosheets in acetonitrile. Scattering of the incident beam renders the path of the green laser clearly visible. Figures reproduced with permission from the RSC.[34]

	Li_2(dms)	Li_2(fum)	LiH(fum)	Li_2(fum)$(H_2O)_2$·$2H_2O$[38b]
Space group	*P*$\bar{1}$	*P*$\bar{1}$	$P2_1/c$	*Pbcn*
d_{calc} (g cm^{-3})	1.455	1.809	1.588	1.37
Connectivity	I^2O^0	I^1O^2	I^0O^3	I^1O^1
Ligand binding	μ_7, κ^4	μ_8, κ^4	μ_4, κ^3	μ_6, κ^4
Li coordination	tetrahedral	tetrahedral	tetrahedral	tetrahedral
Inorganic substructure	2-D sheets	1-D ribbons	Li_2O_6 dimers	1-D chains
Hydrogen bonding	--	--	inter-ligand	inter-sheet *via* water

Table 2. Selected structural features of dilithium 2,2-dimethylsuccinate and lithium fumarates. Note: Li_2(fum)$(H_2O)_2$·$2H_2O$ from Beck et al.[38b]

Li_2(fum) and LiH(fum) form a family of structures with lithium fumarate tetrahydrate, Li_2(fum)$(H_2O)_2$·$2H_2O$, reported previously by Beck *et al.*[38b] Reducing the metal:ligand ratio, from two to one, results in a decrease in the inorganic connectivity, *m*, in the notation I^mO^n, due to a reduction in availability both of lithium atoms and of carboxylate oxygen atoms. This is compensated for in LiH(fum) by additional organic connectivity, *n*, and hydrogen bonding between ligands. In contrast, increasing the degree of solvation, from Li_2(fum) to Li_2(fum)$(H_2O)_2$·$2H_2O$, results in a decrease in *n*. Water molecules cap the inorganic chains, preventing any increase in *m*. In fact, the overall dimensionality, (*m*+ *n*), is reduced to 2, with water molecules acting as hydrogen bond bridges between the layers (Figure 16).

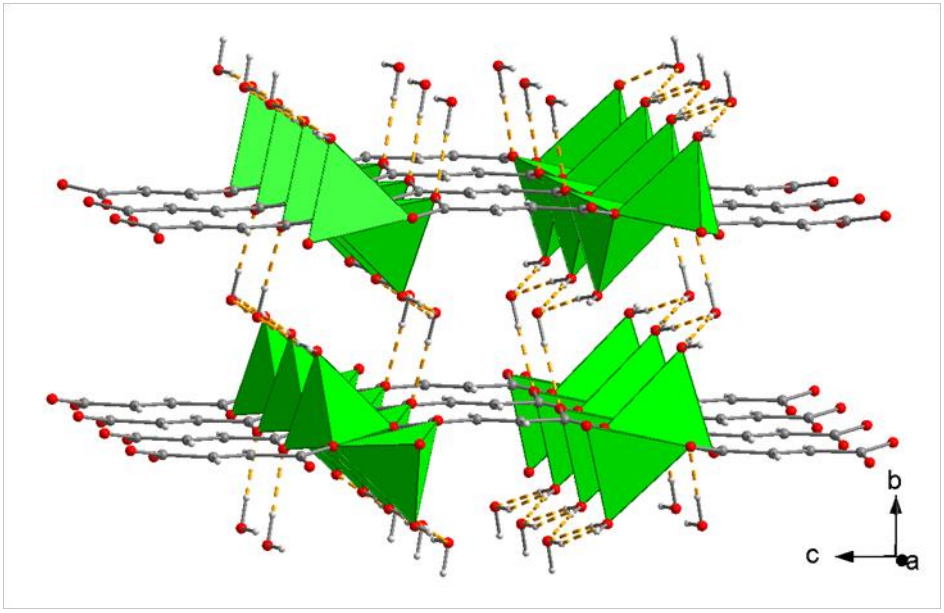

Figure 16. Structure of Li_2(fum)$(H_2O)_2$·$2H_2O$,[38b] viewed down the a-axis, showing hydrogen bonding between I^1O^1 layers. C, H and O atoms and LiO_4 tetrahedra are shown in grey, white, red and green, respectively. Hydrogen bonds are shown as dashed orange lines.

	Li_2(mal)	LiH(D,L-mal)	LiH(mal)[35]	LiH_3(D,L-mal)$_2$[38c]	LiH_3(mal)$_2$[38a]	Li_2(D,L-mal)·$2H_2O$[38c]
Space group	*R*3	*C*2/*c*	$P4_12_12$	*P*1	$P2_1$	$P2_1/c$
d_{calc} (g cm^{-3})	1.666	1.643	1.714	1.631	1.598	1.659
Connectivity	I^3O^0	I^1O^1	I^1O^1	I^0O^0	I^0O^1	I^0O^3
Ligand binding	μ_8, κ^4	μ_4, κ^3	μ_4, κ^3	μ_1, κ^2 + μ_2, κ^3	μ_1, κ^2 + μ_2, κ^3	μ_5, κ^5
Li coordination	tetrahedral	tetrahedral	tetrahedral	square-pyramidal	square-pyramidal	trigonal-bipyramidal + tetrahedral
Inorganic substructure	3-D	parallel 1-D chains	crossed 1-D chains	isolated LiO_5	isolated LiO_5	Li_4O_{14} tetramer
Hydrogen bonding	inter-ligand	inter-sheet	inter-sheet	inter-molecule 2-D	inter-chain 2-D	extensive 3-D

Table 3. Structural features of lithium malates. Notes: LiH(mal) from Van Havere et al.;[35] LiH_3(D,L-mal) and Li_2(D,L-mal)·$2H_2O$ from Fleck et al.;[38c] LiH_3(mal)$_2$ from Kirfel et al.[38a]

The lithium malates reported in this thesis, Li_2(mal) and LiH(D,L-mal), add to an already diverse family, which includes the chiral lithium hydrogen analogue, LiH(mal),[35] achiral and chiral trihydrogen structures, LiH_3(D,L-mal)$_2$[38c] and LiH_3(mal)$_2$,[38a] respectively, and a hydrated structure, Li_2(D,L-mal)·$2H_2O$.[38c] In contrast to the lithium fumarates, hydration of the framework does not reduce the overall connectivity, (m+ n), in Li_2(D,L-mal)·$2H_2O$, although it does change from purely inorganic to purely organic. However, it is reduced upon decreasing the metal:ligand ratio, from (m+ n) = 3 in Li_2(mal) to (m+ n) = 2 in the lithium hydrogen compounds, and to (m+ n) = 1 and (m+ n) = 0 in the chiral and achiral trihydrogen frameworks, respectively.

The main difference between LiH(D,L-mal) and its chiral analogue is the orientation of the inorganic chains, which run parallel in LiH(D,L-mal) but have different orientations in adjacent layers in LiH(mal). Flexibility in the ligand conformation enables hydrogen bonding dimers to form between the layers in both structures, with a *gauche* conformation in LiH(mal) and a *trans* relationship in LiH(D,L-mal). Reactions using D,L-malic acid do not spontaneously form a conglomerate of the chiral forms, indicating that the achiral framework is more stable, despite its lower density. The favourable ligand conformation and the lower bond valence sum of the lithium atoms may contribute to the lower energy of LiH(D,L-mal).

Decreasing the metal:ligand ratio further, to LiH_3(D,L-mal)$_2$ and its chiral analogue, LiH_3(mal)$_2$, results in a change from 4-coordination to 5-coordination due to the increase in available oxygen atoms per lithium (even considering that there are fewer atoms contributing

to framework bonding from each ligand due to protonation of the carboxylate groups). There is also more extensive hydrogen bonding, because of the increased availability of acidic protons within the structure. Unlike the two lithium hydrogen isomers, the trihydrogen frameworks have radically different architectures. $LiH_3(D,L\text{-mal})_2$ consists of molecular units, linked in two dimensions by hydrogen bonding, whilst $LiH_3(mal)_2$ exhibits 1-D organic connectivity. The racemic acid in this case again does not spontaneously form a conglomerate of chiral frameworks; the energy of $LiH_3(D,L\text{-mal})_2$ may be lower due to higher density, despite a lack of extended connectivity.

Finally, it should be noted that single crystals of both LiH(fum) and LiH(D,L-mal) could be crystallized from reaction mixtures involving chlorosuccinic acid and lithium hydroxide in 1:2 ratio (Figure 17). This is indicative of *in-situ* ligand transformation, in which HCl is eliminated to form the fumarate ligand, or substituted for H_2O to form malate. Although *in-situ* ligand transformation has only been observed in a few inorganic-organic frameworks,[39] this finding is unsurprising due to the basic aqueous conditions and lability of HCl as a product. It is likely that the resulting acidic conditions also prevented formation of dilithium products due to the neutralisation reaction of HCl with LiOH.

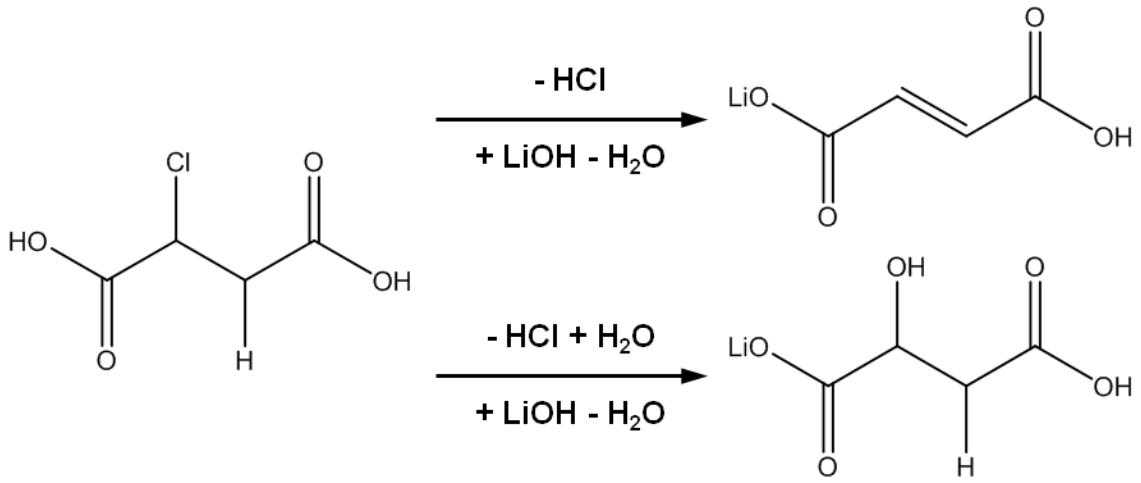

Figure 17. Schematic of the in-situ transformation of chlorosuccinic acid in alkaline solution to form LiH(fum) (above) and LiH(D,L-mal) (below).

5.3.2. *Architecture trends in lithium dicarboxylates*

A survey of lithium-based dicarboxylate frameworks, using the Web of Knowledge and the Chemical Database Service,[40] revealed the occurrence of 29 structures, in addition to the 18 new structures described in this thesis. These are shown together in Table 4, classified by I^mO^n nomenclature.

I^m	O^n		
	0	**1**	**2**
0	$LiH_3(DL\text{-}mal)_2$[38c,*]	$LiH(L\text{-}tar)\cdot H_2O$[41] $LiH_3(D\text{-}mal)_2$[38a]	$LiH(oxy)$[42,*] $Li_2(2,5\text{-}tdc)\cdot DMF$[43,*] $LiH(psu)$[44,*] $Li_2(DL\text{-}tar)\cdot 3H_2O$[45] **$Li_2(DL\text{-}tar)\cdot 2H_2O\_10$** $LiH_3(man)_2$[46] $Li(L\text{-}Hglm)$[47] $Li_3(2,6\text{-}pdc)_2\cdot DMS\cdot(H_2O)_{0.21}$[48]
1	$LiH(2,6\text{-}pdc)\cdot H_2O$[49,*] $LiH(meso\text{-}tar)\cdot H_2O$[51]	$Li_2(1,2\text{-}bdc)\cdot 1.5H_2O$[50,*] **LiH(DL-mal)** $Li_2(fum)(H_2O)_2\cdot 2H_2O$[38b] $LiH(L\text{-}mal)$[35] $Li_2(2,3,4,5\text{-}hhd)\cdot 2H_2O$[52]	$Li_2(1,3\text{-}bdc)\cdot 0.5DMF\cdot H_2O$[2b] **$Li_2(meso\text{-}tar)\cdot 0.5H_2O\_11$** **$Li_2(L\text{-}tar)\_2$** **$Li_2(L\text{-}tar)\_3$** **$Li_2(meso\text{-}tar)\_4$** **$Li_2(D,L\text{-}tar)\_5$** **$Li_2(meso\text{-}tar)\_6$** **$Li_2(meso\text{-}tar)\_7$** **$Li_2(D,L\text{-}tar)\_8$** **$Li_2(L\text{-}tar)\_9$** $Li_2(mae)\cdot H_2O$[38b] **$Li_2(fum)$** $Li_2(3,5\text{-}pdc)$[48]
2	**$Li_2(dms)$***	$Li_2(1,4\text{-}bdc)$[15] $Li_2(2,6\text{-}ndc)$[53] $Li_2(4,4'\text{-}bpd)$[54] $Li_2(oxa)$[55]	
3	$Li_2(suc)$[56] **$Li_2(flu)$** **$Li_2(mal)$** **$Li_2(met)$** $Li_2(man)$[58]		

	***n* = 3**
***m* = 0**	$Li_2(sdb)$[54] **LiH(L-tar)_1** $Li_2(DL\text{-}mal)\cdot 2H_2O$[38c] **LiH(fum)** $Li_2(2,5\text{-}pdc)\cdot DMF$[57] $Li(\beta\text{-}Hglm)\cdot H_2O$[59]

Table 4. Classification of lithium-based dicarboxylate frameworks by I^mO^n nomenclature. Structures in bold type are described for the first time in this thesis; see Figure 1 for ligand codes; DMF = N,N-dimethylformamide, DMS = dimethylsulfoxide. Asterisks mark structures with van der Waals forces in one direction.

In general, only anhydrous, dilithium frameworks in which the ligand has no additional binding sites apart from dicarboxylate oxygen atoms have 2-D or 3-D inorganic connectivity, I^m, i.e. $m = 2$ or 3. $Li_2(mal)$, described in Chapter 4, is the one exception in which the hydroxyl group does not coordinate to lithium but instead participates in a hydrogen bond

trimer within the framework cavity. All I^3O^0 frameworks involve small, conformationally flexible ligands that enable extended connectivity of LiO_4 tetrahedra all around the organic moieties. In contrast, all I^2O^1 frameworks feature conformationally rigid, linear ligands, which stack in parallel to form layers of inorganic connectivity.

The sole example of an I^2O^0 framework is Li_2(dms), which contains the bent 2,2-dimethylsuccinate ligand with a hydrophobic surface provided by the methyl groups. This combination results in 2-D inorganic layers separated by van der Waals forces, which are easily separated by sonication treatment.[34] Both Li_2(1,2-bdc)·1.5H_2O and LiH(2,6-pdc)·H_2O, which have significant van der Waals interactions, also contain bent ligands and this may help to reduce covalent connectivity in one direction. The trend is not general, however, as other bent ligands form 3-D frameworks, e.g. Li_2(sdb), Li_2(mae)·H_2O, Li_2(3,5-pdc) and Li_2(1,3-bdc)·0.5DMF·H_2O. Furthermore, some flexible ligands exhibit van der Waals interactions between sheets or chains in one dimension, e.g. LiH_3(D,L-mal)$_2$, LiH(oxy) and LiH(psu).

With the exception of Li_2(mal), the effect of adding binding sites to the dicarboxylate ligand is to limit inorganic connectivity to m = 1 or 0, as seen in the dilithium tartrates **2** - **11** (Chapter 3), dilithium 3,5-pyridinedicarboxylate, Li_2(3,5-pdc), and dilithium sulfonyldibenzoate, Li_2(sdb). However, these anhydrous, dilithium frameworks retain three-dimensional overall connectivity, compensating with increased organic connectivity. Generally speaking, other I^1O^2 and I^0O^3 structures contain coordinated solvent molecules and/or partially lithiated ligands. Li_2(fum) is the exception here: there are no additional ligand binding sites, but inorganic connectivity is restricted to just one direction by the rigidity of the ligand. As described in Chapter 4, the fumarate ligand can be incorporated into an I^3O^0 structure by dehydration of Li_2(mal) to form $Li_2(mal)_{1-x}(fum)_x$, but complete transformation to form Li_2(fum) in this architecture (i.e. x = 1) could not be achieved.

The only lithium dicarboxylate compound found with both m and n = 0 is LiH_3(D,L-mal)$_2$. It consists of molecules of two formula units, connected in 2-D by hydrogen bonding. This contrasts with its chiral isomer, LiH_3(mal)$_2$, which has I^0O^1 connectivity. This suggests that fine structural features of lower dimensional frameworks are dependent on the ligand geometry and conformation, but matters are complicated in the presence of coordinated solvent and protonated carboxylate groups.

Additional insight is gained by comparing the number of lithium atoms per total binding site, here denoted Λ_{tot}, which takes into account the metal:ligand ratio, number of ligand binding sites and number of solvent molecules, with various structural descriptors (Figure 18).

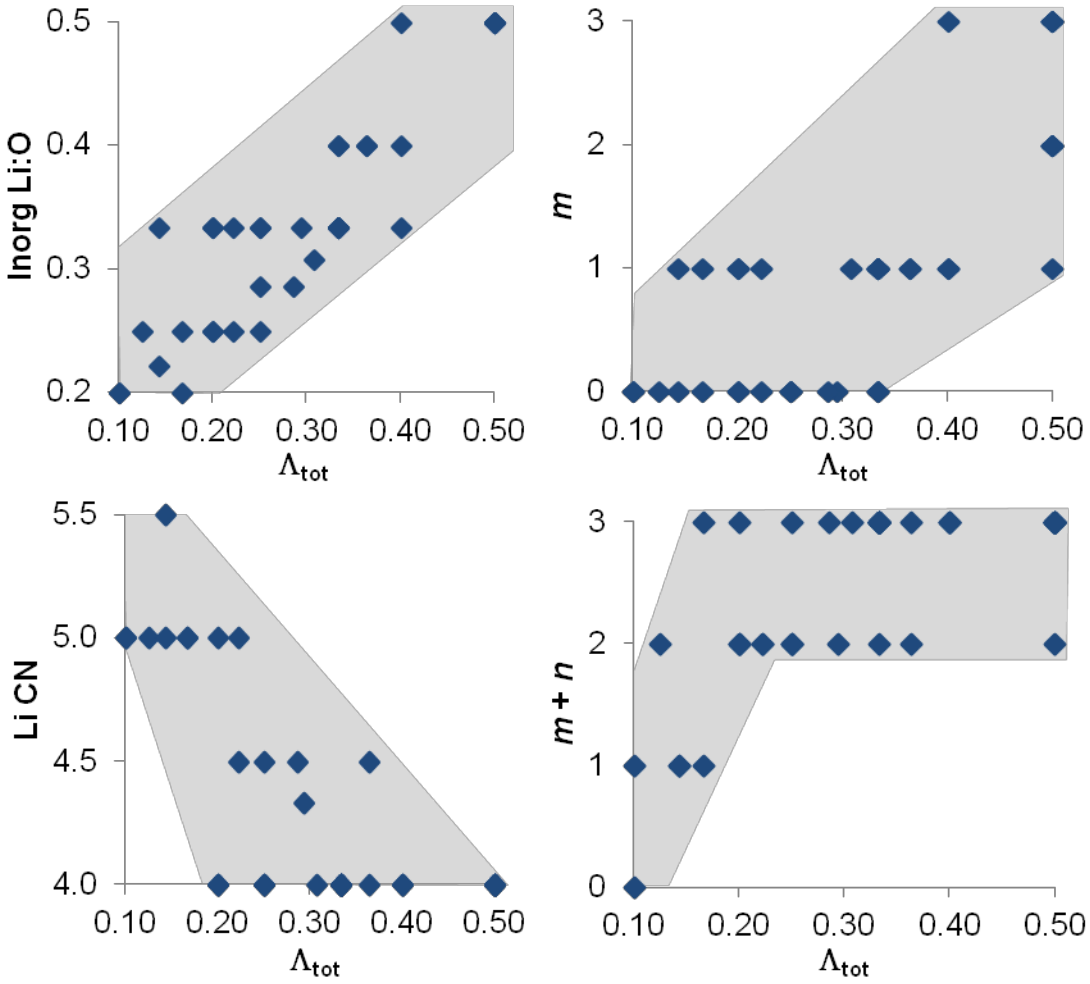

Figure 18. Correlations between the number of lithium atoms per total binding site, Λ_{tot}, and (clockwise from bottom left) average lithium coordination number, Li CN; inorganic structure Li:O ratio, Inorg Li:O; inorganic connectivity, m; and total connectivity, m + n, in lithium-based dicarboxylate frameworks.

A negative correlation is observed between Λ_{tot} and the average coordination number of lithium (Figure 18, bottom left). Due to its small radius, the preferred coordination number of lithium is 4, but this increases in the presence of solvent molecules and additional ligand binding sites. Incorporation of coordinated solvent molecules and/or a reduced metal:ligand ratio also tends to result in frameworks with 1-D or 2-D overall connectivity. This is reflected by positive correlations between Λ_{tot} and the Li:O ratio of the inorganic substructure (Figure 18, top left), and between Λ_{tot} and inorganic connectivity, *m* (Figure 18, top right). As

discussed regarding the lithium malates in section 5.3.1.5, solvent molecules tend to terminate the inorganic units and protonation results in increased hydrogen bonding, reducing organic connectivity. A more complex relationship is observed between Λ_{tot} and the total framework connectivity, (m+ n) (Figure 18, bottom right). At low values of Λ_{tot} there appears to be a positive correlation, as molecular and 1-D structures become more connected, before reaching the maximum value of (m+ n) = 3 for values of Λ_{tot} above approximately 0.30.

These findings reveal that in order to design a lithium-based dicarboxylate framework with connectivity in three dimensions, the number of additional binding sites from solvent molecules and/or ligands must be below approximately one per lithium atom (corresponding to a Λ_{tot} value of 0.33). In addition, in order to produce a framework with inorganic connectivity in two or three dimensions, which should give better thermal stability, no addition binding sites should be present. In this case, the exact topology will depend on the geometry of the ligand.

5.3.3. *Electrochemical behaviour of lithium-based inorganic-organic frameworks*

Li_2(fum) and Li_2(dms) in bulk crystalline form, and Li_2(1,4-bdc) synthesized by mechanochemistry, were investigated by electrochemical cycling *vs.* lithium in galvanostatic mode, between 3.0 V and 0.5 V (Figure 19 - Figure 21).

Both Li_2(fum) and Li_2(dms) show a shallow gradient around 1 V, corresponding to reaction with approximately 1 and 1.5 lithium atoms per formula unit, respectively. The features are irreversible and could be assigned to formation of a solid electrolyte interphase, SEI, but regardless of their origin the measurements indicate that neither compound shows reversible lithium insertion at any potential between 3.0 V and 0.5 V *vs.* Li^+/Li^0. As suggested by Walker *et al.*,[14e] this may be due to the close proximity of the carboxylate groups and short conjugation length (or lack of conjugation in the case of Li_2(dms)), which would result in large repulsion between the negatively charged oxygen atoms and/or low stability of the reduced species.

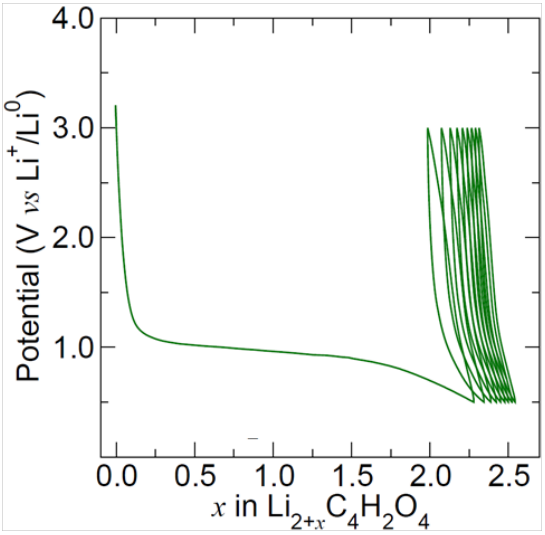

Figure 19. Electrochemical cycling of dilithium fumarate vs. lithium.

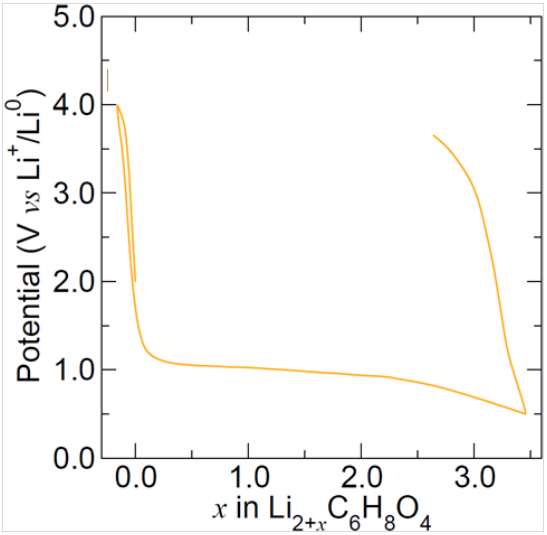

Figure 20. Electrochemical cycling of dilithium 2,2-dimethylsuccinate vs. lithium.

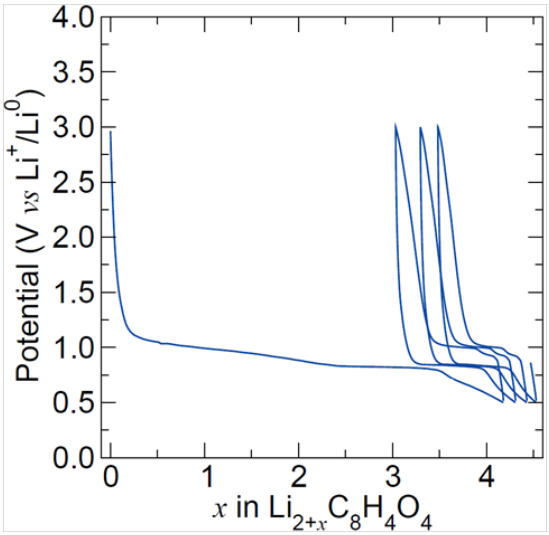

Figure 21. Electrochemical cycling of lithium terephthalate vs. lithium.

The behaviour in Li_2(1,4-bdc) is different to that reported previously, and may be due to the unknown impurities in the sample or the small particle size resulting from mechanochemical synthesis (Figure 22). Reduction begins at approximately 1 V, leading to irreversible reaction with 2 - 3 lithium atoms per formula unit, followed by reversible insertion of approximately one lithium atom. The irreversible reaction could be assigned to SEI formation; however, in the previous work no SEI was reported for cycling of the bulk material. In addition, up to two lithium atoms were found to insert reversibly in this case, compared to just one in the mechanochemically synthesized material. This suggests that the small particles and/or impurities cause not only increased irreversible reaction with the electrolyte, but also reduced capacity. Particle size effects have been well-studied in many materials, with nanomaterials in particular showing very promising properties for battery applications.[60] However, this result shows that the effect of size reduction can in fact be detrimental to battery performance.

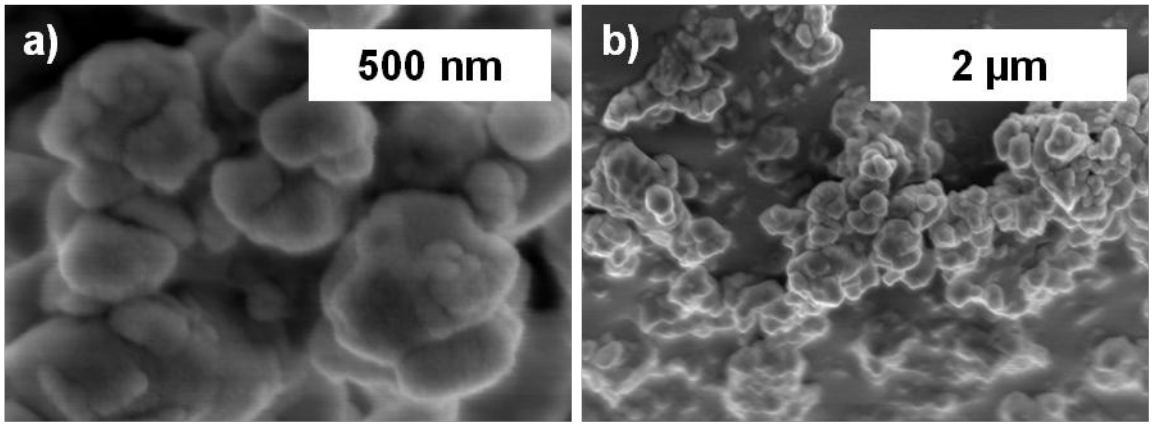

Figure 22. Scanning electron micrographs of lithium terephthalate synthesized by mechanochemistry, showing (b) sub-micron agglomerates of particles of diameter ~50 nm (a).

It is worth noting that these are initial observations and many factors, such as the amount of conducting carbon, ball-milling time and cycling rate, were not optimised. In particular, preparation of carbon/framework anode composites by ball-milling may have lead to amorphization of the crystal structures, as seen in other inorganic-organic frameworks.[61] Polymorphism/isomerism was shown by Walker *et al*. to drastically affect electrochemical properties,[14e, f] therefore distortion of the crystal structures may have a similar consequence in these compounds.

5.3.4. *Ionic conductivity of lithium-based inorganic-organic frameworks*

The ionic conductivities, σ, of seven lithium-based inorganic-organic frameworks were measured by impedance spectroscopy and are shown in Table 5.

	Temperature / K	Conductivity / S cm^{-1}
Li_2(L-tar) **2**	450	$< 10^{-9}$
Li_2(L-tar) **3**	457	$< 10^{-10}$
Li_2(suc)	398	$< 10^{-12}$
Li_2(mal)	398	$< 10^{-12}$
$Li_2(suc)_{0.5}(mal)_{0.5}$	400	$< 10^{-11}$
Li_2(dms)	470	$< 10^{-9}$
LiH(D,L-mal)	398	$< 10^{-12}$

Table 5. Conductivities of various lithium-based inorganic-organic frameworks measured by impedance spectroscopy.[62] Values courtesy of Thomas Pilz.

All the materials studied have values of σ below 10^{-9} S cm^{-1}, indicating that they are insulators. This is due to both the lack of lithium cations acting as charge carriers and their low mobility, as suggested by the equation for conductivity:

$$\sigma = \sum_i c_i q_i u_i$$

where c, q and u represent the concentration, charge and mobility of each type of charge carrier, i. Despite a high spatial concentration of lithium cations, the number of available charge carriers is approximately zero because the ions are all locked into the strongly-bound inorganic framework substructure. In addition, the inorganic substructures, which vary from 1-D chains to 2-D layers and 3-D networks, are highly ordered and have few intrinsic defects that might provide sites for lithium hopping or generate interstitial lithium atoms to diffuse through the framework. The activation energy for creation of defects and lithium mobility is restrictively high due to the strong electrostatic bonding between Li^+ cations and anionic carboxylate groups and the limited flexibility of the crystalline framework, which gives rise to very low mobility.

5.4. Conclusions

Four new lithium-based inorganic-organic frameworks have been synthesized, from three different dicarboxylate ligands, leading to a range of structures. A survey of all lithium dicarboxylate frameworks revealed various trends in their structures, which it is hoped may aid the design of compounds targeting specific applications, such as lithium battery materials. Due to the flexibility of the lithium coordination sphere, it was found that ligands play a key role in directing the structures of lithium-based frameworks. The number of ligand binding sites available and their relative geometry and flexibility have a strong influence on the architectures produced. Also important are coordinating solvent molecules such as water, which tend to terminate inorganic structural units, reducing the overall dimensionality. Finally, the ratio of metal atoms to ligand molecules affects the types of structure obtained. In general, those with protonated carboxylic groups have lower inorganic connectivity and may also have reduced overall dimensionality.

Two new lithium-based inorganic-organic frameworks were investigated by electrochemical cycling *vs.* lithium and found to exhibit irreversible insertion reactions due to the close proximity of the ligand carboxylate groups and short conjugation lengths. Cycling of lithium terephthalate, synthesized by mechanochemistry and therefore having a smaller particle size, revealed poorer performance than that previously reported in the bulk phase.[14c] The ionic conductivities of seven lithium-based inorganic-organic frameworks were measured by impedance spectroscopy. All the materials investigated, which are non-porous and highly ordered, show insulating behaviour due to a lack of charge carriers and low mobility.

Some of the results reported in this chapter have been published in the article "Layered inorganic-organic frameworks based on the 2,2-dimethylsuccinate ligand: structural diversity and its effect on nanosheet exfoliation and magnetic properties", in Dalton Transactions, Volume 41, Pages 8585-8593, May 2012.[34] The article describes the synthesis, structure and exfoliation properties of one of the new compounds, Li_2(dms), alongside similar investigations into other transition metal 2,2-dimethylsuccinate frameworks.[34]

5.5. Future work

Despite their many appealing attributes, very little work has so far been done to look at structure-property relationships of lithium-based inorganic-organic frameworks. Using the insight gained from the analysis in Section 5.3.2, a large range of crystal structures might be synthesized with particular structural attributes in mind, such as dimensionality of inorganic connectivity, hydrogen bonding and overall connectivity. Following synthesis, investigation of their properties, as suggested in Sections 5.3.3 and 5.3.4, may yield interesting results for applications. It would be interesting to follow trends in their properties as a function of structure, in order to better understand the relationship between them and to point towards the structure types that give rise to optimal properties. In addition to lithium-based frameworks, it would be interesting to pursue similar investigations with other *s*-block cations.

Further investigation of lithium-based frameworks may indicate what factors affect their electrochemical properties, such as operating potential and reversibility. In addition, the mechanisms and chemical species involved in lithium insertion into lithium-organic materials are currently poorly understood, and these crystalline materials could yield valuable information about this. For example, *in-situ* studies by X-ray diffraction could probe the evolution of structure as a function of lithium atoms inserted.

Investigation of lithium-based inorganic-organic frameworks containing ligands other than dicarboxylic acids is currently very poorly developed. Use of different binding functional groups, such as phosphate, sulfonate and aromatic nitrogen donors, will surely lead to an even greater diversity of structures, topologies and properties. With electrode applications in mind, materials with higher structural stability upon electrochemical cycling are of great interest. It would be interesting to investigate ligands containing redox-inactive oxygen donors, such as alkyl phosphates R-PO_3^{2-}, which could provide more robust binding when the carboxylate group is reduced. Ligands containing different coordination bonding motifs, such phosphonoacetate, ($^-O_2CCH_2PO_3^{2-}$), may provide the desirable combination of framework rigidity and redox-active functionality. Alternatively, frameworks based on metals with higher charge, such as Mg^{2+} or Zn^{2+}, may also provide robustness by increasing the strength of metal-oxygen bonding.

With lithium mobility in mind, lithium-based frameworks with low Li bond valence sums, such as Li_2(oxalate), which has a bond valence sum of 0.99, are of interest due to the

relatively weak Li-O bonds that make up the inorganic substructure. Alternatively, ligand binding functionalities with weaker bonding to Li^+, such as SO_3^- or neutral N donors, may help to decrease the activation energy for lithium transport. This could be combined with more rigid framework bonding as described above.

Creation of lithium vacancies in the inorganic network of frameworks is currently being investigated. Different strategies for incorporation of defects are being pursued, including doping with divalent cations such as Mg and Zn, and substitution of dicarboxylate ligands with charge-neutral *nitro* groups. Both strategies should lead to creation of one lithium vacancy per dopant moiety; however, a significant synthetic challenge exists to stabilise these defects at the low temperatures at which inorganic-organic frameworks are made. Inorganic materials, in which metal doping is commonly used to alter ionic conductivity, generally have much higher thermal stabilities and so can be synthesized at high temperatures at which the entropic component of a material's free energy becomes significant.

Other strategies to increase lithium mobility in inorganic-organic frameworks include fabrication of composites with ceramic materials, such as CaO and MgO, to create defects at the inter-particle grain boundaries. This strategy has previously enabled enhancement of polymer electrolyte conductivity at ambient temperatures.[63] Lithiation of hydroxyl groups in frameworks such as the lithium tartrates and lithium L-malate may also help to increase conductivity. In this case, the lithium may not be involved in framework bonding but instead could be relatively free to move through the frameworks *via* interstitial sites. Post-synthetic modification of layered frameworks may enable formation of new frameworks in which the original framework bonding is maintained but new functionality is inserted between layers. Such new functionality could be designed to provide a layer through which lithium could migrate and/or redox reactions could occur, leading to electrolyte and electrode behaviour, respectively.

This thesis has focussed on lithium-based systems, with lithium battery materials in mind; however, inorganic-organic frameworks could equally contribute to new materials for other battery systems, such as Na or Mg. Similar principles, adjusted depending on the chemistry of the metal in question, may be employed to create new materials with interesting properties, such as the sodium terephthalates recently reported by Park *et al*,[64] which show tunable sodium insertion behaviour similar to that of lithium terephthalate.[14c]

5.6. References

(1) (a) Tarascon, J. M.; Armand, M. *Nature* **2001**, *414*, (6861), 359-367. (b) Armand, M.; Tarascon, J. M. *Nature* **2008**, *451*, (7179), 652-657.

(2) (a) Mulfort, K. L.; Hupp, J. T. *J. Am. Chem. Soc.* **2007**, *129*, (31), 9604. (b) Liu, Y. Y.; Zhang, J.; Xu, F.; Sun, L. X.; Zhang, T.; You, W. S.; Zhao, Y.; Zeng, J. L.; Cao, Z.; Yang, D. W. *Cryst. Growth Des.* **2008**, *8*, (9), 3127-3129.

(3) (a) Han, S. S.; Goddard, W. A. *J. Am. Chem. Soc.* **2007**, *129*, (27), 8422. (b) Mulfort, K. L.; Farha, O. K.; Stern, C. L.; Sarjeant, A. A.; Hupp, J. T. *J. Am. Chem. Soc.* **2009**, *131*, (11), 3866. (c) Abrahams, B. F.; Grannas, M. J.; Hudson, T. A.; Robson, R. *Angew. Chem., Int. Ed.* **2010**, *49*, (6), 1087-1089.

(4) Thirumurugan, A.; Li, W.; Cheetham, A. K. *Dalton Trans.* **2012**, *41*, (14), 4126-4134.

(5) Kam, K. C.; Young, K. L. M.; Cheetham, A. K. *Cryst. Growth Des.* **2007**, *7*, (8), 1522-1532.

(6) Banerjee, D.; Parise, J. B. *Cryst. Growth Des.* **2011**, *11*, (10), 4704-4720.

(7) Fromm, K. M. *Coord. Chem. Rev.* **2008**, *252*, (8-9), 856-885.

(8) Cheetham, A. K.; Rao, C. N. R.; Feller, R. K. *Chem. Commun.* **2006**, (46), 4780-4795.

(9) Williams, D. L.; Byrne, J. J.; Driscoll, J. S. *J. Electrochem. Soc.* **1969**, *116*, (1), 2.

(10) Liang, Y. L.; Tao, Z. L.; Chen, J. *Adv. Energy Mater.* **2012**, *2*, (7), 742-769.

(11) Yamaki, J.; Tobishima, S.; Hayashi, K.; Saito, K.; Nemoto, Y.; Arakawa, M. *J. Power Sources* **1998**, *74*, (2), 219-227.

(12) (a) Aurbach, D.; Markovsky, B.; Weissman, I.; Levi, E.; Ein-Eli, Y. *Electrochim. Acta* **1999**, *45*, (1-2), 67-86. (b) Flandrois, S.; Simon, B. *Carbon* **1999**, *37*, (2), 165-180.

(13) (a) Winter, M.; Besenhard, J. O. *Electrochim. Acta* **1999**, *45*, (1-2), 31-50. (b) Zhang, W. J. *J. Power Sources* **2011**, *196*, (1), 13-24.

(14) (a) Chen, H.; Armand, M.; Demailly, G.; Dolhem, F.; Poizot, P.; Tarascon, J.-M. *Chemsuschem* **2008**, *1*, (4), 348-355. (b) Chen, H.; Armand, M.; Courty, M.; Jiang, M.; Grey, C. P.; Dolhem, F.; Tarascon, J.-M.; Poizot, P. *J. Am. Chem. Soc.* **2009**, *131*, (25), 8984-8988. (c) Armand, M.; Grugeon, S.; Vezin, H.; Laruelle, S.; Ribiere, P.; Poizot, P.; Tarascon, J. M. *Nat. Mater.* **2009**, *8*, (2), 120-125. (d) Walker, W.; Grugeon, S.; Mentre, O.; Laruelle, S.; Tarascon, J.-M.; Wudl, F. *J. Am. Chem. Soc.* **2010**, *132*, (18), 6517-6523. (e) Walker, W.; Grugeon, S.; Vezin, H.; Laruelle, S.; Armand, M.; Tarascon, J. M.; Wudl, F. *Electrochem. Commun.* **2010**, *12*, (10), 1348-1351. (f) Walker, W.; Grugeon, S.; Vezin, H.; Laruelle, S.; Armand, M.; Wudl, F.; Tarascon, J. M. *J. Mater. Chem.* **2011**, *21*, (5), 1615-1620.

(15) Kaduk, J. A. *Acta Crystallogr., Sect. B: Struct. Sci.* **2000**, *56*, 474-485.

(16) Férey, G.; Millange, F.; Morcrette, M.; Serre, C.; Doublet, M. L.; Greneche, J. M.; Tarascon, J. M. *Angew. Chem.-Int. Edit.* **2007**, *46*, (18), 3259-3263.

(17) de Combarieu, G.; Morcrette, M.; Millange, F.; Guillou, N.; Cabana, J.; Grey, C. P.; Margiolaki, I.; Férey, G.; Tarascon, J. M. *Chem. Mater.* **2009**, *21*, (8), 1602-1611.

(18) (a) Kitagawa, H.; Nagao, Y.; Fujishima, M.; Ikeda, R.; Kanda, S. *Inorg. Chem. Commun.* **2003**, *6*, (4), 346-348. (b) Nagao, Y.; Fujishima, M.; Ikeda, R.; Kanda, S.; Kitagawa, H. *Synth. Met.* **2003**, *133*, 431-432. (c) Nagao, Y.; Kubo, T.; Nakasuji, K.; Ikeda, R.; Kojima, T.; Kitagawa, H. *Synth. Met.* **2005**, *154*, (1-3), 89-92. (d) Fujishima, M.; Enyo, M.; Kanda, S.; Ikeda, R.; Kitagawa, H. *Chem. Lett.* **2006**, *35*, (5), 546-547.

(19) Jeong, N. C.; Samanta, B.; Lee, C. Y.; Farha, O. K.; Hupp, J. T. *J. Am. Chem. Soc.* **2012**, *134*, (1), 51-4.

(20) Yamada, T.; Sadakiyo, M.; Kitagawa, H. *J. Am. Chem. Soc.* **2009**, *131*, (9), 3144+.

(21) Taylor, J. M.; Mah, R. K.; Moudrakovski, I. L.; Ratcliffe, C. I.; Vaidhyanathan, R.; Shimizu, G. K. H. *J. Am. Chem. Soc.* **2010**, *132*, (40), 14055-14057.
(22) Shigematsu, A.; Yamada, T.; Kitagawa, H. *J. Am. Chem. Soc.* **2011**, *133*, (7), 2034-2036.
(23) Okawa, H.; Shigematsu, A.; Sadakiyo, M.; Miyagawa, T.; Yoneda, K.; Ohba, M.; Kitagawa, H. *J. Am. Chem. Soc.* **2009**, *131*, (37), 13516-13522.
(24) Sadakiyo, M.; Okawa, H.; Shigematsu, A.; Ohba, M.; Yamada, T.; Kitagawa, H. *J. Am. Chem. Soc.* **2012**, *134*, (12), 5472-5475.
(25) Pardo, E.; Train, C.; Gontard, G.; Boubekeur, K.; Fabelo, O.; Liu, H. B.; Dkhil, B.; Lloret, F.; Nakagawa, K.; Tokoro, H.; Ohkoshi, S.; Verdaguer, M. *J. Am. Chem. Soc.* **2011**, *133*, (39), 15328-15331.
(26) Umeyama, D.; Horike, S.; Inukai, M.; Hijikata, Y.; Kitagawa, S. *Angew. Chem.-Int. Edit.* **2011**, *50*, (49), 11706-11709.
(27) Hurd, J. A.; Vaidhyanathan, R.; Thangadurai, V.; Ratcliffe, C. I.; Moudrakovski, I. L.; Shimizu, G. K. H. *Nat. Chem.* **2009**, *1*, (9), 705-710.
(28) Wiers, B. M.; Foo, M. L.; Balsara, N. P.; Long, J. R. *J. Am. Chem. Soc.* **2011**, *133*, (37), 14522-14525.
(29) Parr Instrument Company, 211 53rd St., Moline, Illinois 61265 USA.
(30) Retsch Ltd., 3 California Drive, Castleford, West Yorkshire, WF10 5QH, UK.
(31) *WinDeta Version 5.69*, Novocontrol GmbH, Hundsangen, Germany, **2009**.
(32) *Winfit Version 3.2*, Novocontrol GmbH, Hundsangen, Germany, **2005**.
(33) *IUPAC. Compendium of Chemical Terminology*. McNaught, A. D.; Wilkinson, A., Ed.; 2nd ed.; Blackwell Scientific Publications: Oxford, **1997**.
(34) Saines, P. J.; Tan, J.-C.; Yeung, H. H.-M.; Barton, P. T.; Cheetham, A. K. *Dalton Trans.* **2012**, *41*, (28), 8585-8593.
(35) Van Havere, W.; Lenstra, A. T. H. *Acta Crystallographica Section B* **1980**, *36*, (6), 1483-1486.
(36) Etter, M. C.; Macdonald, J. C.; Bernstein, J. *Acta Crystallogr. Sect. B-Struct. Commun.* **1990**, *46*, 256-262.
(37) Yeung, H. H.-M.; Kosa, M.; Parrinello, M.; Forster, P. M.; Cheetham, A. K. *Cryst. Growth Des.* **2011**, *11*, (1), 221-230.
(38) (a) Kirfel, A.; Will, G.; Recker, K.; Wallrafen, F.; Gao, Z. S. *Z. Kristall.* **1983**, *165*, (1-4), 117-125. (b) Beck, H. P.; Trubenbach, P. *Chem. Ber.-Recl.* **1993**, *126*, (2), 339-343. (c) Fleck, M.; Tillmanns, E.; Bohaty, L. *Z. Kristall.* **2001**, *216*, (12), 633-645.
(39) (a) Feller, R. K.; Forster, P. M.; Wudl, F.; Cheetham, A. K. *Inorg. Chem.* **2007**, *46*, (21), 8717-8721. (b) Brown, K. A.; Martin, D. P.; LaDuca, R. L. *CrystEngComm* **2008**, *10*, (10), 1305-1308. (c) Wang, J.; Lin, Z. J.; Ou, Y. C.; Shen, Y.; Herchel, R.; Tong, M. L. *Chem.-Eur. J.* **2008**, *14*, (24), 7218-7235. (d) Farnum, G. A.; Martin, D. P.; Sposato, L. K.; Supkowski, R. M.; LaDuca, R. L. *Inorg. Chim. Acta* **2010**, *363*, (1), 250-256. (e) Banisafar, A.; LaDuca, R. L. *Inorg. Chim. Acta* **2011**, *373*, (1), 295-300.
(40) Allen, F. *Acta Crystallogr., Sect. B: Struct. Sci.* **2002**, *58*, 380-388.
(41) Gelbrich, T.; Threlfall, T. L.; Huth, S.; Seeger, E.; Hursthouse, M. B. *Z. Anorg. Allg. Chem.* **2004**, *630*, (10), 1451-1458.
(42) Herbertsson, H. *Acta Crystallogr. Sect. B-Struct. Commun.* **1976**, *32*, 2381-2384.
(43) El Osta, R.; Frigoli, M.; Marrot, J.; Medina, M. E.; Walton, R. I.; Millange, F. *Cryst. Growth Des.* **2012**, *12*, (3), 1531-1537.
(44) Fischer, A. *Acta Crystallogr. Sect. E.-Struct Rep. Online* **2005**, *61*, M320-M322.
(45) Gelbrich, T.; Threlfall, T. L.; Huth, S.; Seeger, E. *Polyhedron* **2006**, *25*, (4), 937-944.
(46) Sorianogarcia, M.; Parthasarathy, R. *J. Chem. Soc.-Perkin Trans. 2* **1978**, (7), 668-670.

(47) Wiesbrock, F.; Schmidbaur, H. *CrystEngComm* **2003**, *5*, (45), 262-264.
(48) Banerjee, D.; Kim, S. J.; Borkowski, L. A.; Xu, W. Q.; Parise, J. B. *Cryst. Growth Des.* **2010**, *10*, (2), 709-715.
(49) Odoko, M.; Kusano, A.; Oya, N.; Okabe, N. *Acta Crystallogr. Sect. C-Cryst. Struct. Commun.* **2002**, *58*, M215-M216.
(50) Kuppers, H. *Acta Crystallogr. Sect. C-Cryst. Struct. Commun.* **1988**, *44*, 2093-2095.
(51) Stouten, P. F. W.; Verwer, P.; Vaneijck, B. P.; Kroon, J. *Acta Crystallogr., Sect. C: Cryst. Struct. Commun.* **1988**, *44*, 1961-1963.
(52) Lv, Y.-K.; Chen, J.; Wang, X.-J.; Feng, Y.-L. *Jiegon Huaxue* **2010**, *29*, 1483.
(53) Banerjee, D.; Kim, S. J.; Parise, J. B. *Cryst. Growth Des.* **2009**, *9*, (5), 2500-2503.
(54) Banerjee, D.; Borkowski, L. A.; Kim, S. J.; Parise, J. B. *Cryst. Growth Des.* **2009**, *9*, (11), 4922-4926.
(55) Beagley, B.; Small, R. W. H. *Acta Cryst.* **1964**, *17*, (6), 783-&.
(56) Klapper, H.; Kuppers, H. *Acta Crystallogr. Sect. B-Struct. Commun.* **1973**, *B29*, 21-26.
(57) Banerjee, D.; Kim, S. J.; Li, W.; Wu, H. H.; Li, J.; Borkowski, L. A.; Philips, B. L.; Parise, J. B. *Cryst. Growth Des.* **2010**, *10*, (6), 2801-2805.
(58) Sorianogarcia, M.; Rao, S. N. *Acta Crystallogr. Sect. C-Cryst. Struct. Commun.* **1983**, *39*, 850-852.
(59) Wiesbrock, F.; Schmidbaur, H. *J. Chem. Soc.-Dalton Trans.* **2002**, (16), 3201-3205.
(60) Arico, A. S.; Bruce, P. G.; Scrosati, B.; Tarascon, J. M.; van Schalkwijk, W. *Nat. Mater.* **2005**, *4*, (5), 366-377.
(61) Bennett, T. D.; Cao, S.; Tan, J.-C.; Keen, D. A.; Bithell, E. G.; Beldon, P. J.; Friscic, T.; Cheetham, A. K. *J. Am. Chem. Soc.* **2011**, *133*, (37), 14546-14549.
(62) The low precision of the results is symptomatic of their low values: high resistances cause the characteristic semicircle observed in the Nyquist plot (of real vs. imaginery impedance) to extend into lower frequencies, which are associated with lower accuracy.
(63) Kumar, B.; Scanlon, L. G. *J. Electroceram.* **2000**, *5*, (2), 127-139.
(64) Park, Y.; Shin, D. S.; Woo, S. H.; Choi, N. S.; Shin, K. H.; Oh, S. M.; Lee, K. T.; Hong, S. Y. *Adv. Mater.* **2012**, *24*, (26), 3562-3567.

Chapter 6. Appendix

6.1. Single crystal X-ray diffraction (see CD)

6.1.1. *Crystallographic information files*

6.1.1.1. Lithium tartrates **1** - **5**

6.1.1.2. Lithium tartrate **6**

6.1.1.3. Lithium tartrate **7**

6.1.1.4. Lithium tartrate **8**

6.1.1.5. Lithium tartrate **9**

6.1.1.6. Lithium tartrate **10**

6.1.1.7. Lithium tartrate **11**

6.1.1.8. Lithium succinate, 120 K

6.1.1.9. Lithium tetrafluorosuccinate

6.1.1.10. Lithium L-malate

6.1.1.11. Lithium methylsuccinate

6.1.1.12. $Li_2(mal)_{0.2}(fum)_{0.8}$

6.1.1.13. $Li_2(mal)_{0.23}(fum)_{0.77}$

6.1.1.14. $Li_2(mal)_{0.43}(fum)_{0.57}$

6.1.1.15. Lithium 2,2-dimethylsuccinate

6.1.1.16. Lithium fumarate

6.1.1.17. Lithium hydrogen fumarate

6.1.1.18. Lithium hydrogen D,L-malate

6.1.2. *Structure refinement result files (see CD)*

6.1.2.1. Lithium tartrate **1**

6.1.2.2. Lithium tartrate **2**

6.1.2.3. Lithium tartrate **3**

6.1.2.4. Lithium tartrate **4**

6.1.2.5. Lithium tartrate **5**

6.1.2.6. Lithium tartrate **6**

6.1.2.7. Lithium tartrate **7**

6.1.2.8. Lithium tartrate **8**

6.1.2.9. Lithium tartrate **9**

6.1.2.10. Lithium tartrate **10**

6.1.2.11. Lithium tartrate **11**

6.1.2.12. Lithium succinate, 120 K

6.1.2.13. Lithium tetrafluorosuccinate

6.1.2.14. Lithium L-malate

6.1.2.15. Lithium methylsuccinate

6.1.2.16. $Li_2(mal)_{0.2}(fum)_{0.8}$

6.1.2.17. $Li_2(mal)_{0.23}(fum)_{0.77}$

6.1.2.18. $Li_2(mal)_{0.43}(fum)_{0.57}$

6.1.2.19. Lithium 2,2-dimethylsuccinate

6.1.2.20. Lithium fumarate

6.1.2.21. Lithium hydrogen fumarate

6.1.2.22. Lithium hydrogen D,L-malate

6.1.3. *Single crystal hkl files (see CD)*

6.1.3.1. Lithium tartrate **1**

6.1.3.2. Lithium tartrate **2**

6.1.3.3. Lithium tartrate **3**

6.1.3.4. Lithium tartrate **4**

6.1.3.5. Lithium tartrate **6**

6.1.3.6. Lithium tartrate **7**

6.1.3.7. Lithium tartrate **8**

6.1.3.8. Lithium tartrate **9**

6.1.3.9. Lithium tartrate **10**

6.1.3.10. Lithium tartrate **11**

6.1.3.11. Lithium succinate, 120 K

6.1.3.12. Lithium tetrafluorosuccinate

6.1.3.13. Lithium L-malate

6.1.3.14. Lithium methylsuccinate

6.1.3.15. $Li_2(mal)_{0.2}(fum)_{0.8}$

6.1.3.16. $Li_2(mal)_{0.23}(fum)_{0.77}$

6.1.3.17. $Li_2(mal)_{0.43}(fum)_{0.57}$

6.1.3.18. Lithium 2,2-dimethylsuccinate

6.1.3.19. Lithium fumarate

6.1.3.20. Lithium hydrogen fumarate

6.1.3.21. Lithium hydrogen D,L-malate

6.2. Powder X-ray diffraction

6.2.1. *Laboratory data for bulk products*

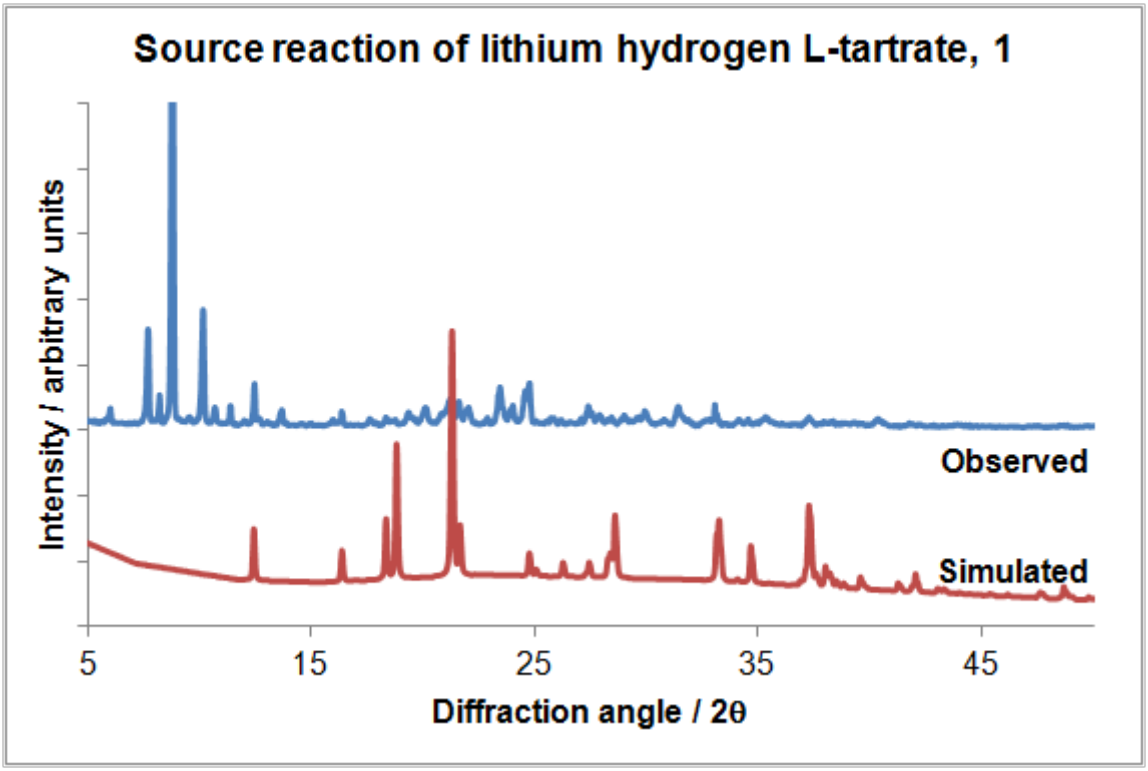

*Figure 1. Source reaction of lithium hydrogen L-tartrate, **1**, PXRD.*

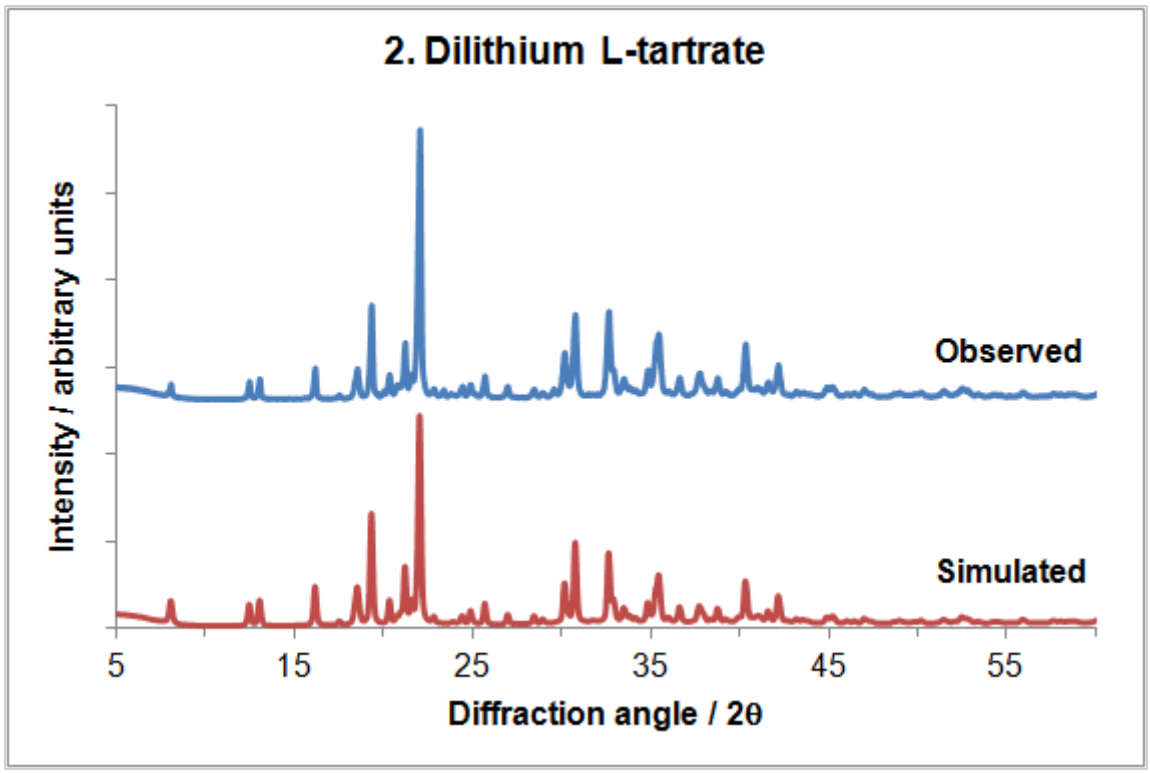

*Figure 2. Dilithium L-tartrate, **2**, PXRD.*

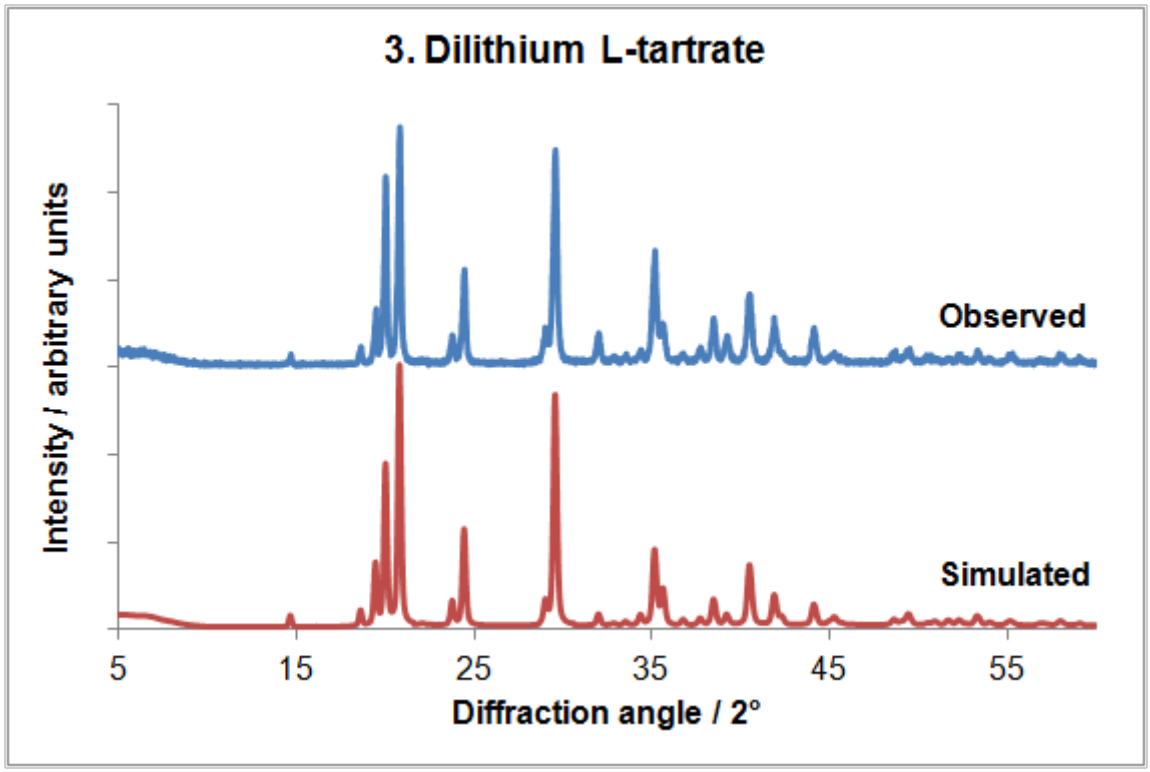

*Figure 3. Dilithium L-tartrate, **3**, PXRD.*

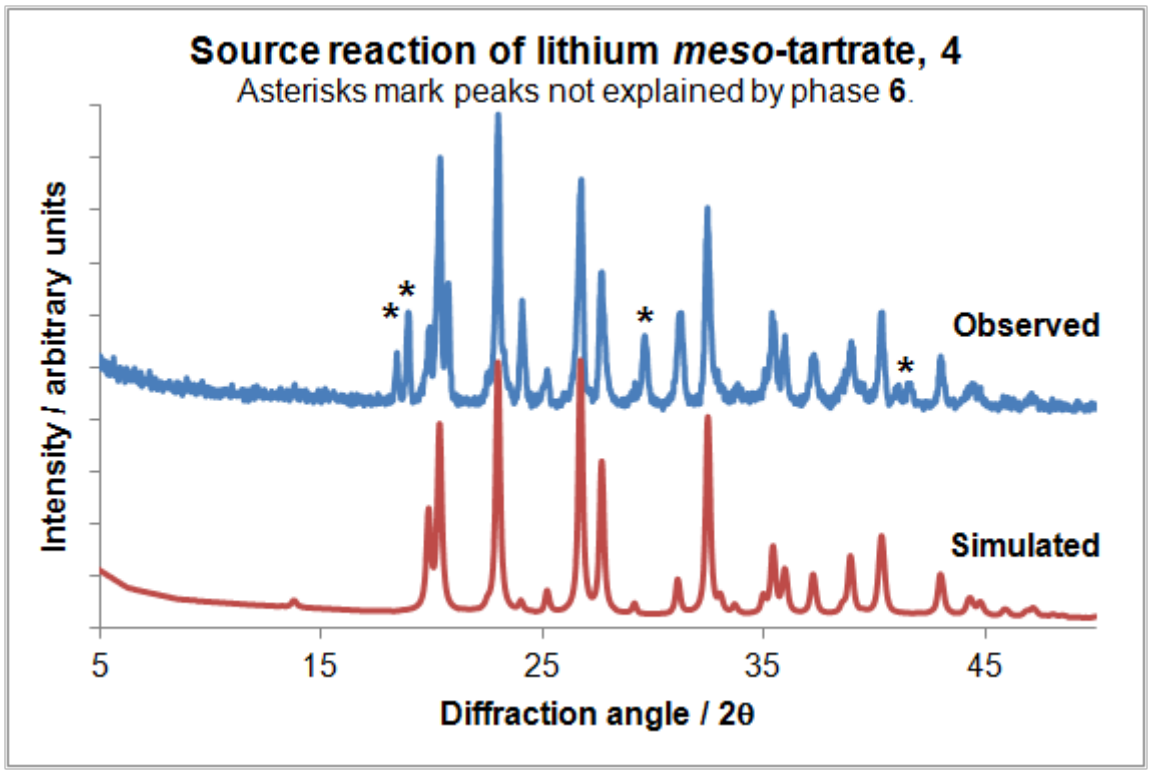

*Figure 4. Source reaction of dilithium meso-tartrate, **4**, PXRD.*

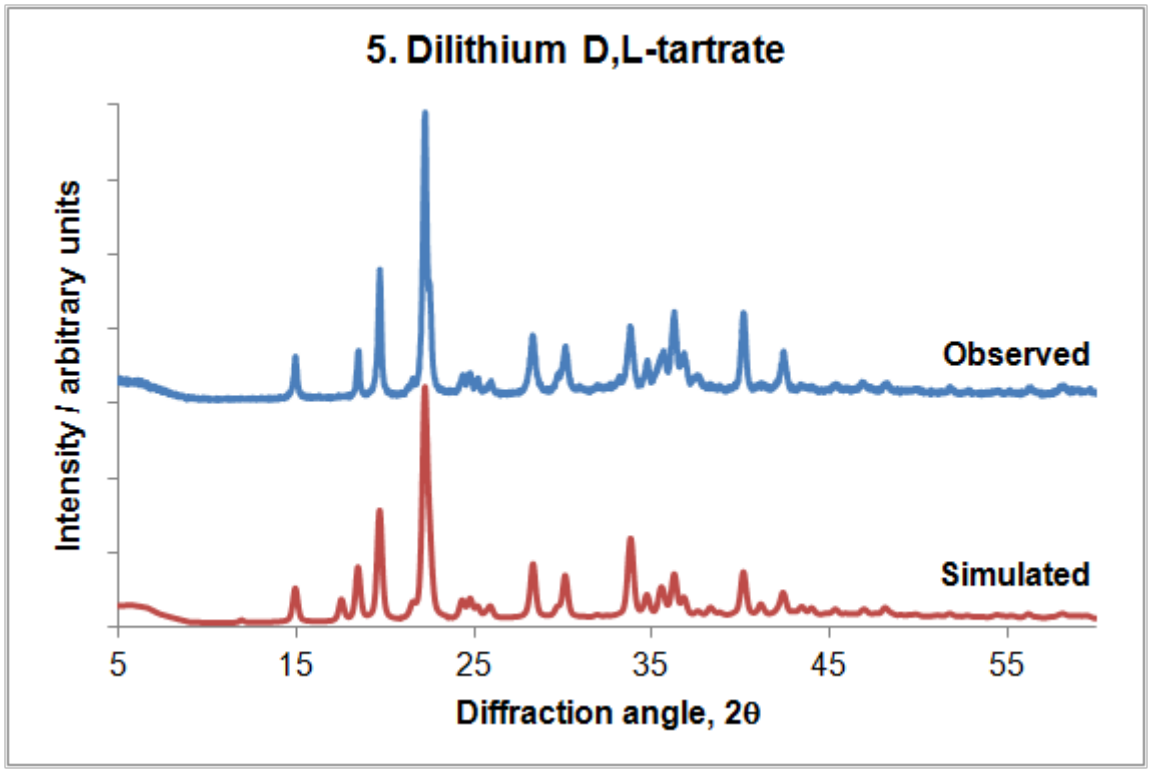

*Figure 5. Dilithium D,L-tartrate, **5**, PXRD.*

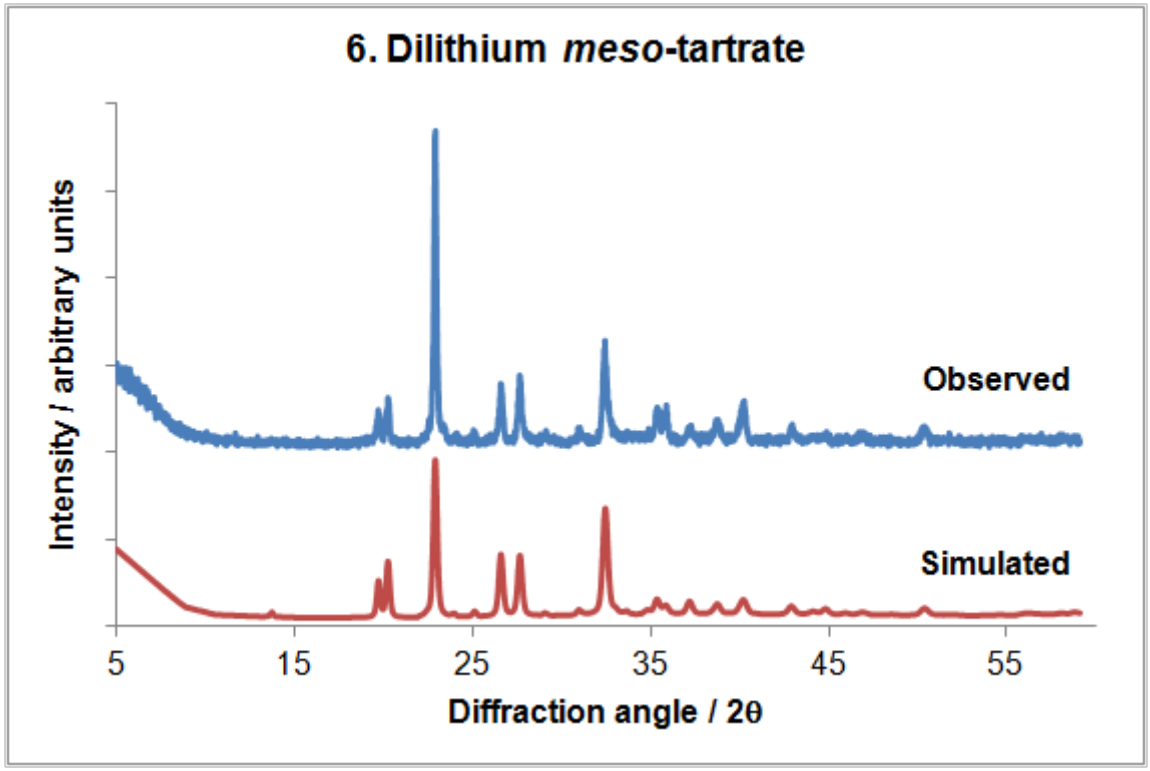

*Figure 6. Dilithium meso-tartrate, **6**, PXRD.*

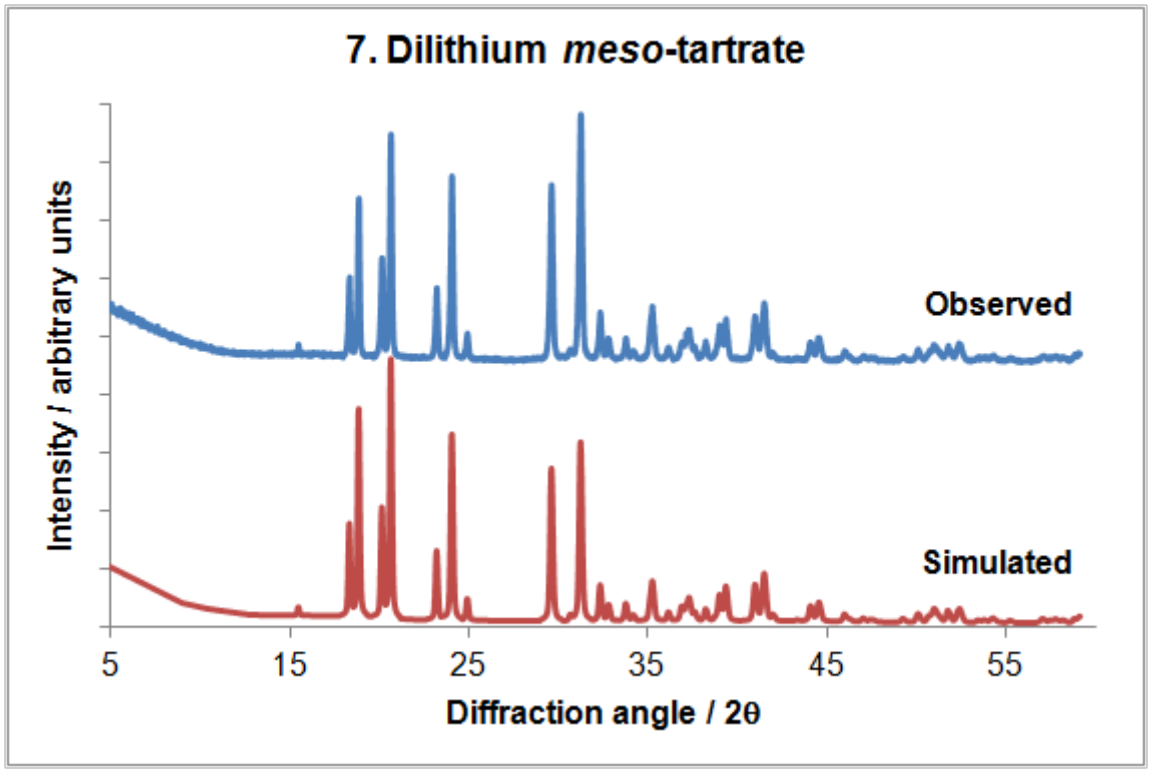

*Figure 7. Dilithium meso-tartrate, **7**, PXRD.*

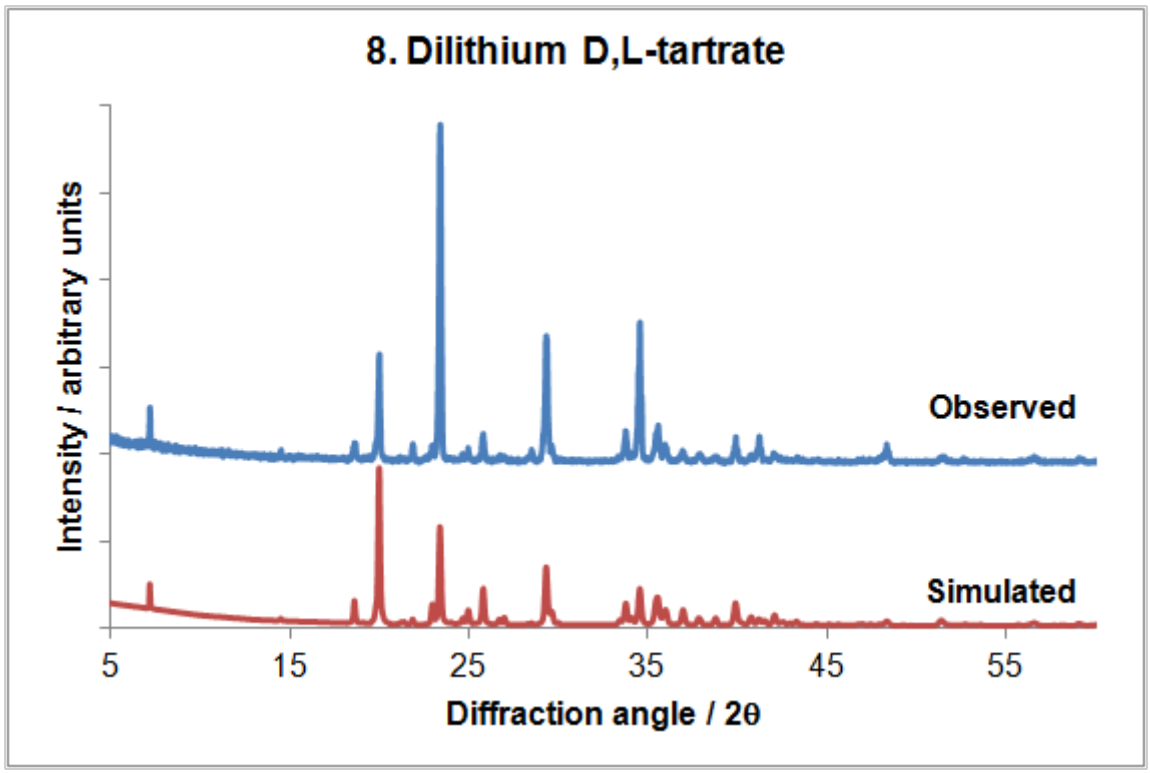

*Figure 8. Dilithium D,L-tartrate, **8**, PXRD.*

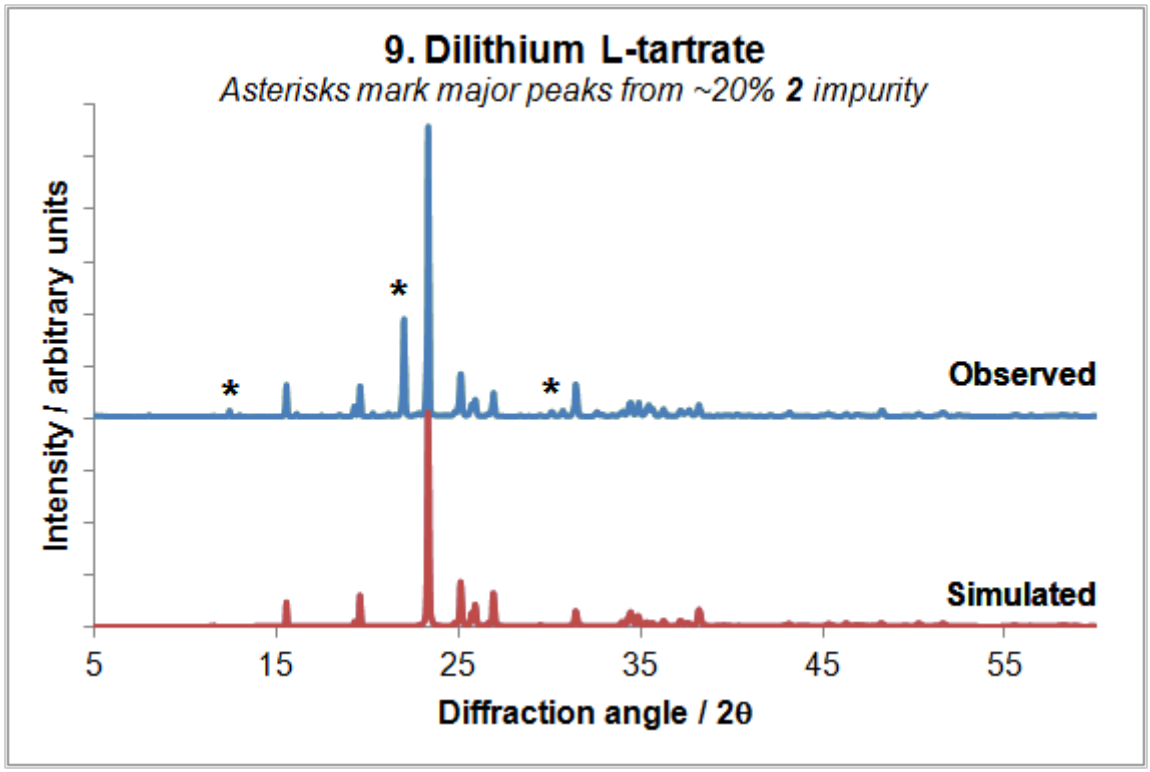

*Figure 9. Dilithium L-tartrate, **9**, PXRD.*

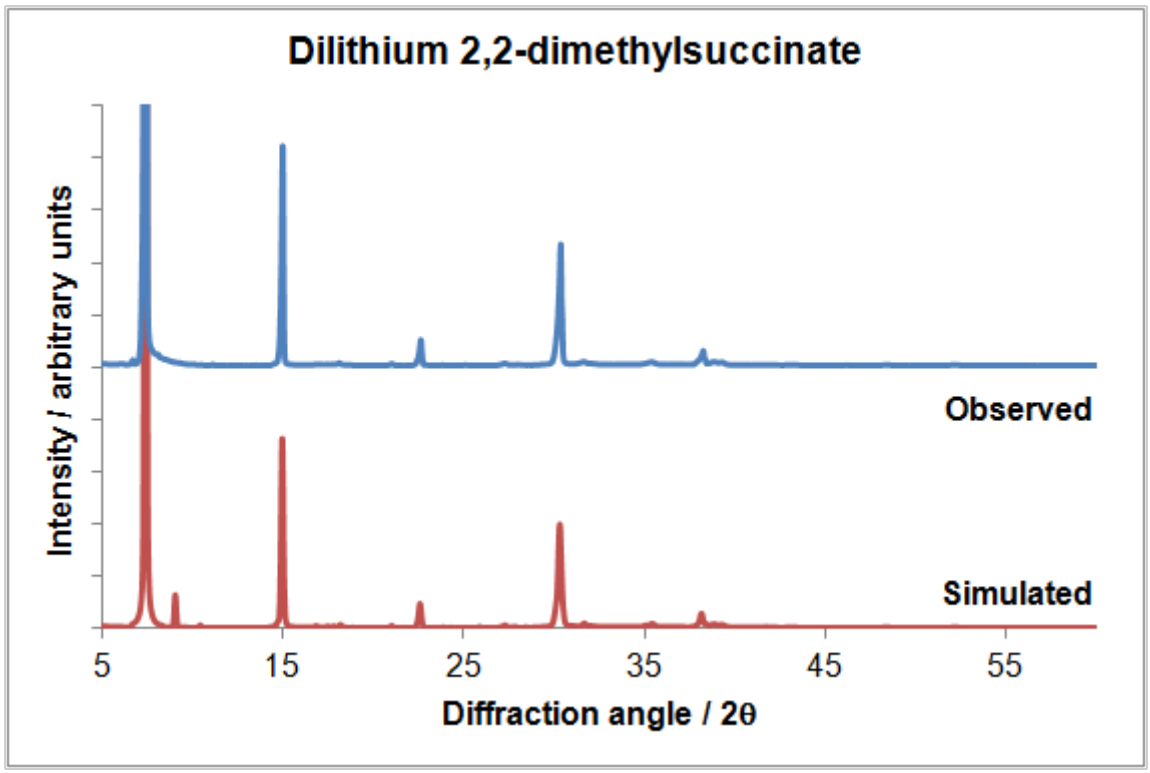

Figure 10. Dilithium 2,2-dimethylsuccinate PXRD.

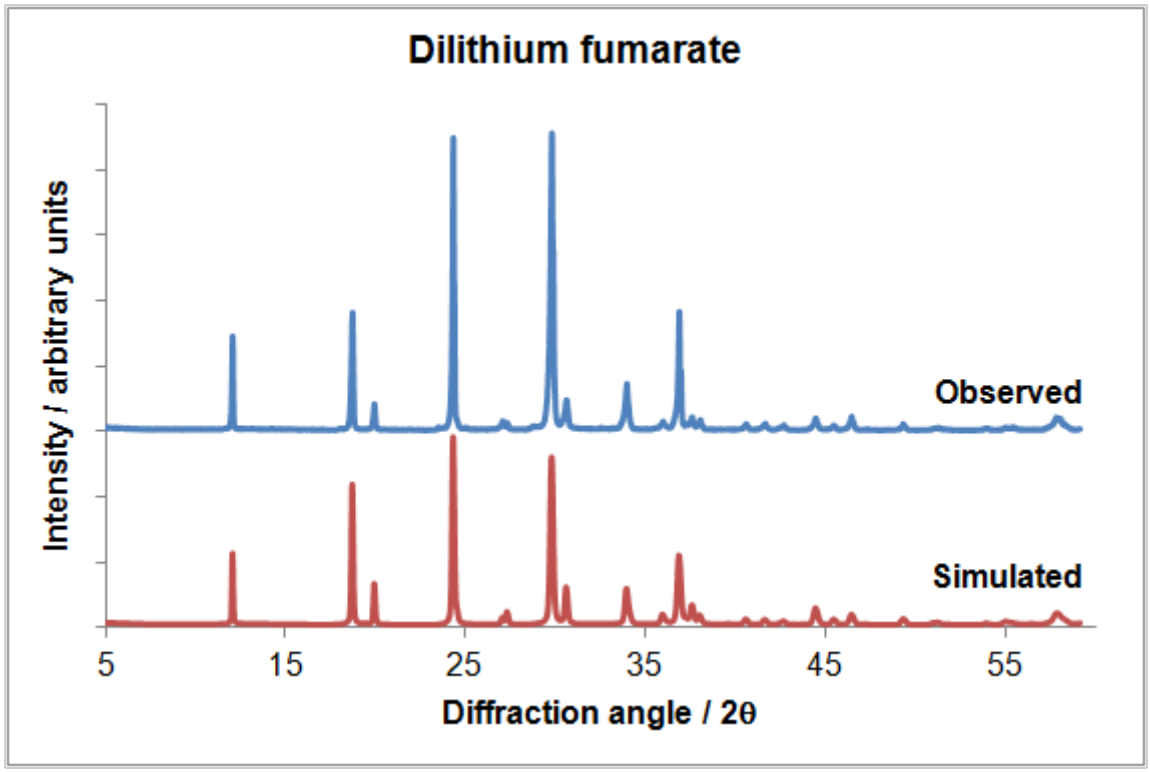

Figure 11.Dilithium fumarate PXRD.

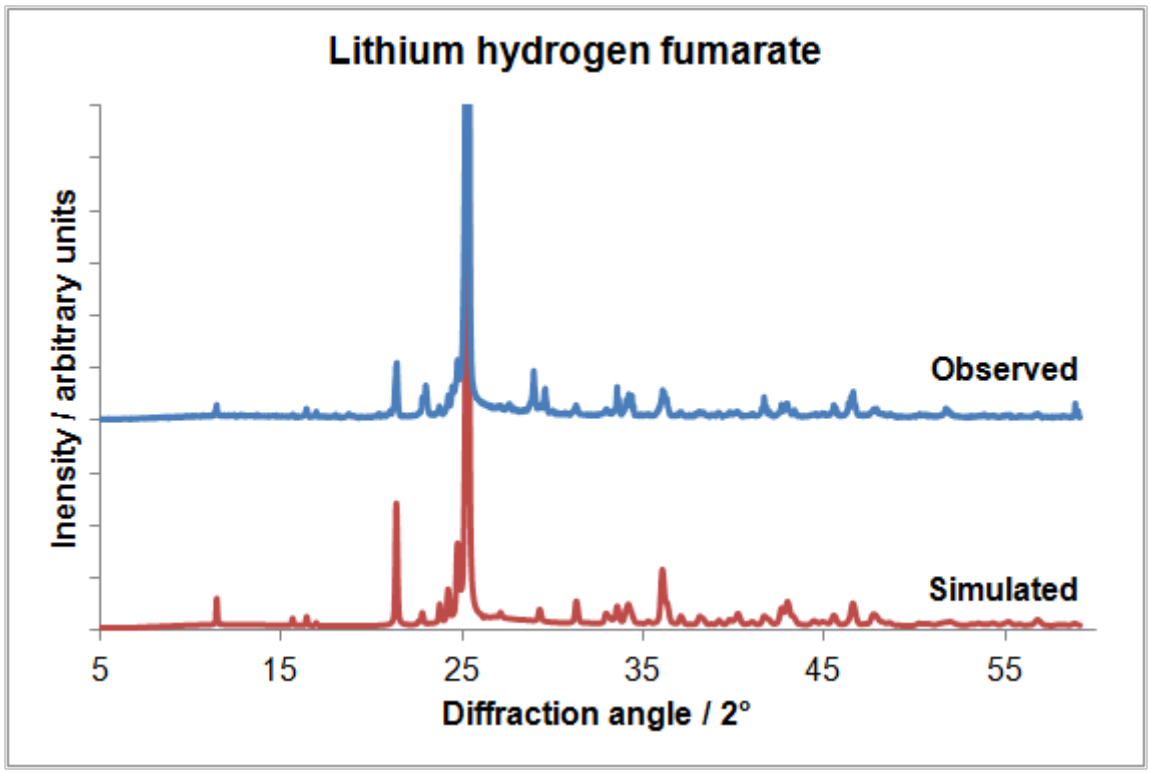

Figure 12. Lithium hydrogen fumarate PXRD.

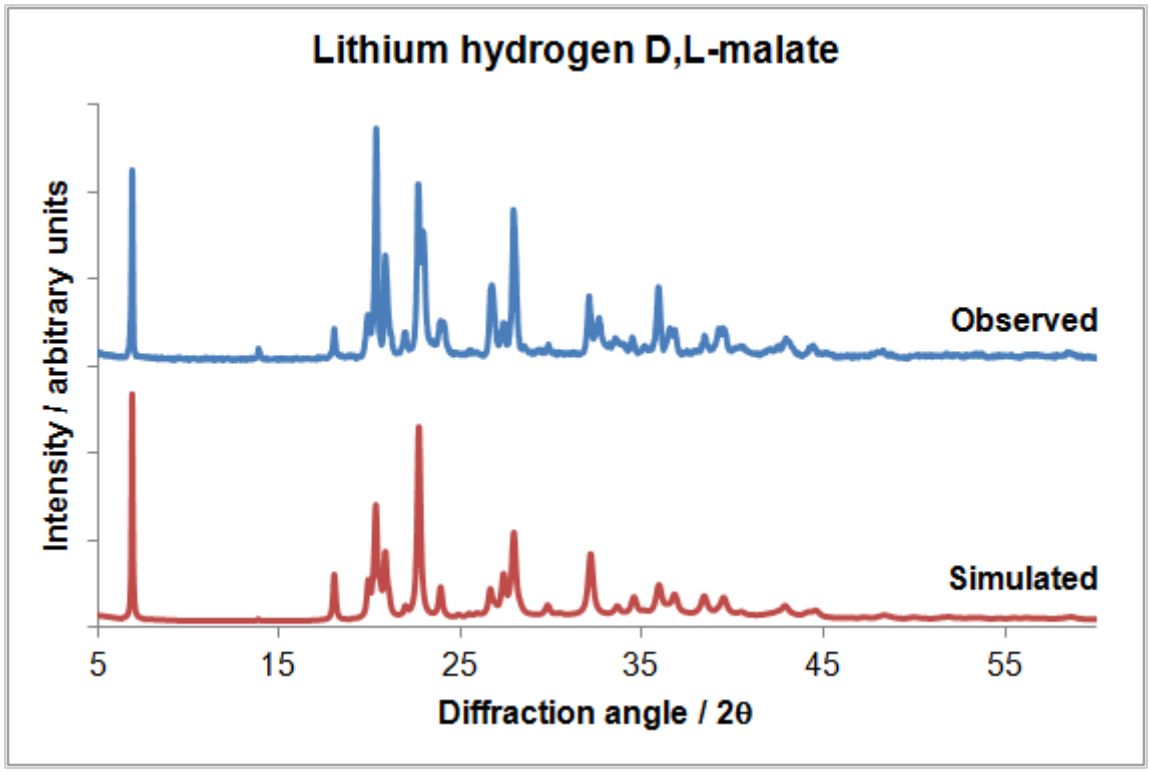

Figure 13. Lithium hydrogen D,L-malate PXRD.

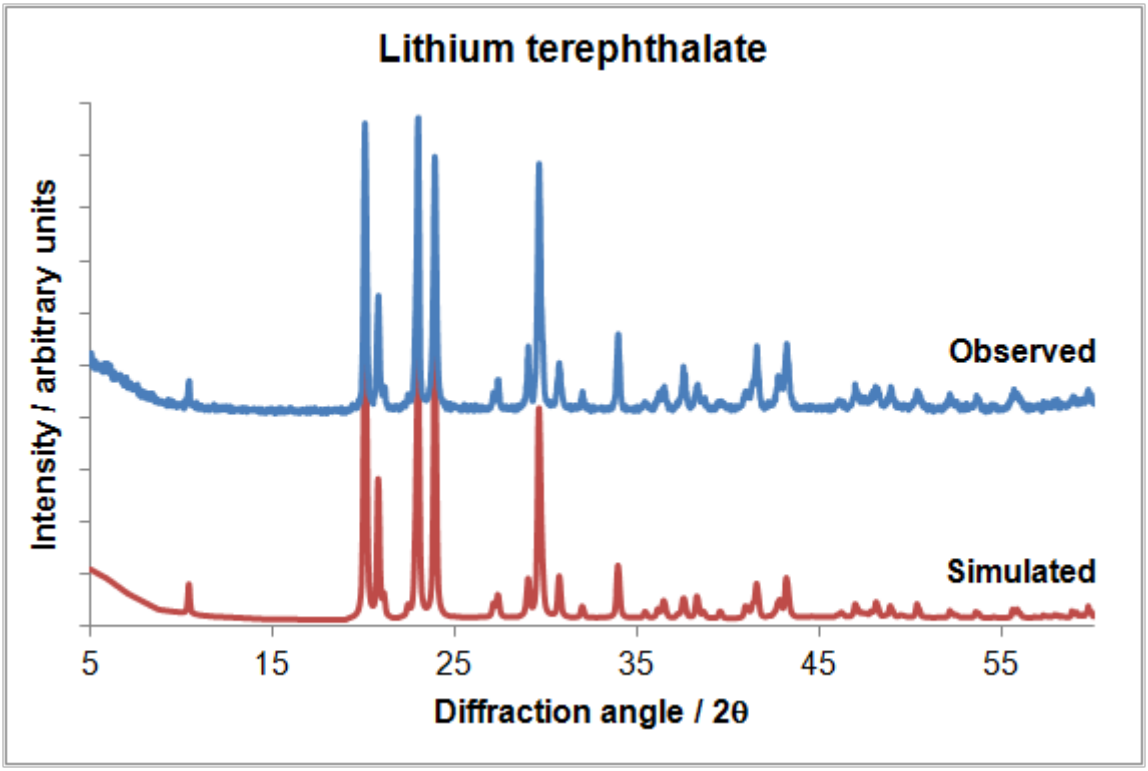

Figure 14. Lithium terephthalate (mechanochemical synthesis) PXRD.

6.2.2. *Synchrotron data (see CD)*

6.2.2.1. Rietveld refinement files for $Li_2(suc)_{1-x}(flu)_x$

6.2.2.2. Le Bail refinement files for $Li_2(suc)_x(mal)_y(met)_z$

6.3. Fourier transform infrared spectra

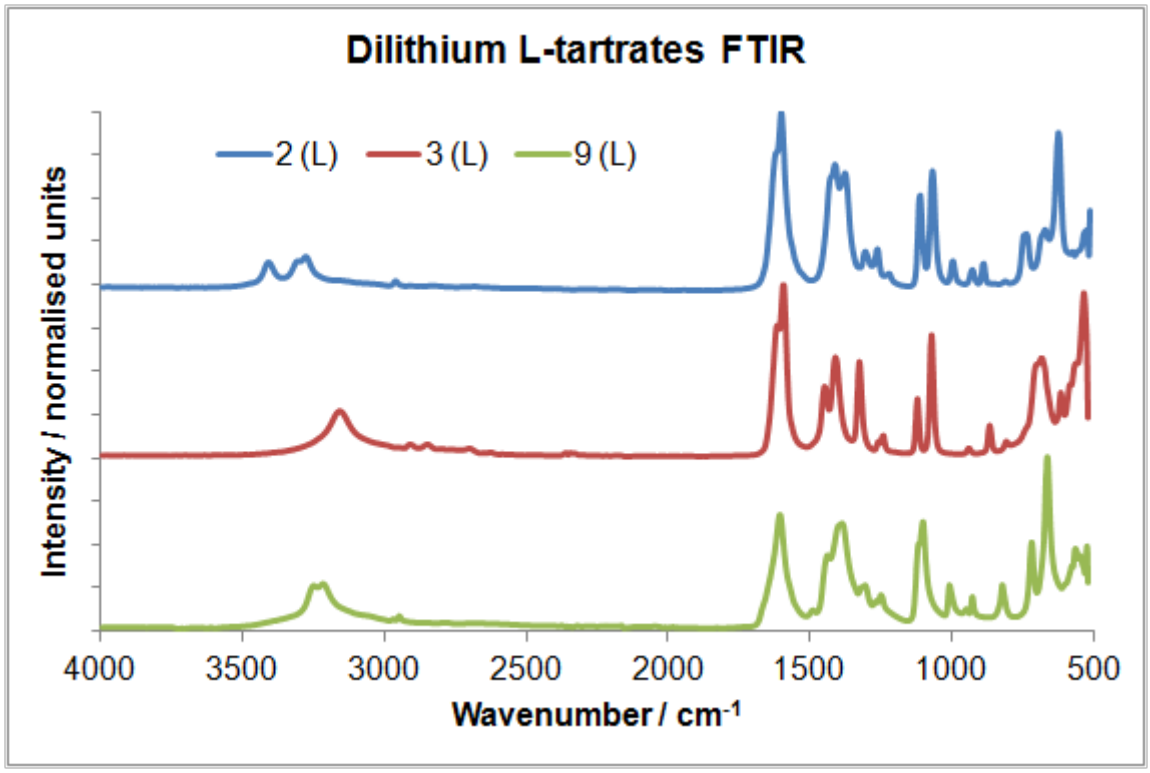

Figure 15. Dilithium L-tartrates FTIR.

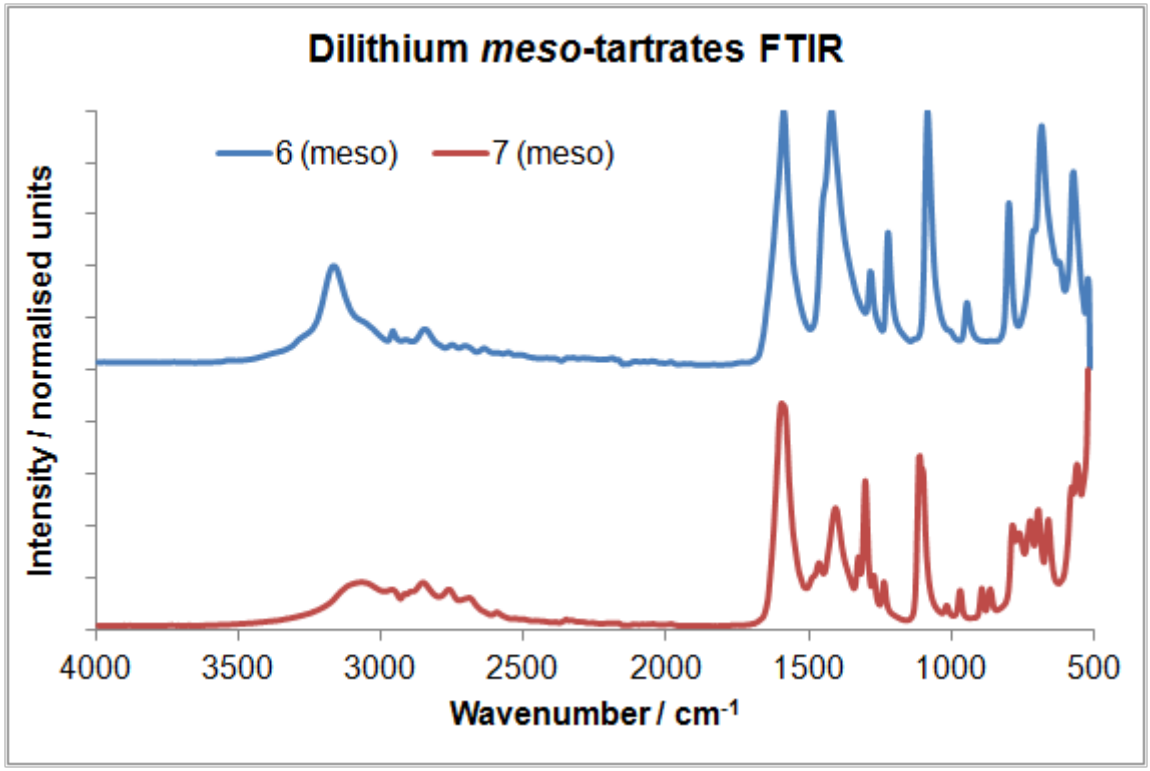

Figure 16. Dilithium meso-tartrates FTIR.

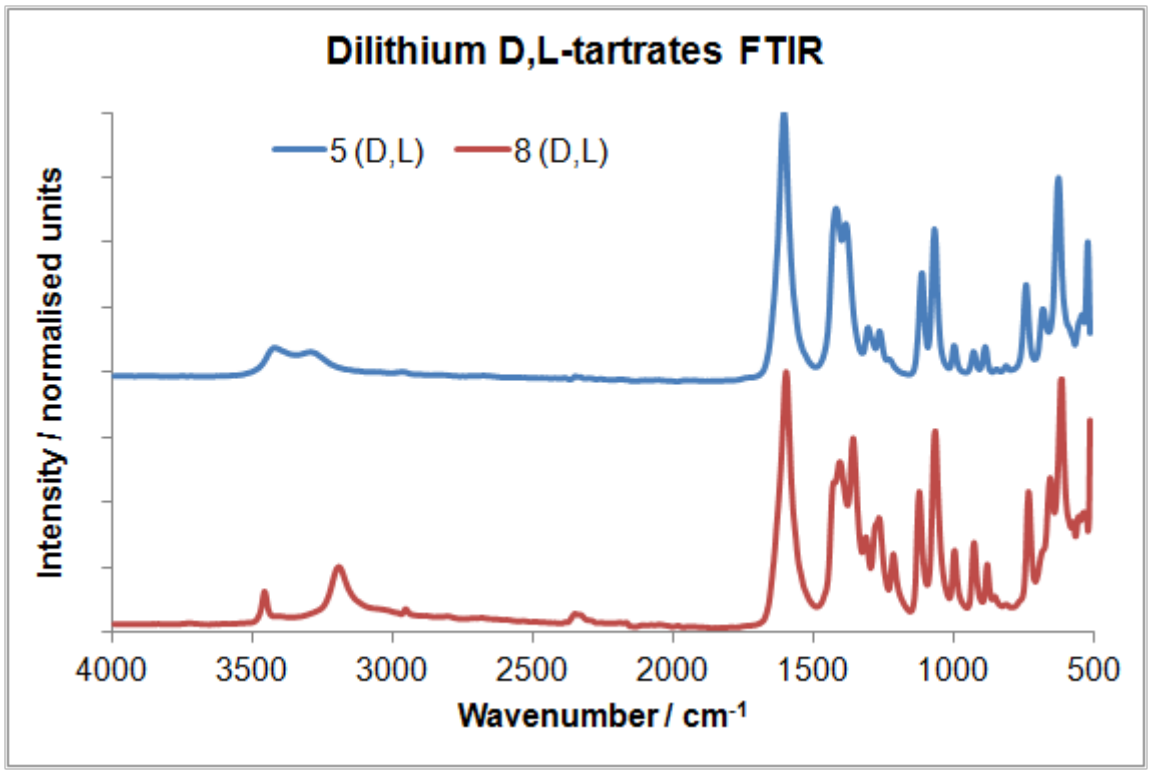

Figure 17. Dilithium D,L-tartrates FTIR.

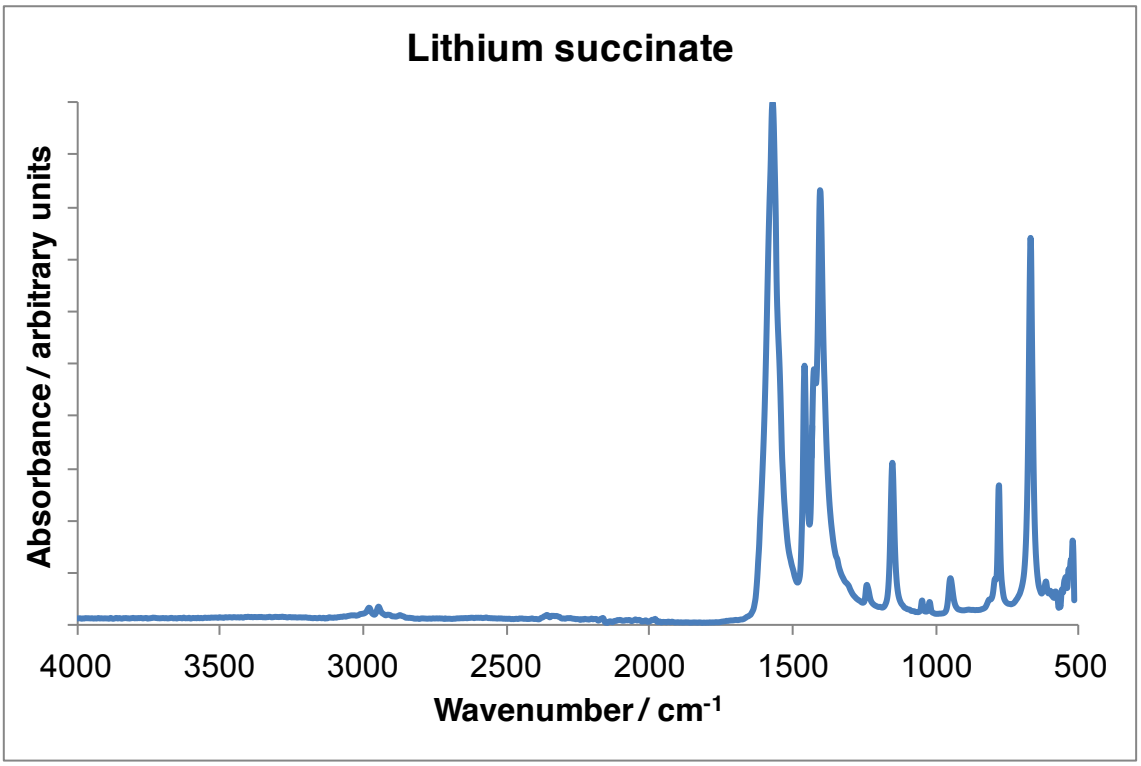

Figure 18. Lithium succinate FTIR.

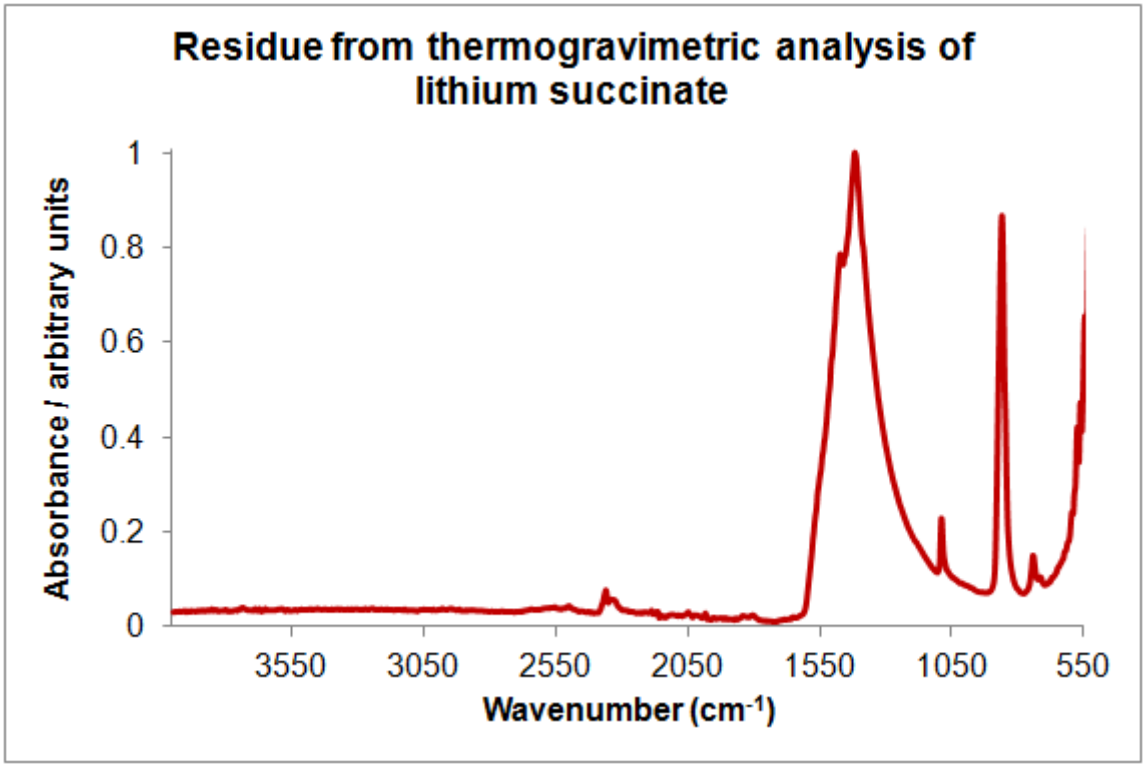

Figure 19. Residue from thermogravimetric analysis of lithium succinate: FTIR.

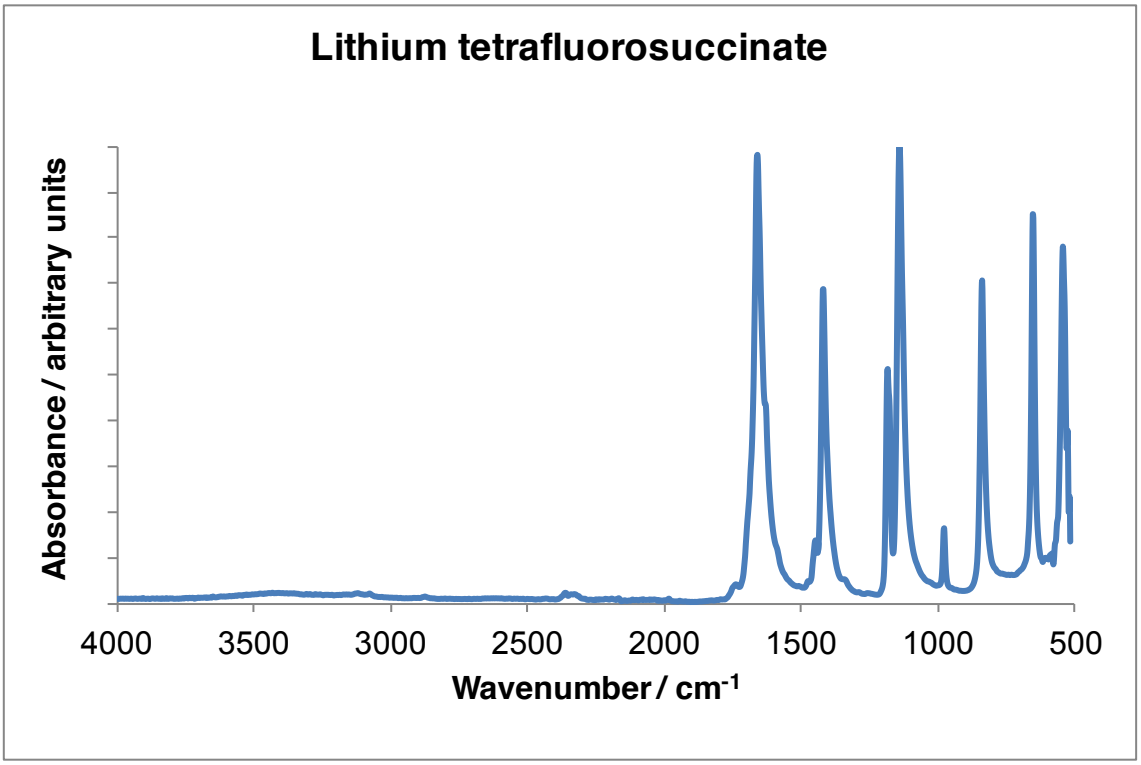

Figure 20. Lithium tetrafluorosuccinate FTIR.

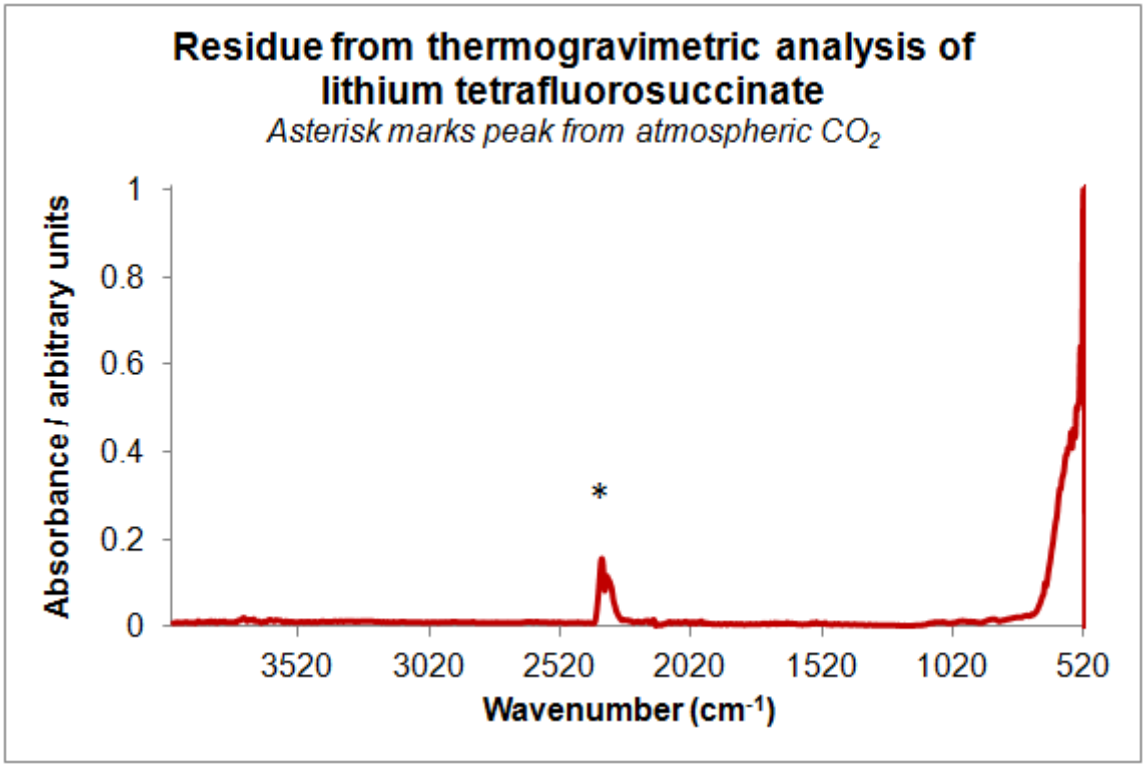

Figure 21. Residue from thermogravimetric analysis of lithium tetrafluorosuccinate: FTIR.

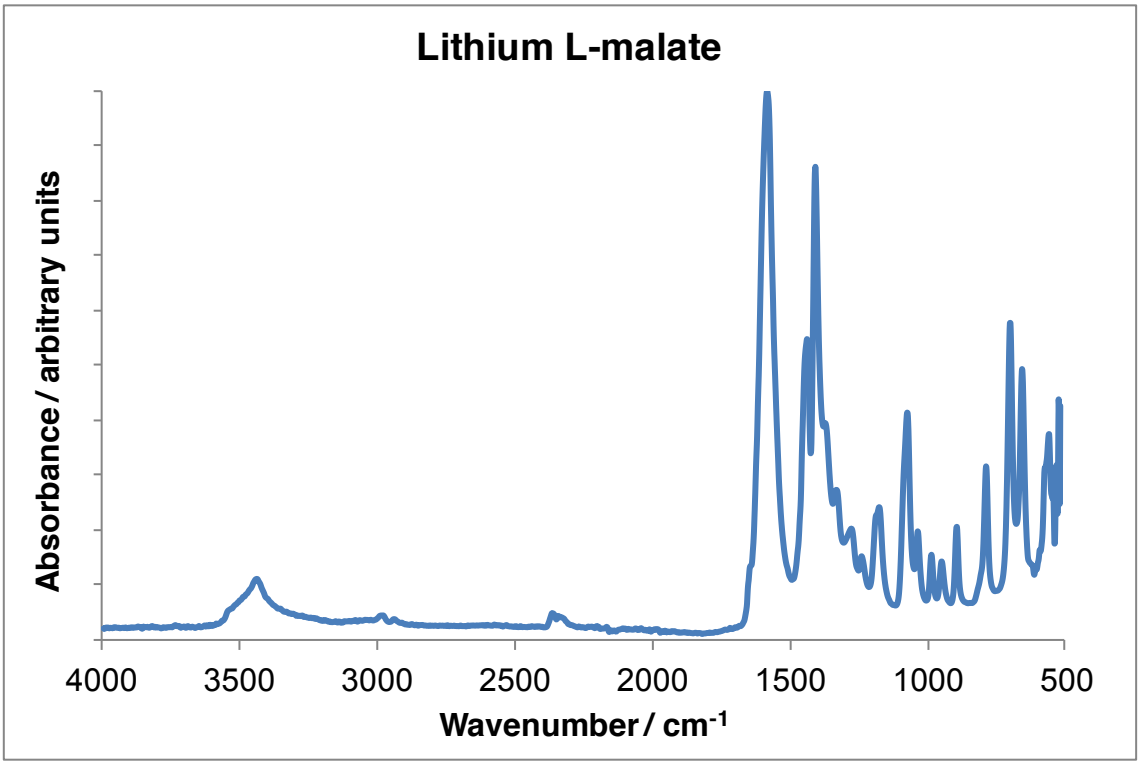

Figure 22. Lithium L-malate FTIR.

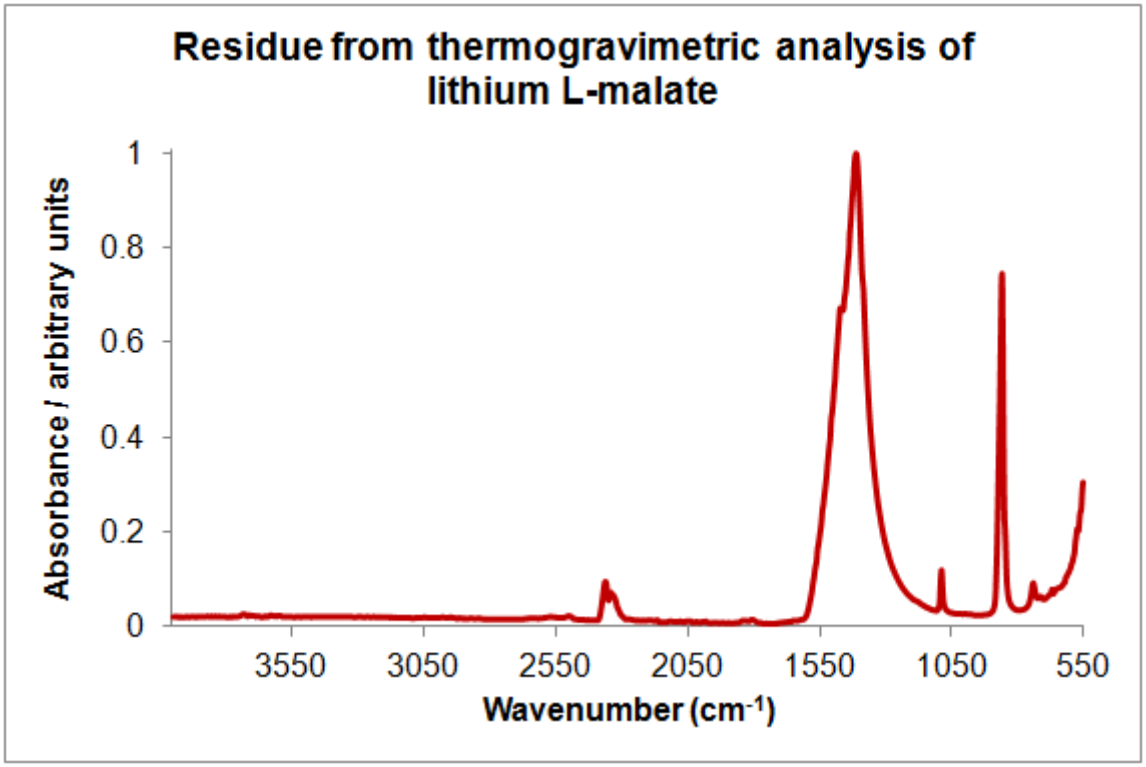

Figure 23. Residue from thermogravimetric analysis of lithium L-malate: FTIR.

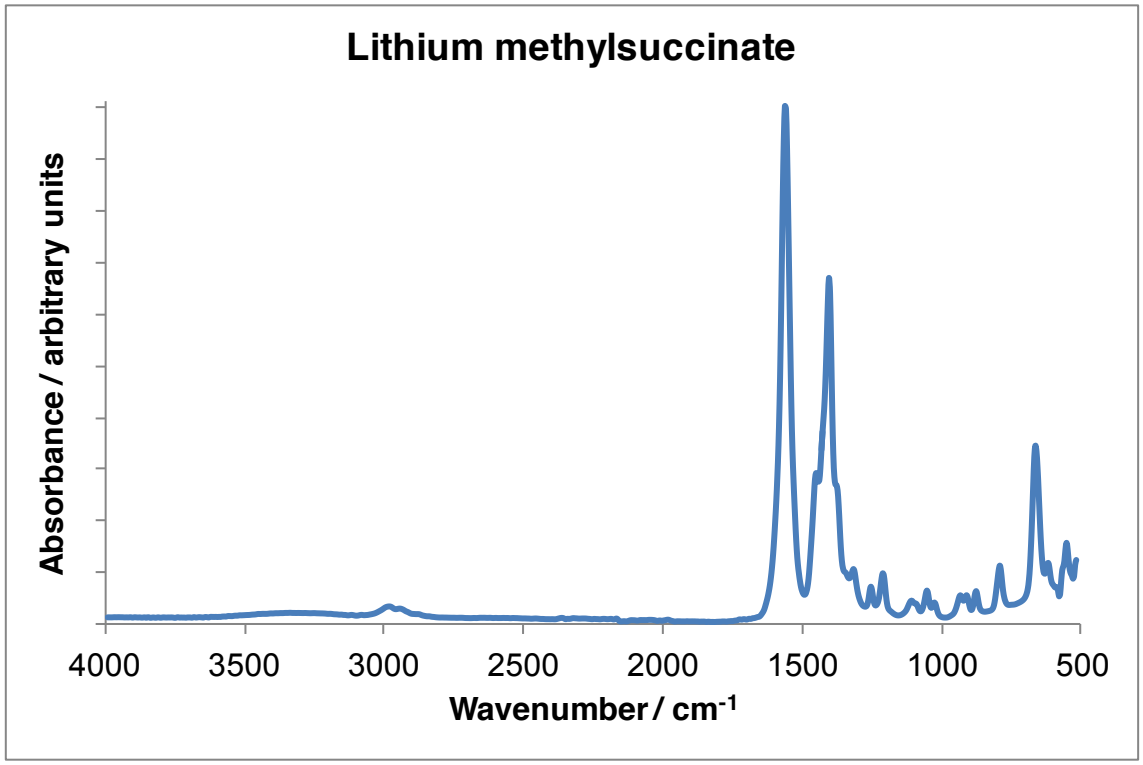

Figure 24. Lithium methylsuccinate FTIR.

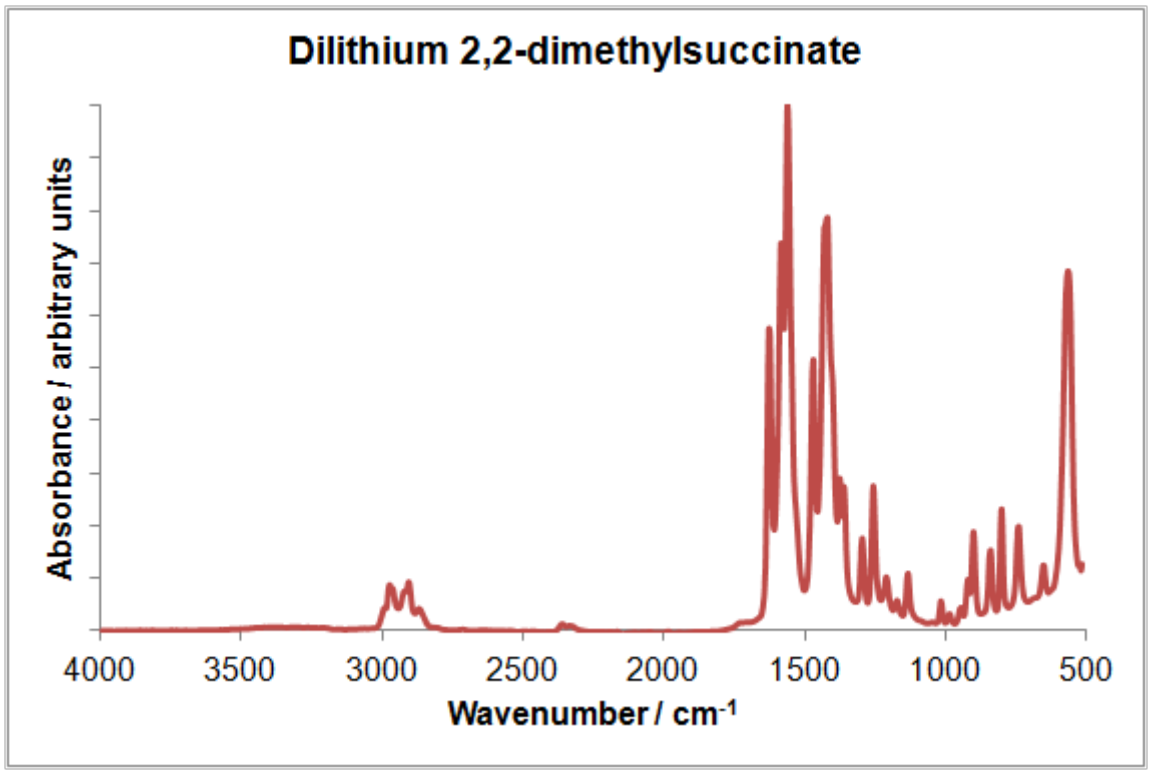

Figure 25. Dilithium 2,2-dimethylsuccinate FTIR.

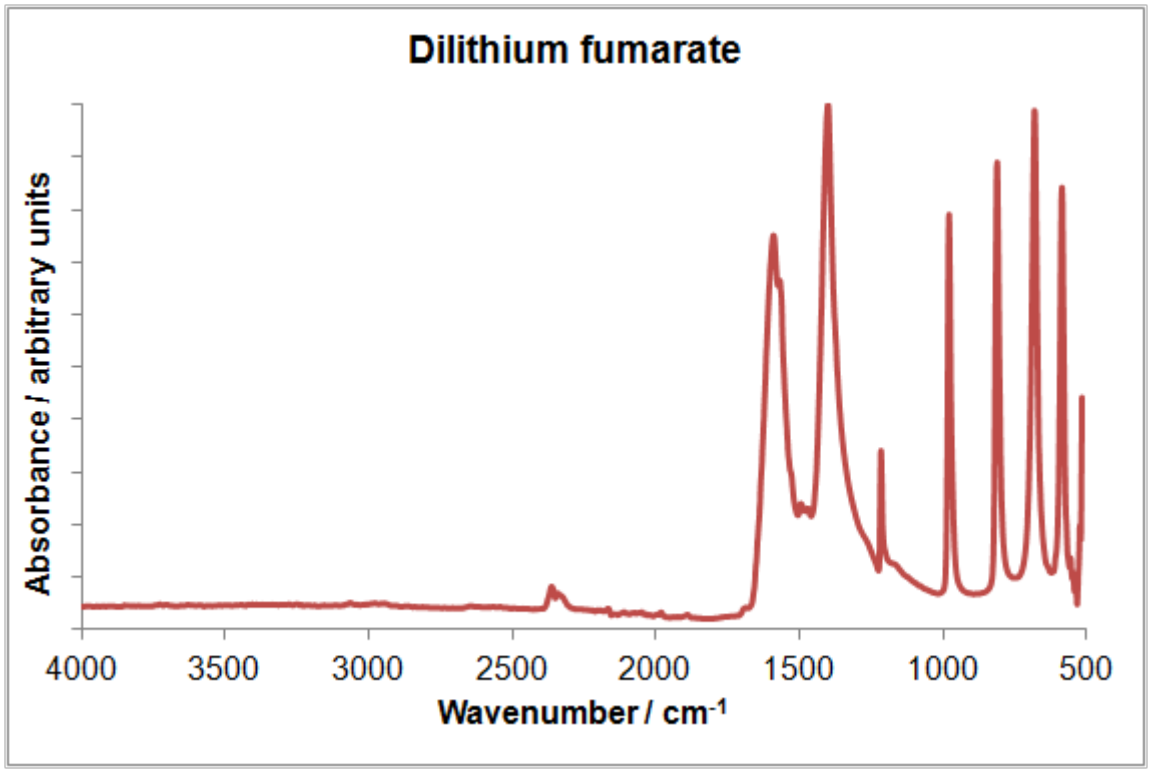

Figure 26. Dilithium fumarate FTIR.

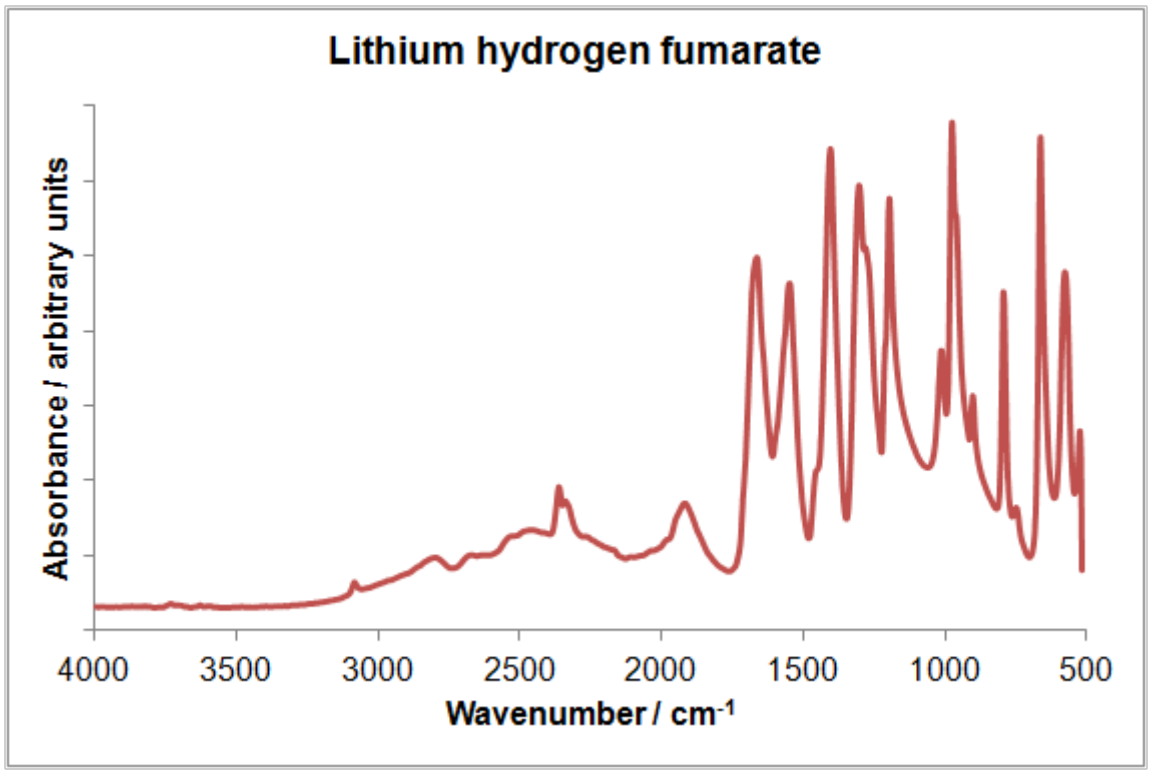

Figure 27. Lithium hydrogen fumarate FTIR.

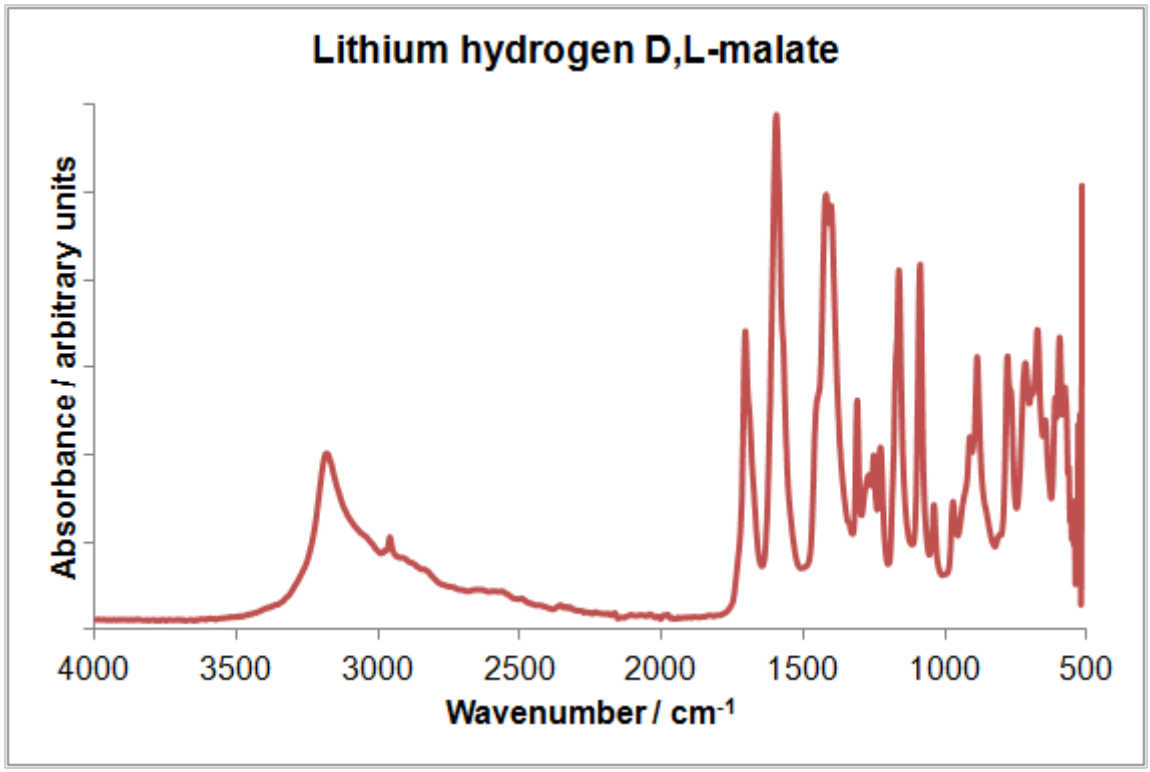

Figure 28. Lithium hydrogen D,L-malate FTIR.

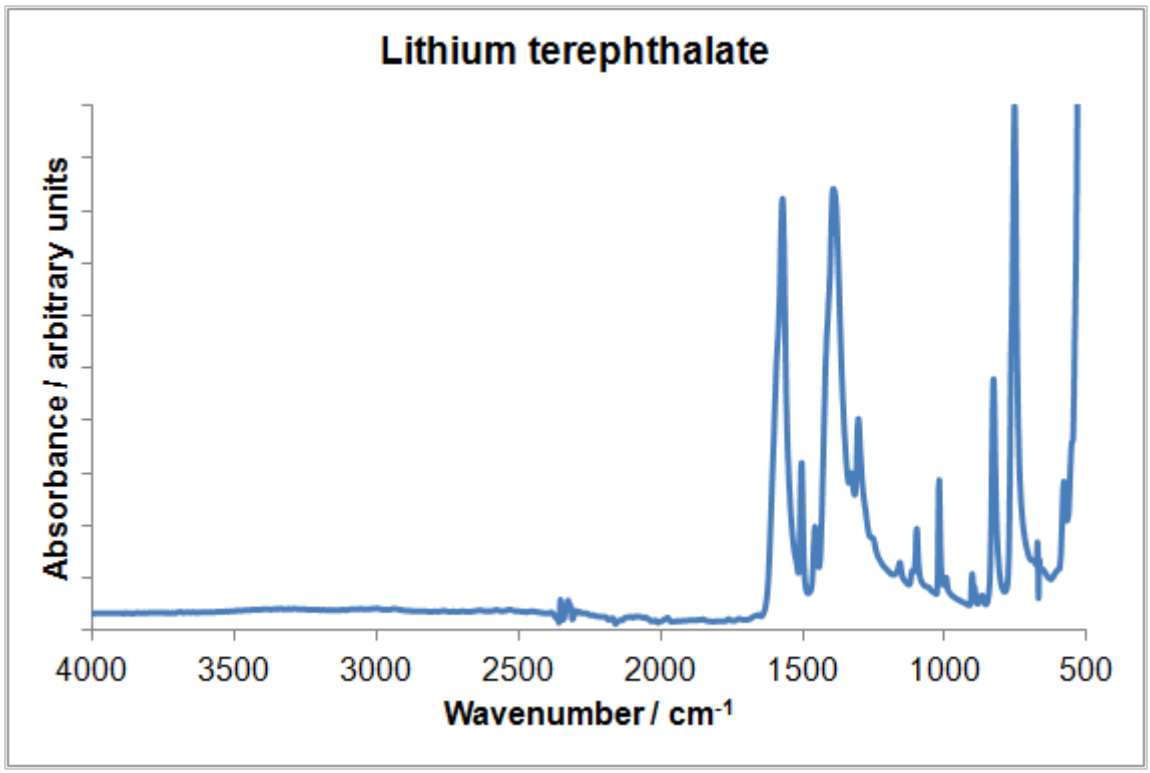

Figure 29. Lithium terephthalate (mechanochemical synthesis) FTIR.

6.4. Thermogravimetric analysis

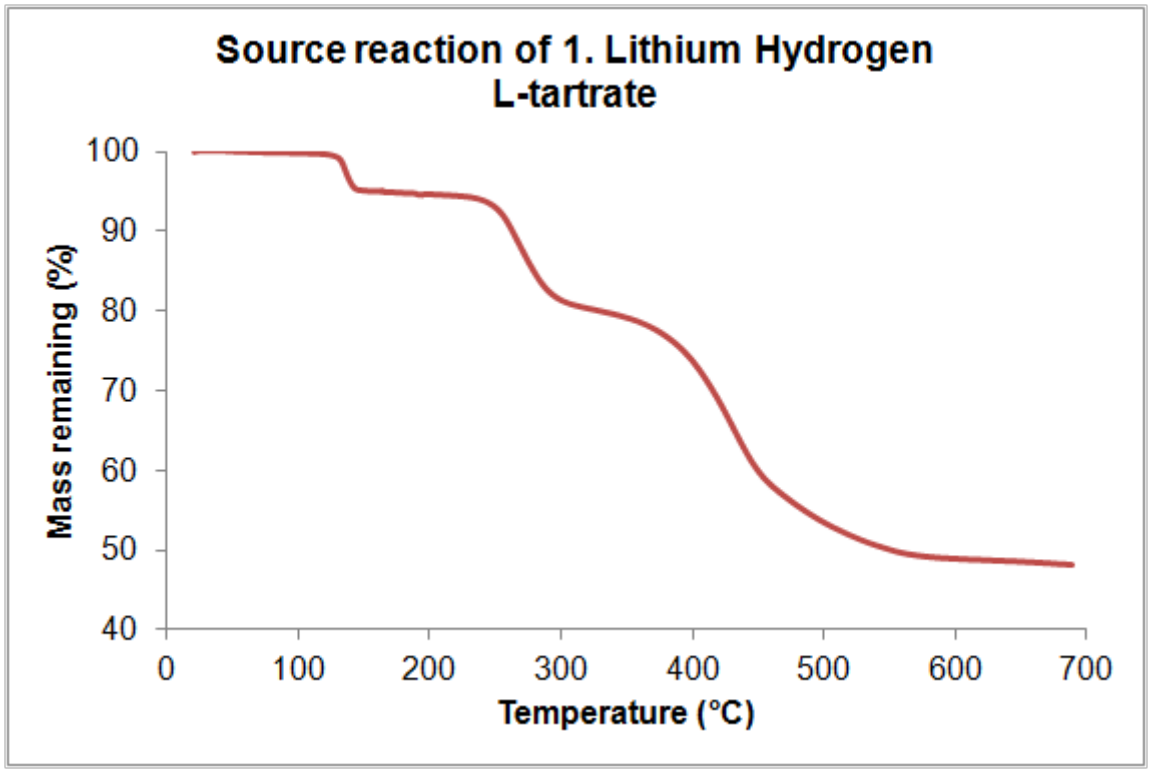

*Figure 30. Source reaction of lithium hydrogen L-tartrate, **1**, TGA.*

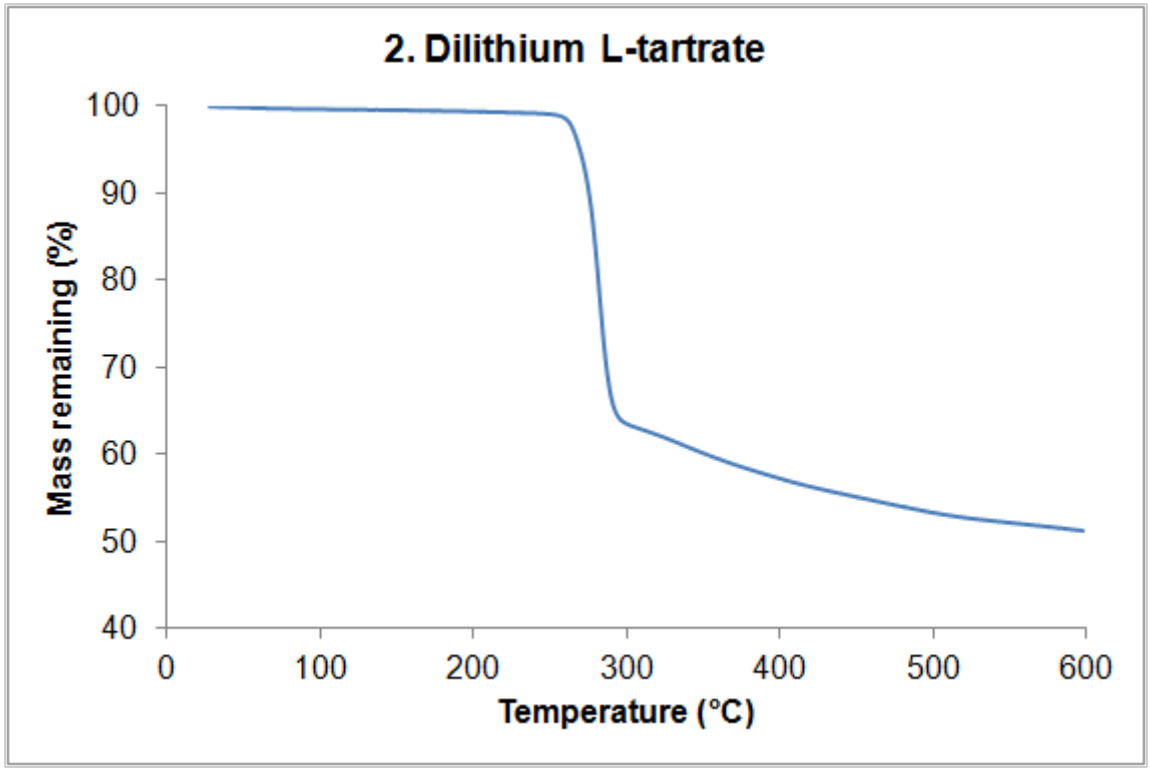

*Figure 31. Dilithium L-tartrate, **2**, TGA.*

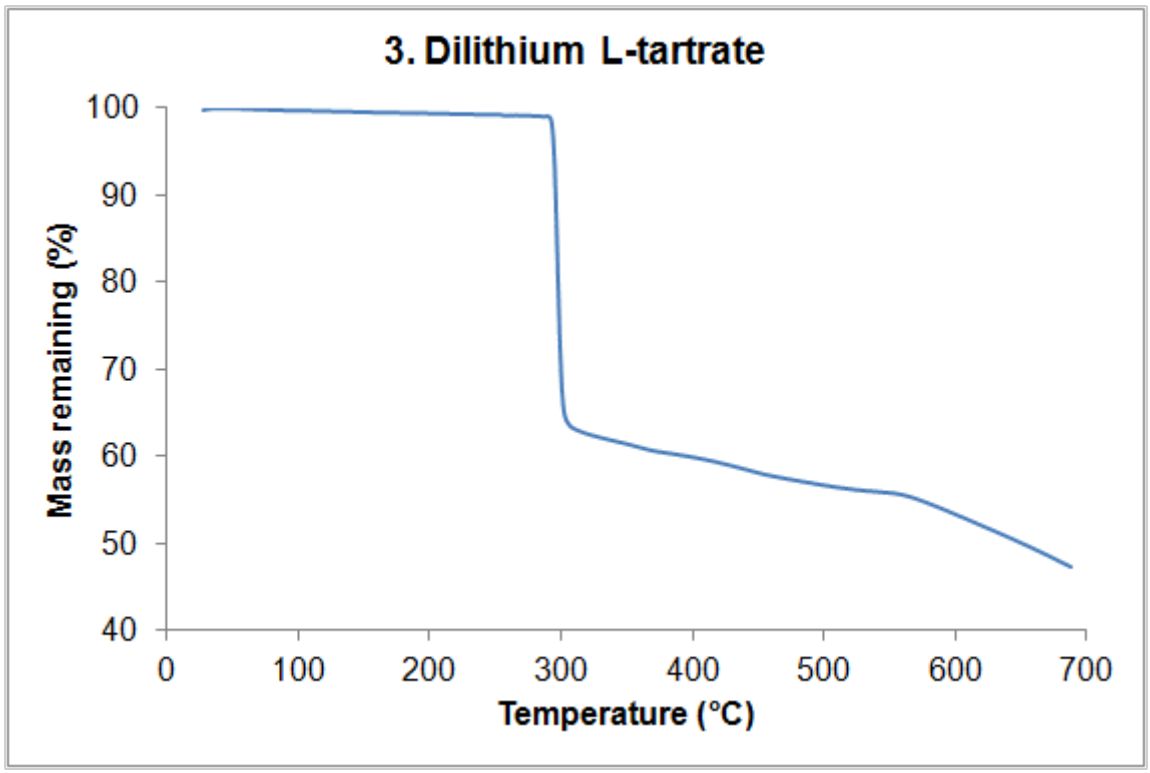

*Figure 32. Dilithium L-tartrate, **3**, TGA.*

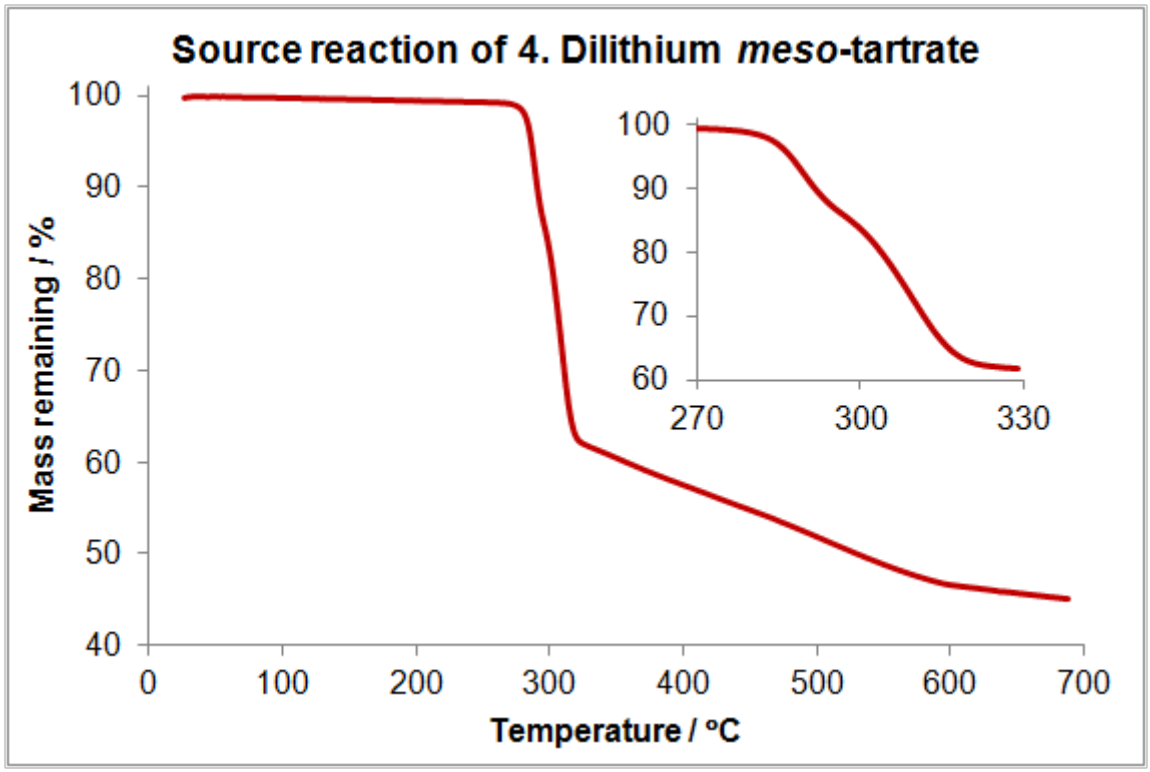

*Figure 33. Source reaction of dilithium meso-tartrate, **4**, TGA.*

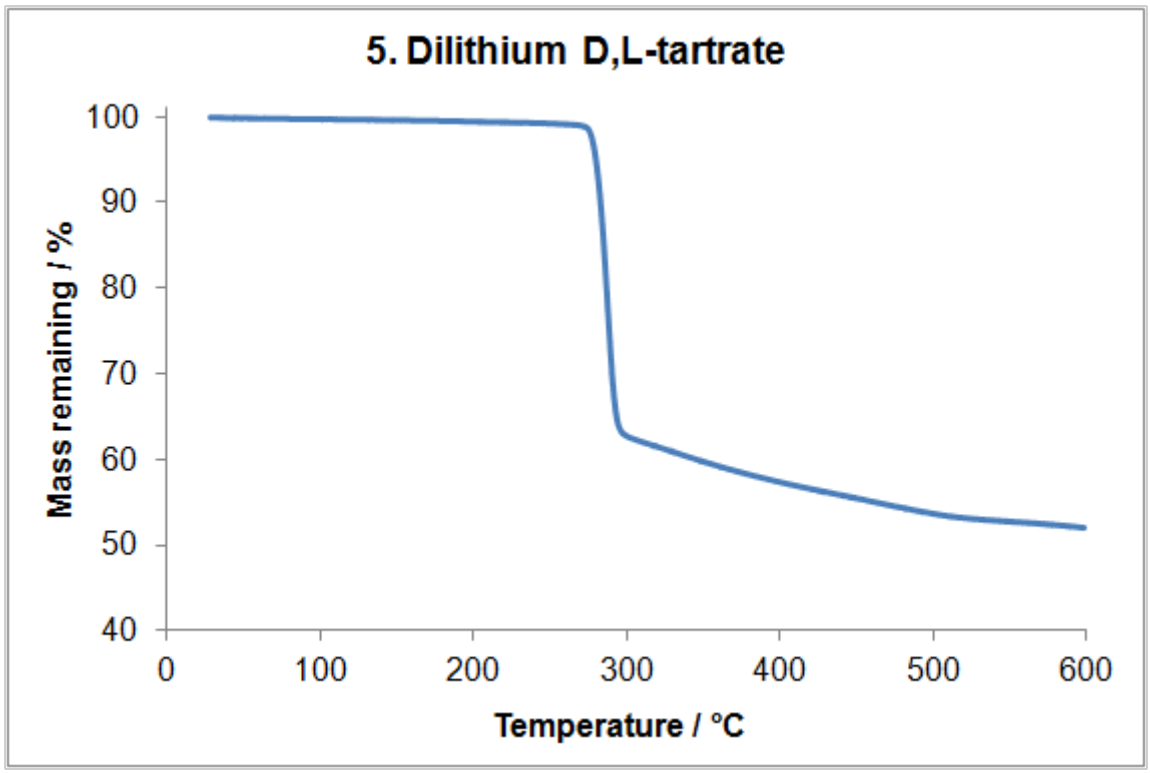

*Figure 34. Dilithium D,L-tartrate, **5**, TGA.*

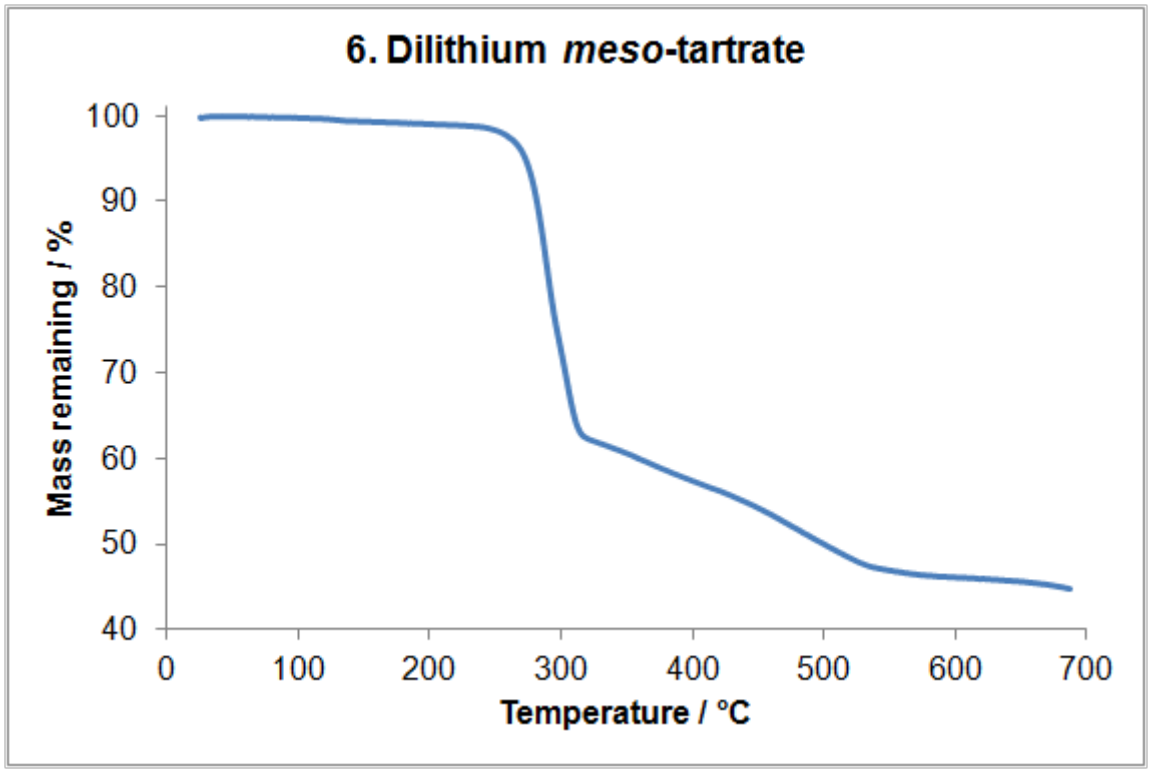

*Figure 35. Dilithium meso-tartrate, **6**.*

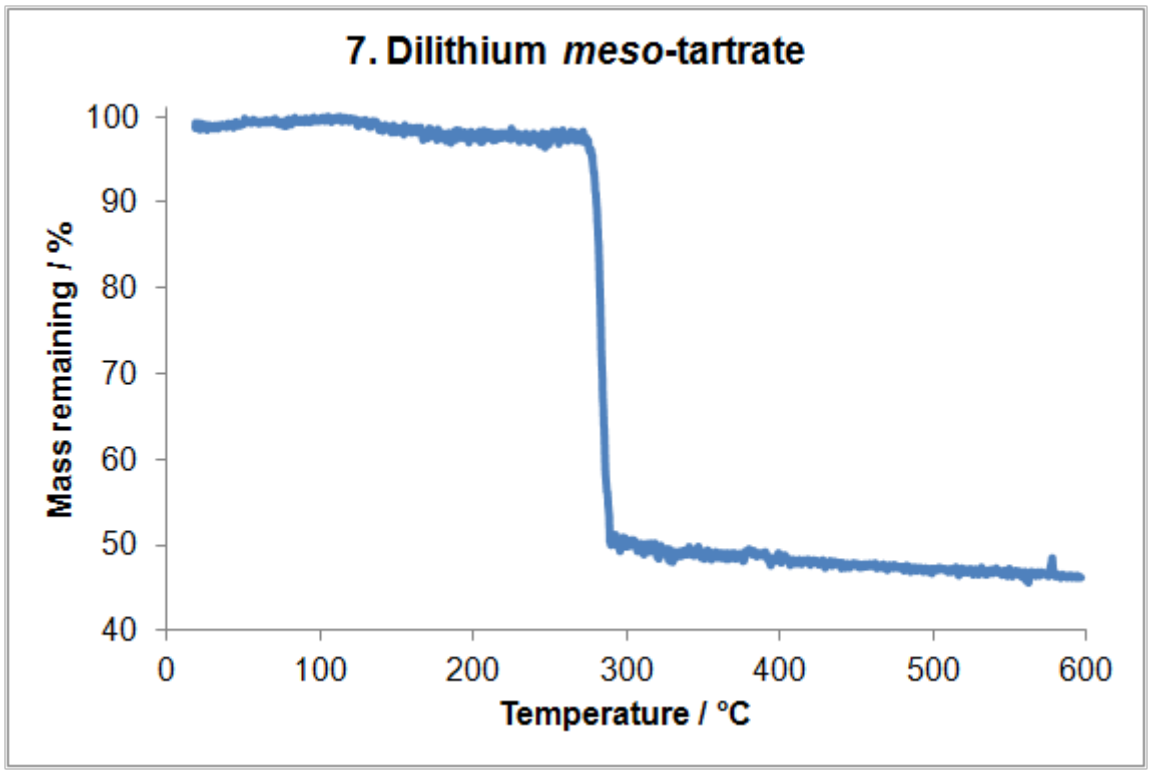

*Figure 36. Dilithium meso-tartrate, **7**, TGA.*

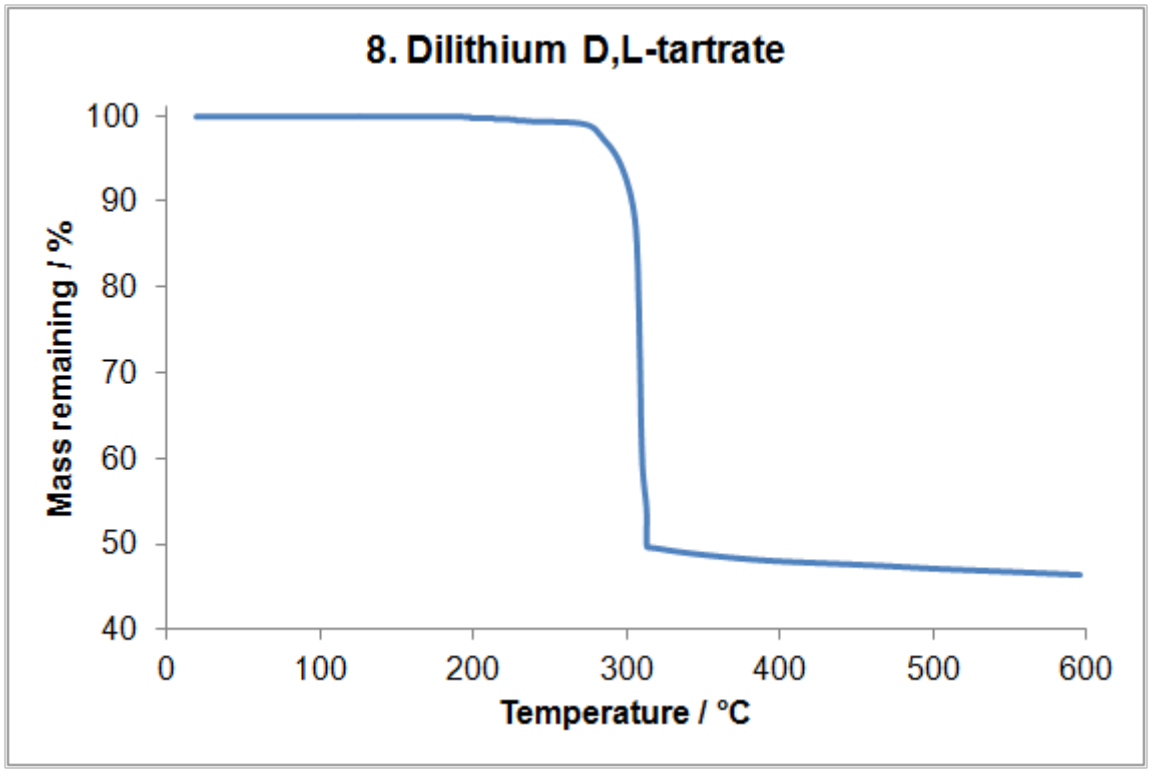

*Figure 37. Dilithium D,L-tartrate, **8**, TGA.*

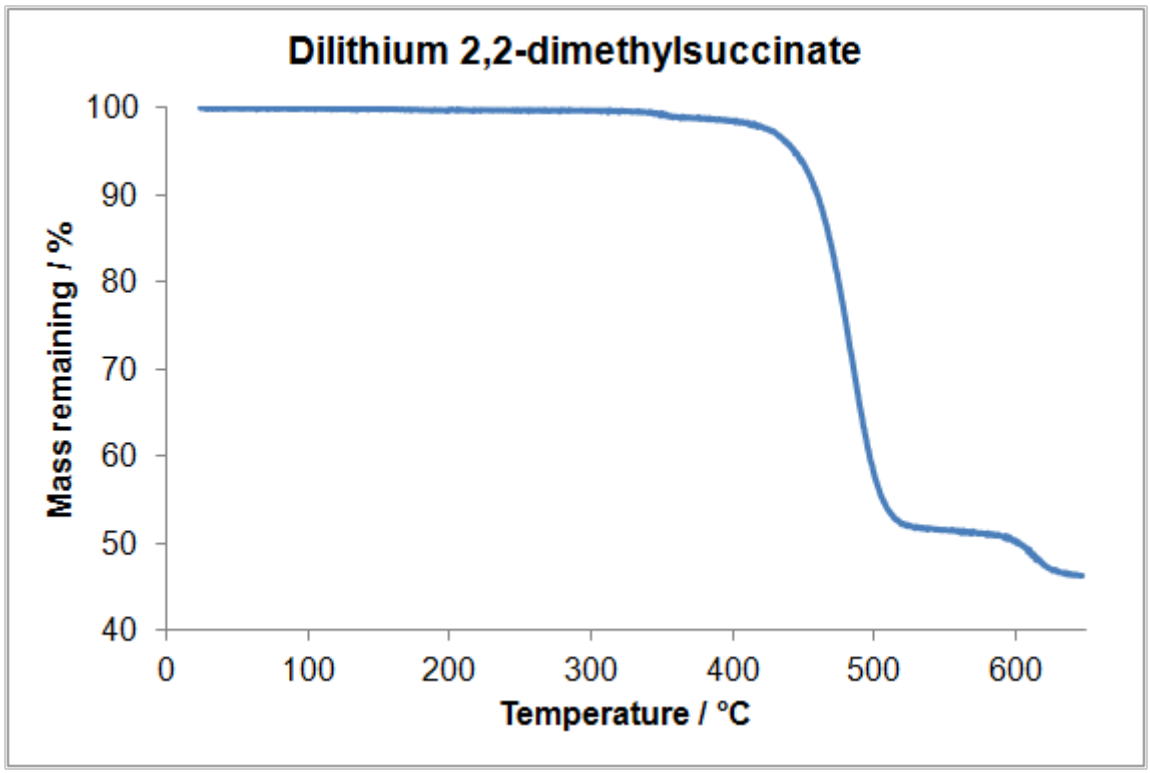

Figure 38. Dilithium 2,2-dimethylsuccinate TGA.

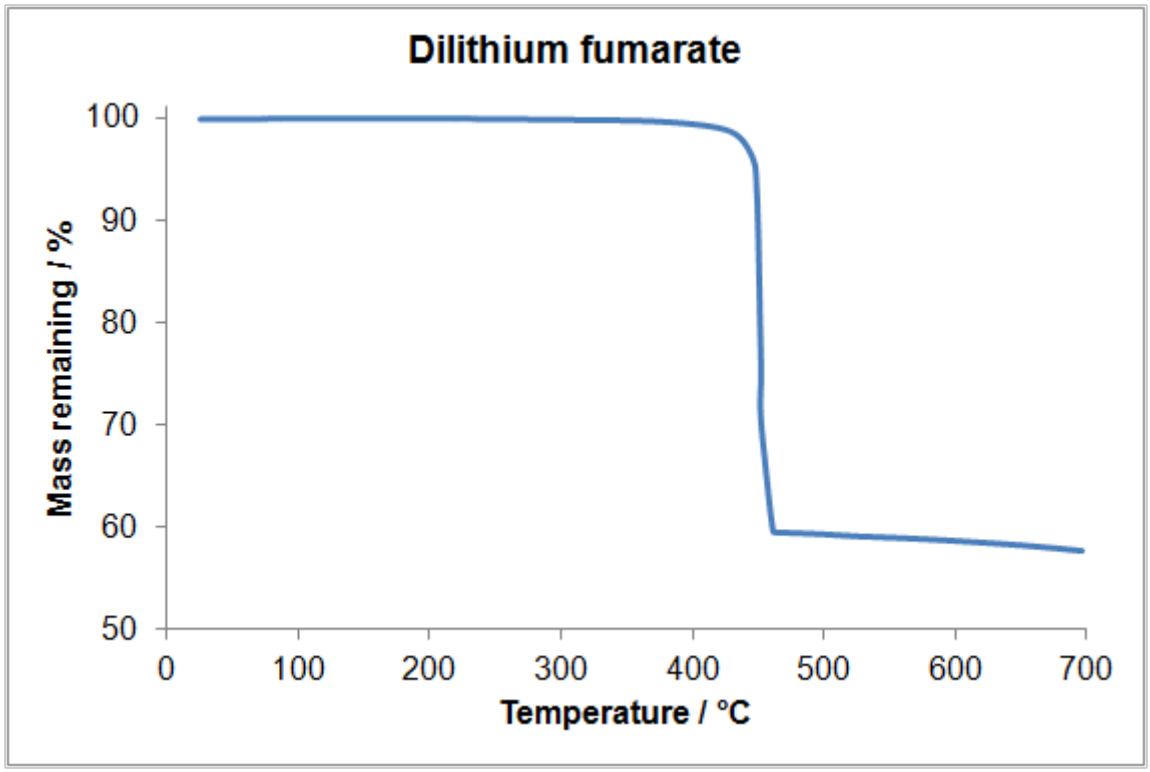

Figure 39. Dilithium fumarate TGA.

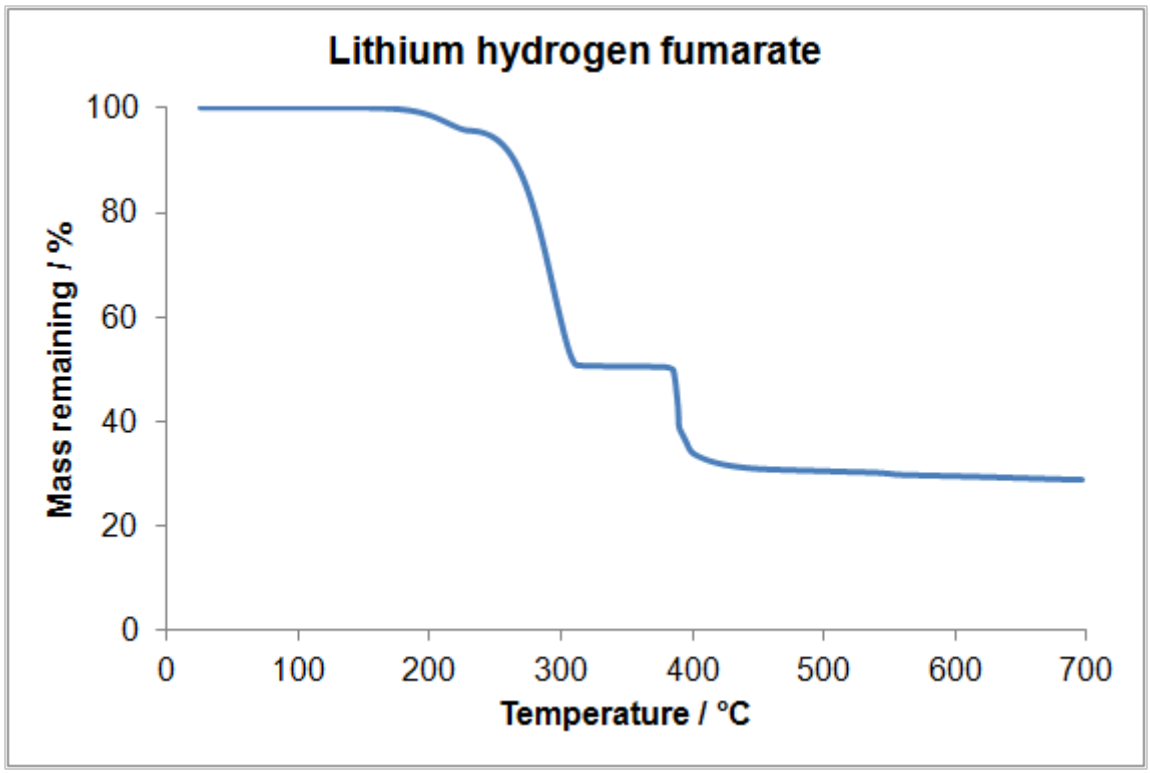

Figure 40. Lithium hydrogen fumarate TGA.

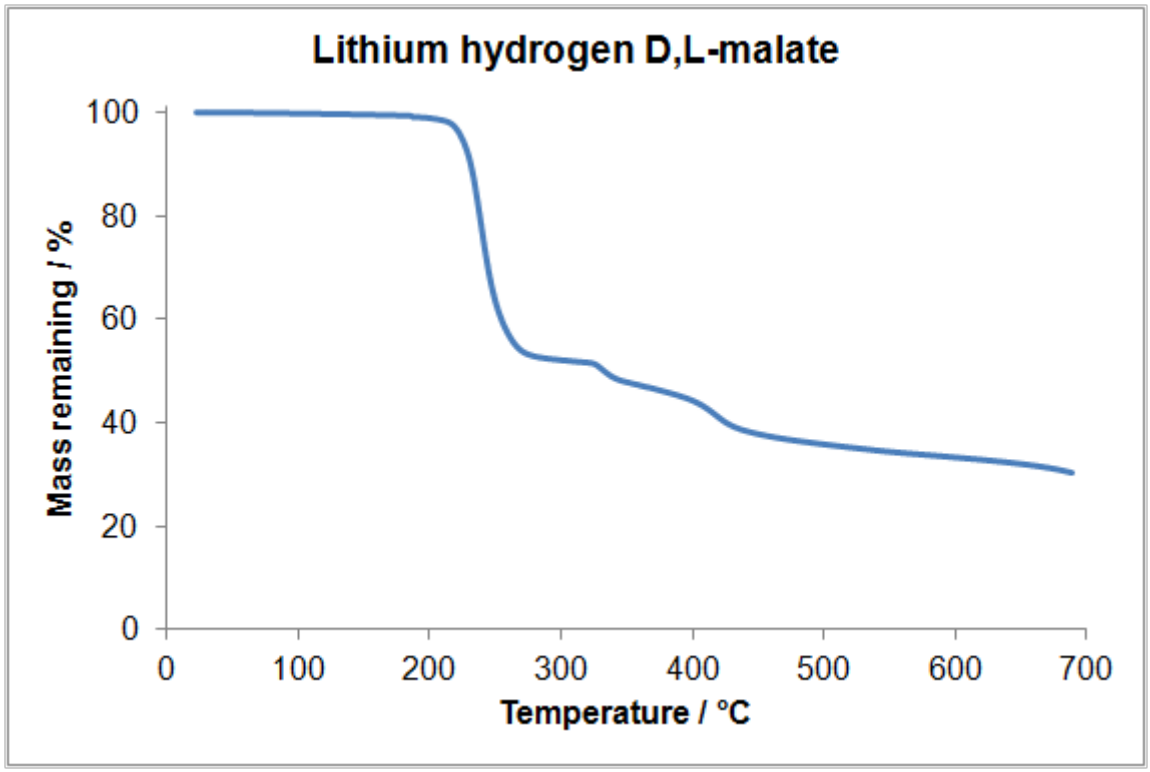

Figure 41. Lithium hydrogen D,L-malate TGA.

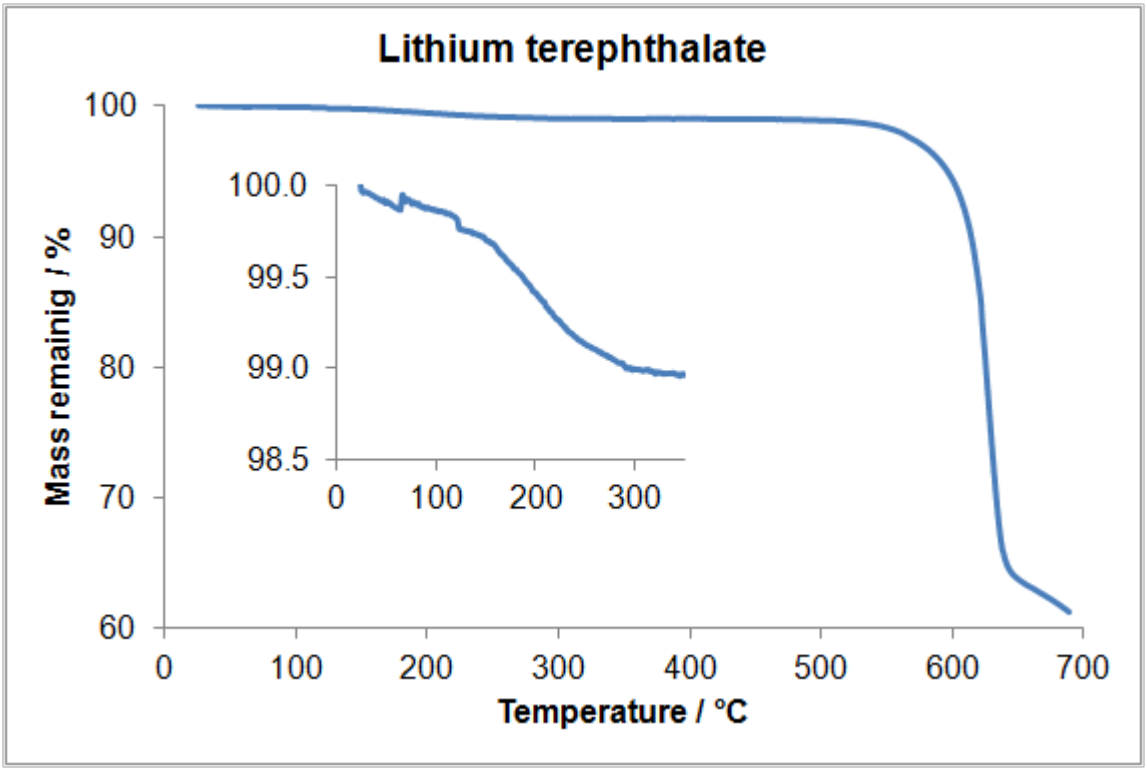

Figure 42. Lithium terephthalate (mechanochemical synthesis) TGA.